



Jan Uwe Schmidt

Synthesis of silicon nanocrystal memories by sputter deposition



Wissenschaftlich-Technische Berichte
FZR-425
März 2005

Jan Uwe Schmidt

**Synthesis of silicon nanocrystal
memories by sputter deposition**

Bibliothek FZ Rossendorf



01278460



Forschungszentrum
Rossendorf

**FORSCHUNGSZENTRUM
ROSSENDORF e.V.**

Institut für Ionenstrahlphysik und
Materialforschung

Jan Uwe Schmidt

**Synthesis of silicon nanocrystal
memories by sputter deposition**

Dissertation

Synthesis of silicon nanocrystal memories by sputter deposition

Untersuchung zur Herstellung von
Silizium-Nanokristall-Speichern durch Sputterverfahren

Dissertation zur Erlangung des akademischen Grades
Doctor rerum naturalium
(Dr. rer. nat.)

vorgelegt der

Fakultät Mathematik und Naturwissenschaften
der Technischen Universität Dresden

von

Jan Uwe Schmidt

geboren am 08.12.1971 in Leipzig

Eingereicht am: 19.03.2004

Verteidigt am: 15.10.2004

Betreuer: Dr. Bernd Schmidt
Forschungszentrum Rossendorf e.V.

Gutachter: Prof. Dr. Manfred Helm
Forschungszentrum Rossendorf e.V.

Prof. Dr. Jörg Weber
Technische Universität Dresden

PD. Dr. Margit Zacharias
Max-Planck-Institut für Mikrostrukturphysik Halle

Abstract

In silicon nanocrystal memories, electronic charge is discretely stored in isolated silicon nanocrystals embedded in the gate oxide of a field effect transistor. The stored charge determines the state of the memory cell. One important aspect in the technology of silicon nanocrystal memories is the formation of nanocrystals near the SiO₂-Si interface, since both, the size distribution and the depth profile of the area density of nanocrystals must be controlled. This work has focussed on the formation of gate oxide stacks with embedded nanocrystals using a very flexible approach: the thermal annealing of SiO₂/SiO_x ($x < 2$) stacks. A sputter deposition method allowing to deposit SiO₂ and SiO_x films of arbitrary composition has been developed and optimized. The formation of Si NC during thermal annealing of SiO_x has been investigated experimentally as a function of SiO_x composition and annealing regime using techniques such as photoluminescence, infrared absorption, spectral ellipsometry, and electron microscopy. To proof the concept, silicon nanocrystal memory capacitors have been prepared and characterized. The functionality of silicon nanocrystal memory devices based on sputtered gate oxide stacks has been successfully demonstrated.

Zusammenfassung

In Silizium-Nanokristall-Speichern werden im Gate-Oxid eines Feldeffekttransistors eingebettete Silizium Nanokristalle genutzt, um Elektronen lokal zu speichern. Die gespeicherte Ladung bestimmt dann den Zustand der Speicherzelle. Ein wichtiger Aspekt in der Technologie dieser Speicher ist die Erzeugung der Nanokristalle mit einer wohldefinierten Größenverteilung und einem bestimmten Konzentrationsprofil im Gate-Oxid. In der vorliegenden Arbeit wurde dazu ein sehr flexibler Ansatz untersucht: die thermische Ausheilung von SiO₂/SiO_x ($x < 2$) Stapelschichten. Es wurde ein Sputterverfahren entwickelt, das die Abscheidung von SiO₂ und SiO_x Schichten beliebiger Zusammensetzung erlaubt. Die Bildung der Nanokristalle wurde in Abhängigkeit vom Ausheilregime und der SiO_x Zusammensetzung charakterisiert, wobei unter anderem Methoden wie Photolumineszenz, Infrarot-Absorption, spektroskopische Ellipsometrie und Elektronenmikroskopie eingesetzt wurden. Anhand von MOS-Kondensatoren wurden die elektrischen Eigenschaften derart hergestellter Speicherzellen untersucht. Die Funktionalität der durch Sputterverfahren hergestellten Nanokristall-Speicher wurde erfolgreich nachgewiesen.

Keywords

Nanocrystal memory, sputter deposition, silicon nanostructures, phase separation, flash memory

Table of Contents

1	Introduction	1
1.1	Motivation	1
1.1.1	Optical applications of silicon nanostructures	1
1.1.2	Memory applications of silicon nanoclusters	3
1.2	Review of silicon quantum dot memory devices	3
1.3	Si NC memories by deposition techniques	4
1.4	Aim and structure of this work	5
2	Principles of Si NC formation by phase separation of SiO_x ($x < 2$)	7
2.1	General aspects of phase separation in supersaturated solid solutions	7
2.1.1	Impurity-matrix phase diagram	7
2.1.2	Homogeneous and inhomogeneous nucleation	9
2.1.3	Growth, ripening and coalescence of precipitates	11
2.2	Phase separation in confined geometry	12
3	Principles of characterization techniques	15
3.1	Transmission electron microscopy (TEM)	15
3.2	Rutherford backscattering spectrometry (RBS)	16
3.3	Elastic Recoil Detection (ERD)	18
3.4	Infrared (IR) absorption spectroscopy	19
3.4.1	IR absorption bands of silicon oxide	19
3.4.2	Model of IR absorption of silicon oxides	21
3.4.3	Experimental support of the model	22
3.4.4	Absorption of infrared light by the silicon substrate	23
3.4.5	Interference effects	24
3.5	Photoluminescence (PL) of Si nanostructures	26
3.5.1	Quantum confinement model of PL of Si nanostructures	26
3.5.2	Si nanoclusters embedded in SiO_2	26
3.5.3	Si nanoclusters embedded in Si_3N_4	28
3.6	Ellipsometry	30

3.6.1	Principles	30
3.6.2	The parametrization of optical constants	30
3.6.3	Effective medium approximations	32
3.7	The capacitance of MOS structures	34
3.7.1	The MOS capacitance at high and low frequencies	34
3.7.2	The effect of trapped charge	36
3.8	Currents in MOS structures	37
3.8.1	Electrode limited currents	37
3.8.2	Bulk limited currents	39
4	Principles of sputter deposition	43
4.1	Deposition modi	43
4.2	General effects of deposition parameters	44
4.3	Sputter deposition of silicon oxide - Review	45
4.3.1	Reactive sputtering from the silicon target	46
4.3.2	Reactive sputtering from fused silica or quartz targets	47
5	Experiments on sputter deposition of Si, SiO_x, and SiO₂ thin films	49
5.1	The deposition tool	49
5.2	Reactive sputter deposition from the Si target in Ar/O ₂	50
5.2.1	Process characterization	50
5.2.2	Limitations of the method	52
5.2.3	Preparation of SiO ₂ /SiO _x /SiO ₂ heterostructures	53
5.2.4	Conclusion and new strategy	56
5.3	Reactive sputter deposition from the fused silica target in Ar/O ₂	56
5.4	Deposition from SiO ₂ and Si targets in pure Ar	57
5.4.1	Deposition of SiO ₂	59
5.4.2	Deposition of Si	59
5.4.3	Future application: Dielectric Si/SiO ₂ NIR Bragg-mirrors	64
6	Co-sputtering of SiO_x and investigation of Si NC formation by annealing	65
6.1	SiO _x films by co-deposition from SiO ₂ and Si targets in pure Ar	65
6.2	Investigation of SiO _x composition by RBS	67
6.2.1	Investigation of SiO _x composition by ERD	69
6.2.2	Remarks on substrate requirements for ion beam analysis	69
6.2.3	XTEM investigation of annealed silicon rich oxide films	72
6.3	Infrared spectroscopy of silicon oxides	76
6.4	PL measurements of annealed SiO _x films	80
6.5	Variable angle spectroscopic ellipsometry (VASE)	83

7	Simulation of Si NC formation by annealing of SiO₂/SiO_x layer-stacks	91
7.1	The kinetic 3D lattice Monte-Carlo method	91
7.2	Investigated configurations	92
7.3	Results	92
7.3.1	Configurations S0, S1 and S2	92
7.3.2	Configurations S3 and S4	97
7.3.3	Conclusions	97
8	Si NC memory capacitors prepared by cosputtering	99
8.1	Sample Preparation	99
8.2	Electron Microscopy	101
8.3	Ellipsometry	103
8.4	Photoluminescence Measurements	105
8.5	Current-Voltage (IV) Measurements	108
8.6	High-frequency capacitance-voltage (HFCV) measurements	111
8.7	Capacitance-voltage cycling test: The memory window of Si NC capacitors	113
8.8	Current-voltage cycling test: Transient currents due to charging of Si NC	116
8.9	Retention tests	120
8.9.1	Basics of charge retention test	120
8.9.2	Ways to test charge retention in MOS memory capacitors	122
8.9.3	Retention measurements	124
8.10	Effect of height and duration of write/erase pulses	126
8.11	Endurance tests	129
9	Summary and outlook	133
9.1	Summary	133
9.2	Outlook	135

List of Figures

1.1	Comparison of EEPROM and Tiwari's Si NC memory.	2
1.2	Principle of a memory transistor.	2
1.3	Single layers of Si NC prepared from SiO/SiO ₂ superlattice	5
2.1	Schematic phase diagram of a binary mixture.	8
2.2	Effect of supersaturation on nucleation barrier.	8
2.3	Illustration of Gibbs-Thomson relation.	11
2.4	Formation of spatial oscillations in the volume fraction of precipitates. .	12
3.1	The used modes of TEM operation.	16
3.2	RBS-principle	18
3.3	Principle of Bragg ionization chamber.	20
3.4	IR transmittance of a 100 nm thermally grown SiO ₂ film.	22
3.5	IR absorption of Si. Interference effects caused by the Si substrate. . .	25
3.6	Three region model of photoluminescence (PL) from Si nanostructures.	28
3.7	Experimental data on PL energy vs. size of Si nanoclusters.	29
3.8	Effect of oxygen passivation on PL of Si nanoclusters.	29
3.9	Principle of ellipsometric measurements.	30
3.10	The MOS capacitance at high (HF) and low frequencies (LF).	35
3.11	Capacitor model of floating gate structures.	36
3.12	Electrode limited currents	37
3.13	Bulk limited currents	40
4.1	Principle of magnetron sputter deposition.	44
4.2	Thornton's zone diagram.	45
5.1	Schematic of NORDIKO 2000 sputter chamber.	49
5.2	Emission spectrum from Ar plasma during deposition of SiO ₂	50
5.3	Dependence of plasma line intensities on oxygen partial pressure.	51
5.4	The intensity of the 251 nm Si I line vs. SiO _x composition x.	51
5.5	SiO _x deposition rates for reactive sputtering from the Si target.	52

5.6	SEM image of particle ejected from the Si target rf sputtered in Ar/O ₂ .	54
5.7	Si line intensity at 251.9 nm during deposition of SiO ₂ /SiO _{1.5} /SiO ₂ stack.	54
5.8	TEM image of memory capacitor prepared by reactive rf sputtering of Si.	55
5.9	AFM measurements of SiO ₂ films sputtered from SiO ₂ target.	58
5.10	Refractive index of sputtered SiO ₂ films.	58
5.11	Deposition rates of SiO ₂ and a-Si in Ar.	60
5.12	Refractive indices of sputter deposited amorphous SiO ₂ and Si films. . .	61
5.13	H-content of a-Si films sputtered in pure Ar determined by NRA. . . .	62
5.14	AFM-images of a-Si films.	63
5.15	Reflectance of Bragg-mirror based on a Si/SiO ₂ multi-stack	64
6.1	Rates for co-sputtering of SiO _x . Thickness of Si sublayers vs. setpoint. .	68
6.2	RBS measurement of SiO _x film composition.	70
6.3	Comparison of SiO _x compositions determined by ERD, RBS and VASE.	71
6.4	ERD depth profiles of H, O, and Si across 120 nm thick SiO _{0.5} film. . .	71
6.5	TEM images of annealed SiO _x films (high resolution / bright field). . .	74
6.6	TEM measurement of annealed SiO _x films (dark field / diffraction). . .	75
6.7	IR transmittance of SiO _x films before and after anneals in Ar.	77
6.8	Energy of oxygen stretch vibration vs. SiO _x composition x.	78
6.9	PL spectra of SiO _x films vs. composition and annealing temperature. .	82
6.10	The dielectric constants of crystalline and amorphous Si.	83
6.11	Effect of annealing on averaged Si NC optical constants 1.	85
6.12	Effect of annealing on averaged Si NC optical constants 2.	89
7.1	Monte-Carlo simulation of annealing of SiO ₂ /SiO _x /SiO ₂ /Si stacks. . . .	93
7.2	Evolution of the Si-excess concentration profiles during annealing: S0-S2.	94
7.3	Evolution of tunneloxide width and mean distance of neighboring Si NC	94
7.4	Evolution of the Si-excess concentration profiles during annealing: S3-S4.	95
7.5	Evolution of mean Si NC diameter and area-density of Si NC	95
8.1	Flow chart for processing of Si NC memory capacitors.	100
8.2	Rapid thermal processes used in preparation of memory capacitors. . .	100
8.3	TEM measurements of Si NC memory capacitors.	102
8.4	The substrate related PL near ~1000 nm vs. power density and anneal.	105
8.5	PL of Si NC memory capacitors in dependence of annealing regime. . .	106
8.6	Current-voltage (IV) characteristics for SiO ₂ reference sample.	108
8.7	Current voltage (IV) characteristics for memory capacitors.	109
8.8	IV characteristics of memory capacitors vs. annealing regime.	109
8.9	Interface state density of memory capacitors vs. annealing treatment. .	112
8.10	Si NC memory capacitors: capacitance-voltage cycling tests.	114
8.11	The memory window of capacitors with 9 nm or 19 nm thick SiO _x film.	115

8.12	Transient charging currents observed by current-voltage cycling tests 1.	117
8.13	Transient charging currents observed by current-voltage cycling tests 2.	118
8.14	The use of constant-capacitance methods to sense the flat-band-voltage.	124
8.15	Short term retention test of capacitors with 10 nm SiO _x layer.	125
8.16	Long time retention tests (intermittent constant capacity mode).	127
8.17	Effect of write pulse duration on flat-band voltage shift.	128
8.18	Principle of an endurance test.	129
8.19	Endurance measurements of selected samples.	130

List of Tables

3.1	IR absorption bands of SiO_2	21
3.2	Elementary bands of the oxygen-stretch vibration in SiO_2 and SiO_x	23
3.3	Multi-phonon and impurity absorption of Si in the infrared region.	24
4.1	Review of reports on sputtered silicon oxide films.	48
6.1	Summary of sample data.	66
6.2	Ellipsometric fit parameters of as deposited and annealed SiO_x films.	84
6.3	Fit parameters for the annealing dependent optical constants of $\text{SiO}_{0.54}$ 1.	86
6.4	Fit parameters for the annealing dependent optical constants of $\text{SiO}_{0.54}$ 2.	88
7.1	Summary of simulated gate stack configurations.	92
8.1	Summary of experimental data on Si NC memory and reference capacitors.	104

1 Introduction

1.1 Motivation

In the past few years the research on nanomaterials has developed enormously, extending today into nearly every field of science and engineering. This strong interest was triggered by the finding that fundamental physical, chemical and biological properties of materials may change drastically when the material structure size decreases into the nanometer range. Among the origins for this change are quantum size effects, the confinement of electronic or vibronic excitations, and the large surface to volume ratio of nanostructures.

1.1.1 Optical applications of silicon nanostructures

Also Si nanostructures have been investigated intensely. Even though Si based devices pervade everyday life, for a long time it has played only a minor role in optoelectronics, since due to the indirect band gap, bulk Si is an extremely inefficient light emitter. Instead, direct band gap materials, such as GaAs, InP and GaN are used for lasers and light emitting diodes (LED). However, an integration of these materials into Si based devices is complicated. Si based light emitters would enable the integration of both electronic and photonic devices on the same chip in Si technology. The several approaches to Si based light emitters recently were reviewed by Pavese [1]. One approach are Si nanostructures or Si nanoclusters (Si NC) with a size below ~ 5 nm, in which quantum confinement, leads to a widening of the energy gap and a relaxation of momentum conservation. The resulting higher probability of direct optical transitions is one reason for the observation of visible light emission from highly porous Si [2, 3] and Si NC. After the demonstration of optical gain from Si NC embedded in SiO₂ by Pavese [4], even a Si based laser seems possible. Recently STMicroelectronics (Catania, Italy) introduced LEDs based on rare-earth implanted SiO₂ films with embedded Si NC. In this case, injected electrons and holes are efficiently captured by the Si NC, and transfer their energy to optical transitions in neighbored rare earth atoms that then efficiently emit the light. Short term external quantum efficiencies of up to 10 % were achieved (comparable to LEDs based on III-V semiconductors), while on the long term still external quantum efficiencies of 0.1 % were reached [5].

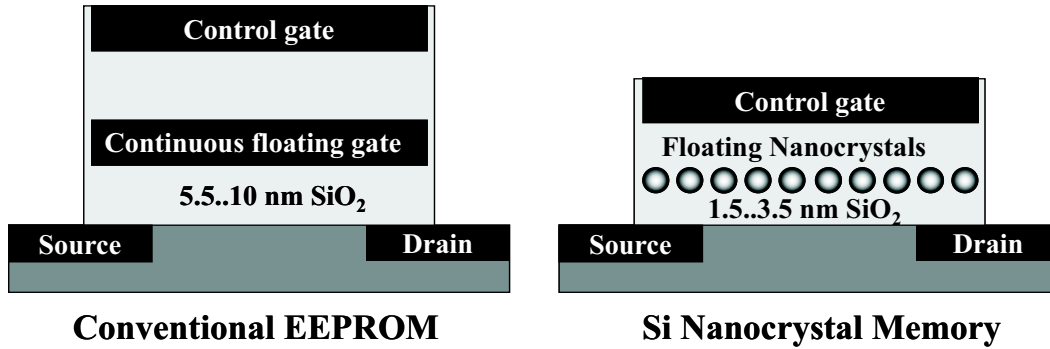


Figure 1.1: Comparison of conventional EEPROM cell (left) and silicon nanocrystal memory proposed 1995 by Tiwari et al. (IBM) [6].

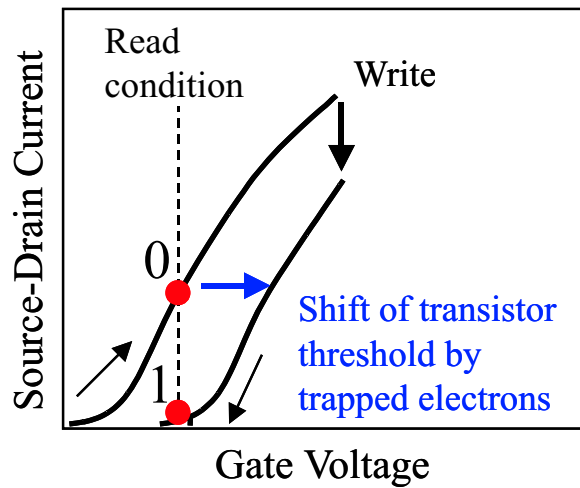


Figure 1.2: During 'Write' operation electrons are injected into the storage node. This leads to a shift of the transistor threshold voltage and changes the memory state, given by the readout current, from '0' to '1'.

1.1.2 Memory applications of silicon nanoclusters

Another application of silicon nanoclusters are memory devices. The left side of Fig. 1.1 depicts schematically a conventional floating gate type memory transistor for use in EEPROM¹ devices and FLASH memories. In a conventional EEPROM a polycrystalline silicon 'floating gate' electrode with finite lateral conductivity serves to trap electrons injected by Fowler-Nordheim tunneling. Electron injection leads to a shift of the threshold voltage of the transistor as indicated in the transistor characteristics of Fig. 1.2. The drawbacks of this concept are the limited scalability and the fact that the number of write/erase cycles to device failure (endurance) is limited to about 10^6 by the damage of the injecting tunnel-oxide caused by hot electrons. Alternative memory concepts include silicon-nanocluster based memories, the most prominent ones being the Yano memory [7] and the Si nanocrystal memory proposed by Tiwari [6]. Since such memories operate with a small number of electrons and have better scaling properties, they are promising candidates for future memory devices, which require high integration density and low-power consumption. The Si nanocrystal memory concept proposed by Tiwari [6] (right side of Fig. 1.1), additionally differs from the EEPROM inasmuch as the injection mechanism is direct electron tunneling and the charge is stored in electrically isolated Si quantum dots, such that the lateral charge transport is suppressed. Today this concept of Si nanocrystal memories is investigated intensely by companies like Motorola [8] and STMicroelectronics [9]. According to Motorola officials in a few years these memories could come on the market as replacements for today's FLASH memories [10]. Simultaneously, the Si nanocrystal memory competes with other novel FLASH concepts in which the traditional continuous polycrystalline Si floating gate is replaced by a discrete-trap type storage node. One example is the NROMtm developed by Saifun semiconductors [11] and currently transferred into production at the Dresden Infineon fab. The NROMtm is based on an ultrathin SiO₂/Si₃N₄/SiO₂ gate stack, with the nitride film acting as storage layer. The depth of Si NC related levels below the edge of the SiO₂ conduction band is according to DiMaria [12] 3-4 eV, according to Afanasev [13] 2.8 eV. Naich [14] found, that the trap levels of the competing SONOS² memories are shallower (0.82 eV, 0.93 eV, 1.09 eV and 1.73 eV). With respect to a desired long charge retention time, the higher activation energies of carriers out of the Si NC memory are beneficial, since they render thermal detrapping less likely. A more detailed review of nanocrystal memory devices is given below.

1.2 Review of silicon quantum dot memory devices

Several routes to produce silicon nanocrystals have been explored: Si nanocrystals were deposited by an aerosol technique in combination with a radial differential mass analyzer [15], self-assembled by chemical vapor deposition (CVD) [6], low-pressure CVD (LPCVD)[16], annealing of silicon rich oxide deposited by CVD [12, 17], oxidation of thin polycrystalline Si layers deposited onto SiO₂ [18], or Si ion implantation and high-temperature annealing [19, 20]. In contrast to memories with a continuous

¹EEPROM: electrically erasable programmable read only memory.

²SONOS: silicon-oxide-nitride-oxide-silicon (the materials of the layered gate stack)

floating-gate (FG), those using discrete-trap-type storage nodes are robust against defects in tunnel oxide, since a single defect no longer leads to complete loss of stored charge. The absence of lateral charge movement even allows to selectively charge the FG layer near the source or near the drain of a transistor, which (in analogy to the NROMTM concept) has been used for the preparation of a two-bit (i.e. 4 state) memory cell [8]. In fact, the use of discrete-trap type storage nodes turns out to be a key issue in conventional FLASH memory technology, as the transistor channel lengths approaches 0.1-0.13 μm [10]. By coupling nano-crystals to the channel of conventional MOS transistors through ultrathin direct-tunneling oxides (thickness lower than 3.5 nm) various 'long-refresh-time dynamic' to 'quasi-nonvolatile' 'multi-dot-nano-flash' memories have been demonstrated [21, 19, 6]. In addition to an improved endurance (the number of write/erase cycles to device failure) resulting from direct tunnel injection instead of hot-electron-injection or Fowler-Nordheim tunneling, the prevention of vertical and lateral charge movement yields an important gain in memory data-retention [21], which enables further shrinkage of the memory cell, lower operational voltages and lower power consumption. When the tunnel oxide thickness is decreased, the tradeoff between shorter write/erase times and worse data retention must be considered. The shortest write/erase times on the order of 10^{-9} s have been achieved at cost of data retention times on the order of minutes or seconds [21]. To obtain a retention time on the order of 10 years, programming times on the order of 10^{-5} s are required, which is slow compared to other concepts like magnetic memories (MRAM) or resonant tunneling devices (RTD) for which write times of 10^{-8} s appear realistic [22]. According to model calculations, this 'Achilles heel' may be overcome by optimized 'crested' multi-layer tunnel barriers [23, 24, 25] that enable both fast writing and high retention. Despite the large number of Si nanocrystals used in the typical multi-dot memory cell (100-1000), at low temperature single electron charging phenomena have been observed in cases, where the size distribution of Si NC was narrow. This suggests that due to the Coulomb barrier effect even a multi-dot nanocrystal memory cell could have more than two discrete states [6]. Field effect transistor (FET) devices with few, or even one single NC in the vicinity of a very narrow channel, show evidence of the Coulomb blockade effect even at room temperature, both in the static regime (plateau regions in the transistor threshold voltage vs. write voltage characteristics) [26, 27, 28, 29] but also in the dynamic regime, i.e. during write [7] and erase [30] processes.

1.3 Si NC memories by deposition techniques

The key issue in the technology of nanocrystal memories is to fabricate the nanometer scale dots in a well defined manner. Although significant progress has been achieved by ion beam synthesis of Si nanocrystals, currently, among the preparation methods for Si NC memories, a deposition method, i.e. the direct growth of Si NC by LPCVD, is leading. One advantage of deposition methods over ion beam synthesis is the good process control by sequential preparation of layers with a different functionality. This includes the option to use predefined tunneling barriers, such that write/erase and retention times can be adjusted independently from the formation of the Si NC. The concept of optimized multilayer tunnel barriers, different from SiO_2 , is not compatible with

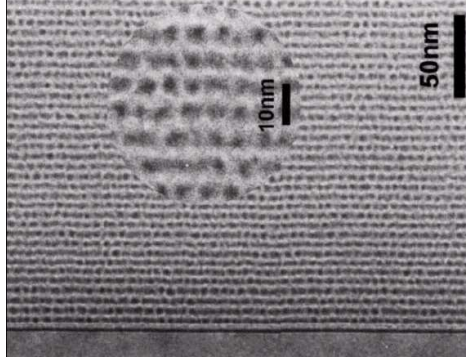


Figure 1.3: Size controlled growth of Si nanocrystals by annealing of a deposited SiO/SiO₂ superlattice (cross-section electron microscopy image from Zacharias [31]).

ion beam synthesis of silicon nanocrystals, since collisional mixing caused by energetic ions would degrade the multilayer barrier. On the other hand, a major challenge of the LPCVD methods is to achieve the required high density of Si NC, while maintaining the homogeneity of size and area density in the diameter range below 5 nm [32], which is interesting for single electron devices. The processing of single electron devices (in which switching between states involves tunneling of only one electron) is very demanding with respect to reliability and involves the formation of crystalline islands of subnanometer size, at good uniformity of size and shape, the accurate island placement, and the minimization of background charge [33]. In this respect, an important step towards the control of order, size, shape and crystallinity of silicon nanocrystals has been made by Grom [34], who succeeded in the control of crystallinity and shape of Si nanocrystals, formed by annealing a deposited Si/SiO₂ superlattice. Unfortunately, in his case the nanocrystals were touching each other, resulting in a finite lateral conductivity [35]. However, in a similar approach, Zacharias succeeded in the formation of mono-disperse, oxide-separated and ordered Si nanocrystals, arranged in single layers by annealing a SiO₁/SiO₂ superlattice, prepared by reactive evaporation of SiO (Fig. 1.3). Hereby the SiO₁ layer thickness was below 3 nm [31].

Thus, an emerging advantage of the formation of Si nanocrystals by annealing of deposited oxygen-deficient silicon oxide over all other methods, is to combine the potential of controlling independently the size of nanocrystals and the vertical localization in the gate oxide, while self-organization during nucleation and growth ensures a homogeneous lateral distribution of nanocrystals.

1.4 Aim and structure of this work

Yet the SiO_x/SiO₂ superlattice approach has not been applied to the formation of memory devices, but it might impact the technology of future single electron and multi-dot-nano-flash memories. When transferring this technological approach into production, probably other deposition techniques, i.e. CVD or sputter deposition will succeed. At present, the deposition of dielectric films in semiconductor industry is dominated by CVD methods. This is because of the established quality of CVD-SiO₂. The use of sputtered gate oxides is limited to thin film transistors (TFT), where

low deposition temperatures are required. However it has been demonstrated that annealed sputter deposited SiO_2 films may reach an electrical quality comparable to thermal oxides [36, 37, 38, 39]. Compared to CVD, an advantage of sputtered oxides is the low hydrogen content, since hydrogen is known as source of oxide instability [40]. While fully functional memory devices prepared by annealing of off-stoichiometric silicon oxides deposited by CVD have been reported [12, 17], so far no convincing reports on a sputter deposited Si NC memories seem to exist.

This work is consequently focused on the investigation of a new technology for the preparation of silicon nanocrystal-memories. In the selected novel approach first a dielectric gate stack of SiO_x ($x < 2$) and SiO_2 layers is sputtered near room temperature onto a thin tunnel-oxide on silicon. Thereafter a high temperature anneal transforms the homogeneous SiO_x layer into a layer of SiO_2 with embedded Si NC and completes the processing of the dielectric gate stack. To realize this approach, the work was structured into the following steps:

- Study and review of relevant literature and methods.
- Development of processes for an ultrathin tunnel-oxide and high quality sputtered SiO_2 for use as control-oxide.
- Evaluation of methods for the preparation of an oxygen-deficient silicon oxide inter-layer (the precursor of the Si NC layer).
- Characterization of as-deposited films.
- Investigation of the phase separation of SiO_x and the formation of Si NC by simulations and experiments.
- Fabrication and of MOS capacitors with embedded Si NC and demonstration of their memory functionality.

2 Principles of Si NC formation by phase separation of SiO_x ($x < 2$)

2.1 General aspects of phase separation in supersaturated solid solutions

Si NC can be prepared by annealing of SiO_x ($x < 2$) films. Since the solubility of Si in SiO_2 is very small, SiO_x ($x < 2$) films are thermodynamically not stable and tend to separate into Si and SiO_2 phases. In the limit of small Si excess this occurs by homogeneous (triggered by thermal fluctuations) or inhomogeneous (defect triggered) *nucleation of precipitates*. In the limit of high Si excess *spinodal decomposition* dominates. Since spinodal decomposition does not result in well isolated Si NC as required for the desired memory devices, this mechanism is not described here. For a literature review see Binder [41]. The following essentials of phase separation by nucleation and growth of precipitates were extracted from the work of Strobel [42].

2.1.1 Impurity-matrix phase diagram

The phase separation of SiO_x can be regarded as formation of interacting precipitates from supersaturated solid solution of a solute, i.e. 'impurity atoms' (IA, here: excess Si atoms) in a solvent or neutral matrix (here SiO_2) and corresponds to a phase transition of first order¹. The evolution of a system depends on its location in the *phase diagram*² schematically illustrated in Fig. 2.1. Systems located at different points (1, 2, 3) in this diagram behave differently with respect to fluctuations of temperature. In the *stable* region, the concentration c of IA is below the solubility limit³. In this region in equilibrium the system is homogeneous (single phase) and stable with respect to thermal fluctuations. In contrast systems located in the *metastable* region, between the *coexistence curve* given by the solubility limit (of Si in SiO_2) $c_{\text{coex}}^1(T)$ and the *spinodal* (defined by $\partial^2 G / \partial T^2 = 0$) undergo a phase separation by *nucleation and growth* of precipitates of the impurity phase. Hereby a nucleation energy barrier must be overcome to form stable precipitates. When approaching the spinodal from the metastable region, the nucleation barrier gradually lowers. It vanishes on the spinodal. The *unstable* region, completely enclosed by the spinodal, is characterized by the ab-

¹During a phase transition the Gibbs free energy G is continuous, but its derivatives with respect to temperature T may jump. If $(\partial^j G / \partial T^j)$ is discontinuous, while all lower derivatives are not, the phase transition is 'of j -th order'.

²Temperature T vs. order parameter (here concentration c of IA)

³Typical example of such a system: Silicon doped with Phosphorus or Boron.

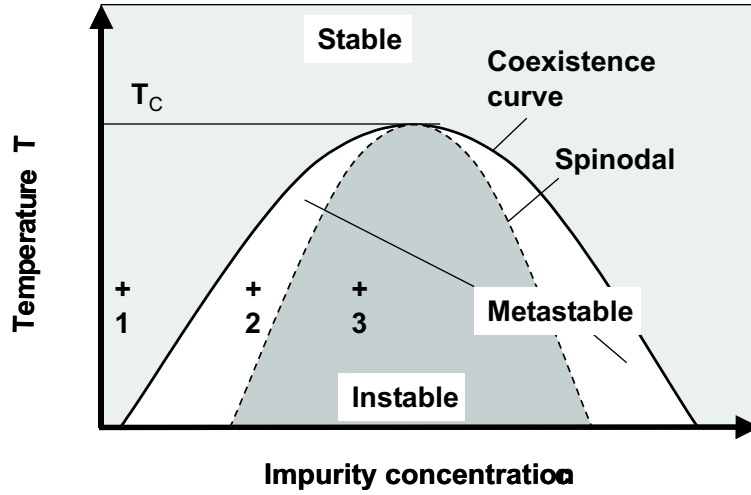


Figure 2.1: Schematic phase diagram of a binary mixture (e.g. excess Si in SiO_2) after [43]. At (1) $c < c_{coex}^1(T)$ (Si conc. below solubility limit): the system is thermodynamically stable. At (2) and (3), $c > c_{coex}^1(T)$ (Si conc. above solubility limit in SiO_2): the system is not thermodynamically stable and tends towards phase separation. In the metastable region (2) a nucleation barrier must be overcome to start *homogeneous nucleation*. In the instable region (3) no nucleation barrier exists and phase separation occurs by *spinodal decomposition*. For temperatures larger than T_C no phase transition from disorder (Si dissolved in SiO_2) to ordered state (separated Si and SiO_2 phases) is observed. For the Si/ SiO_2 mixture temperatures of T_C and above are practically not accessible (diagram after [42], modified).

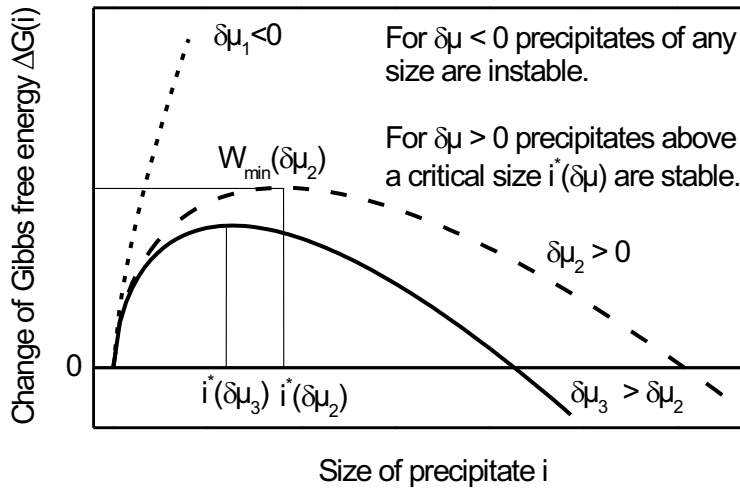


Figure 2.2: Change of Gibbs free energy during attachment of one IA to a precipitate of size i . If the supersaturation $\delta\mu < 0$ then precipitates of any size are instable. For $\delta\mu > 0$ above a critical precipitate size $i^*(\delta\mu)$ corresponding to the nucleation energy $W_{min}(\delta\mu)$ the system gains energy, i.e. the precipitates are stable (diagram after [42], modified).

sence of any nucleation barrier. Here the phase separation proceeds by a mechanism called *spinodal decomposition*⁴. Despite the fact that a supersaturated system in the metastable and instable regions is not in its energetic minimum, its phase separation may take a long time, since it also depends on the mobility of IA, which typically increases exponentially with temperature. To achieve the phase separation within a certain time, depending on the activation energy of diffusion, it may be necessary to expose the system to high temperatures. In this case the the mechanism of phase separation is determined by the concentration c and the annealing temperature. In thermal equilibrium, systems in the metastable and instable regions are inhomogeneous, i.e. made up from two phases. For a given point (c, T) in phase space, according to the *lever rule* [43], the fraction $(c - c_{coex}^1(T))/(c_{coex}^2(T) - c_{coex}^1(T))$ of IA is precipitated in domains of IA concentration $c_{coex}^2(T)$ (Si concentration in Si NC) while the remaining fraction of IA, $(c_{coex}^2(T) - c)/(c_{coex}^2(T) - c_{coex}^1(T))$, is still found in phase 1 with a concentration corresponding to the solubility limit $c_{coex}^1(T)$.

2.1.2 Homogeneous and inhomogeneous nucleation

Many experimentally observed nucleation phenomena can be understood in terms of the classical kinetic nucleation theory developed for equilibrium conditions by Volmer and Weber [44] and extended to steady-state conditions by Becker and Döring [45]. The *chemical potential per impurity atom*,

$$\mu = k_B T \cdot \ln(c) + \phi \quad (2.1)$$

serves as a useful quantity to describe the state of the system. Here the thermodynamic potential ϕ does not depend on the impurity concentration c [43] and k_B is Boltzmann's constant. The transition from stable to metastable phase (the coexistence curve) is characterized by a IA concentration at the solubility limit $c = c_{coex}^1(T)$ and the critical chemical potential $\mu_c = \mu(c_{coex}^1(T))$. The *supersaturation* of a solution is defined by:

$$\delta\mu = \mu - \mu_c = k_B T \cdot \ln(c/c_{coex}^1(T)) \quad (2.2)$$

For a system in the metastable region of the phase diagram, nucleation of second phase precipitates may be triggered by thermal fluctuations, provided that $\delta\mu > 0$ during about the inverse nucleation rate $[I(\delta\mu)]^{-1}$. In general the nucleation rate can be written as $I = A \cdot \exp(-W/k_B T)$, where W is the thermodynamic nucleation barrier and A a dynamical factor increasing with impurity concentration. This case is referred to as *homogeneous nucleation*. In contrast the so-called *inhomogeneous nucleation* is triggered by system inhomogeneities, such as defects, grain boundaries, interfaces or impurities. The inhomogeneous reaction rate $I_i = A_i \cdot \exp(-W_i/k_B T)$ can be much higher than the homogeneous one, since mostly, due to an effectively lower interface energy contribution to the nucleation barrier, $W > W_i$.

⁴Unfortunately a quantitative phase diagram of Si and SiO₂ does not exist, such that an accurate quantitative discussion is not possible. However a Si excess on the order of 1 at% is most likely sufficient to cause supersaturation within the practical temperature range ($T \leq 1200$ °C).

The energy barrier for homogeneous nucleation

The origin of the energy barrier W for homogeneous nucleation is sketched below. Assuming a finite mobility of IA, homogeneous nucleation will lead to the formation of tiny agglomerates of IA. In equilibrium the size distribution U per unit volume for clusters consisting of i IA is given by $U(i > 1) = U(1)\exp(-W_{min}/k_B T)$, $U(1) = c$, where W_{min} is the minimum reversible energy needed to form a cluster of size i , and c is the initial IA concentration. The nucleation involves the energetically unfavorable formation of a phase boundary. The change of Gibbs free energy during attachment of a single IA to a precipitate of size i is [42]:

$$\Delta G(i) = -(\delta\mu)i + \gamma i^{2/3} \quad (2.3)$$

Here the first term denotes the bulk contribution, the second the interface contribution proportional to the surface tension σ : $\gamma = (36\pi V_a^2)^{1/3}\sigma$, where V_a is the atomic volume of an IA. For a concentration of IA below the solubility limit ($\delta\mu < 0$) it is not possible to gain energy by the formation of precipitates, clusters of all sizes i are instable. However, if the solution is supersaturated ($\delta\mu > 0$), a critical precipitate size i^* exists above which precipitates may lower their free energy by attachment of IA, whereas for precipitates of a size $i < i^*$ the detachment of IA is energetically favorable (Fig. 2.2). Associated with i^* , the maximum of $\Delta G(i)$ defines the energy barrier for nucleation, which for spherical precipitates of radius r and $i = -\frac{4\pi r^3}{3V_a}$ is given by:

$$W_{min} = \Delta G(i^*) = \frac{4\gamma^3}{27(\delta\mu)^2} \text{ for } i^* = \left(\frac{2\gamma}{3\delta\mu}\right)^3 \quad (2.4)$$

According to classical nucleation theory, the energy barrier for homogeneous nucleation decreases with increasing supersaturation⁵.

Dependence of steady-state homogeneous nucleation rate on supersaturation

Assuming that growth and shrinking of precipitates are governed by attachment and detachment of single IA or 'monomers' (which is plausible since the mobility of dimers, trimers- rapidly decreases with size) and assuming steady state conditions (the supersaturation $\delta\mu$ is constant), further analysis leads to an expression for the *steady state nucleation rate* I_s of precipitates:

$$I_s = \kappa \cdot c \cdot \exp\left(-\frac{\Delta G(i^*)}{k_B T}\right) \text{ with } \kappa = 4Z\nu(i^*)^{2/3} \quad (2.5)$$

Here Z (Zeldovich factor) is a constant and ν is the atomic jump frequency at the precipitate interface.

The steady nucleation rate is explicitly linear proportional to the concentration c of IA, but nonlinearities arise from the dependence of the critical precipitate size i^* on

⁵Close to the spinodal $W_{min} \sim k_B T$. The instable region of the phase diagram is characterized by the absence of any nucleation barrier.

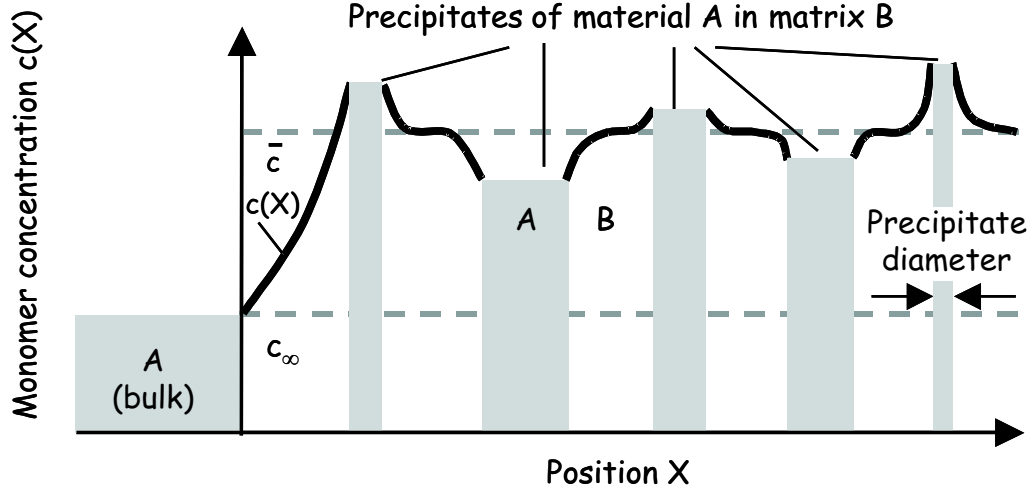


Figure 2.3: Illustration of Gibbs-Thomson relation: The equilibrium concentration $c(x)$ of dissolved monomers of material A in a matrix B higher at the interface of a small precipitate and lower at the interface of big precipitates. In the limit of infinite precipitate radius (flat interface between a material A substrate and matrix B) it approaches the solubility limit c_∞ (after [42], modified).

the concentration of IA, c . Within the steady-state approximation I_s does not depend on time t and cluster size i . Owing to the temperature dependence of ν , the steady state nucleation rate is characterized by a total thermodynamic energy barrier given by the sum of nucleation energy barrier $\Delta G(i^*)$ and activation energy of diffusion E_A .

The nucleation rate increases with the concentration of dissolved impurity atoms and (exponentially) with temperature.

2.1.3 Growth, ripening and coalescence of precipitates

After the tiny nuclei have overcome the critical size, they are stable and continue to grow by exchanging monomers with the matrix through the newly formed common phase boundary. The attachment and detachment rates depend on the curvature of the precipitate interface. A gradient in monomer concentration exists between the nanocluster (NC) interphase and the surrounding matrix. For a spherical isotropic NC of radius R , the equilibrium concentration of monomers at the interface is given by the *Gibbs-Thomson (GT) relation* [46]:

$$c^{GT}(R) = c_\infty(T) \cdot \exp\left(\frac{R_c(T)}{R}\right) \quad \text{where } R_c = \frac{2\sigma V_a}{k_B T} \quad (2.6)$$

Here, c_∞ denotes the equilibrium monomer concentration at a flat ($R \rightarrow \infty$) phase boundary⁶. R_c , the *capillary length* is given by the NC surface tension σ , the atomic volume, V_a and the thermal energy $k_B T$. In a time dependent treatment, the average monomer concentration \bar{c} is no longer constant, but a function of time and the NC

⁶In case of the Si/SiO₂ system for example the interface between a grown SiO₂ film and a Si wafer.

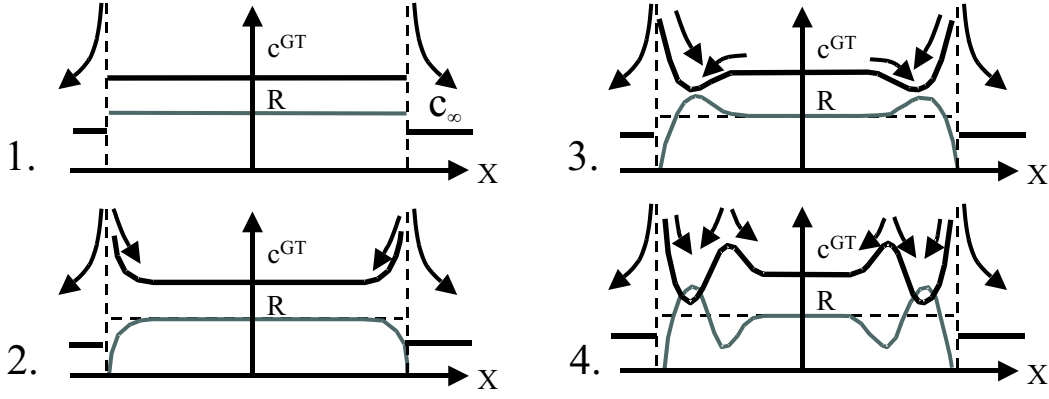


Figure 2.4: Formation of spatial oscillations in the volume fraction of precipitates: (1.) initial stage, (2.) broadening of the initially box-shaped concentration profile at the edges, (3.) enhanced growth of NC in the adjacent inner region, (4.) separation of a first local maximum in the distribution of NC (after [49]).

spatial and size distribution. Because more and more monomers condense onto NC, effectively \bar{c} decreases with time. If the average monomer concentration in the matrix \bar{c} is higher than c^{GT} then the cluster acts as sink of monomers and grows. If in contrast $\bar{c} < c^{GT}$ the NC tends to emit monomers and gradually dissolves as illustrated in Fig. 2.3. Because $R_1 < R_2$ leads to $c^{GT}(R_1) > c^{GT}(R_2)$ the monomer detachment rate for small clusters is higher than for bigger ones. Consequently larger clusters tend to grow on expense of the dissolving smaller ones, which is known as *coarsening* or *Ostwald ripening*. If the density of NC is high, it is possible that NC touch, and then rapidly minimize their energy by surface-diffusion of adatoms, such that a larger spherical cluster emerges (*coalescence*). The theory of Ostwald ripening, developed by Lifshitz and Slyozov [47] and Wagner [48], is known as *LSW-theory*. A more recent theory including the case of ripening during ion-implantation is found in [49, 42, 50].

2.2 Phase separation in confined geometry

In the above description effects of interfaces, surfaces, spacial gradients of supersaturation and the finite size of the supersaturation region were neglected although they have a significant influence on the evolution of spacial and size distribution of NC. So, the effect of sharp gradients in the initial concentration of IA has been discussed by Reiss et al. [49] for ion-beam synthesis of SIMOX⁷ structures. As a consequence of the Gibbs-Thomson relation (eqn.2.6) sharp gradients of the concentration profile may trigger the evolution of local oscillations in the volume fraction of precipitates. In Fig. 2.4 this is illustrated for the special case of an initially box shaped concentration profile of monomers and mono-disperse precipitates: (1) Precipitates at the edge of the profile initially tend to shrink, due to the gradient in monomer concentration. (2) This in turn raises c^{GT} at the edges of the concentration profile. (3) The next neighbors of the shrinking NC profit from the higher monomer concentration by a higher growth

⁷SIMOX: Separation by IMplantation of OXYgen

rate. Two local maxima of the mean NC radius are formed, corresponding to two local minima of c^{GT} acting as monomer sinks that screen the monomer excess at the edges of the initial profile. (4) The larger clusters grow rapidly and thereby lower the monomer excess around their neighbors in the inner part of the profile, which delays their growth. When the local monomer excess around these neighbors is lower than c^{GT} , they shrink and trigger the formation of the next local maximum in the distribution of NC. This leads to the formation of separate 'cluster bands'. The distance between these bands is proportional to the screening length of diffusion [51]

$$\lambda_D(t) = \frac{1}{\sqrt{4\pi \cdot n(t) \bar{R}(t)}} \quad (2.7)$$

where $n(t)$ is the density of NC and $\bar{R}(t)$ is the mean cluster radius. By material conservation, $n(t) \propto 1/\bar{V}_{NC}$ (\bar{V}_{NC} is the mean NC volume), whereas $\bar{R} \propto \bar{V}_{NC}^{1/3}$, such that $\lambda_D \propto \bar{V}_{NC}^{1/3}$. Because the NC grow with time, the spatial period of the oscillations increases with time, i.e. neighbored cluster bands tend to fuse and more distant cluster bands are formed. When the Si supersaturation layer is thin compared to the diffusional screening length and the supersaturation is not too high, then a rather stable layer of single NC is formed. This was experimentally confirmed by Zacharias for the case of Si NC formation in thin SiO_x films in SiO_2 [31]. Flat absorbing interfaces in proximity to the NC ensemble also effects the evolution of the Si NC size distribution. Since the flat interface has the lowest c^{GT} , finally all NC will dissolve and condense onto the flat interface. This process is faster for smaller mean cluster diameters \bar{R} . *Both of the above phenomena affect the formation of Si NC from an SiO_x layer embedded in SiO_2 in proximity of a flat absorbing Si substrate.* While the above discussion considered only the case of nucleation and diffusional ripening similar effects caused by the action of interfaces are known for spinodal decomposition of binary mixtures, which dominates over nucleation in the limit of high supersaturation. A review of relevant literature was given by Binder [41].

3 Principles of characterization techniques

3.1 Transmission electron microscopy (TEM)

The operational modi used for cross-section TEM (XTEM) investigations are described in the following. The scheme in Fig. 3.1-(1) shows the ray diagram for the *imaging mode*. A collimated beam hits the specimen and all, transmitted, and diffracted beams are combined to form an image at the screen. Because each point of the image contains both, transmitted rays, but also rays scattered from all over the specimen, it shows comparably little contrast. Nevertheless, a present contrast mechanism is *mass-thickness* contrast, largely originating from elastic scattering of electrons. Because the efficiency of scattering is related to the strength of Coulomb interaction, the amount of scattering increases not only with the specimen thickness, but also with atomic number Z (approximately as Z^2). In the present work this image mode is mainly used for *high resolution* imaging of nano-crystals in an amorphous matrix. If the electron beam enters a crystalline sample region along a lattice plane, coherent scattering from the piled up atomic columns allows to image individual lattice planes, provided the (point)-resolution of the microscope is smaller than the lattice spacing. Crystallites oriented in a different manner do not show lattice contrast. For a state-of-the-art TEM as the used PHILLIPS CM300, the point resolution is limited to about 0.15 nm. The resolution is governed by the phase distortion imposed onto the wavefronts by the objective lens, i.e. by the effect of spherical aberration, rather than by the electronic wavelength. If an aperture is placed in the back focal plane of the TEM, an image is made selectively with those electrons scattered by a specific angle. If the aperture allows only the transmitted (undiffracted) electrons to pass, a *bright-field* (BF) image is formed (Fig. 3.1-(2)). If similarly only a specific part of the diffracted electrons are allowed to pass the aperture, a *dark-field* (DF) image is formed (Fig. 3.1-(3)). These two modi are mostly used to investigate crystalline materials. Here the variation of electron diffraction due to different crystallite orientations across the specimen leads to strong and complementary contrast in the separate bright- and dark-field images, whereas the 'recombined' image taken without aperture shows much lower contrast. If by using of one of the above imaging modes a feature of interest is observed, an intermediate aperture may be inserted in the image plane around the feature, whereafter the TEM may be switched to diffraction mode to obtain a *selected area diffraction* (SAD) image as indicated in Fig. 3.1-(4). Only electrons transmitted through or diffracted by the selected sample volume pass the aperture and contribute to the diffraction image. SAD is performed on regions of about 50 nm to 1 μ m in diameter, depending on aperture size.

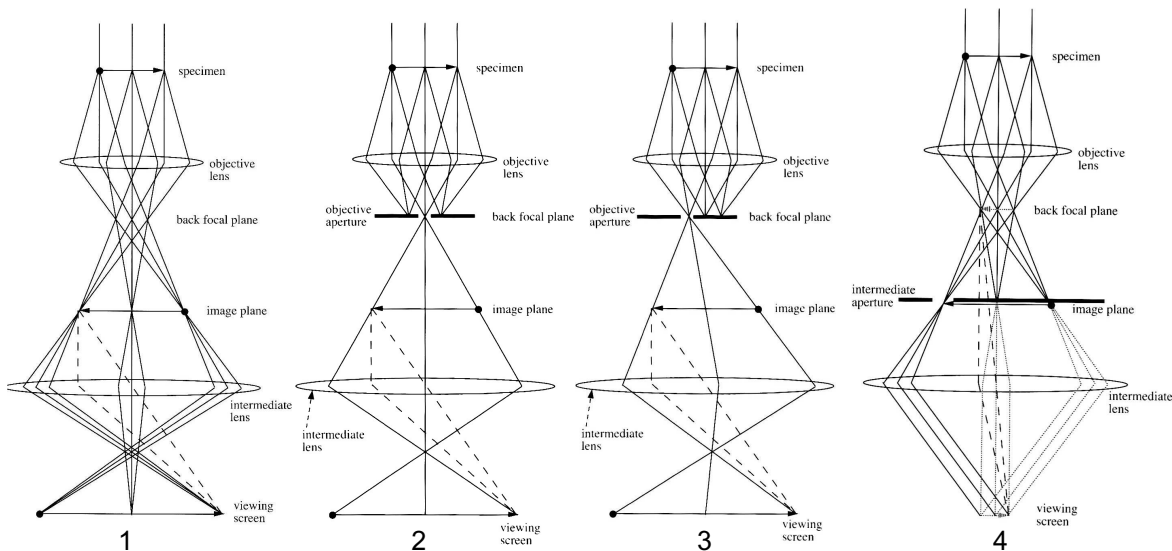


Figure 3.1: Ray paths for the used three modes of TEM operation: (1) imaging mode (used for high resolution), (2) bright field, (3) 'dirty' dark field, and (4) selected area diffraction (after [52]).

After having passed the sample the initially monochromatic electron beam consists of polychromatic electrons which were either not scattered, elastically scattered or inelastically scattered. As described above in conventional electron microscopy all electrons contribute to the image. In contrast, a relatively new analytical TEM technique, *energy-filtering transmission electron microscopy* (EFTEM) achieves chemical selectivity using only inelastically scattered electrons with a specific energy loss to generate an image. This powerful technique allows the mapping of chemical elements with nearly the same resolution as TEM based on the fact that in energy loss spectroscopy (EELS) each core-loss edge of a spectrum occurs at an energy that is characteristic for a specific chemical element. This way compounds can be identified qualitatively by the core loss energies of their constituents. ELNES (*electron energy loss near edge structure*) mappings use the fact that chemical bonding and short-range order in the environment of a specific chemical element cause a slight 'chemical' shift of the energy-loss edge (between 0.1 and 8 eV) and modifies the near-edge fine structure of the electron energy-loss spectrum. By ELNES mappings Si, Si₃N₄ and SiO₂ layers have been successfully distinguished in advanced microelectronic devices [53]. Therefore this technique allows not only the determination of the constituents of a system. It can also differentiate between compounds of the same binary or multi-component system but with different composition (and consequently different bonding and valency).

3.2 Rutherford backscattering spectrometry (RBS)

Rutherford backscattering spectrometry (RBS) is based on bombarding a target (the sample) mounted in a vacuum chamber by light ions of a single energy (usually ⁴He⁺ with an energy $E_0 = 1-10$ MeV) and measuring the energy spectrum of the elastically backscattered ions. The method allows to determine the areal density of elements

(atoms of a certain mass) present in the near surface region (1 nm to 1 μm) of a sample with a depth resolution on the order of 5-30 nm. An introduction to RBS is found in [54, 55].

Principles The number of backscattered ions in a certain peak in an RBS spectrum depends on the absolute number of identical atoms within a resolving depth interval and the kinematics of ion-atom interaction. The width of the peak depends (aside from the energy resolution of the detector) on the depth distribution of identical atoms within the substrate. On their way through the target the ions are decelerated by interaction with valence electrons (electronic stopping). Most of them finally lose their energy by inelastic collisions, are implanted into or transmitted through the target. Some ions experience electronic stopping, followed by a single elastic collision with a target atom at a depth X redirecting them back to the surface. A small fraction of those backscattered ions has an energy high enough to exit the sample with a residual energy $E_1(X)$ given by [54]:

$$E_1(X) = (E_0 - \Delta E_{in}(X))K - \Delta E_{out}(X) \text{ where } \Delta E_{in}(0) = \Delta E_{out}(0) = 0 \quad (3.1)$$

$\Delta E_{in}(X)$ is the energy loss by electronic stopping between surface and scattering atom. K , the relative energy loss by elastic scattering, is the *kinematic factor*, and $\Delta E_{out}(X)$ is the energy loss between scattering atom and surface. The kinematic factor follows from a consideration of energy and momentum conservation in an elastic two body collision:

$$K = \frac{E_1(0)}{E_0} = \frac{(M_2^2 - M_1^2 \sin^2 \theta)^{1/2} + M_1 \cos \theta}{M_1 + M_2} \quad (3.2)$$

Here θ is the laboratory angle through which the incident ion is scattered, M_1 and M_2 are the masses of the incident ion and the target atom respectively. Since K , M_1 , E_0 and θ are known, this expression can be used to determine M_2 . The formula is restricted to Coulomb collisions. This approximation is reasonable for ion energies far from relativistic and off-resonance nuclear reactions (i.e. for $^4\text{He}^+$ ions about 0.5-5 MeV). The determination of the area density n_i (cm^{-2}) of an element i involves the following experimental parameters: the detector solid angle Ω (sr)¹, the integrated peak counts for this element A_i , measured for a total number Q of incident ions, and the cross section $\sigma(E, \theta)$ (cm^2/sr).

$$n_i = \frac{A_i \cos \theta}{Q \cdot \Omega \cdot \sigma(E, \theta)} \quad (3.3)$$

In case of Rutherford Scattering (elastic scattering of two charged particles in a Coulomb potential) the cross section is calculated as follows ([54] p. 39):

$$\sigma(E, \theta) = \left(\frac{Z_1 Z_2 q^2}{4E} \right)^2 \cdot \frac{4[(M_2^2 - M_1^2 \sin^2 \theta)^{1/2} + M_2 \cos \theta]^2}{M_2 \sin^4 \theta (M_2^2 - M_1^2 \sin^2 \theta)^{1/2}} \quad (3.4)$$

This equation is in cgs-units. Z_1 and Z_2 are the atomic number of the incident ion and target atom respectively. E (MeV) is the energy of the ion before collision. A

¹sr: steradian

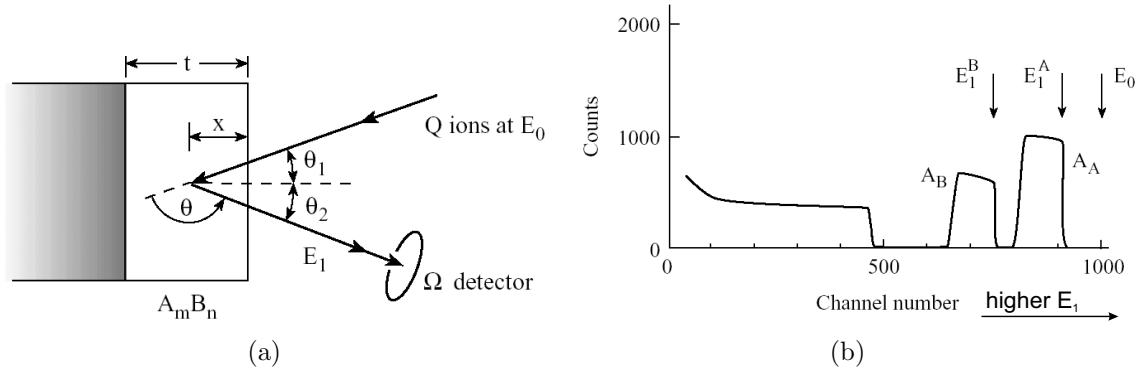


Figure 3.2: (a) Schematic of the experimental geometry used for RBS. (b) Associated RBS spectrum for a two-element material (A_mB_n) on a lower-mass substrate, e.g. SiO_x film on Graphite. (After Harding [55]).

useful number in evaluating this equation is $q^2 = 1.44 \cdot 10^{-13} \text{ MeV}\cdot\text{cm}$. This analysis yields about 3 % uncertainty for area density measurements and about 1 % for the average composition. The precision decreases as deeper layers are analyzed owing to energy straggling. For material analysis one typically uses $^4\text{He}^+$ ions with modest energies of about 0.5-2 MeV. At higher and lower energies the cross section departs from Rutherford cross section, at lower energies because the charge of the incident ion is partially screened by the electron shells of both nuclei, at higher energies due to short range nuclear forces. Helium is often used because its back-scattering cross sections in this energy range are Coulomb like for all atoms larger than Beryllium, and extensive experimental data on kinematic factors and Rutherford back-scattering cross sections exist.

3.3 Elastic Recoil Detection (ERD)

Principles In an ERD experiment heavy incident ions transfer their energy by elastic collisions to lighter sample atoms. Those light recoil atoms having sufficient energy to leave the sample, are measured. The physics of the process is, as in an RBS experiment, determined by elastic scattering and electronic stopping of energetic ions. In contrast to RBS, ERD is more sensitive to light ions. The fact that the recoils differ not only in their energy, but also in their atomic number, enables a dedicated detector, the so called 'Bragg ionization chamber (BIC)', which allows a real discrimination of signals from different elements, whereas in the common surface barrier detectors the signals from different elements may energetically overlap. Because the BIC turned out to be very useful for the ERD composition analysis of SiO_x films, the detector principle is briefly summarized below.

Bragg Ionization Chamber The Bragg ionization chamber consists mainly of three components [56]: the cathode, the Frisch-grid and the anode (Fig. 3.3a). It allows to determine energy, atomic number and the projected range of the recoils. The recoils enter through the cathode, are decelerated by the electric field between cathode and

Frisch-grid, whereby they generate electrons and positive ions by ionization of the chamber gas. These are then separated in the electric field. The anode is screened against this charges by the Frisch-grid, until the electrons drift through the grid and induce mirror-charges at the anode. The resulting current signal vs. time corresponds to a mirror image of the specific ionization along the ion track as shown in (Fig. 3.3b). It is processed by two amplifiers with different time constants, integrating over different regions of the signal. One resulting measure is the area under the Bragg peak, which is proportional to the atomic number Z . The second measure is the integral over the total ionization current, which is proportional to the kinetic energy E of the recoil when entering the chamber. Result of such an ERD measurement is a plot of Bragg peak area (Z) vs. total area (E), in which the different recoiled elements appear in different branches, while identical elements with different energy appear at different positions of the same branch (Fig. 3.3c). Each branch can be converted into a plot of recoiled atoms vs. energy for a single element, which in turn is used to obtain the depth profile of the element, as described for RBS.

3.4 Infrared (IR) absorption spectroscopy

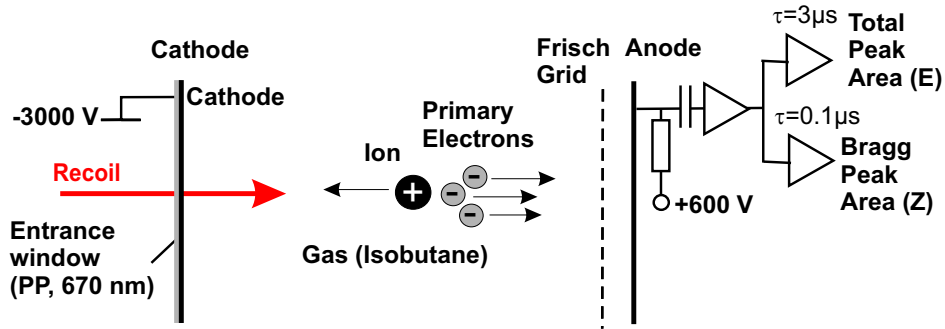
Infrared (IR) absorption spectroscopy determines the wavelength and intensity of the absorption of mid-infrared light (2.5-50 μm , 4000-200 cm^{-1}) by a sample. Mid-infrared light is energetically sufficient to excite molecular vibrations to higher energy levels. A precondition for the absorption of infrared light by a molecular vibration along the normal coordinate u is a change in dipole moment μ : $\partial\mu/\partial u \neq 0$. The wavelength of many IR absorption bands are characteristic of specific types of chemical bonds. That is why it can be applied for structural investigations. Most analytical applications of IR spectroscopy are based on the Bourger-Lambert-Beer law [57].

$$\Phi(\nu) = \Phi_0(\nu) \cdot e^{-\sigma_\nu Nl} \quad (3.5)$$

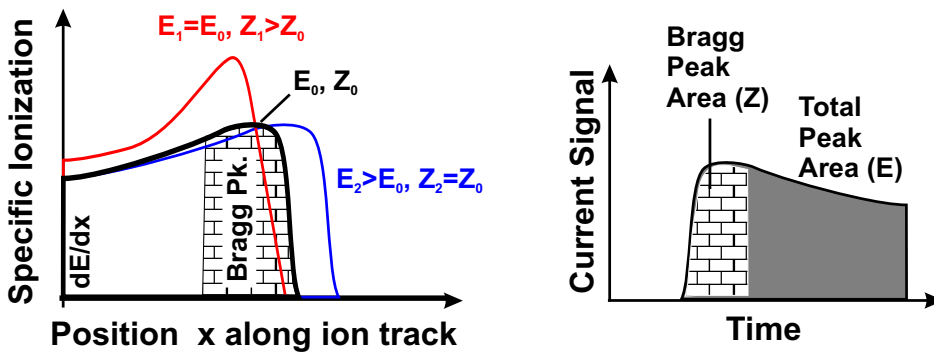
It states that from a given light flux Φ_0 , traversing a sample of thickness l , containing a molecule with an absorbance cross section σ_ν (cm^2) at a density N (cm^{-3}), the fraction $\tau = \Phi/\Phi_0$ (the transmittance) is transmitted. $\nu = 1/\lambda$ (with λ being the wavelength of light) is the energy of light in wavenumbers. $\alpha_\nu = \sigma_\nu \cdot N$ is the absorption coefficient given in units of (cm^{-1}). The fraction of the light flux absorbed by the sample is proportional to the number of absorbing molecules. Practically one must take into account that a fraction of incident light is also reflected or scattered by the sample.

3.4.1 IR absorption bands of silicon oxide

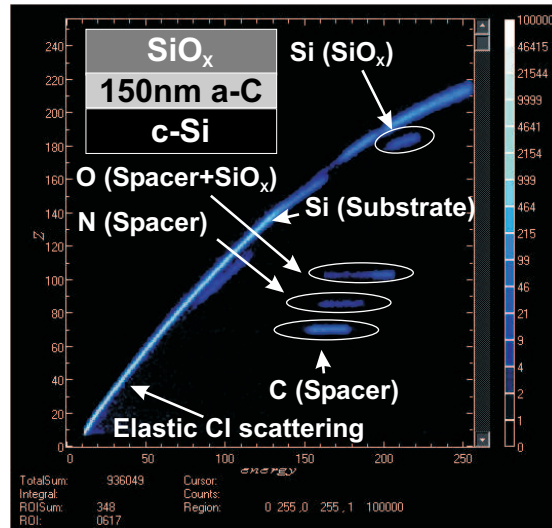
The chemical bonds of SiO_2 in its various structural forms are to about 50% ionic [59]. Hence, IR active vibrations are associated with strong electrical moments, which leads to strong infrared absorption bands. The infrared absorption spectra of amorphous silicon oxides have been discussed extensively in literature [60, 58, 61, 62, 63, 64, 65]. They consist of 4 pairs of longitudinal optical (LO) and transverse optical (TO) vibrations summarized in table 3.1. The modes are the *rocking vibration* of oxygen,



(a) Operation principle of Bragg ionization chamber.



(b) Specific ionization vs. distance from cathode and the corresponding current vs. time signal.



(c) ERD measurement of 77 nm $\text{SiO}_{1.1}$ on 150 nm C on Si (sample A6, see p. 69). Bragg-peak area (Z) vs. total area (E) of ionization peak (Measurement: U. Kreissig).

Figure 3.3: Principle of ERD measurements with a Bragg ionization chamber.

Energy cm ⁻¹	Type	Description SiO ₂ vibrational modes
457	TO ₁	Rocking mode
810	TO ₂	Bending (or symmetric stretching) mode
1076	TO ₃	(Asymmetric) stretching mode with adjacent O atoms in phase
1200	TO ₄	(Asymmetric) stretching mode adjacent O atoms 180° out of phase
507	LO ₁	associated to TO ₁
820	LO ₂	associated to TO ₂
1160	LO ₃	associated to TO ₃
1256	LO ₄	associated to TO ₄

Table 3.1: IR absorption bands of SiO₂ after Kirk [58].

perpendicular to the plane made up by the oxygen atom and the two silicon neighbors, the *bending (or symmetrical stretch) vibration* of oxygen in the plane of the three atoms along the perpendicular bisector of the axis through the two silicon atoms, and the *asymmetric oxygen stretching vibration* parallel to the axis through the two silicon atoms. The latter gives actually rise to two modes: one in which the adjacent oxygen atoms move in phase and another where they move 180° out of phase (Fig. 3.4). LO modes are not observed in normal-incidence and s-polarization oblique incidence IR absorption spectra, since they cannot interact directly with the transverse optical light wave. They are observed only for p-polarization oblique incidence absorption spectra owing to the Berreman effect [66].

3.4.2 Model of IR absorption of silicon oxides

Case of pure SiO₂: A model of infrared absorption of silicon oxides was developed by Lehmann et al. [61]. In this *central/non-central force model* the main absorption bands of SiO₂ are adequately described. The vibrational energy of the TO₃ mode is linked to the bond angle θ (depending on the oxide structure), the mass of the oxygen atom M_O and the central and non-central force constants α and β by²:

$$\nu = a \cdot \sqrt{\frac{2}{M_O} \left(\alpha \cdot \sin^2 \frac{\theta}{2} + \beta \cdot \cos^2 \frac{\theta}{2} \right)} \quad (3.6)$$

Case of SiO_x (x<2): To extend the theory to the case of (not annealed) silicon rich oxides, Lehmann took into account that oxygen atoms that belong to different types of O_y-Si-Si_{4-y}-clusters ($0 \leq y \leq 4$) have different bond angles θ_y [62]. The *random-bond-model* of SiO_x by Phillip [67, 68] gives the probability of these bond angles according to

$$P(\theta_y) = y \cdot p_y(x)/2x \quad (3.7)$$

²The factor $a = 5.305 \cdot 10^{-12}$ converts ν to units of cm⁻¹. The force constants were given as $\alpha = 600 \text{ Nm}^{-1}$ and $\beta = 100 \text{ Nm}^{-1}$.

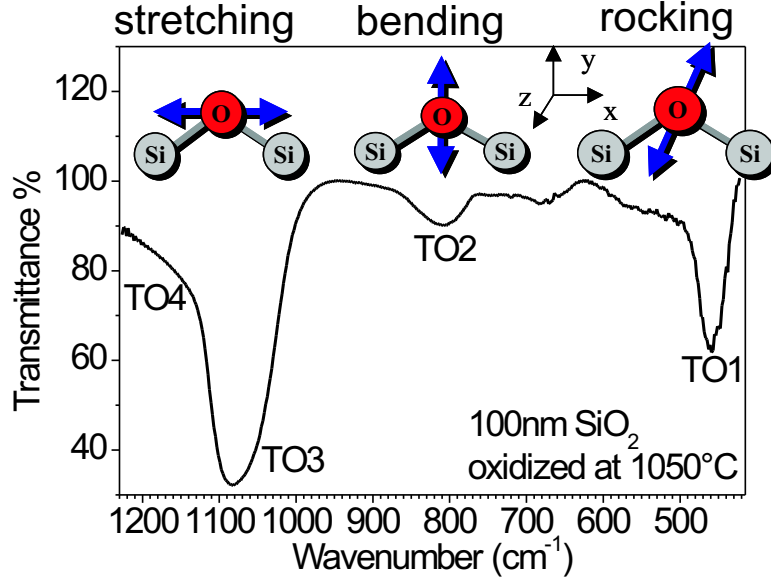


Figure 3.4: IR transmittance of a 100 nm SiO_2 layer prepared by oxidation of Si in pure O_2 at 1050 °C, acquired at normal incidence (own measurement).

Here $p_y(x)$ is the probability of existence of a $\text{O}_y\text{-Si-Si}_{4-y}$ -cluster in SiO_x and given as:

$$p_y(x) = \binom{4}{y} \cdot \left(\frac{x}{2}\right)^{(4-y)} \cdot \left(1 - \frac{x}{2}\right)^y \quad \text{with} \quad \binom{4}{y} = \frac{4!}{(4-y)! \cdot y!} \quad (3.8)$$

The vibrational energy of the TO_3 mode in case of SiO_x films is a weighted average of the 4 sub-bands caused by the different bond angles θ_y of the 4 $\text{O}_y\text{-Si-Si}_{4-y}$ clusters:

$$\nu(x) = \sum_{y=1}^4 \frac{y \cdot p_y(x)}{2x} \nu(y) \quad \text{with} \quad \nu(y) = a \cdot \sqrt{\frac{2}{M_O} \left(\alpha \cdot \sin^2 \frac{\theta_y}{2} + \beta \cdot \cos^2 \frac{\theta_y}{2} \right)} \quad (3.9)$$

3.4.3 Experimental support of the model

Case of pure SiO_2 The model is supported by the observation that the TO_3 absorption band is sensitive to the oxide composition (i.e. the oxygen/silicon ratio x), the method of oxide preparation and successive thermal treatments: Lisovskii [64] found that at least two elementary bands jointly make up the TO_3 band of SiO_2 . They belong to the two dominant structural components of amorphous SiO_2 , the 4- and 6-fold rings of SiO_4 tetrahedra (see table 3.2). Band 1 has a higher relative weight in more dense (e.g. implanted or sputter deposited) oxides, while band 2 dominates for thermally grown or annealed SiO_2 .

Case of SiO_x Lehmann [62] found a linear relation between the composition and the peak energy of the TO_3 mode: $\nu = (48.8 \cdot x + 987) \text{ cm}^{-1}$. Lisovskii [63] was able to deconvolute the IR spectra of oxygen-deficient silicon oxides (SiO_x , $x < 2$) into four

Band	Maximum cm ⁻¹	Full width at half max. cm ⁻¹	Si-O-Si angle	Dominant structural component
SiO ₂				
1	1054±4	57±3	131±1°	fourfold SiO ₄ rings
2	1090±5	43±3	143±1°	four- and sixfold SiO ₄ rings
SiO _x				
x1	1000±10	56±5	118±2°	Si-O-Si ₃ complex
x2	1038±3	47±7	127±1°	Si-O ₂ -Si ₃ complex
x3	1066±5	55±5	136±2°	Si-O ₃ -Si complex
x4	1092±7	63±1	145±3°	Si-O ₄ tetrahedron

Table 3.2: Elementary bands of the TO₃ absorption band after Lisovskii [63].

major sub-bands (x1, x2, x3 and x4) which corroborates Lehmann's theory. The TO₃ mode elementary bands are listed in table 3.2. Kahlert [69] suggested to modify the above model, since using Si as central atom of O_y-Si-Si_{4-y}-clusters does not reflect the symmetry of the problem. Starting from the assumption that each oxygen atom is bound to two Si atoms he considered the effect of the next neighbors of those two Si atoms on the vibration of the central oxygen. The possible vibrational frequencies are then determined by all combinations of bonding tetrahedra, the two silicon neighbors of the vibrating oxygen may be part of. Ten of them are IR active. Kahlert found that both absorption energy and oscillator strength tend to decrease with increasing number of Si atoms in the neighborhood of the vibrating oxygen atom. Thus, a fixed number of vibrating oxygen atoms causes weaker absorption in an off-stoichiometric oxide than in pure SiO₂. Hinds [70] tried to quantitatively relate the extend of SiO_x decomposition during a thermal anneal to the shift of the TO₃ center frequency. Such a quantitative analysis appears to be not unambiguous, since, for disordered deposited films in particular in the limit of low Si excess, both the structural reorganization of the oxide network and the phase separation occur simultaneously and have comparable impact on the spectrum.

In summary: the decomposition of SiO_x manifests not only in a frequency shift of the oxygen stretching vibration, but also in an increased absorption intensity (integrated band area) of this vibrational mode.

3.4.4 Absorption of infrared light by the silicon substrate

If the IR absorption of a silicon oxide film on a silicon wafer is determined using a normal incidence transmission geometry, substrate absorption bands overlap with oxide bands. To obtain the IR spectra of only the oxide layer it is necessary to subtract the spectrum of a bare Si wafer from the spectra of the oxide coated wafer. The two origins of Si infrared absorption are impurities and lattice vibrations. Wafers prepared by the Czochralski (CZ) method contain oxygen and carbon impurities absorbing in the spectral region of interest. The interstitial oxygen absorption band interferes with the TO₃ band of SiO₂. One way to overcome this problem is the use of float-zone (FZ) silicon substrates in which the concentration of these impurities is two orders

Energy (cm ⁻¹)	Energy (eV)	Assignment
	Phonons in Si	
1448	0.1795	3TO
1378	0.1708	2TO+LO
1121	0.1614	2TO+LA
964	0.1195	2TO
896	0.1111	TO+LO
819	0.1015	TO+LA
740	0.0917	LO+LA
689	0.0756	TO+TA
610	0.0702	LO+TA
1105	impurities	Interstitial oxygen [72]
1012	in CZ-Si	Oxygen dimer [73]
1060		Oxygen dimer [73]
607		Carbon [72]

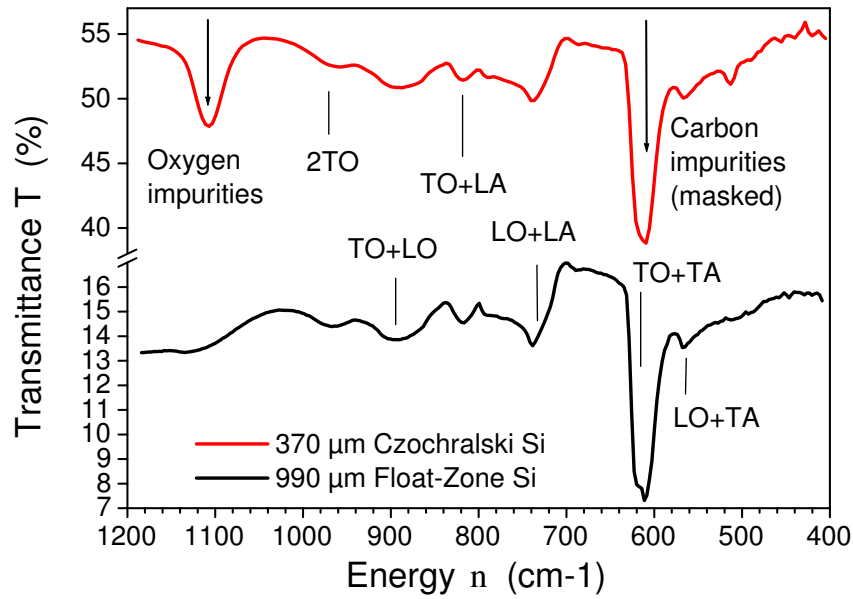
Table 3.3: Multi-phonon absorption bands of silicon after Johnson [74] and impurity absorption bands in Czochralski-silicon.

of magnitude smaller³. In addition absorption is caused by Si lattice phonons. Since the optical phonons of covalently bound point-symmetric crystals as silicon do not modulate the dipole moment, they do not absorb infrared light. Nevertheless silicon absorbs infrared radiation by joint action of two or more phonons: The first one breaks the inversion symmetry and induces charges on the two atoms in the primitive cell. The second vibration causes these charges to oscillate and generates an electric dipole moment that couples to the electromagnetic wave. Both the multi-phonon absorption bands of silicon and the carbon and oxygen impurity absorption bands are shown in Fig. 3.5a and summarized in Table 3.3.

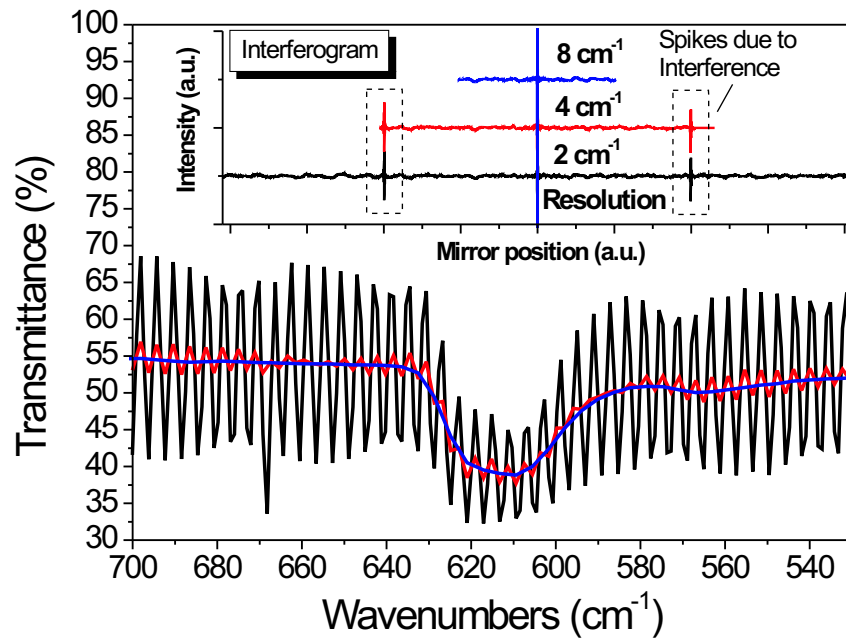
3.4.5 Interference effects

For normal-incidence transmittance measurements the interference of reflections from front and backside of the wafer may introduce fringes to the spectrum. Fig. 3.5b displays an own measurement showing this effect. As for a Fabry-Perot-etalon, maxima occur at energies where the condition $\nu = \frac{j}{2nt}$ is fulfilled, where j is an integer, n is the silicon refractive index ($n \sim 3.418$ at $\nu = 1100 \text{ cm}^{-1}$) and t the wafer thickness [57]. From the period of interference, $\nu_p = \frac{1}{2nt}$, the wafer thickness can be derived (in Fig. 3.5b $\nu_p = 3.98 \text{ cm}^{-1}$ correspond to $t = 367 \text{ }\mu\text{m}$). When using a Fourier-transform infrared (FTIR) spectrometer the fringes can be avoided easily: The interference components appear as spikes in the interferogram (plot of intensity versus position of the movable mirror) at an optical path difference of $2nd$, as shown in the inset of Fig. 3.5b. The fringes are eliminated by reducing the amplitude of the mirror oscillation and spectral resolution $\Delta\nu$ such that no spikes appear in the interferogram, which is the case for $\Delta\nu > \frac{1}{2nt}$ (e.g. $\Delta\nu = 8 \text{ cm}^{-1}$ in Fig. 3.5b. For double-side polished substrates interference effects

³Typical impurity concentrations in Cz-Si are 10^{18} cm^{-3} for oxygen and 10^{16} cm^{-3} for carbon. In FZ-Si the oxygen concentration is about 10^{16} cm^{-3} [71].



(a) IR transmittance of Float-Zone (FZ) and Czochralski (Cz) silicon wafers measured at normal incidence.



(b) IR-transmission spectrum of a 370 μm thick Czochralski Si wafer, measured at normal incidence for different resolutions. The oscillations are caused by interference of reflections from the wafer interfaces.

Figure 3.5: Substrate effects on IR transmission spectra of thin films on Si (own measurements).

are strong and the substrate thickness must be chosen carefully to obtain interference free spectra at a reasonable resolution. Alternatively silicon wafers polished on one side and rough on the backside may be used, but in this case the frequency dependent scattering at the rough side of the wafer may degrade the spectrum base-line.

3.5 Photoluminescence (PL) of Si nanostructures

3.5.1 Quantum confinement model of PL of Si nanostructures

Despite a large number of studies on mechanisms of the red and near infrared photoluminescence (PL) of Si NC a controversy is still present. In case of hydrogen terminated or bare Si nanostructures the PL can be reasonably well modelled by quantum confinement in Si quantum dots or quantum wires respectively [2, 3, 75]. According to the quantum confinement model, the band gap of the Si NC would vary with the NC diameter d as $1/d^2$. For Si NC radii smaller than the radius of free excitons in Si (~ 5 nm) a blue shift in PL emission is observed. According to Kovalev [76] both, indirect phonon-assisted transitions and zero-phonon transitions contribute to the PL emission with their relative contributions depending on d . The oscillator strength of phonon assisted transitions is expected to be inversely proportional to the volume of the NC and scales as $(1/d)^3$, while the probability of the zero-phonon transitions depends on the k -space overlap of the electron and hole envelope functions and scales as $(1/d)^6$. So the emission intensity decreases rapidly with cluster size. The phonon-assisted transitions are dominated by the silicon TA and TO phonons. The broad visible PL of porous Si has been successfully modelled treating the material as an ensemble of Si quantum dots and wires, both with Gaussian size distributions [77]. One should note also that the spectral shape of Si NC PL emission depends not exclusively on the sizes of the Si NC, but also on energy and the power density of the exciting laser. According to Kovalev [76] very high power densities may lead to a broadening and red-shift of the spectrum.

3.5.2 Si nanoclusters embedded in SiO₂

In the case of Si NC embedded in SiO₂, the experimental results contradict the simple quantum confinement model. A much weaker dependence of the gap energy on the Si NC diameter has been found. Also it was observed that oxidation of Si NC caused a red-shift of the PL spectra. Kanemitsu [78] therefore proposed that, in case of oxidized Si NC, excitons are confined within the sub-stoichiometric oxide layer between the Si NC and the SiO₂ matrix (see Fig. 3.6). The Si-rich composition of this layer causes it to have a gap energy of about 1.6 eV, much lower than that of the SiO₂ matrix (≈ 8.5 eV). In case of clusters with a core diameter below ~ 5 nm the Si NC band-gap would be larger than that of the interfacial layer, leading to exciton confinement in the interfacial layer. According to this model, one should observe hardly any dependence of PL energy on the Si NC radius. In fact the dependence is weak in some experiments. Valenta et al. [79] were able to show PL spectra of single silicon quantum dots (oxidized Si nano-

pillars) and they confirmed two important features, namely the blue shift of PL with decreasing diameter of the nano-pillar and the large width of the PL band ~ 150 meV by probing individual Si quantum dots, which proves the action of quantum confinement and contradicts Kanemitsu's model. Summarizing the work of several groups also Takeoka [80] presented convincing experimental data on the correlation between the energy of red PL emission from Si NC in SiO₂ and the measured mean Si NC size (Fig. 3.7). Garrido proposed that indirect optical transitions of oxygen-terminated NC might involve Si-O phonons [81]. Theoretical investigations led to the conclusion that by the oxygen termination of the Si NC new localized states are introduced with an energy within the band-gap of the Si NC [82, 83, 84]. A model proposed by Wolkin et. al [84] resolves some of the mentioned discrepancies. It considers the dependence of the PL on the size of the NC and takes into account also localized-state-to-band transitions originating from trapping of excitons in bonds at the NC surface. He suggests three different recombination mechanisms depending on the cluster size as illustrated in Fig. 3.8: In zone 1 (Si cluster diameter above 3 nm) the recombination is via free excitons. The PL energy increases with decreasing cluster diameter as expected from the quantum confinement model. Here the PL energy for clusters with oxygen or hydrogen passivation would be the same. For the smaller clusters of zone 2 (between 1.8 nm and 3 nm diameter) recombination involves a trapped electron and a free hole. The PL energy would still rise for smaller cluster diameters, but slower than predicted by the quantum confinement model, since the trapped electron state is independent of cluster size. In clusters with a diameter below 1.8 nm the recombination is via trapped excitons. As a consequence of the model the PL energy of H-passivated clusters of the same size would be higher, and their oxydation would lead to a redshift of the PL energy owing to the different recombination mechanism, as observed in experiments. Vasiliev [83] pointed out that the reduction of the effective Si NC band-gap owing to the oxygen termination is not unambiguously associated with the Si = O double bond, Si-O-Si bonds were shown to have similar effects. The internal structure of the Si NC effects their PL behavior. Calculations of Allen et al. [85] showed that the radiative recombination rates and thus the PL intensity of (not-hydrogenated) amorphous and crystalline Si NC are comparable for small clusters (~ 1 nm), but are up to two orders of magnitude higher for larger clusters (~ 2 nm) of the amorphous phase due to disorder induced breaking of selection rules. Rinnert et al. [86] showed that in fact red PL is obtained also from amorphous Si NC embedded in SiO₂. The decay time of the PL contains information on Si NC spacing, which might be useful to distinguish localized or delocalized charge storage in Si NC memories. If Si NC are very close to each other, the electron wave-functions overlap, and the carriers are delocalized. According to Bassani et al. [87] therefore a short relaxation time, independent of PL energy and a lower PL efficiency are expected for strongly interacting Si NC, whereas well-isolated non-interacting Si NC show a longer relaxation time decreasing with PL emission energy and a more efficient PL. Hanaizumi et al. [88] have observed blue defect based PL, but also the red PL emission typical for Si NC embedded in oxide from sputtered SiO_x films without annealing. According to their interpretation it is possible to form Si NC by sputtering without any annealing - an important aspect for applications in which the thermal budget is limited (for example thin film transistors on organic substrates).

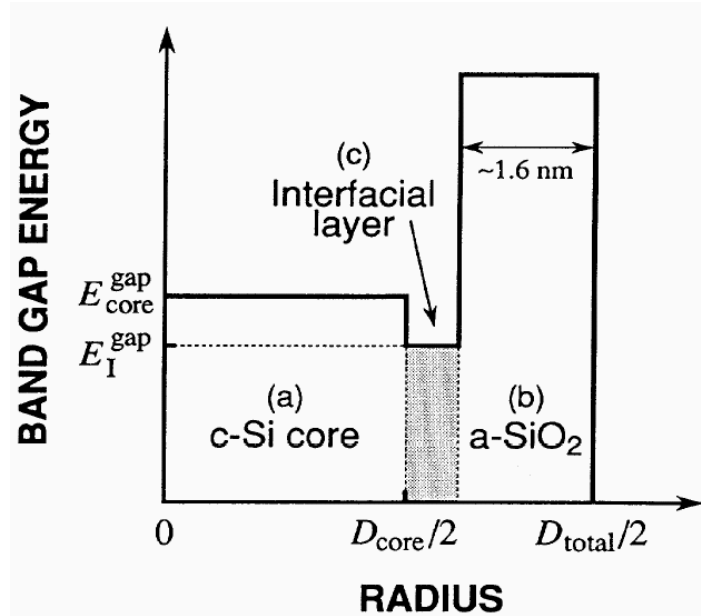


Figure 3.6: Energy-gap diagram of the three-region model. The band-gap energy of the interfacial layer E_I^{gap} is 1.6 eV including the exciton binding energy. The energy gap of the core E_{core}^{gap} increases with decreasing core diameter. In case of $d_{core} \leq 5-7$ nm the exciton is confined in (c) the interfacial region, surrounded by (a) the Si core and (b) the a-SiO₂ surface layer (after Kanemitsu [78]).

3.5.3 Si nanoclusters embedded in Si₃N₄

Park et al. [89, 90] have investigated light emitting diodes (LED) based on amorphous Si NC embedded in silicon nitride films. They found an intense electroluminescence (EL), with an emission maximum that could be continuously tuned from blue (420 nm) to red (680 nm) by variation of the Si NC diameter, according to the relation $E = 1.56 + 2.40/d^2$, where the energy E is in units of eV and the NC diameter d is in nm. The behavior reflects the bulk band-gap of amorphous Si, which is in the range of 1.5–1.6 eV and the $1/d^2$ dependence of the gap energy expected from the pure quantum confinement model. Apparently, in contrast to the surface passivation by oxygen, the surface passivation of Si NC by nitrogen does not introduce optically active gap states, which renders the Si NC / Si₃N₄ system very interesting for LED applications.

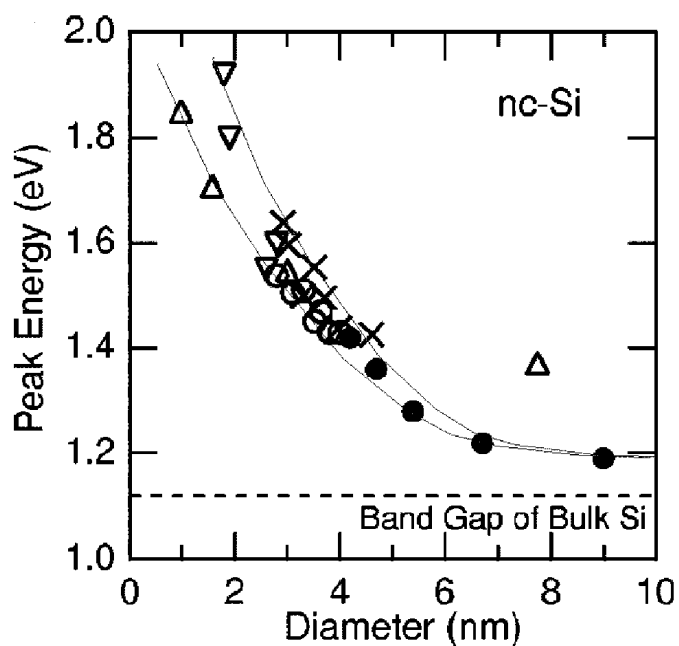


Figure 3.7: Experimental results on the size dependence of the peak energy of Si NC related PL. (after Takeoka [80]). The two limiting dotted lines are drawn as guide for the eye.

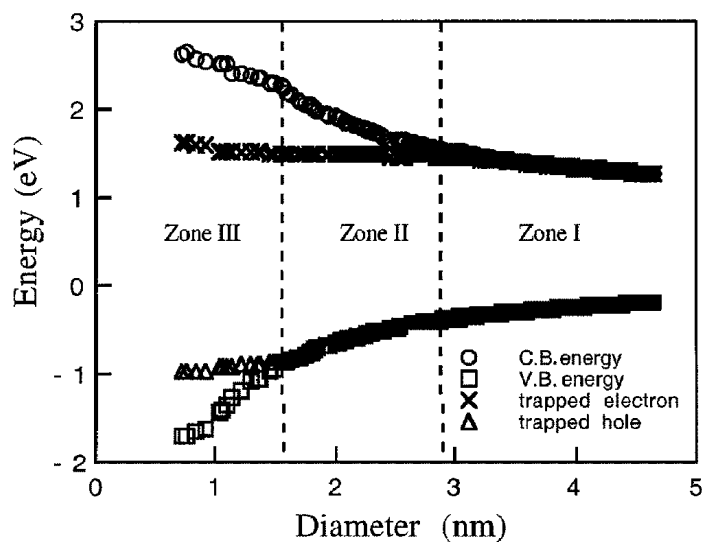


Figure 3.8: Electronic states in Si nanocrystals as a function of cluster size and surface passivation with oxygen. The trapped electron state is a p-state localized on the Si atom of the Si = O bond and the trapped hole state is a p-state localized on the oxygen atom. (after Wolkin [84])

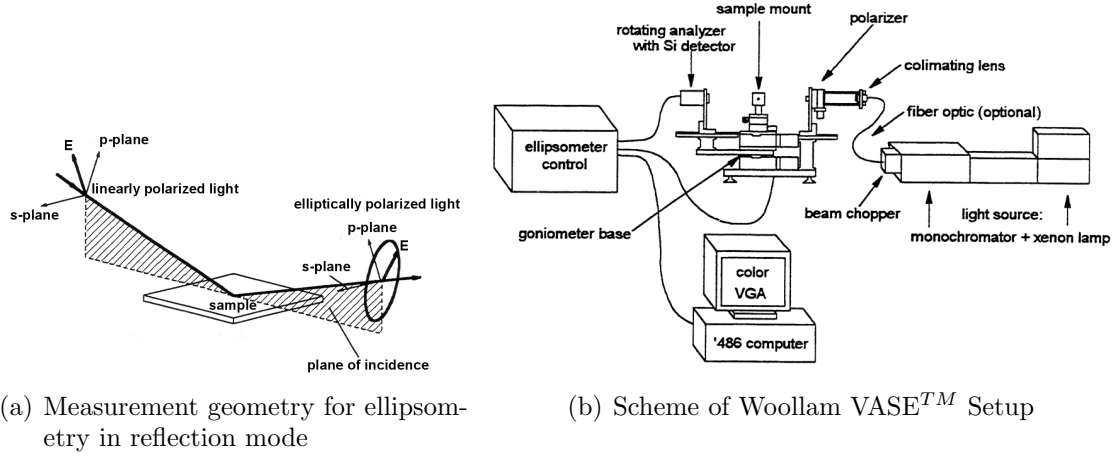


Figure 3.9: Principle of ellipsometric measurements.

3.6 Ellipsometry

3.6.1 Principles

Ellipsometry investigates the change of polarization when an electromagnetic wave is reflected from or transmitted through a sample (Fig. 3.9a). In reflection mode, the Fresnel reflection coefficient ratio ρ is measured:

$$\rho = r_p/r_s = \tan(\Psi)e^{i\Delta} \quad (3.10)$$

The quantity r_p (r_s) is the Fresnel reflection coefficient for light polarized parallel (perpendicular) to the plane of incidence and the angles Ψ and Δ are the traditional ellipsometry parameters. By fitting the experimental data to the parameters of an appropriate model representing the sample, in principle the following types of information can be obtained: Optical constants, thicknesses of single layers or layer-stacks, composition, crystallinity, surface and interfacial roughness, sample anisotropy/birefringence, constituent and void fractions, band-gap energy and electronic transitions. A scheme of the used variable angle spectroscopic ellipsometer by Woollam (VASE™) is shown in Fig. 3.9b.

3.6.2 The parametrization of optical constants

Kramers-Kronig relations Real and imaginary part of the complex index of refraction $\tilde{n} = n + ik$ (n : refractive index, k : extinction coefficient) are not independent quantities, the same holds for real and imaginary parts of the complex dielectric function $\tilde{\epsilon} = \epsilon_1 + i\epsilon_2$ ($\epsilon_1 = n^2 - k^2$, $\epsilon_2 = 2nk$). The Kramers-Kronig relation, resulting from the requirement that a material cannot respond to an electric field prior to its application, connects the real and imaginary parts of the complex dielectric function $\tilde{\epsilon} = \epsilon_1 + i\epsilon_2$ as follows:

$$\epsilon_1(E) = 1 + \frac{2}{\pi} P \int_0^\infty \frac{E' \cdot \epsilon_2(E')}{E'^2 - E^2} dE' \quad (3.11)$$

Here E is the energy of light and P is the Cauchy principal value of the integral taken at $E = E'$. In the analysis of optical constants parameterized dispersion formulas are employed. Many of them comply with the Kramers-Kronig relations. This is achieved by choosing a particular function to describe either the real or the imaginary part of the optical constants, and calculating the other part from the Kramers-Kronig relations. Parameterizations used for the optical constants of Si and SiO₂ are relevant for the present work and briefly discussed below.

Forouhi-Bloomer dispersion formula A model proposed by Forouhi and Bloomer (F-B) [91] has been applied successfully to describe the dispersion of amorphous dielectrics and amorphous semiconductors, in particular amorphous Ge and Si. From a derived expression for the extinction coefficient, the refractive index is obtained by Kramers-Kronig integration. The F-B equations are:

$$k(E) = \sum_i^q \frac{A_i(E - E_g)^2}{E^2 - B_iE + C_i} \quad (3.12)$$

$$n(E) = n(\infty) + \sum_{i=1}^q \frac{B_{0i}E + C_{0i}}{E^2 - B_iE + C_i} \quad (3.13)$$

$$B_{0i} = \frac{A_i}{Q_i} \left(-\frac{B_i^2}{2} + E_g B_i - E_g^2 + C_i \right) \quad (3.14)$$

$$C_{0i} = \frac{A_i}{Q_i} \left((E_g + C_i) \frac{B_i}{2} - 2E_g C_i \right) \quad (3.15)$$

$$Q_i = \frac{1}{2} (4C_i - B_i^2)^{1/2} \quad (3.16)$$

where E_g represents the optical energy band-gap, $B_i/2$ is equal to the i th term (peak) energy, A_i and C_i denote amplitude and broadening terms (all in units of eV). A characteristic feature of the F-B equations is their simplicity.

Tauc-Lorentz dispersion formula Jellison and Modine presented a Kramers-Kronig consistent parameterization for the optical functions of amorphous semiconductors and insulators in the interband region [92, 93]. Based on experimental results, the authors consider their more sophisticated model to be superior to the F-B-model. The model is formulated as follows:

$$\epsilon_2(E) = 2nk = \frac{AE_0C(E - E_g)^2}{(E^2 - E_0^2)^2 + C^2E^2} \cdot \frac{1}{E} \quad , \quad E > E_g$$

$$0 \quad , \quad E \leq E_g \quad (3.17)$$

$$\begin{aligned}
 \epsilon_1(E) = & \epsilon_1(\infty) + \frac{AC}{\pi\zeta^4} \cdot \frac{\alpha_{ln}}{2\alpha E_0} \ln \left(\frac{E_0^2 + E_g^2 + \alpha E_g}{E_0^2 + E_g^2 - \alpha E_g} \right) \\
 & - \frac{A}{\pi\zeta^4} \cdot \frac{\alpha_{atan}}{E_0} \left[\pi - \operatorname{atan} \left(\frac{2 \cdot E_g + \alpha}{C} \right) + \operatorname{atan} \left(\frac{-2 \cdot E_g + \alpha}{C} \right) \right] \\
 & + 2 \cdot \frac{AE_0}{\pi\zeta^4\alpha} \cdot E_g \cdot (E^2 - \gamma^2) \cdot \left[\pi + 2 \cdot \operatorname{atan} \left(2 \cdot \frac{\gamma^2 - E_g^2}{\alpha C} \right) \right] \\
 & - \frac{AE_0C}{\pi\zeta^4} \cdot \frac{E^2 + E_g^2}{E} \cdot \ln \left(\frac{|E - E_g|}{E + E_g} \right) \\
 & + 2 \cdot \frac{AE_0C}{\pi\zeta^4} \cdot E_g \cdot \ln \left[\frac{|E - E_g| \cdot (E + E_g)}{\sqrt{(E_0^2 - E_g^2)^2 + E_g^2 \cdot C^2}} \right], \tag{3.18}
 \end{aligned}$$

$$\alpha_{ln} = (E_g^2 - E_0^2)E^2 + E_g^2C^2 - E_0^2(E_0^2 + 3E_g^2), \tag{3.19}$$

$$\alpha_{atan} = (E^2 - E_0^2)(E_0^2 - E_g^2) + E_g^2C^2, \tag{3.20}$$

$$\zeta^4 = (E^2 - \gamma^2)^2 + \frac{\alpha^2 C^2}{4}, \tag{3.21}$$

$$\alpha = \sqrt{4E_0^2 - C^2}, \tag{3.22}$$

$$\gamma = \sqrt{E_0^2 - C^2/2} \tag{3.23}$$

The fit parameters A , E_0 , C and E_g denoting amplitude, energy and broadening of the main optical transition and the band gap energy respectively are all in units of energy (eV).

Sellmeier dispersion formula The Sellmeier dispersion formula is used to parameterize the optical constants of transparent dielectrics in the region of normal dispersion. The model reflects the response of isotropic and uniformly distributed identical charged harmonic oscillators to the excitation by a plane electro-magnetic light wave. Far from the resonance, the absorption is small and the oscillators affect mainly the real part of the dielectric function ϵ_1 :

$$\epsilon_1(\lambda) = n^2 = 1 + \sum_{j=1}^M A_j \frac{\lambda^2 \lambda_j^2}{\lambda^2 - \lambda_j^2} \tag{3.24}$$

In the visible spectral region, typical values for SiO_2 are $M = 1$, $A_1 = 0.000126 \text{ nm}^{-2}$ and $\lambda_1 = 93.4 \text{ nm}$.

3.6.3 Effective medium approximations

The description of optical constants of silicon nanoclusters embedded in SiO_2 involves the use of effective medium approximations (EMA). The idea of EMA is based on the assumption that, in terms of optical constants, a heterogeneous material can be replaced by a virtual homogeneous effective medium, whose optical constants are constructed from the known ones of the constituent materials. The optical constants of the

effective medium are derived as follows: The included entities are assumed to be small compared to the wavelength of light, so that for the electromagnetic field the results of electrostatics provide a good approximation. Because the incoming light polarizes the entities of the composite, an averaged dielectric function is observed that depends on the spectral behavior of the optical constants of all composite constituents, their volume fraction and geometrical shape. The averaged dielectric function has to be derived by summing over all local fields within the microscopic heterogeneous medium assuming dipole-dipole interaction between the entities of the composite. The general relation between the optical constants of the effective medium and the constituents is given below:

$$\frac{\epsilon - \epsilon_w}{\epsilon + y\epsilon_w} = \sum_{n=1}^k f_n \cdot \frac{\epsilon_n - \epsilon_w}{\epsilon_n + y\epsilon_w} \quad (3.25)$$

Here ϵ , ϵ_w and ϵ_n are the dielectric constants of the effective medium, host medium and inclusions respectively. f_n is the volume fraction of inclusion n and y is a factor describing the shape of the inclusions, related to the screening factor sf by:

$$y = \frac{1}{sf} - 1 \quad (3.26)$$

In case of spherical inclusions $sf = \frac{1}{3}$ and $y = 2$. This value is also frequently used as first approximation. Additional assumptions about the host medium lead to some special cases of effective medium approximations.

Lorentz-Lorenz-approximation This model is suited for a small concentration of polarizable entities embedded in vacuum ($\epsilon_w = 1$). The general expression becomes:

$$\frac{\epsilon - 1}{\epsilon + y} = \sum_{n=1}^k f_n \cdot \frac{\epsilon_n - 1}{\epsilon_n + y} \quad (3.27)$$

Maxwell-Garnett-approximation If the volume fraction of the inclusions ($n = 2, 3, \dots$) in a matrix ($n = 1$) different from vacuum is very low, than the Maxwell-Garnett approximation ($\epsilon_w = \epsilon_1$) is used [94].

$$\frac{\epsilon - \epsilon_1}{\epsilon + y\epsilon_1} = \sum_{n=1}^k f_n \cdot \frac{\epsilon_n - \epsilon_1}{\epsilon_n + y\epsilon_1} \quad (3.28)$$

Problems arise, if the volume fractions of matrix and inclusions get comparable, because the expression above is not symmetric with respect to an exchange of inclusion and matrix. In these cases, the following approach is used.

Bruggemann-approximation The self-consistent Bruggemann effective medium approximation (BEMA) [95] regards the effective medium to be completely made up by irregularly arranged spherical ($f = \frac{1}{3}$) inclusions of volume fraction f_n . The host medium is identified with the effective medium itself ($\epsilon = \epsilon_w$) while all constituents (n

= 1,2,..) are treated as inclusions, which leads to:

$$0 = \sum_{n=1}^k f_n \cdot \frac{\epsilon_n - \epsilon}{\epsilon_n + 2\epsilon} \quad (3.29)$$

This mixed medium approximation has been assessed to provide best results in a variety of applications including the modelling of surface roughness [96] and embedded nanoparticles.

3.7 The capacitance of MOS structures

3.7.1 The MOS capacitance at high and low frequencies

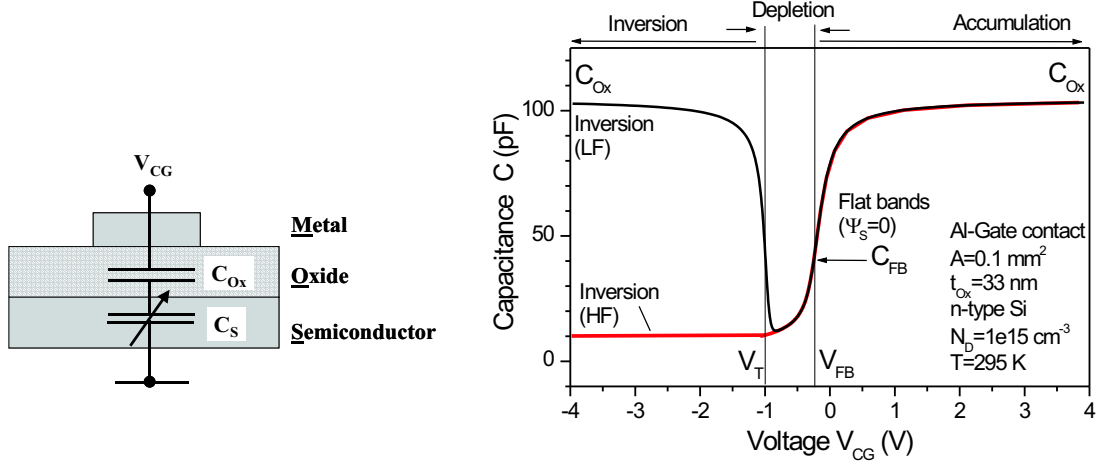
A powerful approach to characterize MOS structures are capacitance-voltage measurements. Their theory is comprehensively described in books like [97, 98, 99]. In the simplest equivalent circuit a MOS capacitor is represented by a series combination of the fix oxide capacitance C_{Ox} and the variable capacitance of the silicon substrate C_S (Fig. 3.10a). In the following sheet capacitances normalized to the gate area A are used. C_{Ox} (As/Vcm²) is given by:

$$C_{Ox} = \frac{\epsilon_0 \epsilon_{SiO_2}}{t_{Ox}} \quad (3.30)$$

A is the gate area, t_{Ox} the oxide thickness, $\epsilon_0 = 8.854 \cdot 10^{-12}$ F/m is the permittivity of vacuum, and $\epsilon_{SiO_2} \approx 3.9$ [98] is the relative permittivity of SiO₂. The total MOS capacitance C is then:

$$C = \frac{C_{Ox} C_S}{C_{Ox} + C_S} \quad (3.31)$$

Considering the dependence of the MOS capacitance on the gate voltage V_{CG} , three regimes are distinguished: accumulation, depletion and inversion of charge carriers in the Si substrate near the Si/SiO₂ interface. For n-type Si, in accumulation ($V_{CG} > V_{FB}$), the energy bands in the substrate bend downwards near the interface: The positive gate voltage induces the accumulation of majority carriers (electrons) at the semiconductor surface. When V_{CG} equals the flat-band voltage V_{FB} , the energy bands in the Si substrate are flat. For voltages slightly below V_{FB} , the bands start to bend upward. Up to the depletion layer width W , the surface region of the substrate is depleted of majority carriers. For more negative V_{CG} , at the surface, the Fermi-level E_F crosses midgap. Now minority carriers accumulate near the surface (substrate inversion), and the depletion layer disappears. The the quasistatic or low frequency (LF) capacitance is measured at dc bias or at a dc bias superimposed with a low frequency (≤ 100 Hz) modulation, such that the concentration of minorities is able to follow the voltage modulation. In contrast, the dynamic or high frequency capacitance is defined as $-dQ_S/dV_{CG}$, where Q_S is the charge at the semiconductor surface induced by the gate voltage. To measure the HF capacitance-voltage (HFCV) characteristics, a small (10 to 20 mV) high frequency (≥ 100 kHz) modulation is superimposed to the dc bias voltage at the gate. Fig. 3.10b shows the corresponding capacitance-voltage (CV) diagram for



(a) Simplest scheme of MOS capacitor. (b) Simulated HF and LF capacitance curves. The parameters are shown in the inset.

Figure 3.10: The MOS capacitance at high (HF) and low frequencies (LF).

a low-frequency (LF) and a high frequency (HF) measurement respectively. In accumulation, both HF and LF capacitances are very close to C_{Ox} , and decrease in depletion with extending width of the space charge region. The LF capacitance reaches a minimum, and with the onset of inversion and decreasing width of the space charge region, it raises to reach C_{Ox} again. At inversion, the HF-capacitance has a constant minimum value, since the fast modulation of gate voltage cannot be compensated by adjustment of the minority carrier density. Instead it is compensated by the modulated width of a space charge region. The modulation depth of this space charge region, and hence the HF capacitance at inversion depend on the substrate donor density N_D , which can be used to determine the substrate doping level. An empirical relationship between the HF capacitance at inversion C_{inv} and N_D at room temperature is

$$\log_{10}(N_D/[cm^3]) = 30.38759 + 1.68278 \log_{10}(z) - 0.03177 [\log_{10}(z)]^2 \quad (3.32)$$

$$z = \frac{C_{inv}}{A(1 - C_{inv}/C_{Ox})}$$

According to Schröder ([98]), the MOS capacitance at flat-bands C_{FB} is for homogeneous substrate doping:

$$C_{FB} = \frac{A\epsilon_0\epsilon_{SiO_2}}{t_{Ox} + (\epsilon_{SiO_2}/\epsilon_{Si})L_D} = C_{Ox} \frac{1}{1 + \frac{136\sqrt{T/300}}{t_{Ox}\sqrt{N_D}}} \quad (3.33)$$

Here $L_D = \sqrt{\frac{k_B T \epsilon_{Si}}{q^2 N_D}}$ is the extrinsic Debye length for holes, T is the absolute temperature, k_B Boltzmann's constant and q the elementary charge.

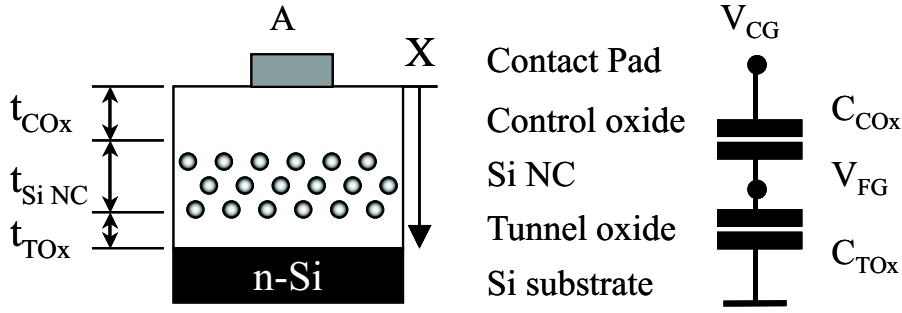


Figure 3.11: Schematic structure of MOS-capacitors with an embedded Si NC layer and the corresponding traditional memory capacitor model for the substrate in accumulation. The potential V_{FG} of the Si NC 'floating gate' depends on both the control gate voltage V_{CG} and the charge stored in the Si NC.

3.7.2 The effect of trapped charge on the capacitance-voltage characteristics

If charge is trapped in the gate oxide or if the centroid of trapped charge is moved, the potential at the surface of the Si substrate changes, such that the CV-curve shifts along the voltage axis. Often, the shift of the flat-band voltage, ΔV_{FB} , is used for quantitative analysis. ΔV_{FB} relates to the charge per area Q_{Ox} [C/cm^2] stored in the gate oxide according to:

$$\Delta V_{FB} = -\frac{Q_{Ox}}{C_{Ox}} \cdot \gamma \quad \text{where} \quad \gamma = \frac{\int_0^{t_{Ox}} \frac{x}{t_{Ox}} \cdot \rho(x) dx}{\int_0^{t_{Ox}} \rho(x) dx} \quad (3.34)$$

is the location of the charge centroid, x is the position in the oxide as defined in Fig. 3.11 and $\rho(x)$ is the vertical charge distribution within the oxide. This effect has been used for the investigation of MOS memory capacitors schematically shown in Fig. 3.11, in which Si NC embedded in the gate oxide act as the dominant trapping sites. Considering the Si NC memory structure shown on the left of Fig. 3.11, and assuming the center of charge in the middle of the SiO_x layer, one finds $\gamma = (t_{COx} + 0.5 \cdot t_{Si NC})/t_{ox}$, where t_{COx} and $t_{Si NC}$ are the thicknesses of the cap-oxide and SiO_x layer. If the inhomogeneous dielectric constant caused by the Si excess depth profile is taken into consideration, according to Tiwari [100] the above expression results in:

$$\Delta V_{FB}(t) = \frac{Q_{Ox}}{\epsilon_0} \cdot \left(\frac{t_{COx}}{\epsilon_{SiO_2}} + \frac{t_{Si NC}}{2 \cdot \epsilon_{SiO_x}} \right) \quad (3.35)$$

Here ϵ_0 is the permittivity of free space and $\epsilon_{SiO_2} \approx 3.9$ and ϵ_{SiO_x} are the relative permittivities of the stoichiometric cap-oxide and the SiO_x layer respectively. Considering the SiO_x layer as a compound of spherical Si NC occupying a volume fraction f_{Si} in a SiO_2/Si mixture, and the dielectric strength $\epsilon_{Si} = 11.9$ of the Si NC ϵ_{SiO_x} can be obtained from the Bruggemann Effective Medium Approximation (BEMA, p. 34) [95]:

$$0 = f_{Si} \cdot \frac{\epsilon_{Si} - \epsilon_{SiO_x}}{\epsilon_{Si} + 2\epsilon_{SiO_x}} + (1 - f_{Si}) \cdot \frac{\epsilon_{SiO_2} - \epsilon_{SiO_x}}{\epsilon_{SiO_2} + 2\epsilon_{SiO_x}} \quad (3.36)$$

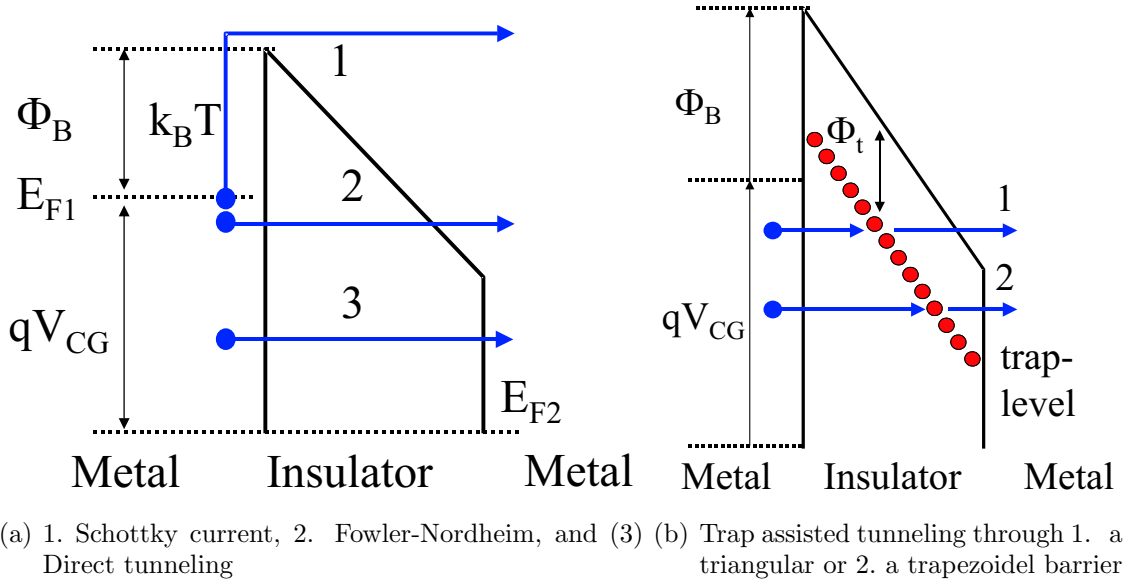


Figure 3.12: Electrode limited currents

3.8 Currents in MOS structures

3.8.1 Electrode limited currents

Currents through an insulator can be limited by the charge injection (electrode limited currents) or by the conduction in the bulk of the insulator (bulk limited currents). In the case of MOS structures, usually electrode limited currents dominate. Hereby, depending on the energy of the electron in the direction perpendicular to the barrier, two cases are distinguished (Fig. 3.12a): If the electron (by thermal or optical activation) has an energy above the barrier, ($\mathcal{E}_x > \Phi_B$), it can classically traverse it and is quantum mechanically described by a progressing wave. This is called the *thermionic effect*, associated with the *Schottky current*. For ($\mathcal{E}_x < \Phi_B$) the electron is associated with an evanescent wave and a finite transmission probability exists if the barrier is thin. The transit mechanism is called *tunnel effect*. Two limits are distinguished: In case of small bias the electron traverses the complete barrier. This is called *direct tunneling (DT)*. In case of large bias, the effective tunnel thickness is reduced by the action of the electric field. This mechanism is called *Fowler-Nordheim (FN) tunneling*. Considering tunneling through metal-SiO₂-Si (MOS) structures, for oxides thicker than 4 nm FN tunneling is the governing mechanism. DT becomes dominant in oxides thinner than 4 nm. FN tunneling is known as write/erase mechanism for many conventional non-volatile memories and replaced by DT in the investigated Si NC memory devices. Another mechanism is *trap assisted tunneling (TAT)*, where carriers tunnel through the barrier using energetic levels of oxide traps as intermediate stations (Fig. 3.12b).

In the following, expressions for the different current densities are summarized. The derivations assume that electrons in the emitting electrode can be described by a free Fermi gas that electrons in the oxide have a single effective mass m_{ox} and that an effective energy barrier height Φ_B [eV] at the Si-oxide interface accounts for barrier lowering and quantization of electrons at the semiconductor surface.

Thermionic/Schottky Current (SC)

The thermionic current density is given by the Richardson-Schottky equation, modified by introducing an effective mass m_{ox} of the electron in SiO₂ [101]:

$$J_S = \frac{4\pi m_{ox} q}{h^3} \cdot (k_B \cdot T)^2 \cdot \exp\left(\frac{-(\Phi_B - \sqrt{\frac{qE_{ox}}{4\pi\epsilon_0\epsilon_{SiO_2}}})}{k_B T}\right) \quad (3.37)$$

Direct Tunneling (DT)

The current density for direct tunneling [102, 98] is calculated according to:

$$J_{DT} = A \cdot E_{ox}^2 \cdot \exp\left(\frac{-B[1 - (1 - qV_{CG}/\Phi_B)^{1.5}]}{E_{ox}}\right) \quad (3.38)$$

Here A and B are constants, defined as:

$$A = \frac{q^3(m/m_{ox})}{8\pi h \Phi_B} = 1.54 \cdot 10^{-6} \frac{(m/m_{ox})}{\Phi_B} \left[\frac{A}{V^2} \right] \quad (3.39)$$

and

$$B = \frac{8\pi\sqrt{2m_{ox}\Phi_B^3}}{3qh} = 6.83 \cdot 10^7 \sqrt{(m_{ox}/m)\Phi_B^3} \left[\frac{V}{cm} \right] \quad (3.40)$$

Fowler-Nordheim (FN) Tunneling

The current density for FN tunneling is given by [103] [104]:

$$J_{FN} = A \cdot E_{ox}^2 \cdot \exp\left(\frac{-B}{E_{ox}}\right) \quad (3.41)$$

Trap-assisted tunneling (TAT)

Thin SiO₂ films may contain a high density of traps caused by stress or radiation damage, which give rise to 'trap assisted tunneling'. In TAT the electron or hole tunnels through the barrier using one or more trapping sites acting as intermediate levels. Depending on the carrier energy the effective barrier may have a triangular or a trapezoidal form (see processes 1 and 2 in Fig. 3.12b). For the case of electron injection from the metal contact and for high fields (current through triangular barrier dominates) the qualitative current-voltage relationship can be expressed as follows [105]:

$$J_{TAT} \propto \exp\left(-\frac{4\sqrt{2qm_{ox}}}{3\hbar} \phi_t^{3/2} / E_{ox}\right) \quad (3.42)$$

This dependence allows to determine the trap energy ϕ_t using a simple current-voltage curve. If the current density J_{TAT} [A/cm²] is plotted versus $1/E_{ox}$ [MV⁻¹cm] then the

relation between the slope S of the linear region in this diagram and the trap energy ϕ_t is:

$$\phi_t[eV] = S^{2/3} \cdot 0.075398 \quad (3.43)$$

3.8.2 Bulk limited currents

If the interface between contact material (doped silicon or metal) and SiO_2 is injecting, the current is limited by the characteristics of the bulk insulator. In general in an insulator exist deep donor levels (some eV below the conduction band) and shallow electron traps located a few eV below the conduction band. An electron travelling in such an insulator easily gets trapped, but electronic conduction can still proceed, if the electron can transit from one trapping site to the next. The electron can overcome the energy barrier between two trapping sites, Φ_M , by two different ways [106, 101]: If $\mathcal{E}_x > \Phi_M$ through a thermionic mechanism, i.e. *Poole-Frenkel (PF) conduction*, which is substituted by *Poole (P) conduction* in the limiting case of a very high trap density with overlapping trap potentials. If $\mathcal{E}_x \leq \Phi_M$ the electron moves through a tunnel mechanism, the so called *hopping-conduction*. All currents are derived in the low injection limit, i.e. assuming negligible charge trapping, such that the electric field is constant throughout the oxide.

Poole-Frenkel (PF) Conduction

The PF-law describes the phonon-assisted thermionic emission of an electron out of a defect corresponding to a single pure coulombic potential well (Fig. 3.13a). After the emission the carrier stays near the bottom of the quasi-conduction band until it is recaptured at a second ionized site. The density of ionizable sites is low, such that the potentials of adjacent defects don't overlap. Given an ionizable impurity center at a depth ϕ_i below the quasi-conduction band of the amorphous SiO_2 , the expression of the PF current takes the following form [101]:

$$J_{PF} = qN_c\mu \cdot E_{ox} \cdot \exp\left(\frac{-(\Phi_i - \sqrt{\frac{qE_{ox}}{\pi\epsilon_0\epsilon_{\text{SiO}_2}}})}{k_B T}\right) \quad (3.44)$$

N_c [cm^{-3}] is the density of states in the SiO_2 conduction band, μ [cm^2/Vs] is the mobility

Poole (P) Conduction

PF conduction is replaced by Poole conduction when the density of ionized coulombic centers is high and the perturbations in potentials overlap, so that the ionization barrier becomes ϕ_a (see process 1 in Fig. 3.13b). For two identical centers of distance s , the

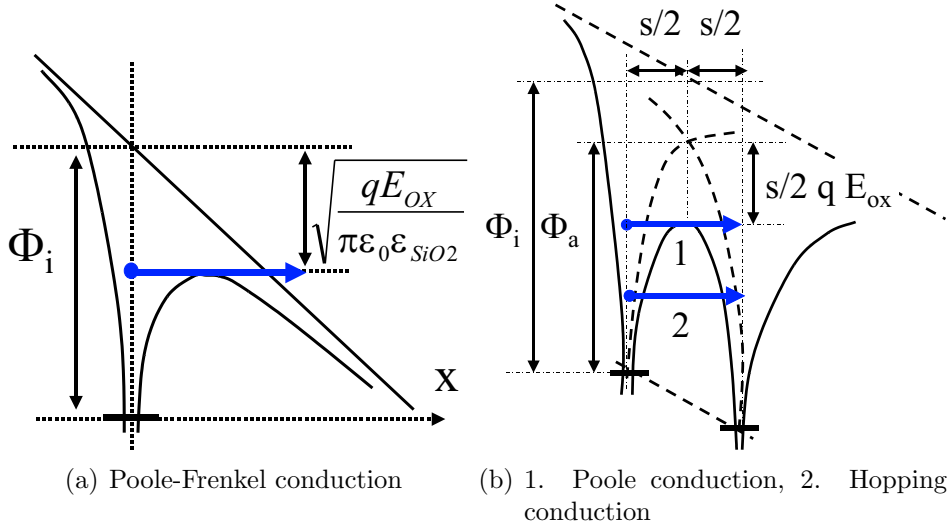


Figure 3.13: Bulk limited currents

peak in the barrier is close to $s/2$. The current then becomes [106]:

$$J_P = J_{P0} \cdot \exp\left(\frac{-(\Phi_a - \frac{1}{2}q \cdot s \cdot E_{ox})}{k_B T}\right) \quad (3.45)$$

Here J_{P0} is a proportionality constant.

Hopping (H) Conduction

Hopping conduction implies that the electrons have an energy inferior to the energy barrier between two sites, ϕ_a , and they proceed from one to the next by tunnel effect (process 2 in Fig. 3.13b). The current density [101] is expressed as:

$$J_H = \frac{q^2}{k_B \cdot T} \cdot n^* \cdot D \cdot E_{ox} \quad (3.46)$$

D is the diffusion coefficient depending on the jump frequency Γ_S between two sites separated by a distance a and n^* is the electron density on the sites. With

$$D = \Gamma_S \cdot a^2 \quad (3.47)$$

and

$$\Gamma_S = \frac{1}{\tau_0} \cdot \exp\left(-\frac{2m_{ox}}{\hbar} \phi_a a\right) \quad (3.48)$$

where m^* is the electron effective mass, \hbar is Planck's constant and τ_0 is a time constant on the order of $7 \cdot 10^{-14} s$ the hopping current density becomes:

$$J_H = \frac{q^2}{k_B \cdot T} \cdot \frac{a^2}{\tau_0} \cdot n^* \cdot E_{ox} \cdot \exp\left(-\frac{2m_{ox}}{\hbar} \phi_a a\right) \quad (3.49)$$

If the insulator contains no traps, then n^* corresponds to the density of shallow (i.e. ionized) donor sites and the current is little dependent on temperature. If the insulator contains traps we have $n^* = N^* \cdot \exp\left(-\frac{\phi^*}{k_B T}\right)$, where N^* is the trap density and ϕ^* is an activation energy. The hopping current is then strongly temperature dependent. In either case it is proportional to the bias voltage.

4 Principles of sputter deposition

4.1 Deposition modi

Sputter deposition enables the preparation of thin films of metals, dielectrics and compounds at rather low temperatures. During sputter deposition gas ions out of a plasma are accelerated towards a target, which consists of the material to be deposited. Material detached ('sputtered') from the target by the impinging ions traverses the plasma and condenses onto a nearby substrate. The process is realized in a vacuum chamber, which is pumped down to a vacuum base pressure before deposition starts. Then a gas, mostly argon, is fed into the chamber up to a pressure between 0.5-12 Pa. In the *direct current (dc) sputtering mode* a negative bias potential of some hundred Volts is applied to the target, while the chamber is grounded. As a result, positive Ar ions are accelerated towards the target. When they collide with target atoms, target material is set free and secondary electrons are produced, which are accelerated away from the target and by ionization of argon atoms help to sustain the plasma. The bombardment of a non-conducting target with positive ions results in a screening of the electrical field by accumulated surface charges. Consequently the ion current in a dc-plasma would cease. While dc sputtering is therefore restricted to conducting target materials, dielectrics may be sputtered using *radio frequency (rf)* or *pulsed power supplies*. In rf mode, the target is decoupled from the power supply by a capacitor and an ac-voltage¹ with a frequency of typically 13.56 MHz is applied. In a negative half cycle positive ions are accelerated to the target. In the following positive half cycle the target is flushed with electrons that overcompensate the positive surface charge because of their higher mobility. Thus a negative mean self-bias voltage is established at the target. *Magnetron* sputtering systems [107] achieve higher deposition rates applying an auxiliary magnetic field in the plane of the target surface (Fig.4.1). It confines the electrons close to the target, where they move on cycloid tracks. The increased electron dwell time in the plasma leads to a higher ionization probability of Ar atoms resulting in higher rates. Magnetrons may operate at lower pressure than conventional sputtering systems, which favors the formation of smooth and dense films. On the other hand the magnetron significantly reduces the electron bombardment of the substrate. *Reactive sputtering* allows to deposit composite coatings using elemental targets. Reactive gases (like oxygen or nitrogen) added to the sputter gas form a compound at the target surface and are simultaneously incorporated in the growing film. If the compound has a lower sputtering yield than the element, the stoichiometric compound may be sputtered at high rate by controlling the reactive gas flow such that the target is only partly covered with the compound. A review of plasma generation and plasma sources is found in [108], surveys on plasma deposition methods are found in [109, 110].

¹ac: alternate current

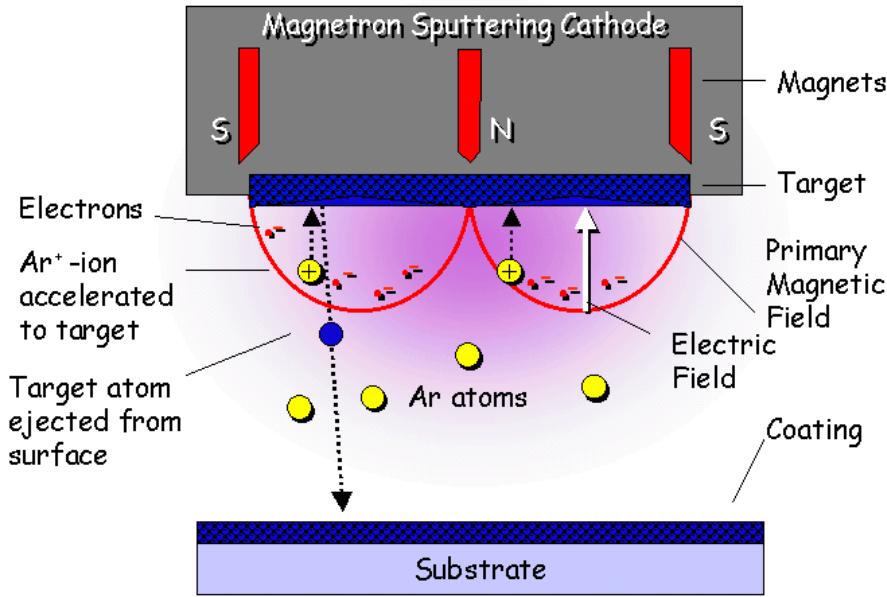


Figure 4.1: Principle of magnetron sputter deposition.

4.2 General effects of deposition parameters

The properties of the sputtered films (structure, roughness, hardness, crystallinity, texture etc.) depend sensitively on deposition parameters [112]: The *sputter current* adjusted via *target power* or *bias voltage* determines the deposition rate and the time available for surface diffusion and agglomeration of adsorbed atoms on existing growth centers or nucleation with other adatoms. The *target bias voltage* roughly equals the potential difference between plasma and target. It determines the sputter yield (number of sputtered particles per incoming ion) and (reduced by the binding energy) corresponds to the maximum energy of sputtered particles escaping from the target. The mean free path for the sputtered material is inversely proportional to the *pressure* p in the deposition chamber. The probability of collisions between sputtered material and atoms or ions in the plasma scales with the product $p \cdot D$, where D is the target-substrate distance. A small $p \cdot D$ product typical for magnetron systems lowers the probability of collisions. Thus sputtered species and reflected Ar atoms impinge onto the substrate with almost the initial kinetic energy. This enhances the surface mobility of adsorbed atoms, increases re-sputtering and results in very dense coatings typically showing compressive stress due to peening by incident particles². The surface mobility of adatoms also increases with the ratio of substrate temperature T_S to melting temperature T_M of the film. During sputtering of rather thick films even without external heating the substrate temperature may rise considerably. A control of the substrate temperature is essential, since higher temperatures may result in a gradient of film properties and also lead to an increased desorption of adatoms, which lowers the effective deposition rate. Thornton [111] represented the effect of pressure and substrate temperature on the structure of deposited metallic films in his famous *zone diagram* (Fig. 4.2). Another option to influence the film properties is the use of a substrate bias voltage. Depending on the conductance of the film this can be a

²In contrast evaporated films often have a less dense structure and show tensile stress.

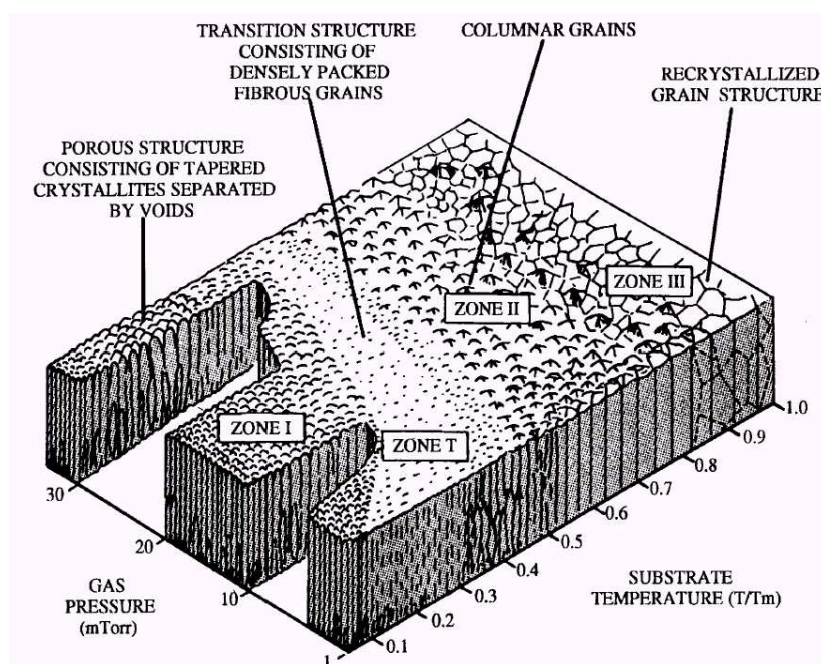


Figure 4.2: Thornton's zone diagram. An experimental study of sputtering (e.g. Ti, Cr, Fe, Cu, Mo and Al) revealed the universal dependence of microstructure on deposition parameters: an improving material quality with higher temperature and lower chamber gas pressure (after [111]).

simple dc voltage or a (negative) self bias-voltage, if the substrate is operated using a pulsed or rf-power supply. A substrate bias increases the resputtering rate, the ion bombardment and increases the edge coverage of substrate features. The choice of the *sputter gas* (usually a noble gas) strongly effects the sputter yield, since the mass ratio of gas ions and target atoms determines the energy transfer in atomic collisions. When the sputtered particles are collimated the morphology of the film surface may depend on their angle of incidence. Sputtering under oblique incidence imposes a preferential direction for the film growth, such that potentially anisotropic films or surface ripples can be produced.

4.3 Sputter deposition of silicon oxide - Review

An excellent review on sputter deposition of insulating films was given by Pliskin[113]. The applications of sputtered SiO₂ films include optical coatings for the visible and deep ultra-violet spectral range[114, 115], passivation and protection layers [113], dielectric inter-layers in semiconductor devices and gate dielectrics in field effect transistors [37, 39] and thin film transistors [116, 117]. Table 4.1 is a selection of references on sputter deposited silicon oxide films focussing on applications in semiconductor technology. The incomplete list demonstrates the steady development in the field. Two basic options for the deposition of silicon oxide films are described in the following: reactive sputtering from a silicon target and sputtering from a fused silica target.

4.3.1 Reactive sputtering from the silicon target

Silicon targets are either poly- or single-crystalline and available with a purity ranging from 3N to 9N (wafer quality). Silicon oxide films are usually formed in an Ar/O₂ mixture in a process called *reactive sputtering*. Reactive sputter deposition has been modelled comprehensively by Berg and coworkers [118, 119, 120, 121, 122]. Because oxygen adsorbs to the target surface and is simultaneously incorporated into the growing film, it is possible to deposit stoichiometric SiO₂ coatings, even if only a small fraction of the silicon target is oxidized. Since the sputter yield for an elemental Si target is much higher than for an oxidized target, this way high deposition rates are achieved. On the other hand the different sputter yields for the bare and oxidized silicon target lead to an instability of the oxygen coverage of the target, which manifests in a hysteresis effect between rate and oxygen gas flow. If the sputtering rate decreases locally, more oxygen is adsorbed and the rate decreases even more until the target is completely oxidized. The hysteresis effect is strong in systems, where most of the supplied reactive gas is incorporated into the growing film. It can be avoided in the limit of large pumping speeds, where most of the reactive gas leaves the chamber through the pump [123]. To stabilize the target in a partly oxidized state external feedback loops are used. These feedback loops adjust the oxygen flow based on the measurement of plasma impedance [114], target self bias voltage or the optical emission intensity of silicon or oxygen plasma lines [124]. This way both stoichiometric and oxygen deficient (silicon rich) silicon oxide films (SiO_x, x<2) may be deposited. Compared to SiO₂, the latter show an increased index of refraction and are in a thermodynamically metastable state. A thermal anneal transforms the single phase supersaturated solution of Si in SiO₂ into a two phase system of Si and SiO₂ as described on p. 7. Using this process SiO₂/SiO_x multilayers can be produced in a single sequence, by simply adjusting the setpoint [125] as will be described in the experimental section. In some cases the target has to be incompletely oxidized during deposition, for example if oxygen-deficient films are prepared or if high SiO₂ deposition rates are required. In this case target regions with a low local sputter rate are oxidized completely (and charge up in case of dc-sputtering) while those areas with a high local sputter rate remain elemental (and conductive). In magnetron systems the variations in sputter rate and local oxygen coverage are even enhanced by the inhomogeneous magnetic field. It has been observed in reactive dc Al₂O₃ sputtering that arcing between oxidized and elemental target regions leads to the ejection of micrometer-sized flakes from the target, which incorporate in the growing film and degrade its properties [126]. Compared to dc reactive sputtering, arcing should be less pronounced if rf and pulsed power supplies are used. In case of reactive sputtering of silicon oxide even this does not completely suppress particle generation (see experimental section). One might speculate whether rate dependent gradients of target temperature and stress contribute to particle generation. If the Si target is completely oxidized during sputter deposition hardly any flaking is observed. High quality reactively sputtered gate oxides have been reported by Haberle [37]. However, for the majority of recent publications on sputter deposited SiO₂ for gate-oxide applications, fused silica targets were used.

4.3.2 Reactive sputtering from fused silica or quartz targets

In 1966 Davidse first described the deposition of SiO₂ by rf sputtering from a fused silica target [127]. Also Macchioni [128, 129] discussed the effect of process parameters on oxide properties. Although by rf sputtering very good MOS transistors (oxide thickness 100 nm-150 nm) were obtained [37], most recent works on ultrathin (down to 6.5 nm [117]) device quality oxide films involved rf *magnetron* sputter deposition.

Conditions for device-quality oxide films by rf magnetron sputtering

Deposition system and choice of target: Pore-free glassy SiO₂ targets of at least 5N purity should be used. A chamber base pressure on the order of 10⁻⁵ Pa should be obtained using turbo-pumps (oil-diffusion pumps cause organic contamination). Initially, the chamber surface, substrate holders etc. should be coated by SiO₂, since metal contamination by re-sputtering would degrade the oxide quality [130]. *Reactive gases:* A 10 % oxygen fraction in the sputter gas helps to compensate the slight oxygen deficiency of films sputtered in pure argon [131] and greatly reduces the density of interface states. Oxides deposited at higher oxygen concentrations (up to 40 %) showed increased electron trapping [39]. Substoichiometry causes a variety of oxide defects [132] such as the neutral oxygen vacancy (NOV) and the related charged paramagnetic E' centers, which manifest in an increased etch rate in buffered hydrofluoric acid (BHF) and poor electrical quality. Also the addition a few percent H₂ to the sputter gas lowered BHF etch rate and increased electrical quality [133, 134]. H₂/Ar mixtures with high H₂ fraction have been used to form SiO_x films with high Si excess from a SiO₂ target [135]. A slight nitridation has been reported to yield increased breakdown strength in annealed oxides [136]. *Pressure, substrate-target separation and substrate temperature:* Low pressures (~0.3 Pa) at a small substrate-target distance (~7 cm) lead to a small probability of collisions between gas atoms and sputtered particles, such that the latter arrive at the substrate with almost the initial kinetic energy and contribute to a higher surface mobility. This leads to very smooth, dense films under compressive stress [39]. Similarly, the use of moderate substrate heating (200-300°C) [137, 129] serves to further lower the density of defects and the concentration of incorporated argon. But even deposition temperatures of 350°C are too low to anneal radiation induced atomic defects in the oxide [132]. Therefore, if a high electrical quality is required, high temperature post-deposition anneals are essential [38]. *Deposition rate/discharge voltage:* Higher deposition rates result from a higher flux and a higher energy of Ar ions incident on the silica target. Because silica has a low thermal conductivity this results in a significantly increased target temperature. The target acts then as source of substrate heating ³. At the same time the higher kinetic energy of sputtered particles and reflected neutralized Ar atoms increases the re-sputtering from the substrate and enhances the substrate surface mobility. Both effects yield a more dense film structure. On the other hand the sample bombardment with highly energetic particles increases the density of interface states [39]. A comprehensive discussion on deposition parameters of device quality sputtered oxides is found in [139, 39].

³According to Westwood [138] a power density of 1 W/cm² may increase the temperature of a SiO₂ target by about 70 K.

Target	Method	Comment on topic	Year	Ref.
SiO ₂	rf	deposition parameters vs. properties	1966	[127]
SiO ₂	rf	effect of re-emission	1970	[130]
SiO ₂	rf	edge coverage, charge accumulation	1970	[140]
SiO ₂	rf	Ar incorporation	1972	[141]
SiO ₂	rf	defect centers, ESR	1974	[132]
Si	reactive rf	edge coverage, Ar/O ₂ = 90/10	1976	[142]
Si, SiO ₂	(reactive) rf	MOS capacitors, t _{Ox} ~ 160 nm	1976	[143]
Si	reactive rf	MOS transistor, t _{Ox} ~ 120 nm	1980	[37]
SiO ₂	rf magn.	effect of H ₂ and O ₂ addition	1984	[133]
SiO ₂	rf magn.	conduction mech., MOS capacitors	1987	[144]
SiO ₂	rf magn.	varied Ar/O ₂ ratio, MOS capacitors	1987	[131]
SiO ₂	rf magn.	Ar/O ₂ , T _S = 200 °C, MOSFET	1987	[137]
SiO ₂	rf magn.	Ar/O ₂ ratio vs. el. properties	1989	[145]
SiO ₂	rf	varied deposition parameters	1991	[129]
SiO ₂	rf magn.	electr. prop. of MOSFET at 4.2 K	1992	[146]
SiO ₂	rf magn.	H ₂ , N ₂ , O ₂ , currents, etch rate	1994	[134]
SiO ₂	rf magn.	el. quality of nitrated SiO ₂	1995	[36]
SiO ₂	rf magn.	parameters for TFTs, t _{Ox} = 20 nm	1995	[147]
SiO ₂	rf magn.	stability of nitrated oxides	1995	[139]
SiO ₂	rf magn.	annealing vs. electric stability	1997	[38]
SiO ₂	rf magn.	el. quality vs. anneal, t _{Ox} = 25 nm	1997	[136]
Si	react. rf magn.	ion assistance, electr. tests	1998	[148]
SiO ₂	rf magn.	TFT on steel foil	1998	[116]
SiO ₂	rf magn.	TFT on glass, t _{Ox} = 6.5-100nm	1998	[117]
Si	react. rf magn.	SiO _x	1998	[125]
SiO ₂	rf magn.	charge relaxation in SiO ₂ , SiO _x N _y	1999	[149]
Si	react. rf magn.	SiO ₂ /SiO _x stacks	2001	[124]
SiO ₂	react. rf magn.	SiO _x films (>20 at% Si), dep. in Ar/H _s	2001	[135]
SiO ₂ /Si	rf/dc magn.	SiO _x by co-sputtering of Si and SiO ₂	2003	[150]

Table 4.1: Selected reports on sputtered silicon oxide films for application in semiconductor technology.

TFT: thin film transistor, MOSFET: metal oxide silicon field effect transistor
t_{Ox}: oxide film thickness.

5 Experiments on sputter deposition of Si, SiO_x, and SiO₂ thin films

5.1 The deposition tool

A NORDIKO 2000 sputter tool was used for thin film deposition (Fig. 5.1). The four targets of 20 cm diameter are arranged above a rotatable substrate table with four holders (two water cooled, two heatable up to 500 °C, one of the latter equipped with a thermocouple) for 8 inch substrate platens. Two of the four magnetrons operate in dc mode, the other two are powered either in dc or in rf mode. Simultaneous operation of one dc (up to 5 kW) and one rf magnetron (13.6 MHz, up to 2 kW) is possible. The used polycrystalline Si and fused silica targets had a purity of 5N and 4N, respectively. The central and the ring shaped outer magnets generate a fixed ring-like race track-region. Regions with low erosion rate (re-sputter zones) are in the center and at the edges of the target. For reactive sputtering from the silicon target a piezoelectric reactive gas inlet valve (MV-112, MAXTEK [151]) is driven by a controller (REACTAFLO, Megatech [152]) using the optical line intensity of excited Si atoms in the plasma to sense the degree of target oxidation. The optical plasma emission from the race track region is picked up in about 4 cm distance from the target. A fiber-optic link guides it to the spectrometer (VM3000, Verity [152]) consisting of a photomultiplier tube and a rotatable grating. The approximate partial pressures of gases are determined by means of a micropole sensor system (Ferran Scientific [153]). Since the tool geometry did not enable an in-situ thin film analysis, the thin films were analyzed ex-situ.

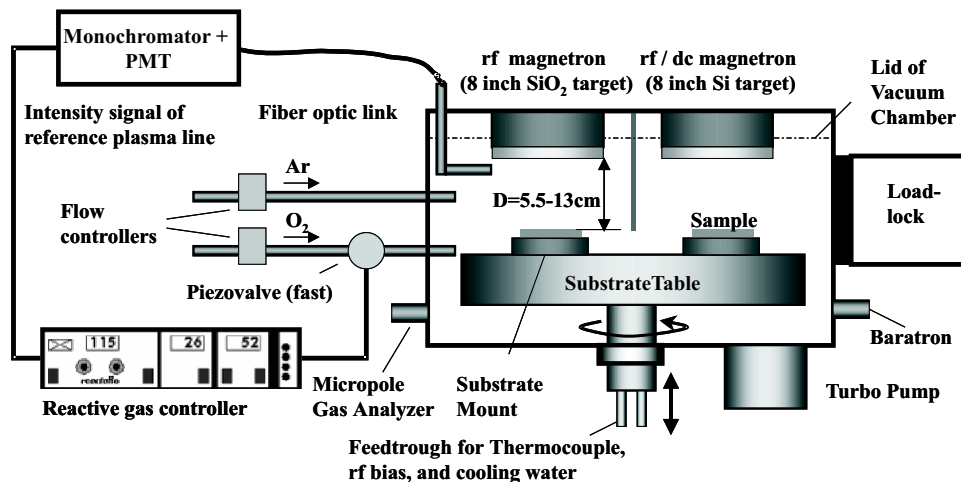


Figure 5.1: Schematic cross section of NORDIKO 2000 sputter chamber.

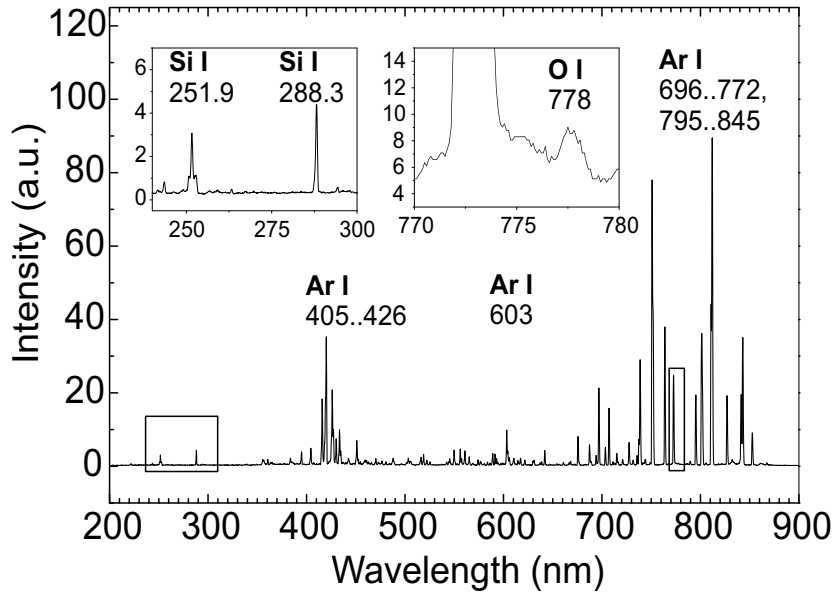


Figure 5.2: Optical emission spectrum from Ar plasma during deposition from SiO₂ target at a rf-power of 1.5 kW and a pressure of 5 mTorr

5.2 Reactive sputter deposition from the Si target in Ar/O₂

5.2.1 Process characterization

Reactive sputtering allows the deposition of stoichiometric and oxygen-deficient silicon oxide from the same target. It was therefore considered initially for the deposition of SiO₂/SiO_x stacks for use in Si NC memories. The reactive deposition of SiO_x from the Si target was done at fixed Ar pressure, whereas the oxygen supply through the piezoelectric valve was adjusted by the REACTAFLO controller to stabilize the degree of target oxidation. Details of the process along with a phenomenological model of reactive rf magnetron sputtering of SiO_x in Ar/O₂ have been published elsewhere [124]. Fig. 5.2 shows a typical plasma emission spectrum acquired from a SiO₂ target (representing a completely oxidized Si target). The intensity of an optical emission line related to excited Si atoms (Si I line at 251.9 nm) was used to define a deposition setpoint: After power and Ar-pressure were adjusted, at zero oxygen flow the line intensity was measured for the non-oxidized target. The addition of oxygen to the sputter gas led to an increased oxidized target fraction, fewer Si atoms present in the plasma and thus to a lower intensity of the Si line. The ratio of intensities determined with the Ar/O₂-mixture and Ar respectively is defined as setpoint I_{Si} . This normalized intensity serves as input signal for the REACTAFLO controller. The use of a normalized intensity instead of an absolute intensity eliminates a possible long-term setpoint-drift as it would result for example from a gradual coating of the collimating lens of the fiber optics. Any plasma line whose intensity changes owing to the formation of the reactive gas compound on the target surface is suited for process control, provided that its intensity is an unambiguous function of oxygen pressure p_r . Fig. 5.3 shows the dependence of several plasma lines on p_r for deposition from a silicon target. The Si

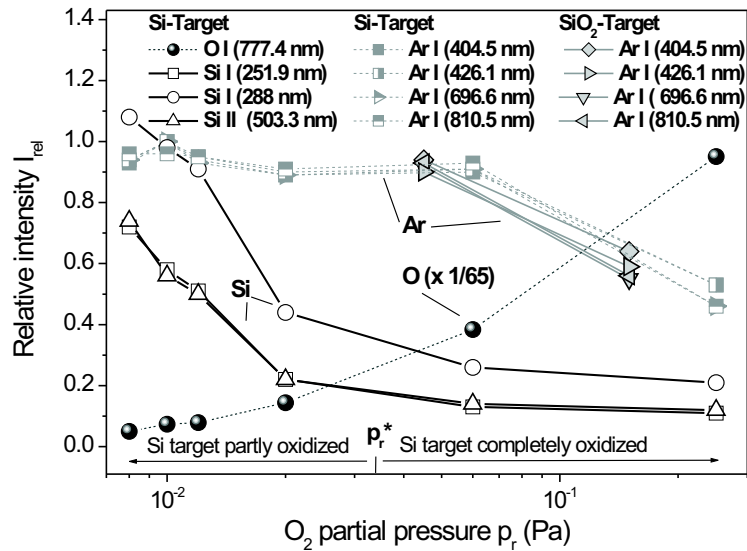


Figure 5.3: Dependence of the relative intensity I_{rel} of plasma lines on the oxygen partial pressure. Intensities are normalized to those for the deposition in pure argon (Si target not oxidized). Indicated are data acquired for a Si and a SiO₂ target. In both cases the target power was 1.5 kW.

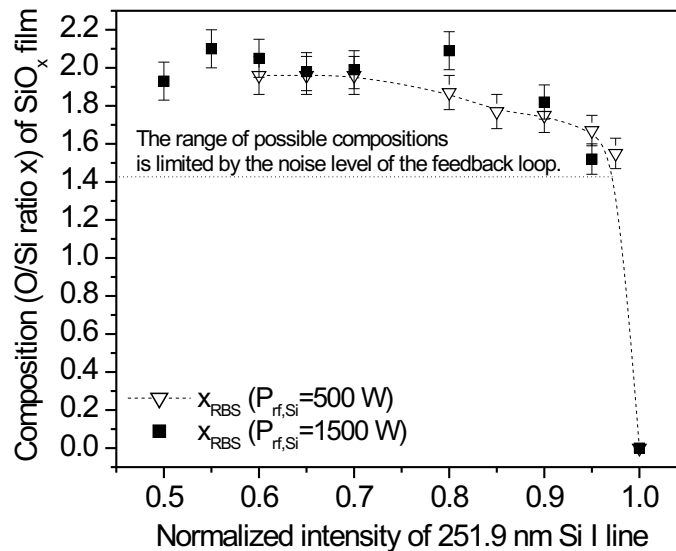


Figure 5.4: Relation between the intensity of the 251 nm Si I plasma line (normalized to the non-oxidized Si target) and the silicon oxide composition x for a power $P_{rf,Si}$ of 0.5 kW and 1.5 kW (RBS measurements by R. Grötzschel, FZ Rossendorf).

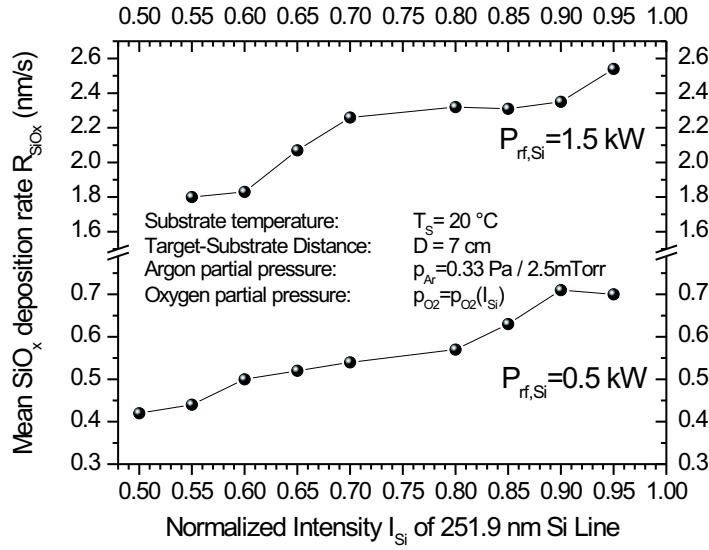


Figure 5.5: Deposition rates of SiO_x for reactive rf magnetron sputtering from the Si target in an Ar/O₂ mixture.

line intensities decrease rapidly with increasing oxygen pressure and increasing degree of target oxidation. Using an rf power of 1.5 kW and an Ar pressure of 0.35 Pa the target is completely covered with SiO₂ for an oxygen pressure $p_r^* \approx 3.5 \cdot 10^{-2}$ Pa, the corresponding setpoint is $I^* \approx 0.175$. A further increase of p_r has almost no effect on the Si line intensities. In contrast, the oxygen line intensity increases steadily throughout the measured range of p_r . For $p_r \leq p_r^*$ the intensities of all atomic Ar lines are almost independent on p_r , implying that in this p_r range the electron energy distribution is not significantly altered by the presence of oxygen. For $p_r > p_r^*$ they decrease in the same manner for the Si target and the SiO₂ target since target and plasma conditions are the same in both cases. Alternatively to the 251.9 nm atomic Si line also the atomic Si line at 288 nm, the singly ionized silicon line at 504 nm or the atomic oxygen lines at 777.4 nm and 844 nm may be used as a deposition setpoint variable. Oxygen plasma lines increase with increasing oxygen partial pressure and must be normalized to the intensity at a known oxygen flow, at which the target is completely oxidized. When oxide films are deposited from the Si target, their composition can be related to the normalized Si line intensity I_{Si} . Fig. 5.4 shows the relation between the atomic ratio x of oxygen and silicon atoms and I_{Si} . The values of x were determined by Rutherford backscattering (RBS) measurements of films deposited on carbon coated Si wafers [124]. The feedback loop based on I_{Si} enabled the deposition of SiO_x with x between about 1.45 and 2.

5.2.2 Limitations of the method

An accurate composition control is possible provided the Si line intensity signal has a high signal to noise ratio and the total oxygen flow is not too small. The piezoelectric gas valve MV-112 (MAXTEK [151]) enables a flow of 300 sccm oxygen at maximum

and should be used with flows above 30 sccm to ensure stable operation. The only competitive product, the PCV25 piezoelectric valve by v. Ardenne Anlagentechnik [154], has the same range and faces the same problem. Both features render the process useful for the deposition rates above about 2 nm/s, whereas the accuracy of film composition is strongly compromised at lower deposition rates¹. In addition, any inhomogeneities in the oxygen supply across the surfaces of target and film results in inhomogeneities of the film composition. Despite the use of an rf power supply during deposition from an only partially oxidized Si target the generation of micro-particles was observed. In EDX² line scans, the micro-particles showed a much higher silicon signal than the underlying oxide matrix (Fig. 5.6). It seems likely that silicon-particles are ejected from the target as a result of target cracking. Temperature or stress gradients caused by the inhomogeneous target erosion typical for magnetrons may be relevant factors. Obviously particles seriously deteriorate the properties of the deposited films. In optical applications, the substitution of doped high purity Si targets by silicon alloy targets leads to lower particle generation. Examples are the SISPATM or the SiAl targets offered by Heraeus³ and GFE⁴ respectively for the deposition of SiO₂ and Si₃N₄ films. These Si alloys contain Al as the main constituent. They have a higher electrical and thermal conductivity and form a rougher surface which improves the sticking of redeposit to the target. Because of the high level of metallic impurities (typical purity: 99.5 %) standard targets of this type appear not suited for the deposition of high quality gate-oxides. However, customized high-purity Si-Al targets can be made on request.

5.2.3 Preparation of SiO₂/SiO_x/SiO₂ heterostructures

It is possible to deposit stacks of silicon oxide layers with different composition x in a single step by simply changing the setpoint I_{Si} . Fig. 5.7 shows the setpoint sequence used to deposit a stack of 5 nm SiO₂ / 10 nm SiO_{1.5} / 45 nm SiO₂ onto a Phosphorus doped Czochralski type Si monitor wafer. The deposition conditions were: $P_{rf,Si} = 500$ W, $p_{Ar} = 0.35$ Pa, $D = 7$ cm and $T_S = 20$ °C. During a subsequent anneal at 1000 °C for 1 h in N₂ precipitation of Si-nanoclusters occurred and the metastable SiO_{1.5} layer turned into a two phase compound of Si nanoclusters embedded in SiO₂. Fig. 5.8 shows a cross-section high resolution TEM image of the annealed sample, obtained using a PHILLIPS CM300 device. The Si NC-layer is located about 6 nm above the substrate interface. The white lines indicate its abrupt boundaries. The substrate is oriented with the (110) direction along the incident electron beam. Crystalline Si NC oriented in the same direction show lattice contrast. Their diameters vary between 3 nm and 5 nm. The Fourier transform of the marked area shows two reflexes corresponding to

¹By a slight modification of the rf magnetron matching unit a feedback based on the target self-bias voltage could be implemented. Such a feedback would work also with low deposition rates. If the reactive gas inlet tubing beyond the piezo-valve would be arranged closer to the pump, an increased fraction of the supplied oxygen would be lost to the pump instead of being adsorbed to target or substrate. Then, to obtain a certain composition larger oxygen flows at the valve were needed and the oxide composition could be adjusted more precisely.

²EDX: energy dispersive x-ray analysis

³<http://www.wc-heraeus.com>

⁴<http://www.gfe-online.de>

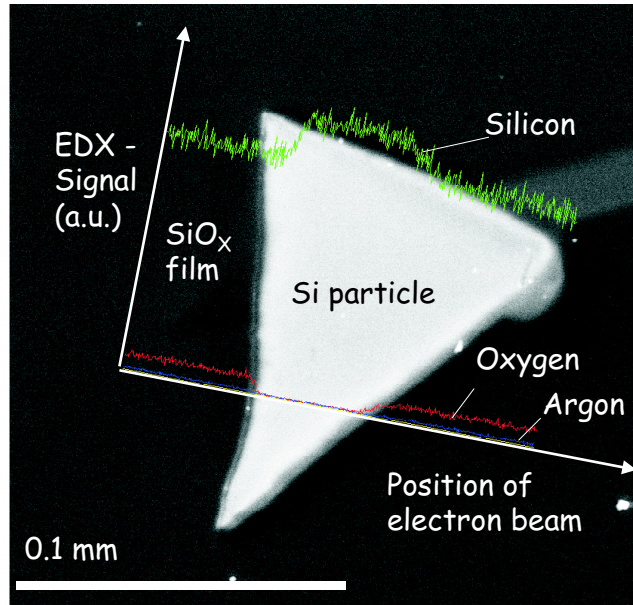


Figure 5.6: Scanning electron microscopy (SEM) image of Si microparticle emitted from the Si target during reactive rf magnetron sputtering of SiO_x from the Si target. The EDX-linescan across the particle (shown as inset) indicates that the generated particles consist of pure silicon (measured by Mrs. Christalle, FZ Rossendorf).

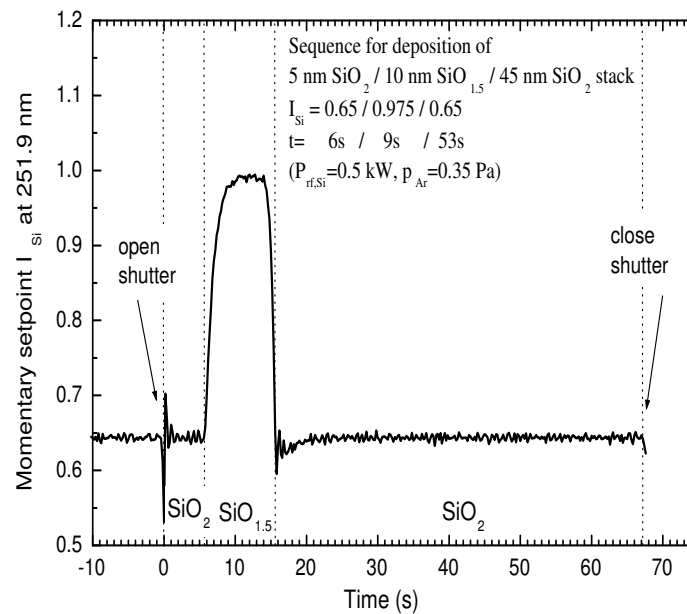


Figure 5.7: Response of Si I (251.9 nm) line intensity to the setpoint sequence $I_{Si} = 0.65$ (6 s) / $I_{Si} = 0.975$ (10 s) / $I_{Si} = 0.65$ (53 s) applied to the REACTAFLO-controller during the preparation of a 5 nm SiO₂ / 10 nm SiO_{1.5} / 45 nm SiO₂ layer stack.

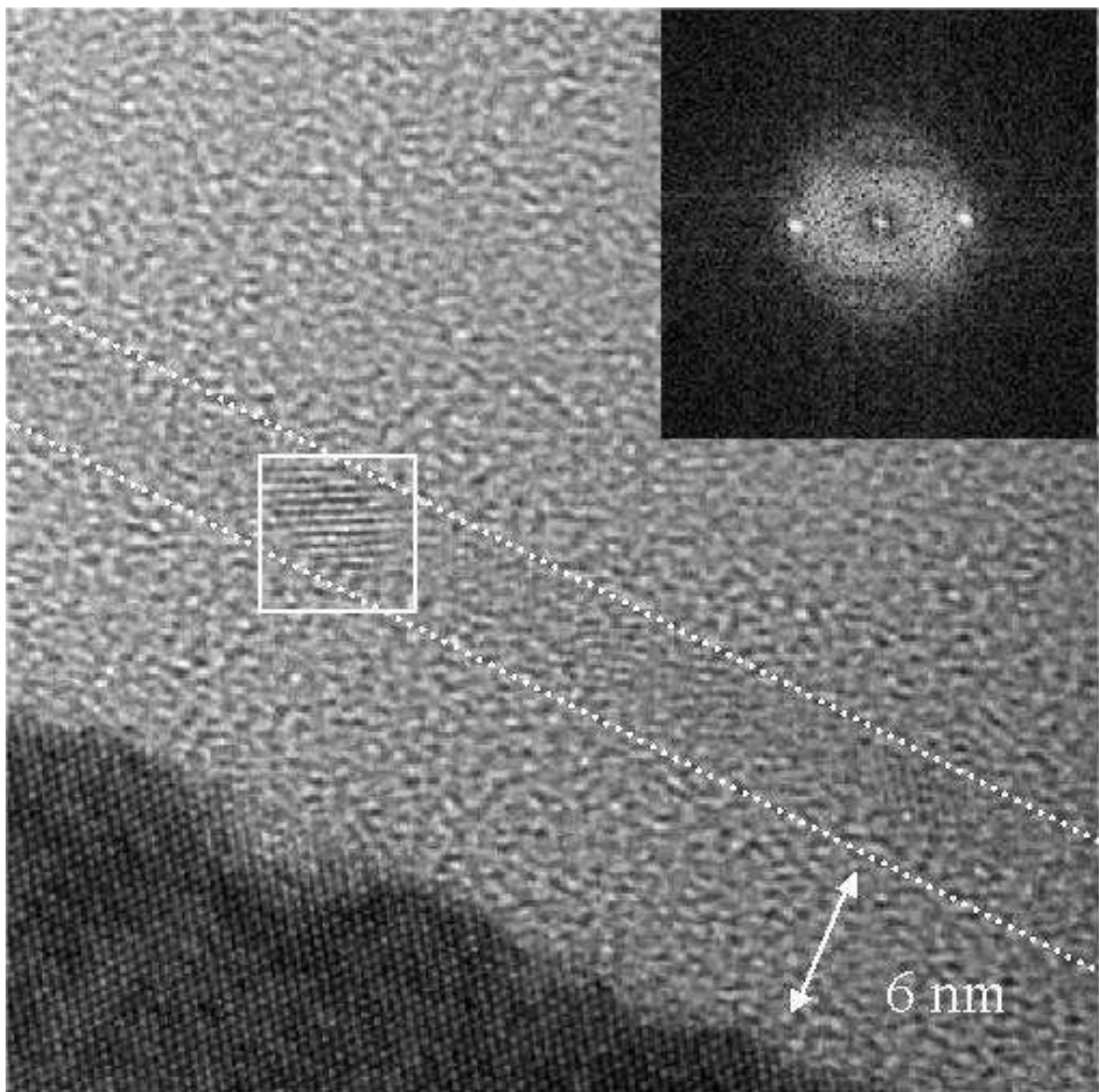


Figure 5.8: High resolution cross-section TEM image of Si NC memory capacitor prepared by reactive sputtering from the Si target. After deposition the 5 nm SiO₂ / 10 nm SiO_{1.5} / 45 nm SiO₂ stack was annealed for 1h at 1000 °C in N₂ to transform the SiO_{1.5} layer (indicated by dotted white lines) into a layer of Si nanocrystals. The substrate is oriented with the (110) direction along the electron beam. The substrate and appropriately oriented Si nanocrystals show contrast from (111) lattice planes. The fourier transform of the marked square enclosing a Si nanocrystal shows two reflexes corresponding to the period of (111) planes (measured by M. Klimenkov, FZ Rossendorf).

(111) Si nanocrystal lattice planes with $d_{111} = 0.313$ nm. Stacks like this could be used in the desired Si NC memory devices. To allow an efficient injection of electrons by direct tunneling, the tunnel-oxide (TOx) between Si NC and Si substrate must be less than 4 nm wide (see p. 37). Because of the 6 nm thick TOx layer, an efficient charging was not expected for the presented stack. Measurements of Al-gate MOS-capacitors showed that the annealed gate stacks had low electrical quality and breakdown fields below 1 MV/cm for positive gate voltage, such that Si NC related charging effects could not be measured.

5.2.4 Conclusion and new strategy

The low electrical quality of the gate stack was attributed partly to the low quality surface of the substrate (see Fig. 5.8) but mainly to a particle induced degradation of the gate oxide properties. The main obstacles of the reactive sputtering from the Si target are problems to operate at low deposition rates and particle induced defects observed when the target coverage with SiO₂ was incomplete, as for the deposition of oxygen deficient SiO_x films. The high quality SiO₂ films reported by Haberle et al. [37] do not contradict the presented results. Haberle did not use an external feedback. In his case the known process instability caused a complete oxidation of the target resulting in a low-rate deposition of particle-free stoichiometric films. Because of the mentioned limitations, no additional attempts were made to prepare oxygen-deficient SiO_x films for use in Si NC memories by reactive sputter deposition from a Si target. Instead a new strategy to deposit SiO₂ / SiO_x stacks has been developed. As a result stoichiometric SiO₂ films were deposited from a fused silica target in an Ar/O₂-mixture while SiO_x films were prepared co-sputtering from Si and SiO₂ targets in Ar. The development of these processes is described in the following.

5.3 Reactive sputter deposition from the fused silica target in Ar/O₂

A literature review showed, that a high electrical quality SiO₂ films may be expected for oxides deposited from a fused silica target in Ar/O₂ mixtures. In several experiments the influence of the following parameters investigated: O₂/Ar flow ratio $O_2/Ar = 0-0.3$, total pressures $p = 0.2-0.67$ Pa, target rf power $P_{SiO_2} = 330-1500$ W, nominal substrate temperatures T_S between 20°-400° and a substrate rf power $P_{sub} = 0-250$ W at a substrate-target distance $D = 5-7$ cm. In the following some characteristics of the deposited SiO₂ films are summarized.

Films deposited at ($O_2/Ar = 0.33$, $p = 0.2$ Pa, $D = 7$ cm, $P_{SiO_2} = 330$ W, $P_{sub} = 0$, $T_S = 20$ °C) are very smooth both for small (37 nm) and high (684 nm) film thicknesses (see Fig. 5.9). A scan along the diagonal of a 200 nm wide area showed peak-to-valley roughnesses of only 0.5 nm and 0.8 nm respectively. No particles are observed by visual inspection. During the extended (2 h) deposition of the 684 nm thick film, the substrate platen positioned on a water cooled mount reached a temperature of roughly

60 °C, indicating an insufficient heat contact between the substrate platen and the mount.

In another experiment, the influence of substrate temperature, substrate rf bias and annealing on the optical constants of SiO₂ films deposited on silicon substrates was investigated. The deposition conditions were (O₂/Ar = 0.13, p = 0.67 Pa, D = 5.5 cm, P_{SiO₂} = 1500 W, P_{sub} = 0-500 W, T_S = 20-400 °C). Part of the samples were annealed for 30 min at 1000 °C in N₂. Spectroscopic ellipsometry between 1.2 eV and 4.9 eV was used to determine the optical constants. Raw data were fit to the Sellmeier model (see p. 32). As shown in Fig. 5.10a, SiO₂ films deposited without substrate heating generally have a higher refractive index than thermal SiO₂. The use of a rf substrate bias may even increase the refractive index. Increased refractive index values of sputtered SiO₂ have been attributed to an increased density resulting from the particle bombardment of the growing film. Devine [60] pointed out that the link between density ρ and refractive index n is given by the Lorentz-Lorenz law:

$$\frac{n^2 - 1}{n^2 + 2} = 4\pi\rho A_{mol}(N_A V_{mol}) \quad (5.1)$$

Here A_{mol} is the molar polarizability, V_{mol} the molar volume and N_A Avogadro's number. Devine's regression analysis of refractive index data at 632.8 nm from plastically densified amorphous SiO₂ and crystalline phases resulted in the relationship

$$n = 1.029 + (0.195 \pm 0.021)\rho \quad (5.2)$$

yielding for the thermal SiO₂ reference of Palik [155] a density of $\rho = 2.195$ g/cm³ and for the SiO₂ films sputtered without heating with $n \approx 1.463$ a density of $\rho = 2.226$ g/cm³. Consistent with a compaction of the films by particle bombardment is the decreasing net-deposition rate for increasing rf bias, caused by re-sputtering of deposited material. The hypothesis, that sputter deposited SiO₂ films have a higher density is corroborated by infrared absorption measurements of Lisovskii [64] (see p.22). The high temperature anneal lowers the refractive index down to the value of thermal SiO₂ corresponding to a structural relaxation and a slight decrease in film density. Fig. 5.10b shows that at elevated substrate temperature the refractive indices before and after annealing are nearly the same. This implies that even moderate substrate heating helps to ensure a relaxed film structure. The increase of deposition rate with substrate temperature is probably caused by radiation heating of the target. The Bruggemann effective medium approximation shows that also a slight Si excess might lead to an increases refractive index. However, the inert gas anneal would not change the effective oxide composition, such that complete relaxation of the refractive index is not consistent with this possibility.

5.4 Deposition from SiO₂ and Si targets in pure Ar

In order to develop a co-deposition process for SiO_x films, both dc magnetron sputtering of a-Si and rf sputtering of SiO₂ in Ar were investigated at the following conditions: p_{Ar} = 0.667 Pa, D = 5.5 cm, T_S ~20 °C. For comparison stoichiometric SiO₂ films

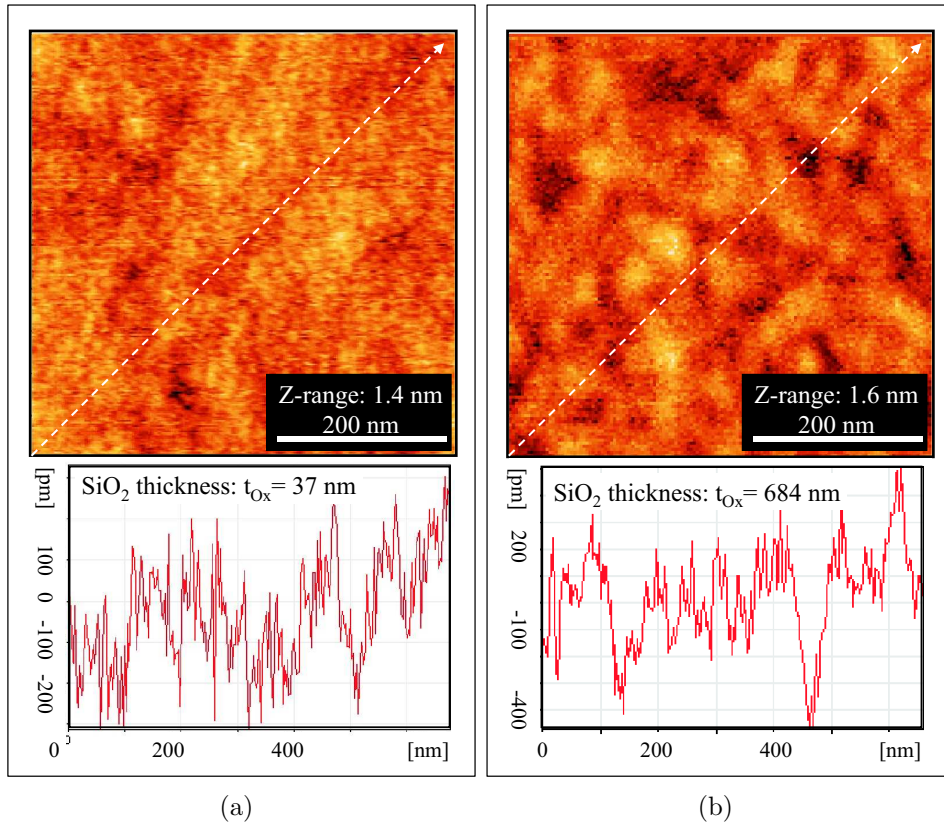


Figure 5.9: AFM-images of 37 nm and 684 nm thick SiO₂ films sputtered from an SiO₂ target. Both films are very smooth. For the indicated diagonal profile the peak-valley roughnesses are 0.5 nm and 0.8 nm.

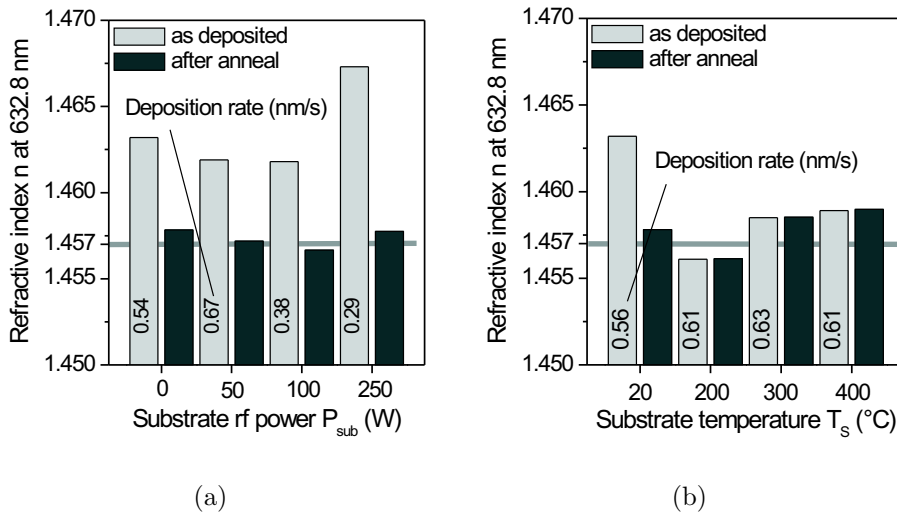


Figure 5.10: Effect of rf substrate bias (a) and substrate temperature (b) on refractive index of sputtered SiO₂ films at 632.8 nm. The reference value of thermal SiO₂, n = 1.457 [155] is indicated by the grey bar. The use of cooled substrates and the application of substrate bias result in a compacted film with increased refractive index. Substrate heating favors a relaxed film structure with a refractive index close to thermal oxide and increases the deposition rate.

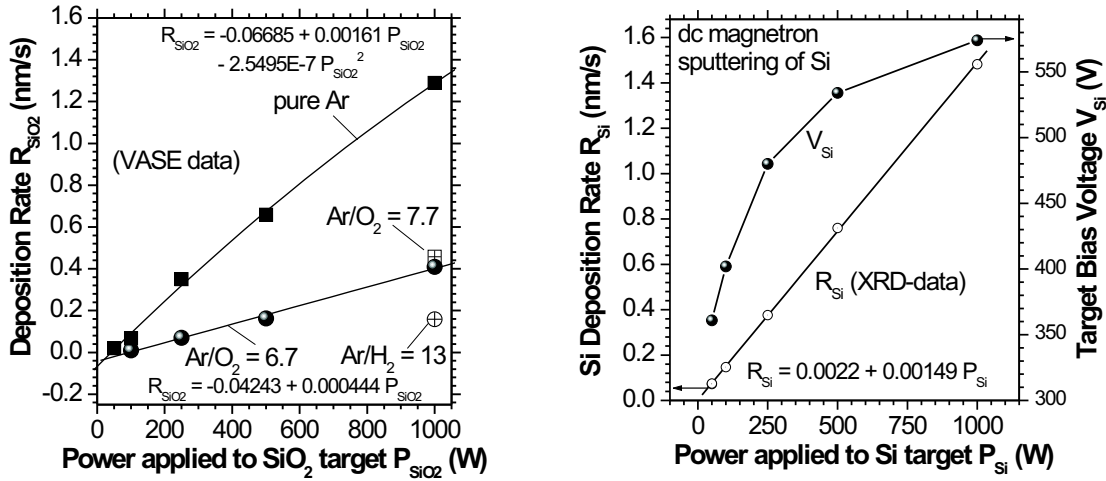
were deposited by rf sputtering of SiO₂ in an Ar/O₂ = 6.7 mixture at p = 0.667 Pa, D = 5.5 cm, T_S ~20 °C. To check the effect of the gas mixture on the deposition rate in two cases Ar/H₂ = 13 and Ar/O₂ = 7.7 mixtures were used.

5.4.1 Deposition of SiO₂

The *deposition rates* for rf sputtering of SiO₂ in Ar and Ar/O₂ mixtures are shown in Fig. 5.11a. The highest rate is observed for deposition in pure Ar. In agreement with Serikawa [133], an increase of oxygen partial pressure lowers the rate, the same is observed for addition of hydrogen. The *optical constants* of the deposited films were determined using spectroscopic ellipsometry. Fig. 5.12a shows Sellmeier fits (p. 32) of the index of refraction n, assuming that the extinction coefficient k ≈ 0. The refractive index of silicon oxide films deposited in Ar is slightly increased. If the increased refractive index was related to a pure compaction, according to Eqn. 5.2 the highest refractive index observed (n = 1.485) would yield a density of 2.34 g/cm³, which is highly above the typical value for thermal SiO₂ of 2.2 g/cm³. Here in addition to the density the composition is important. It is widely accepted that films deposited from a SiO₂ target in Ar are slightly oxygen-deficient [39], resulting in an increased n. If the oxide is modelled as Bruggemann effective medium medium (p. 34) of thermal SiO₂ and a-Si, an upper limit of the excess Si volume fraction is obtained, which lies between 0.3-1 vol%, corresponding to an oxygen/silicon ratio of x = 1.98-1.95.

5.4.2 Deposition of Si

The deposition rates for dc magnetron sputtering of Si in Ar onto a room-temperature Si wafer, determined from X-ray diffraction (XRD) measurements are shown in Fig. 5.11b. According to XRD, 50 nm a-Si films deposited at P_{Si} = 50-1000 W are amorphous, have a density of 2.35 ± 0.04 g/cm³ and a surface roughness of 0.86 ± 0.1 nm. The refractive index of a-Si is described best by the Tauc-Lorentz (TL) model (p. 31) developed by Jellison [92, 93]. The extracted parameters of the TL dispersion model are listed in Fig. 5.12b. The optical constants of a-Si are known to depend strongly on preparation conditions, density, structure and hydrogen content. Therefore a slight deviation from the reference data obtained from evaporated a-Si is expected. For some films the depth profiles of hydrogen were determined by nuclear reaction analysis (NRA). The total hydrogen concentration of the a-Si films has been measured at the 5 MV tandem accelerator of the Forschungszentrum Rossendorf using the nuclear reaction $^{15}\text{N} + ^1\text{H} \rightarrow ^{12}\text{C} + ^4\text{He} + \gamma$ (4.43 MeV). This reaction has a narrow resonance at a ¹⁵N kinetic energy E_{res} = 6.385 MeV. By increasing the energy of the ¹⁵N ions above E_{res} the ions reach the resonance energy at a certain depth of the sample due to energy loss in the material. Measuring the yield of the γ-rays with an energy of 4.43 MeV as a function of the beam energy the hydrogen depth profiles were measured. The γ were detected by a 2 in. x 34 in. NaJ(Tl) scintillation detector. No hydrogen loss of the samples was observed due to the analysis beam, using typically a ¹⁵N ion beam current of 15-20 nA and a beam spot of 5x5 mm². As shown in Fig. 5.13a, the upper 10 nm of the film contain 3-4.5% hydrogen. The origin of hydrogen is assumed to be

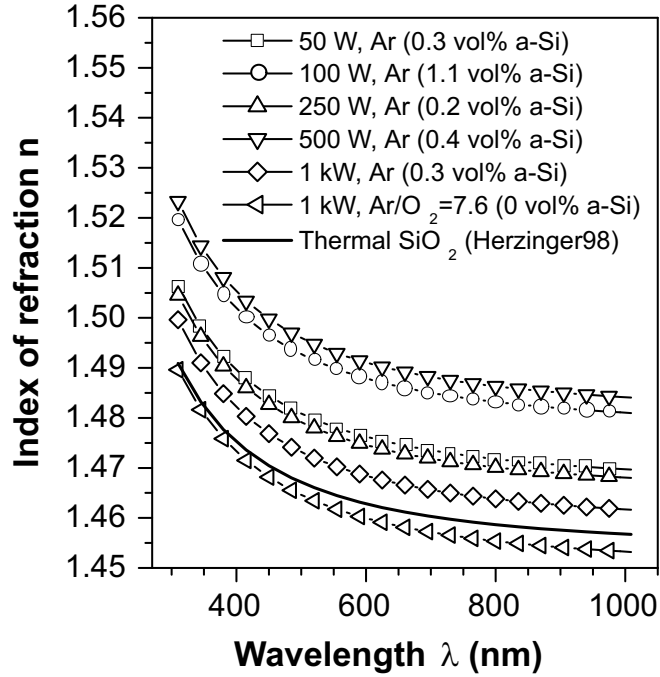


(a) Rates for rf sputtering of SiO₂ from a fused silica target (spectroscopic ellipsometry). (b) Rate and bias voltage for dc magnetron sputtering of Si from a poly-Si target (x-ray reflectometry measurement by F. Prokert, FZ Rossendorf).

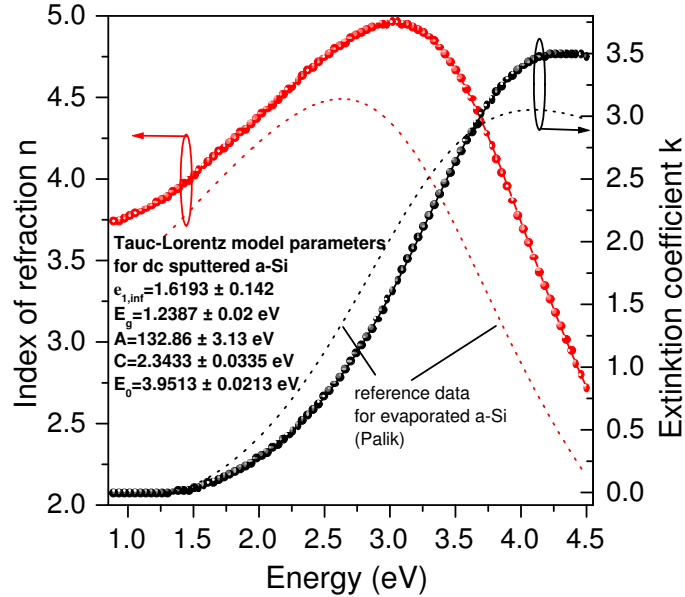
Figure 5.11: Deposition rates of SiO₂ and a-Si in Ar.

mainly water, either adsorbed from the ambient air or from the water based cleaning solution. In the bulk of the film, where the diffusion limits effects of ambient humidity, one finds that the concentration of hydrogen incorporated during film growth is below the detection limit of NRA (about 0.5 at%).

Evolution of a-Si roughness with film thickness The growth front of a sputtered a-Si film roughens with increasing thickness. To investigate this effect, a-Si films were deposited at a power of 1 kW and substrate temperatures of 20 ° and 250 °C. The ratio of deposition temperature to melting temperature, often used as a measure of surface mobility, is small in both cases. Consequently the influence of substrate temperature was found to be insignificant. Fig.5.14 illustrates the roughening of the a-Si growth front for deposition at 250 °C and a film thickness increasing from 100 nm to 10 μm. Details on the roughening mechanism are found in Karabacak et al. [156].



(a) Index of refraction of oxygen deficient and stoichiometric oxide films deposited from the SiO₂ target in Ar and Ar/O₂ = 6.7 respectively. Oxygen deficient films have an increased refractive index, which at least partly is due to the silicon excess.



(b) Refractive index of a-Si films dc-sputtered at $P_{Si} = 100$ W. The dotted reference data for evaporated a-Si was taken from Palik [155]. A comparison of both results underlines the effect of deposition conditions on film structure and optical constants.

Figure 5.12: Refractive indices of sputter deposited amorphous SiO₂ and Si films.

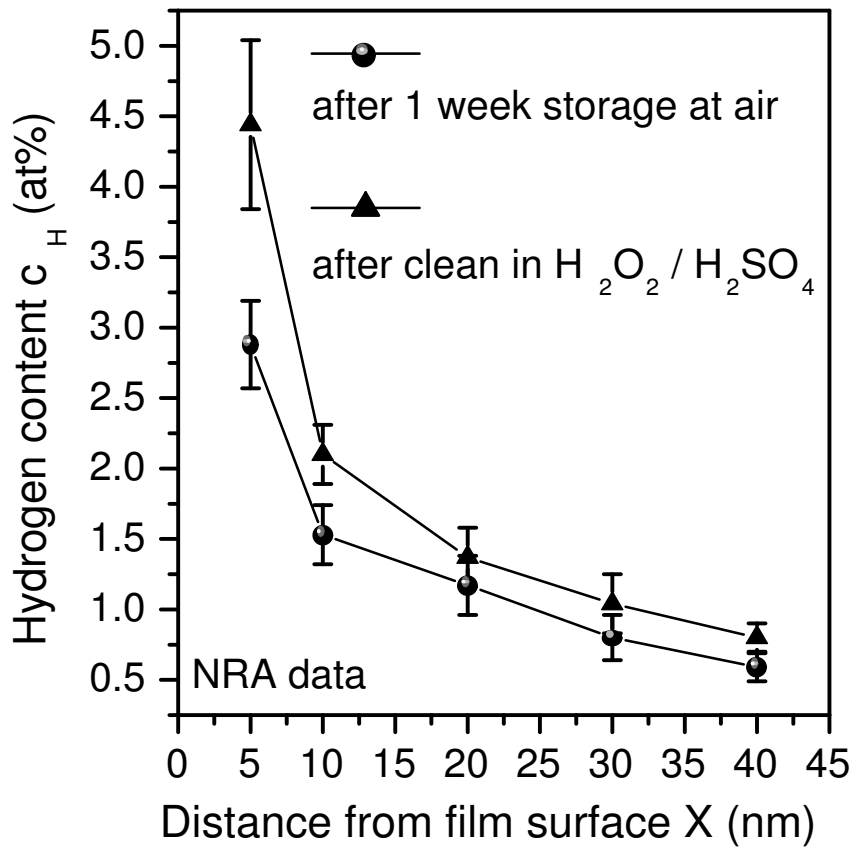
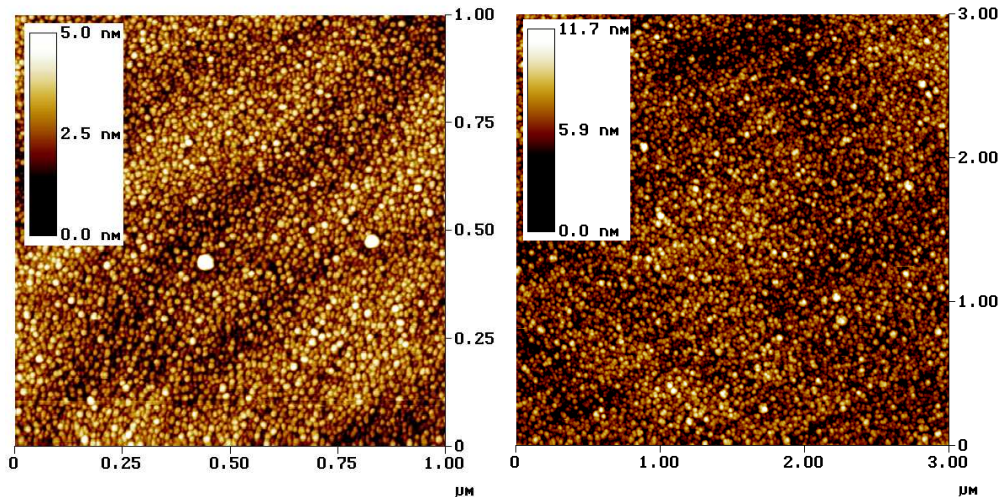
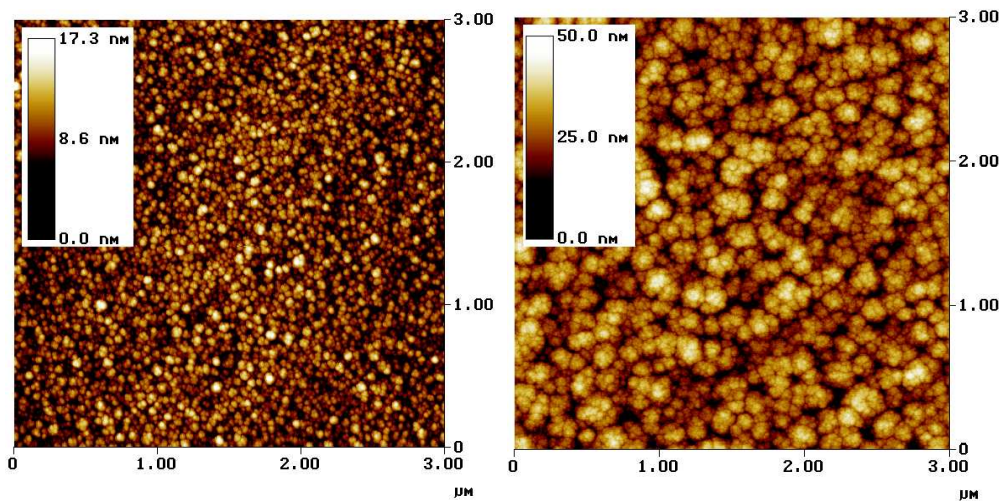


Figure 5.13: H-content of a-Si films sputtered in pure Ar determined by NRA (Measurement: D. Grambole, FZ Rossendorf).



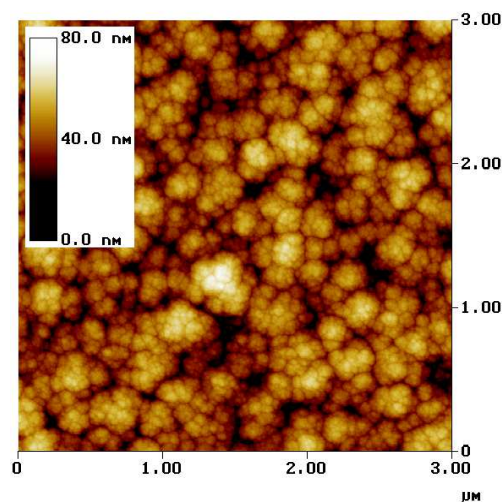
(a) 100 nm a-Si film.

(b) 500 nm a-Si film.



(c) 1000 nm a-Si film.

(d) 5000 nm a-Si film.



(e) 10000 nm a-Si film.

Figure 5.14: AFM images showing the coarsening of the a-Si growth front with increasing film thickness for deposition at 250 °C onto silicon wafers (Measurement: R. Gago, FZ Rossendorf).

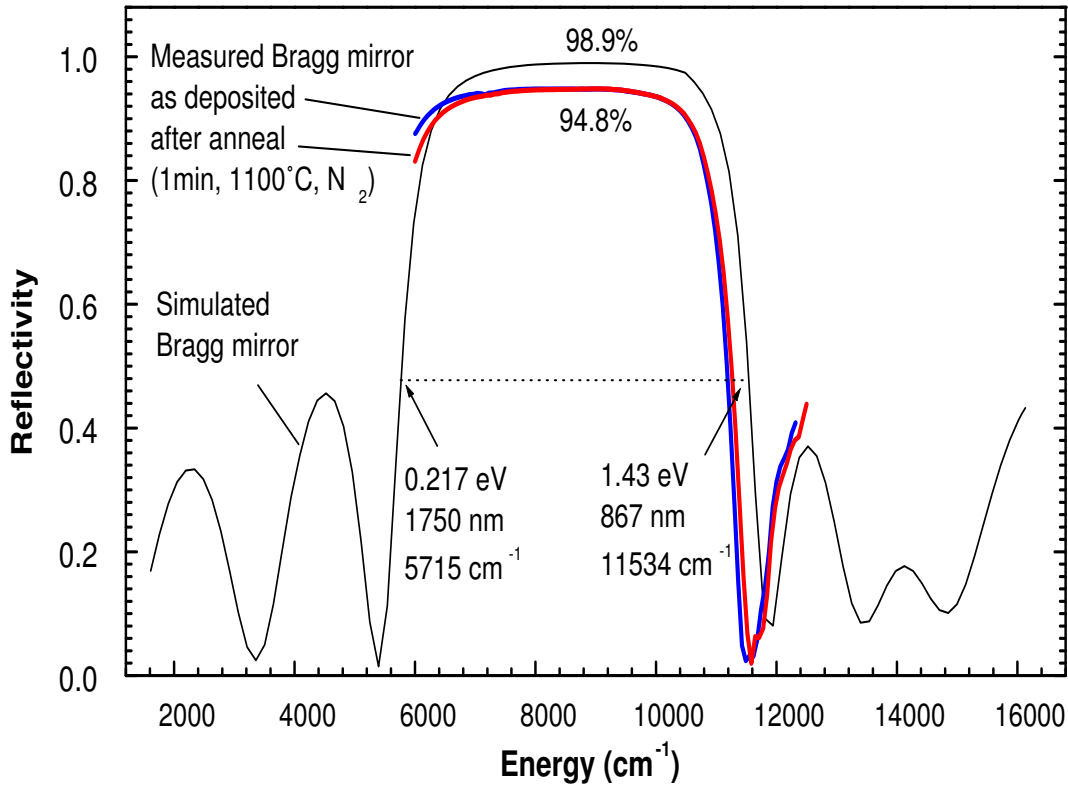


Figure 5.15: Reflectance of the Bragg-mirror (200 nm SiO₂ + 3x [80 nm Si / 200 nm SiO₂] on Si) as deposited and after an anneal for 1 min at 1100 °C in N₂. (Measurement by Y. Sun, FZ-Rossendorf).

5.4.3 Future application: Dielectric Si/SiO₂ NIR Bragg-mirrors

To assist a collaborating group in the development of optical cavities for use with Si based light emitting diodes, dielectric multi-layer mirrors were developed in which a-Si and SiO₂ act as high (H) and low (L) refractive index materials. A L(HL)³ quarter-wave stack was deposited on a Si wafer heated to 300 °C by alternating deposition from the Si and SiO₂ target respectively in Ar using the same conditions as above. The layer thicknesses used for the target wavelength of 1 μm were L: SiO₂, 200nm and H: Si, 80 nm. To check the effect of a possible Si crystallization on the reflectance of the mirror, reflectance spectra were acquired before and after an anneal for 1 min at 1100 °C in N₂ (Fig. 5.15). The crystallization mainly effects the optical transitions near 3.2 eV and 4.5 eV and therefore had almost no effect on the NIR-reflectance. In both cases the maximum reflectivity was 94.8 %, which is slightly below the value obtained for the simulated spectrum. The difference arises probably from a finite absorption in the Si layers, which was neglected in the simulation. A simple way to shift the onset of absorption toward higher energy would be hydrogen doping of a-Si, and could be achieved by deposition in Ar/H₂ mixtures. Also variations of the layer thicknesses and accumulating interface roughness may degrade the mirror performance.

6 Co-sputtering of SiO_x and investigation of Si NC formation by annealing

The NORDIKO 2000 setup allows the simultaneous deposition from a rf powered and a dc powered magnetron and a rotation of the substrate table with rates up to $f = 30 \text{ min}^{-1}$. Thus, SiO_x can be deposited by simultaneous dc sputtering of Si and rf sputtering of SiO_2 in pure Ar onto a substrate mounted on the rotating substrate table. This method has the following advantages: (1) the film composition can be reproducibly tuned in a wide range by adjusting the ratio of Si and SiO_2 deposition rates. (2) Since oxidation of the Si target is negligible the generation of micro-particles is eliminated. (3.) the method works stable at low deposition rates because no external feedback is required.

SiO_x films deposited by this method were analyzed with respect to composition by RBS and ERD. In addition the effect of different annealing temperatures on phase separation and precipitation of silicon clusters was probed by XTEM, PL, FTIR and variable angle spectroscopic ellipsometry (VASE).

6.1 SiO_x films by co-deposition from SiO_2 and Si targets in pure Ar

Experimental Si wafers coated with 150 nm amorphous carbon were used as substrates for ion beam analysis (substrate type A). For annealing experiments (100)-oriented Cz-Si wafers were cleaned in $\text{H}_2\text{O}_2/\text{H}_2\text{SO}_4$ solution and rinsed in deionized water (substrate type B). SiO_x films were deposited by co-deposition from the dc-powered Si target and the rf-powered SiO_2 target in pure Ar. At each setpoint one substrate of type A and B were coated simultaneously. Both substrates, mounted to a rotating table passed the two targets sequentially at a rotation speed of 30 min^{-1} for a constant deposition time of 270 s. Fixing the SiO_2 target power at 1 kW and adjusting the Si target power (P_{Si}) between 50 W and 900 W the composition x of the films was varied (**method 1**). For reference, a SiO_2 film was sputtered from the silica target in an $\text{Ar}:\text{O}_2 = 7:1$ mixture (**method 2**). In both cases the substrate temperature was $20 \text{ }^\circ\text{C}$, the target substrate separation 5.5 cm and the pressure before plasma ignition 0.667 Pa. The coated wafers of type B were cut to pieces, which remained as deposited or were exposed to a 30 s rapid thermal anneal (RTA) at temperatures between $700 \text{ }^\circ\text{C}$ and $1150 \text{ }^\circ\text{C}$ in an $\text{Ar}:\text{N}_2 = 1:1$ mixture at the maximum gas flow of 5 sccm to reduce

Samples: Films on 150 nm C on Si	A0	A1	A2	A3	A4	A5	A6	A7	A8	A9	A10
Films on Si	B0	B1	B2	B3	B4	B5	B6	B7	B8	B9	B10
Power at Si target $P_{Si}(W)$	0	50	70	90	130	210	270	340	900	0	0
Power at SiO ₂ target $P_{SiO_2}(kW)$	1	1	1	1	1	1	1	1	1	1	1
Process gas	Ar	Ar	Ar	Ar	Ar	Ar	Ar	Ar	Ar	Ar+ O ₂	Ar+ H ₂
Composition by RBS $x_{as\ deposited}$ (set A)	1.71	1.72	1.52	1.42	1.44	1.27	1.04	0.96	0.49	-	1.86
Composition by ERD $x_{as\ deposited}$ (set A)	2.07	1.9	1.84	1.76	1.61	1.33	1.13	0.95	0.54	2.09	-
XTEM (set B) $t_{Ox, 1050^\circ C}$ (nm) Si Nano- crystals	-	-	-	60	63	70	77.5	80	122	-	-
VASE (set B) $t_{Ox, 1050^\circ C}$ (nm) $x_{1050^\circ C}$	45.7	54.2	-	59.6	62.8	71.2	75.9	78.9	119.7	87.0	-
PL (set B) $\lambda_{max, 800^\circ C}$	-	700	705	715	720	750	728	778	810	-	-
$\lambda_{max, 950^\circ C}$	-	700	715	725	740	780	790	805	q.	-	-
$\lambda_{max, 1050^\circ C}$	-	700	730	750	760	785	q.	q.	q.	-	623
$I_{max, 800^\circ C}$	-	21	46	107	237	540	760	432	30	-	-
$I_{max, 950^\circ C}$	-	33	59	110	183	200	118	65	q.	-	-
$I_{max, 1050^\circ C}$	-	59	48	76	118	85	q.	q.	q.	-	32

Table 6.1: Summary of sample data. For annealed samples the RTA temperature is displayed as subscript.

humidity related effects. Samples prepared this way are named 'set B'. The sample data are summarized in table 6.1.

Remark on SiO_x homogeneity To deposit homogeneous SiO_x films, it is necessary to ensure that the Si sublayer thickness L_{Si} is on the order of one or two atomic monolayers. Assuming that the deposition rates of the two magnetrons are not interdependent (which should be a good estimate at $p = 0.667$ Pa), L_{Si} can be determined according to $L_{Si} = (R_{SiO_x} - R_{SiO_x,0})/f$, where R_{SiO_x} is the deposition rate of SiO_x, $R_{SiO_x,0}$ is the deposition rate at $P_{Si} = 0$ and f is the rotating speed of the substrate table. The deposition rates shown in Fig. 6.1a were extracted from electron microscopy (XTEM) and spectroscopic ellipsometry (VASE). Fig. 6.1b shows L_{Si} for various setpoints of P_{Si} . The right axis in this figure shows the excess silicon concentration in at% determined by elastic recoil analysis (ERD). The figure confirms that for a Si excess concentration c_{Si} between 0 and 30 at% the Si sublayer thickness L_{Si} is below 0.25 nm, i.e. the SiO_x films are truly homogeneous. Details of the measurements are discussed below.

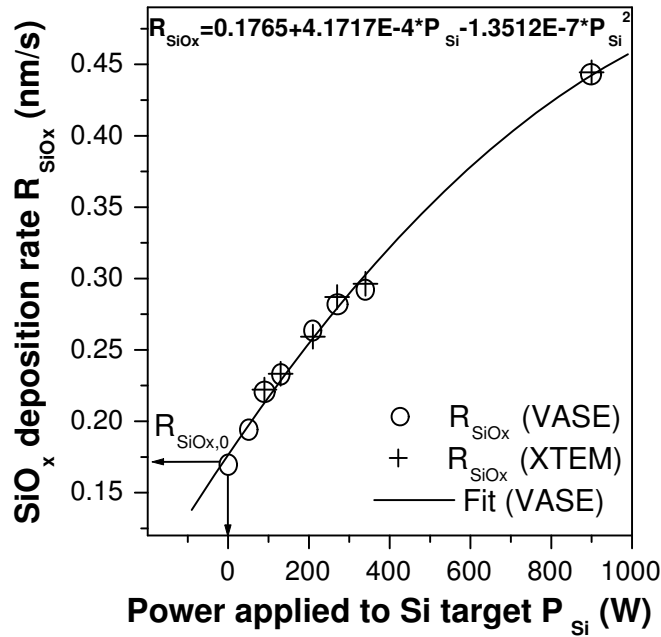
6.2 Investigation of SiO_x composition by RBS

Experimental The O/Si ratio the samples A0 to A8 were measured using the following parameters: projectile $^4\text{He}^+$, energy $E = 1.7$ MeV, number of detected ions $Q' = 1.248 \cdot 10^{14}$, incident angle (with respect to axis perpendicular on sample surface) $\theta_1 = 0$, detection angle $\theta_2 = 10^\circ$, scattering angle $\theta = 170^\circ$, solid angle of detector $\Omega = 1.29$ msr.

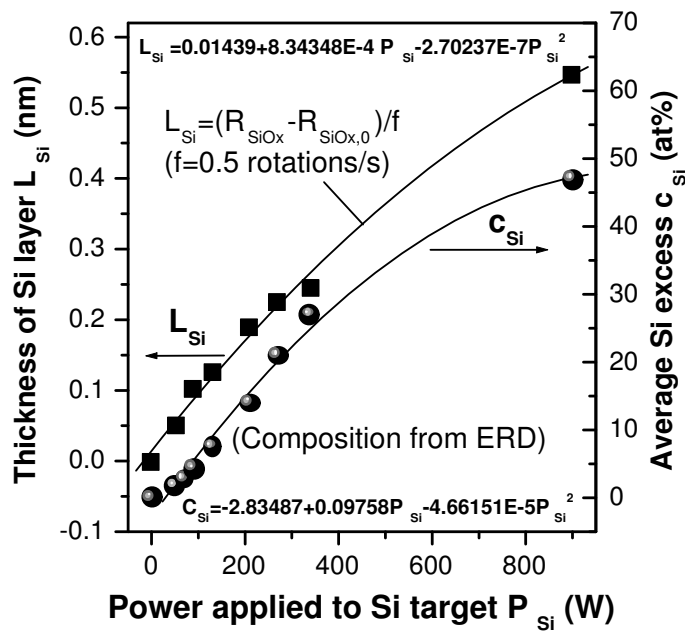
In the used standard RBS setup the target holder was slightly tilted and rotated during the measurement to avoid ion channelling. The suppression of backscattered ions from the Si substrate by channelling would allow the oxygen peak on top of the Si signal to be measured at higher accuracy. However, by stopping in rather thick coatings the velocity vector of incident ions may be slightly tilted, such that only a small fraction of them reaches the substrate in channelling direction. That is why channelling was not used in the present analysis of the 50-120 nm thick oxides.

Results A RBS spectrum of sample A8 is shown in Fig. 6.2a. The carbon spacer layer separates energetically the He^+ ions scattered by the Si substrate and those scattered by Si atoms in the oxide film. The simulation (*SIMNRA5.0*¹) does deviate at low energies. Here multiple scattering events affect the experimental data, while the used model was restricted to single nuclear collisions. The atomic concentration of oxygen was therefore obtained from integrating the oxygen peak after subtraction of the Si random spectrum. The noise of the oxygen signal limits the accuracy of the derived O/Si ratio. From the spectra it is further evident that between one and two percent of Ar are incorporated into the oxide film during deposition. The Ar concentration slightly increases with the power at the Si target (Fig. 6.2b). According to Macchioni [129] the Ar incorporation can be further decreased by moderate substrate heating

¹Download <http://www.rzg.mpg.de/mam/>



(a) Rates for co-sputtering of SiO_x from Si and fused silica targets in pure Ar at $p = 0.667$ Pa, $D = 5.5$ cm and $T_S \sim 20$ °C.



(b) Thickness of Si sublayers L_{Si} for various setpoints of P_{Si} . In addition c_{Si} , the concentration of excess Si in at% is shown.

Figure 6.1:

(320 °C) during deposition. Reference experiments with Ar-implanted thermal SiO₂ films showed that most Ar is released already in a 30 s anneal at 500 °C in inert gas. According to Perkins [157], between 670 °C and 900 °C the diffusion coefficient D_{Ar} of Ar in SiO₂ can be described by an Arrhenius equation:

$$D = D_0 \cdot \exp\left(-\frac{W_0}{k_B T}\right) \quad (6.1)$$

with $D_0 = 1.21 \cdot 10^{-4} \text{cm}^2/\text{s}$ and $W_0 = 28.7 \text{ kcal/mole}$. These values are comparable to that of the O₂ molecule given by Norton [158], which with 0.32 nm has the same size: $D_0 = 2.71 \cdot 10^{-4} \text{cm}^2/\text{s}$ and $W_0 = 27 \text{ kcal/mole}$ respectively. The compositions determined by RBS are summarized in Fig. 6.3.

6.2.1 Investigation of SiO_x composition by ERD

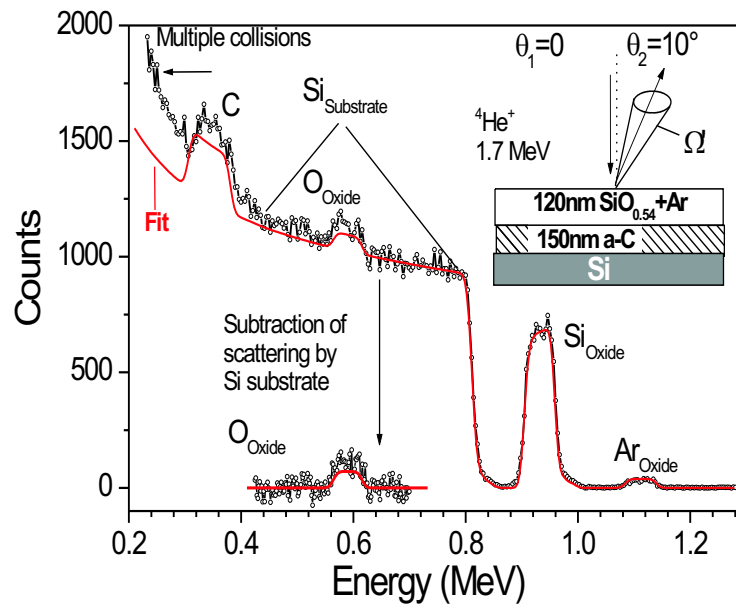
Experimental details Projectile: ³⁵Cl⁷⁺, E = 35 MeV, total particles on sample Q' = $3.03 \cdot 10^{12}$. Hydrogen recoils were detected with a silicon telescope detector ($\theta_1 = 15^\circ$, $\theta_2 = 38^\circ$, $\theta = 142^\circ$, detector solid angle $\Omega = 2.97 \text{ msr}$). For a definition of angles see Fig. 3.2 on p. 18. Heavier elements like C, N, O and Si were analyzed using a Bragg ionisation chamber ($\theta_1 = 15^\circ$, $\theta_2 = 30.76^\circ$, $\theta = 149.24^\circ$, $\Omega = 0.411 \text{ msr}$).

Results Fig. 3.3c (p. 20) shows a ERD measurement (Bragg-curve) of sample A6 obtained using a BIC detector. Clearly signals from Si-atoms from the SiO_x film are well separated from those of the substrate, owing to the energy loss in the 150 nm carbon spacer layer. A depth profile of H, N, O and Si is shown in Fig. 6.4. A slight contamination of the carbon layer by H, N and O is evident. The elemental ratio of oxygen and silicon is determined in the plateau region, where the signal from oxygen impurities in the carbon film is negligible. The oxide composition in dependence of the power applied to the Si target is shown in Fig. 6.3. Owing to the higher sensitivity for light elements and the profitable use of the BIC, ERD is the ion beam analysis technique of choice to determine the composition of SiO_x thin films.

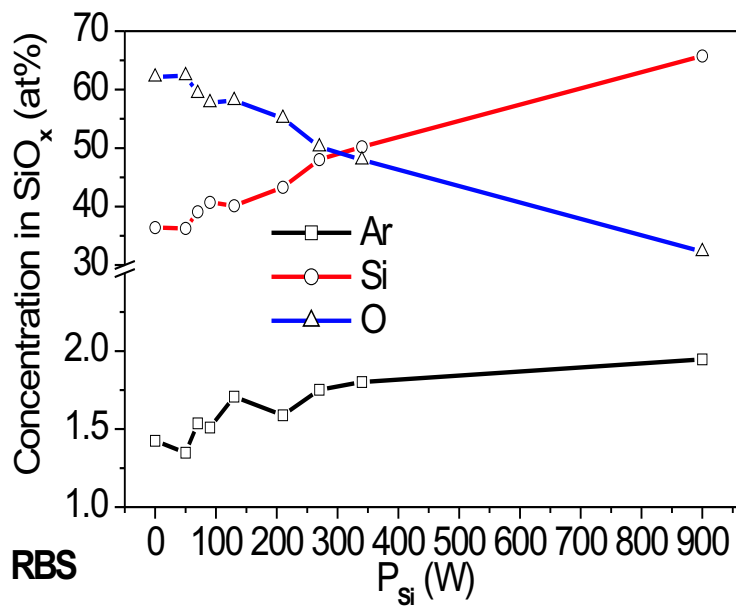
6.2.2 Remarks on substrate requirements for ion beam analysis

The ideal substrate for RBS and ERD analysis of thin films does not contain elements heavier than those occurring in the film, because in this case the signals from atoms in substrate and film respectively are energetically clearly separated. It must be stable under ion bombardment (rules out most hydrocarbons) and should not cause health hazards (as Be). The substrates should be smooth and non-porous to avoid a take-up of water from the ambient. Water might chemically modify the film during ion bombardment. This rules out the sponge-like pyrolytic carbon. Often vitreous (glassy) carbon like SIGRADURTM is used. For measurements in this work Si wafers coated with a 150 nm thick amorphous carbon layer in a He plasma were used ².

²a-C films prepared by J. S. Liebig, Fraunhofer Institut für Elektronenstrahl- und Plasmatechnologie, Fabrikstrasse 17, 01833 Stolpen-Helmsdorf



(a) Experimental RBS spectrum of sample A8 and fit using SIMNRA.



(b) SiO_x composition for different deposition conditions.

Figure 6.2: RBS measurement of SiO_x film composition
(Raw data provided by R. Grötzschel, FZ-Rossendorf).

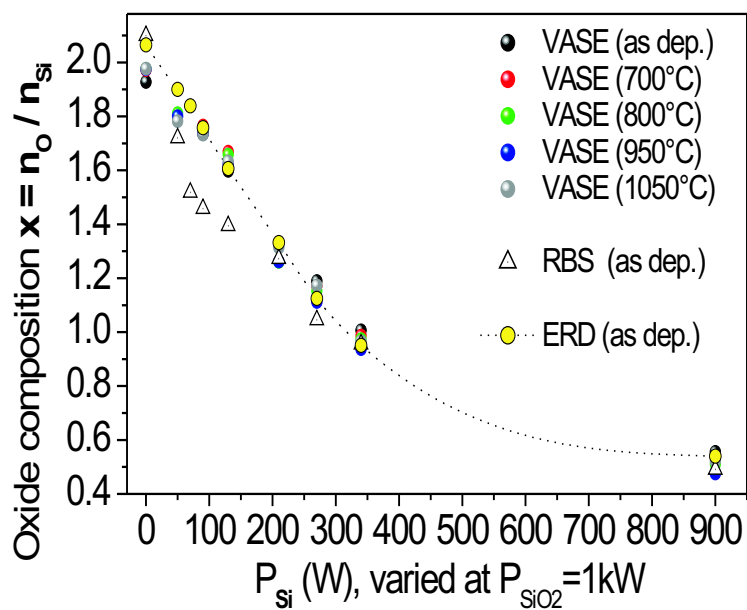


Figure 6.3: Composition of silicon oxide films sputter deposited at $P_{SiO_2} = 1\text{ kW}$ and different P_{Si} determined by ERD, VASE and RBS.

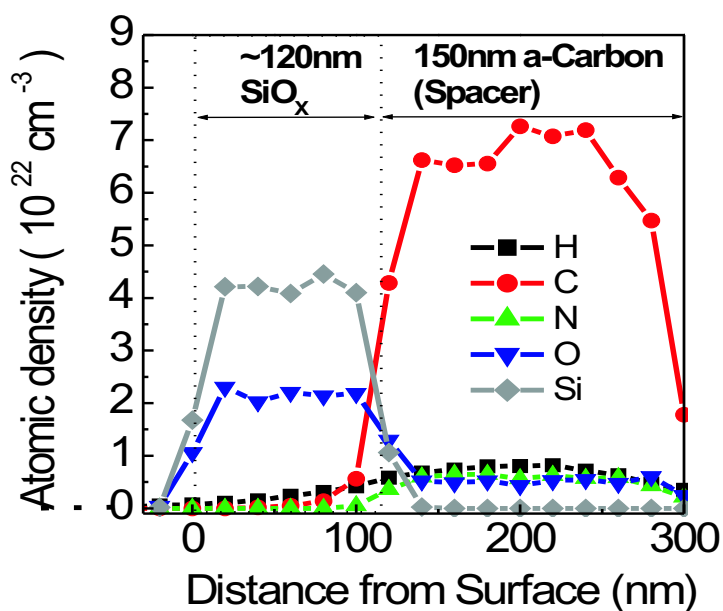


Figure 6.4: ERD depth profiles of H, C, N, O, and Si across a 120 nm thick $\text{SiO}_{0.5}$ film on 150 nm C on Si, i.e. sample A8 (Measurement by U. Kreissig, FZ Rossendorf).

6.2.3 XTEM investigation of annealed silicon rich oxide films

For the XTEM measurements a PHILLIPS CM300 electron microscope (Voltage 300 kV, LaB_6 cathode, resolution 0.14 nm) was used to measure the SiO_x film thickness and to probe the presence of crystalline Si NC in SiO_x films, annealed at 1050 °C using the imaging modes described on p. 15). Fig. 6.5a is a low-resolution bright field image of sample B6, as typically used for film thickness measurements. The Si substrate, the deposited oxide film and remainders of glue used in the XTEM sample preparation process are clearly distinguished. The substructure in the oxide film is probably caused by Fresnel fringes which are observed due to discontinuities in the scattering potential (such as Si NC embedded in the oxide matrix) when the specimen is slightly out of focus [159]. Figures 6.5b, 6.5c and 6.5d are high resolution images of sample B5, B4 and B8 respectively. In these images the silicon substrate is oriented such that the [110] direction is perpendicular to the image plane. The [110] direction is, in the diamond structure of crystalline silicon, the intersection of two (111) planes and one (200) plane. In the high resolution images the silicon substrate atoms of these planes are piled up on top of each other and these lattice plane (marked by the white lines in Fig. 6.5d) are individually resolved. In the same manner Si nano-crystals embedded in the oxide may show lattice contrast, if the electron beam coincides with a nano-crystal lattice plane. The plane types are identified by their lattice constants³. Often, as in the present work, only (111) lattice plane are observed, in some cases also the (220) planes [69]. Imaging of lattice planes with smaller spacings is limited owing to factors, such as the spatial (point) resolution of the TEM, which for a state-of-the-art TEM is limited to about 1.5-2 Å.⁴ In addition there are problems caused by thermal drift of the sample and the fact that the contrast from small clusters is easily lost in the noise when the thickness of the sample is too high.

In case of samples B5 and B8 crystalline Si NC are clearly identified. The three marked clusters in Fig. 6.6d show (111) lattice planes. No crystallites are observed for sample B4, having the lowest Si excess of the three shown samples. Fig. 6.6a and 6.6b are dark-field images of sample B4 and B8 simultaneously using the (111) and (200) reflexes. Bright spots indicate opportunely oriented nano-crystals in sample B8. Also the oxide region of sample B4 shows a sub-structure, but no clear indication of nano-crystals. Fig. 6.6c and 6.6d are electron diffraction images of the oxide region of samples B4 and B8. Because many randomly oriented clusters contribute, a powder-diffraction-like pattern is expected. Indeed, ring structures due to reflexes from (111), (220), and (311) Si lattice plane confirm the presence of small randomly oriented nano-crystals for sample B8. The (400) reflex is barely visible. Sample B4 shows a dot pattern due to the electron beam grazing slightly the Si substrate with the [110] direction oriented along the electron beam. An indexed scheme of the diffraction pattern is shown in the inset. The weak and diffuse radially symmetric diffraction pattern from the oxide region indicates amorphous material. For all investigated samples, no evidence of crystalline clusters has been found for oxide compositions $x > 1.3$ after the 30 s anneal

³(111): 3.1355 Å, (200): 2.715 Å, (220): 1.9201 Å and (311): 1.6375 Å

⁴The resolution is governed by the instrumental phase distortion of the objective lens, which is largest for those rays bent furthest from the optical axis, i.e. carrying information about small spacial details. The fact that these rays cannot be used for the image formation, causes the degradation in spatial resolution.

at 1050 °C. In contrast, Kahlert [69] observed crystalline Si NC also for annealed oxides with lower Si excess ($x = 1.17-1.63$), but he used more extensive anneal (1h at 1000 °C). It is anticipated that in his case, the phase separation was nearly complete for all samples, whereas the 30 s rapid thermal anneal used in the present work did not lead to complete phase separation in the case of low Si excess samples of set B. Therefore in Kahlert's case the average Si NC size was higher, increasing the chances of successful Si NC imaging. This interpretation is corroborated by investigation of sample set B by IR-spectroscopy discussed below.

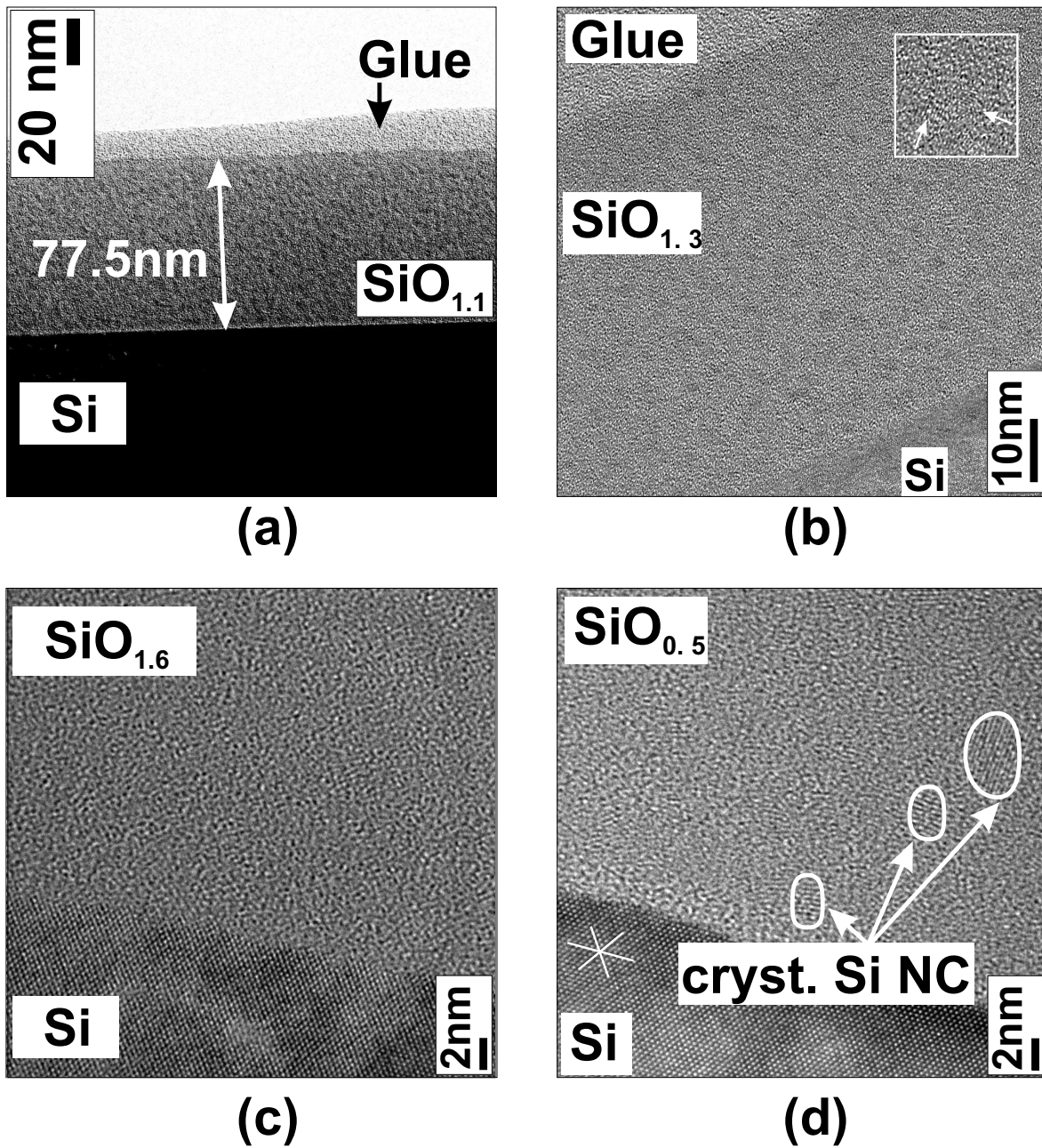


Figure 6.5: (a) B6: bright field image of SiO_x on Si. Reminders of glue from the preparation are also seen. ;
 (b), (c) and (d): high resolution images of samples B5, B4 and B8 respectively. In (b) and (c) lattice planes of Si nanocrystals are resolved. For samples with an oxide composition $x > 1.3$ no crystallites were found (Measurements by A. Mücklich, FZ Rossendorf).

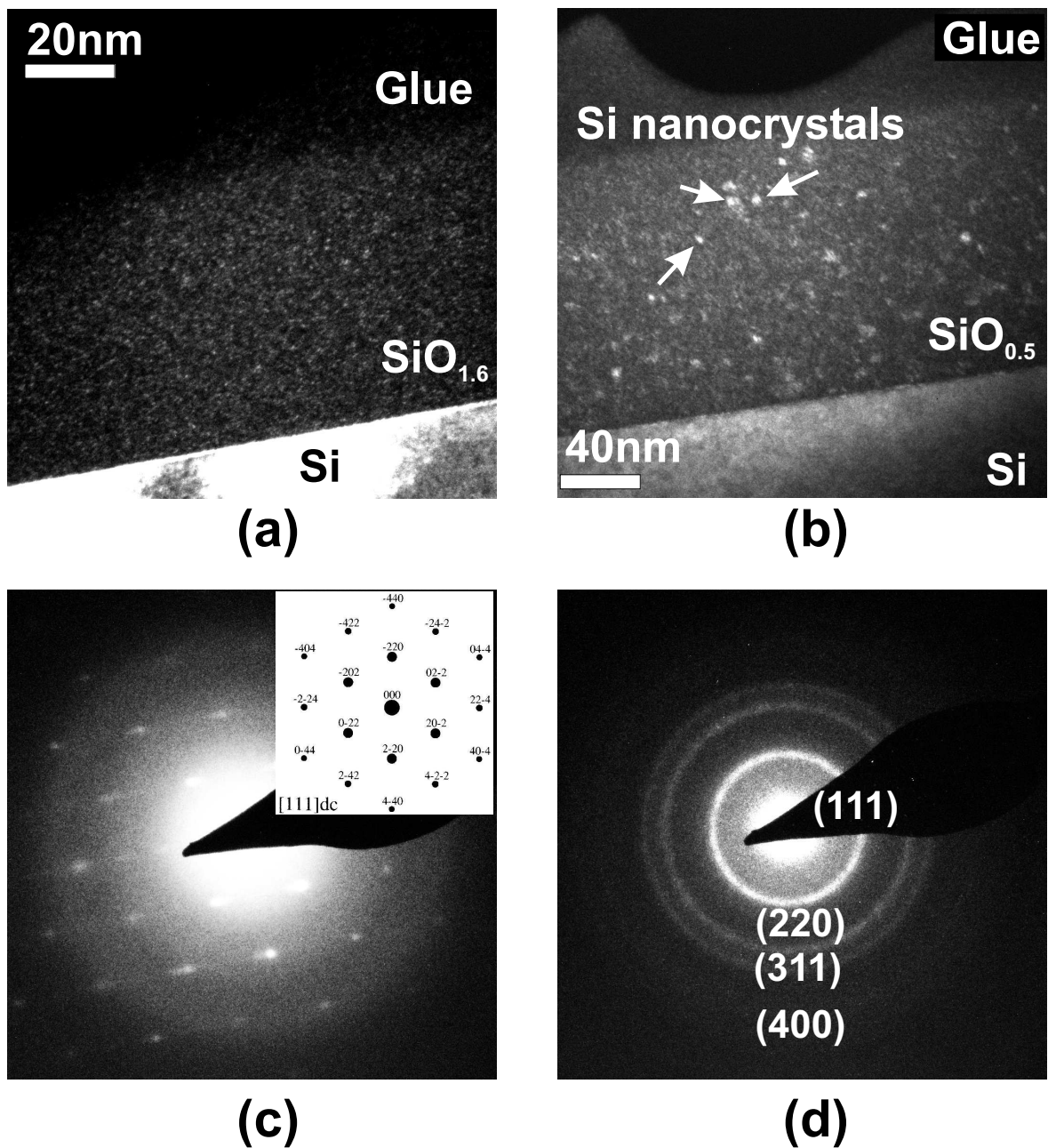


Figure 6.6: (a), (b): Dark-field images of samples B4 and B8
 (c), (d) Electron diffractogram from the oxide layer of samples B4 and B8. The sharp reflexes observed in (c) are due to the beam partly grazing by the substrate. The assignment of reflexes is shown in the inset (after [52]). The ring structure in (d) is due to the random orientation of Si crystallites (Measurements by A. Mücklich, FZ Rossendorf).

6.3 Infrared spectroscopy of silicon oxides

Summary of experiment As described in the fundamentals section on p. 19, the asymmetric oxygen stretching mode (TO_3 mode) is sensitive to the structure and composition of silicon oxide and can be used to probe the annealing process. Here the effect of different annealing conditions on the phase separation of SiO_x films is investigated, with the oxide composition x being a parameter.

Experimental For sample set B IR transmittance spectra were acquired under normal incidence in the range of $450\text{-}4000\text{ cm}^{-1}$. Under these conditions only the transverse optical modes are observed. Raw spectra were appropriately rationed to a bare silicon substrate spectrum to compensate the substrate absorption. The sample compartment was flushed with dry N_2 .

Effect of annealing on IR absorption of sputter deposited SiO_2 Fig. 6.7 shows representative IR transmittance spectra of sample set B in the region of interest $750\text{-}1270\text{ cm}^{-1}$, for fresh samples and after 30s anneals at $800\text{ }^\circ\text{C}$, $950\text{ }^\circ\text{C}$, and $1050\text{ }^\circ\text{C}$. For all as deposited oxide films the TO_3 mode is shifted to lower energies compared to a standard thermal oxide grown at $1000\text{ }^\circ\text{C}$. In case of the stoichiometric oxide (sample B9) the effect is attributed to a compaction of the film owing to the bombardment by Ar^+ ions or reflected neutrals during growth, resulting in compressive films stress and an increased density. Also the a slight incorporation of Argon found by RBS might contribute to the disorder in the unannealed film. The compressive stress of the oxide is partly or completely released during post-deposition annealing, simultaneously the structural disorder decreases. After the anneal at $1050\text{ }^\circ\text{C}$ the TO_3 peak frequency ν_{TO_3} is close to the value for thermally grown oxide. In the process of annealing both the intensity and area of the TO_3 band increases. This observation is consistent with those of Garrido [160], who studied the relaxation of stress and disorder in Argon implanted SiO_2 . The densification of sputter deposited SiO_2 films was confirmed by Macchioni [129]. Lisovskii [63] linked the lower ν_{TO_3} of sputtered SiO_2 films with an increased higher density. A similar behavior was found for the dense low temperature thermal oxides by Lucovsky [161].

Silicon-rich oxides For silicon rich oxide films apart from the **compaction related shift** of ν_{TO_3} , a **chemical shift** is observed (Fig. 6.7, samples B1 to B8). This chemical shift is proportional to the mean Si excess in the film. The effect is largest for as-deposited films. As a typical feature of suboxides [161] it is observed that the chemical shift of the TO_3 band is accompanied by an increase in the full width at half maximum (FWHM), related to the diversity of chemical environments an oxygen atom may have in SiO_x (see p. 23). In contrast the FWHM of the stoichiometric oxide (B1) stays nearly constant between the anneals, the observed energy shift is therefore most likely compaction related. Figure 6.8 shows the energies of the TO_3 minimum for as deposited and annealed samples with different compositions x (derived by ERD). Data points on a vertical line correspond to identically prepared samples, but different anneals. For reference, on the right, the data for the SiO_2 reference sample B1 are shown.

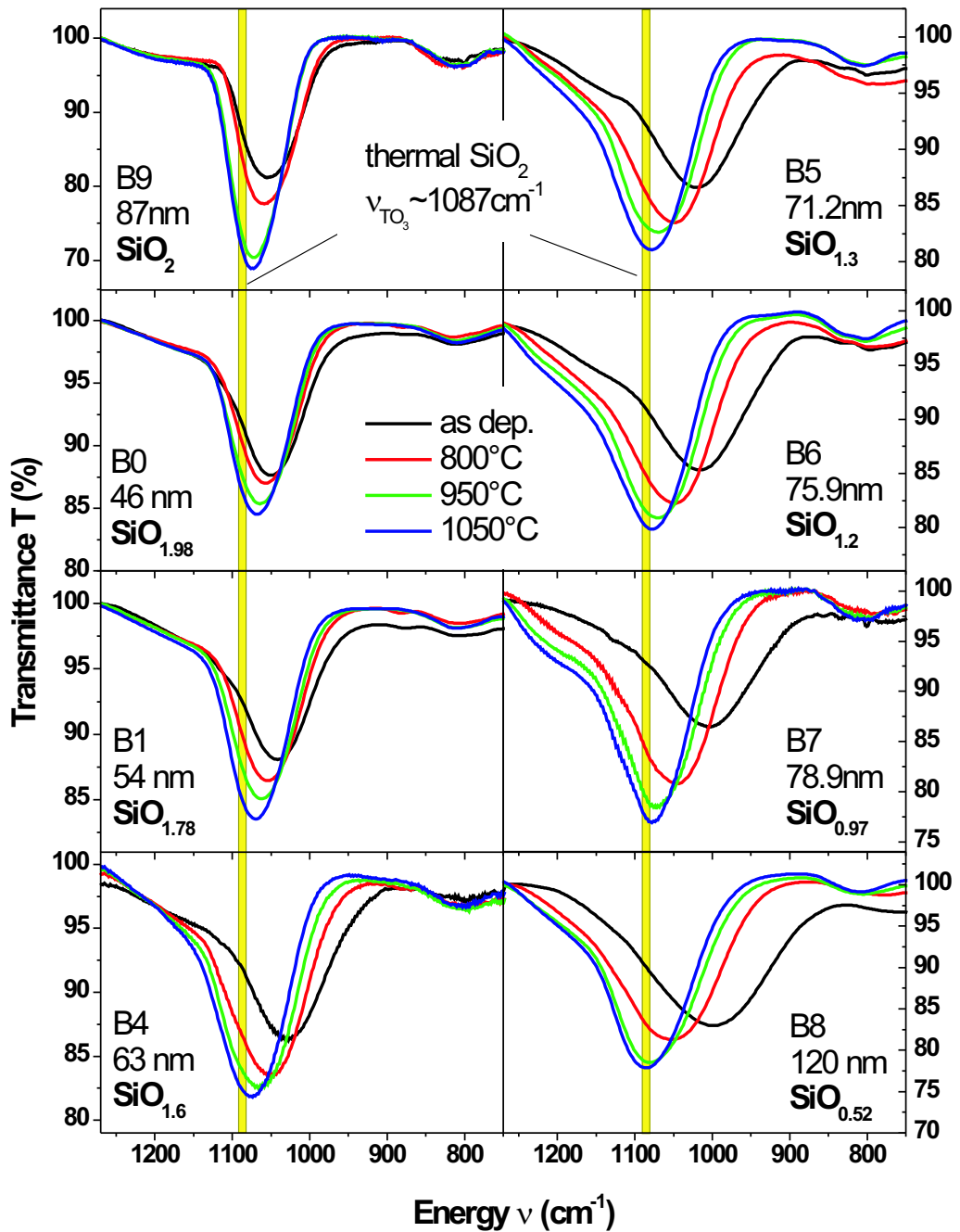


Figure 6.7: IR transmittance of sputter deposited SiO_x films before and after annealing for 30s at 800 °C, 900 °C and 1050 °C in Ar. The yellow bar indicates the typical TO_3 peak energy of thermally grown stoichiometric SiO_2 .

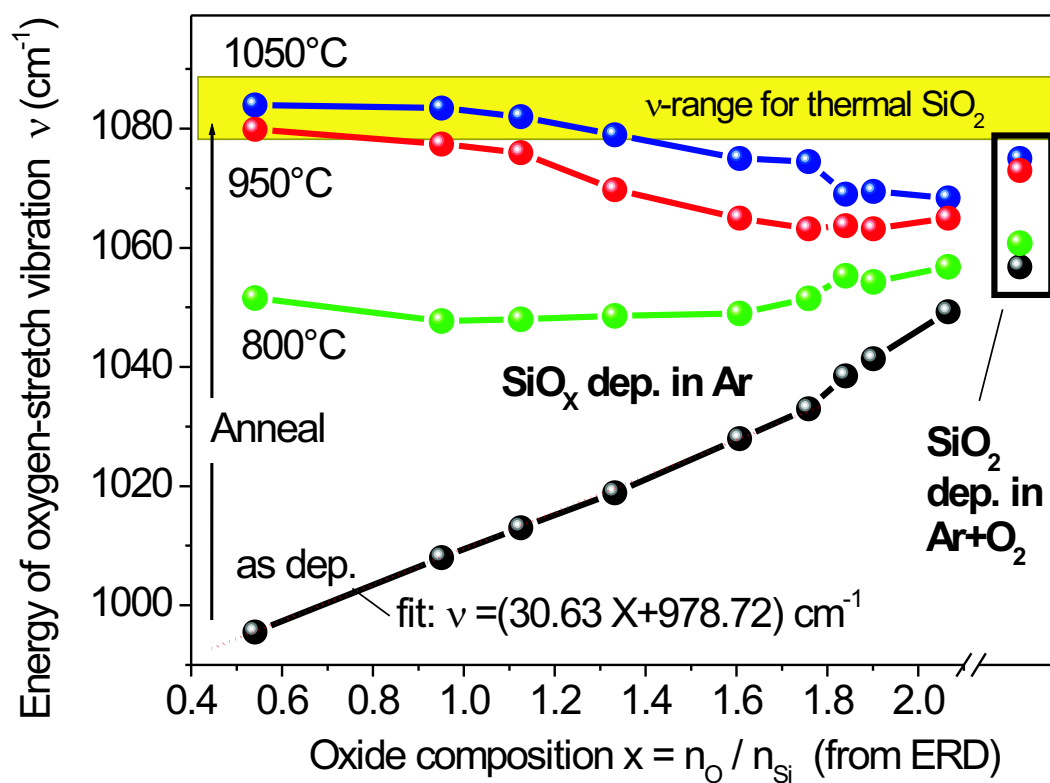


Figure 6.8: Vibrational energies of TO_3 mode versus oxide composition x . Parameter: temperature of the 30s anneal in Ar. The yellow bar indicates the TO_3 energy of relaxed stoichiometric SiO_2 .

The frequency of the TO_3 band in case of as deposited SiO_x films (for $x \leq 1.6$) shifts nearly linear with silicon excess, according to $\nu = (30.63 \cdot x + 978.72) \text{ cm}^{-1}$. In the process of annealing, owing to the phase separation into Si and SiO_2 , the concentration of excess silicon decreases, which lowers the chemical shift. Simultaneously the structural relaxation discussed for stoichiometric SiO_2 proceeds, and ν_{TO_3} approaches the values characteristic of pure relaxed SiO_2 . Considering Fig. 6.8, it is found that for a certain annealing temperature the annealing effect depends strongly on the initial SiO_x composition x : The process in phase separation (i.e. the extend of the gradual shift of the TO_3 band energy towards the limit of 1090 cm^{-1}) is higher for SiO_x samples with a higher silicon excess (smaller x). In contrast, considering the final ν_{TO_3} value, samples with an oxygen/silicon ratio $x > 1$ do not complete phase separation during a 30 s anneal even at $T = 1050 \text{ }^\circ\text{C}$ ⁵. One reason for this behavior can be derived from classical nucleation theory [44]. In order to form a silicon precipitate, a nucleation energy barrier must be overcome. This barrier rises with declining silicon excess due to a higher probability for Si atoms to detach from the precipitate and diffuse into the oxide matrix. Consequently, *for a given annealing temperature, the initial precipitate density is always higher in films with higher silicon excess. The mean distance between an excess Si atom and a precipitate is therefore smaller and growth and ripening processes governed by diffusion proceed faster, compared to samples with a lower precipitate density.* For very high precipitate densities an additional contribution of Si monomer transport by surface diffusion is expected to accelerate the growth and ripening processes. This finding is very important for memory applications where two conflicting requirements must be met: To minimize the conductivity between clusters, the concentration of excess silicon between the clusters should be minimized, which requires a high thermal budget. On the other hand the thermal budget is limited to avoid broadening of narrow or shallow doping profiles in the silicon substrate (i.e. transistor channels). Figure 6.8 shows that the thermal budget required to achieve complete phase separation in silicon rich oxides can be lowered, if the silicon excess is increased.

⁵This finding is important for the use of annealed SiO_x layers as memory nodes in Si NC memories: As a consequence of oxygen deficiency related defects the effective electronic band gap of SiO_x is much smaller than the band gap of a pure SiO_2 . On the other hand the energy levels of trapping centers are fixed. An incomplete phase separation leads therefore to an increased rate of detrapping of trapped carriers into the oxide conduction band and reduces the retention time of the memory.

6.4 PL measurements of annealed SiO_x films

The PL of Si nanoclusters as optical probe of SiO_x decomposition and nanocluster size The PL from a NC ensemble can be used as a sensitive probe of phase separation and NC evolution during a thermal anneal. In the initial nucleation phase the density of silicon precipitates per volume increases rapidly, and so does the PL intensity. Because of the mentioned size effects, the PL intensity is expected to saturate and later to decline when the nucleation of new luminescent nuclei is too small to compensate for the decreasing intensity due to cluster growth (mean diameter L increases) and ripening (Si NC density decreases). If the cluster diameter exceeds the free exciton radius the NC related PL drastically decreases as discussed above. This allows to experimentally distinguish the nucleation and growth/ripening phases. By comparison to data summarized by Takeoka [80] and shown in Fig. 3.7, p.29 from the energy of the PL emission the Si NC size can be roughly estimated. Even though there might be a considerable error in the derived diameters, it should be emphasized that in the limit of very small ($d < 2.5$ nm) clusters the PL measurement is one of the few non-invasive techniques containing information on size of Si NC embedded in homogeneous SiO₂ films. For example the size measurements by TEM for the smallest clusters (diameter $d < 2$ nm) of Fig. 3.7 were possible only because the Si NC were free-standing on a thin holey carbon film [162]. For Si NC embedded in a thin SiO₂ film TEM-based size measurements of Si NC smaller than 2 nm are not possible because of a lack of contrast.

Results and discussion The energetic position and height of the NC related PL maxima are summarized in Tab. 6.1 on p. 66. The intensity data has been corrected for the detector response, interference and thickness effects were not corrected. Arbitrary units are comparable for all samples. Evidently, the effect of the RTA step depends strongly on the silicon excess. For the sample B1, with a low silicon excess and a composition of $x = 1.78$, the energetic position of the PL maximum is nearly constant for all three temperatures, while the intensity rises with higher temperature: here at the end of all anneals the nucleation is still the dominant process (Fig. 6.9). A completely different behavior is observed for samples B4 to B8, with increasing Si excess and compositions x between 1.63 and 0.52. Here the energetic position of the PL maximum shifts clearly to lower energies, accompanied by a decrease in intensity, both facts indicating that, after the 950°C anneal and during the whole 1050°C anneal, cluster growth and ripening are the dominant processes (Fig. 6.9). The temperature needed to obtain a maximum PL intensity, i.e. to reach the end of nucleation phase, where the number of precipitates saturates, depends on the sample composition and decreases with rising silicon excess. This is due to the more rapid phase separation in samples with a higher precipitate density. One reason for this behavior can be derived from classical nucleation theory [44]. To form a precipitate, a nucleation energy barrier must be overcome. This energy barrier rises with declining silicon excess due to a higher probability of Si-NC atoms to detach and diffuse into the oxide matrix. As a consequence, *for a given anneal, the precipitate density is much higher in films with higher Si excess*⁶. The mean distance

⁶An important implication is found for applications where the thermal budget is limited (For example the thermal budget for preparation of down-scaled memory transistors in a CMOS process is

from a diffusing Si monomer to a precipitate is much lower, and therefore growth and ripening processes governed by diffusion will proceed much faster, compared to samples with a lower precipitate density. For very high precipitate densities an additional contribution of Si monomer transport by surface diffusion is expected to accelerate the growth and ripening processes. This interpretation assumes the dominance of structural effects, but a decreasing density of Si/SiO₂ interface defects acting as radiative recombination killers (P_b centers) might also lead to an increased PL intensity as observed for samples B10 and B1. However lowering the concentration of these interface defects requires rather long treatments at high temperature [81]. That is why in the present case, these effects are believed to be dominated by the ongoing phase separation and precipitation of Si NC.

restricted to rapid (about 1 min) thermal annealing at temperatures of about 950 °C): As far as the Si NC formation is concerned, a low thermal budget can be balanced by an increased Si excess. Recently PL from Si nanostructures has been observed even in un-annealed sputter-deposited Si rich oxide [88] - most likely as a consequence of a quite high Si excess (5-11 vol%) resulting in a low energy barrier for nucleation.

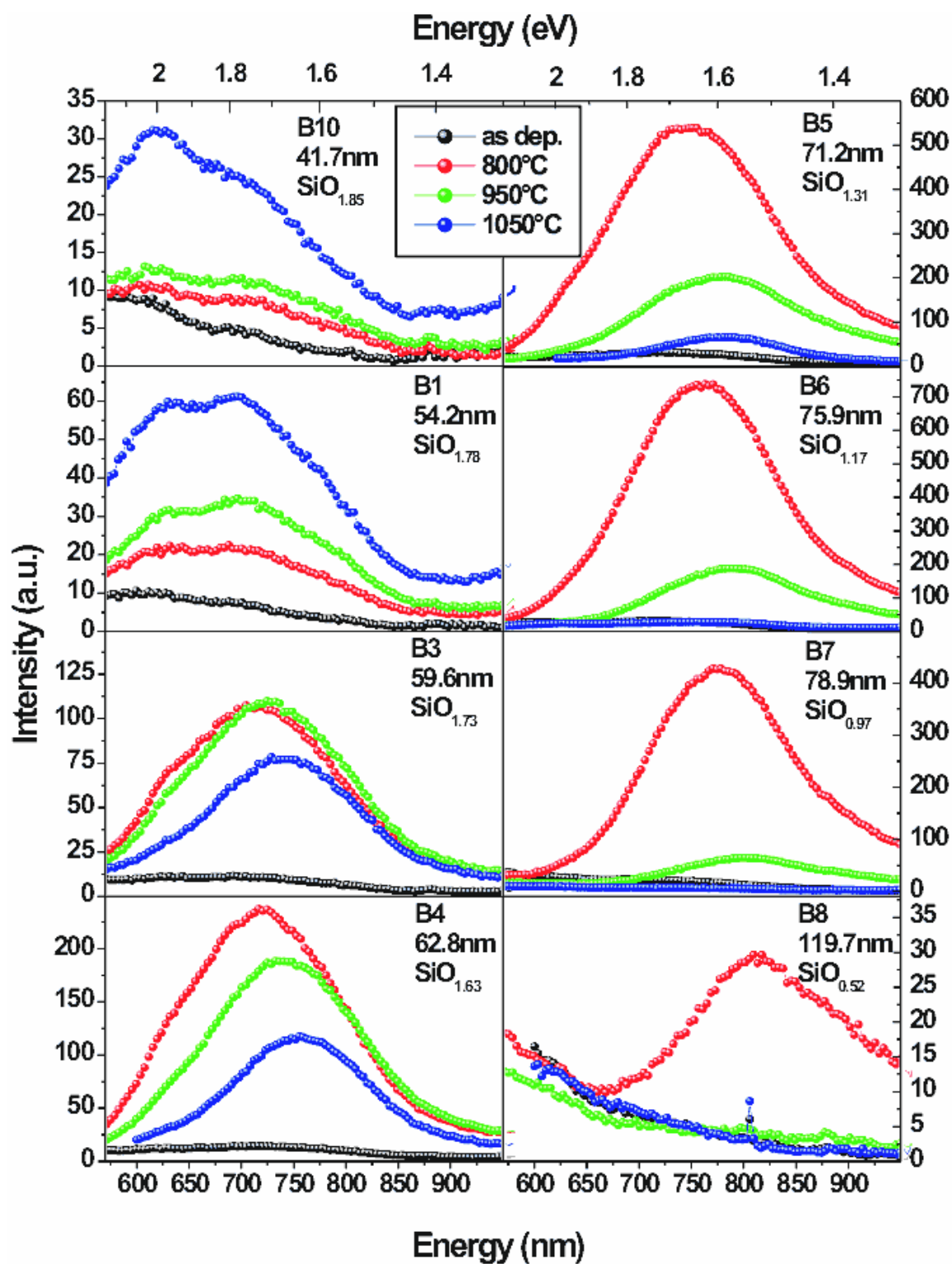


Figure 6.9: Change of SiO_x photoluminescence with increasing Si excess: as deposited, and after 30 s anneal at 800 °C, 950 °C and 1050 °C. For the same temperatures a higher Si excess speeds up the Si NC evolution.

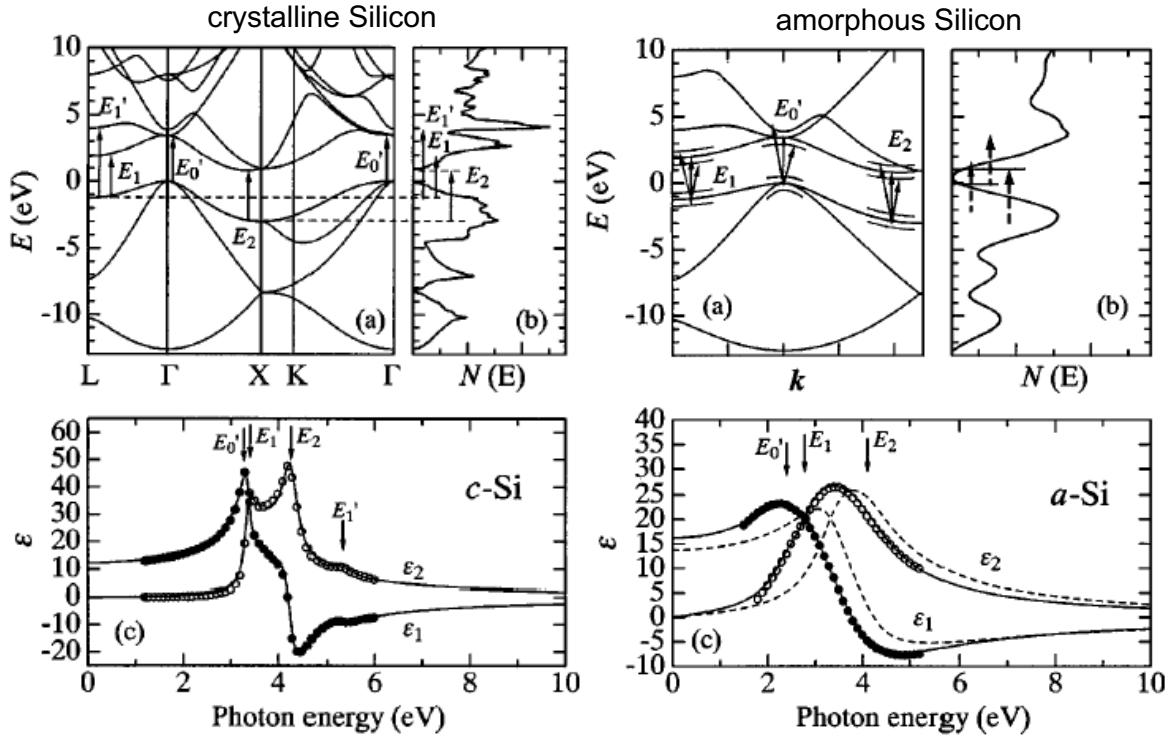


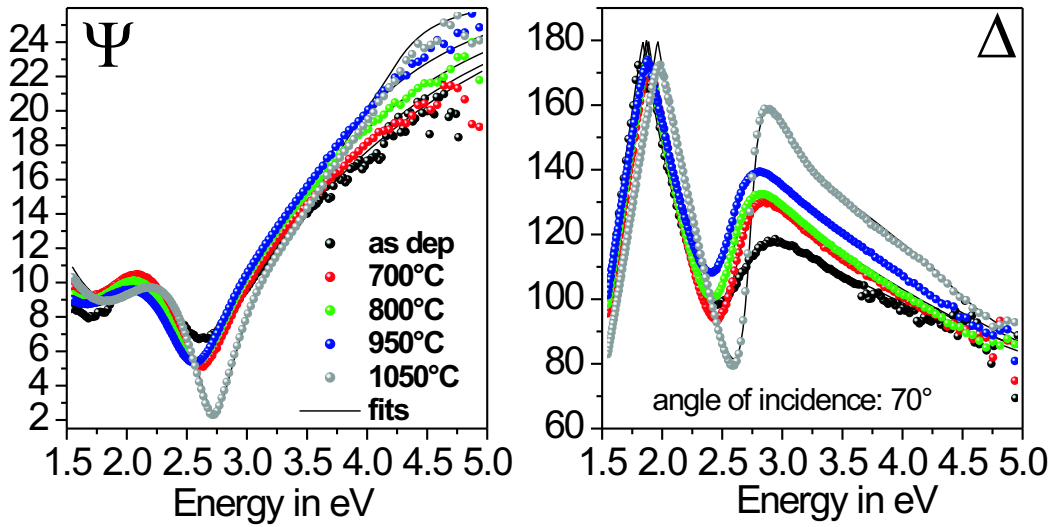
Figure 6.10: (a) Modelled electronic energy-band structure, (b) density of states and (c) $\epsilon(E)$ raw data and 'model dielectric function' - fit for crystalline and amorphous Si. Adapted from [163].

6.5 Variable angle spectroscopic ellipsometry (VASE) of SiO_x films

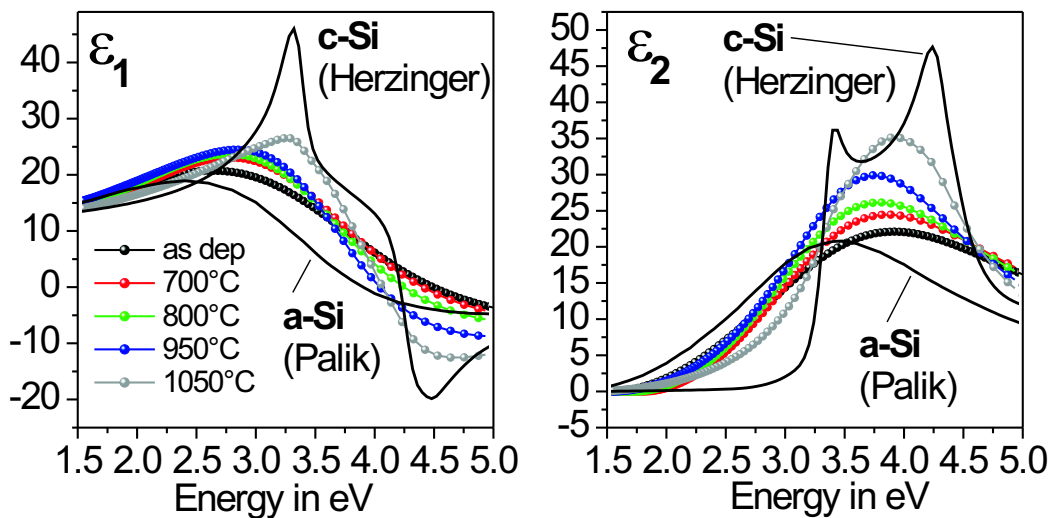
Extraction of composition and thickness of SiO_x films For an arbitrary SiO_x film, the thickness t_{Ox} and composition x can be roughly obtained using variable angle spectroscopic ellipsometry. To check the effect of annealing, the samples of set B (see Tab. 6.1 on p. 66) were alternatively measured by ellipsometry and annealed at temperatures increasing from 700 °C to 1050 °C. To obtain thickness and composition the sample was represented by a two layer-model (**Model 1**), considering a substrate layer of c-Si [164] and a SiO_x layer. The latter was described as two phase Bruggemann effective medium (see p. 34) of SiO_2 [164] and a Bruggemann mixture of a-Si [155] and c-Si. A mixture of a-Si and c-Si is known to be a good representation of polycrystalline silicon, and it is also a good representation for the Si NC phase. It introduces some flexibility to the optical constants. At the same time the optical constants of c-Si and a-Si can be considered as limiting cases of the average Si NC optical constants. That is why this approach can be expected to yield the Si excess in the oxide with reasonable accuracy. A surface roughness layer was omitted to reduce the free parameters and since it had little effect on the fit quality. The remaining fit parameters are the oxide thickness t_{Ox} , the total excess Si volume fraction f_{Si} and volume fraction of a-Si, $f_{\text{a-Si}}$, in the Si phase. The volume fraction of c-Si is then $f_{\text{c-Si}} = f_{\text{Si}} - f_{\text{a-Si}}$. The fit results are summarized in detail in Tab. 6.2. Fig. 6.3 (p. 71) shows the good agreement between oxide compositions obtained from ERD and ellipsometry results. Also

Sample	f _{a-Si} (%)	f _{c-Si} (%)	d _{SiO_x} (nm)	MSE	f _{Si} (%)	x
B0 _{ad}	0±0.30	1.61±0.47	49.1±0.2	2.79	1.6	1.928
B0 ₇₀₀	0.63±0.25	0±0.32	46.1±0.1	1.401	0.63	1.971
B0 ₈₀₀	0.51±0.29	0±0.38	46.1±0.1	1.684	0.51	1.977
B0 ₉₅₀	0.55±0.29	0±0.37	45.7±0.1	1.636	0.55	1.975
B0 ₁₀₅₀	0.50±0.29	0±0.37	45.7±0.1	1.741	0.50	1.977
B0 ₁₁₅₀	0.64±0.25	0±0.32	45.4±0.1	1.396	0.64	1.971
B2 _{ad}	3.9408±2.84	0±3.95	65.831±2.18	32.09	6.781	1.716
B3 _{ad}	1.66±0.30	4.63±0.39	63.9±0.2	4.456	6.29	1.735
B3 ₇₀₀	1.76±0.54	3.73±0.70	60.8±0.3	5.531	5.49	1.767
B3 ₈₀₀	1.90±0.41	4.02±0.52	60.4±0.2	6.318	5.92	1.750
B3 ₉₅₀	2.90±0.52	3.37±0.68	59.8±0.3	6.012	6.27	1.736
B3 ₁₀₅₀	2.47±0.53	3.89±0.69	59.6±0.3	6.123	6.36	1.732
B4 _{ad}	0.52±0.21	9.43±0.25	64.6±0.1	12.62	9.95	1.599
B4 ₇₀₀	5.85±0.21	2.16±0.22	64.8±0.1	9.225	8.01	1.670
B4 ₈₀₀	5.96±0.17	2.34±0.26	64.4±0.2	8.402	8.29	1.659
B4 ₉₅₀	5.51±0.29	3.75±0.44	62.8±0.3	8.643	9.26	1.646
B4 ₁₀₅₀	4.16±0.63	4.84±0.86	62.8±0.4	9.962	9.00	1.633
B6 _{ad}	13.14±0.26	9.93±0.37	80.9±0.4	7.369	23.07	1.189
B6 ₇₀₀	13.14±0.26	10.60±0.33	78.7±0.3	5.809	23.74	1.171
B6 ₈₀₀	15.19±0.25	9.24±0.33	77.9±0.3	6.598	24.43	1.153
B6 ₉₅₀	18.16±0.26	7.82±0.33	77.4±0.3	7.134	25.98	1.113
B6 ₁₀₅₀	10.26±0.31	13.40±0.40	75.9±0.3	7.367	23.66	1.173
B7 _{ad}	18.76±0.26	11.50±0.36	83.2±0.3	3.811	30.26	1.007
B7 ₇₀₀	18.04±0.35	13.03±0.46	82.8±0.4	8.201	31.07	0.988
B7 ₈₀₀	19.96±0.39	11.68±0.52	82.8±0.4	9.178	31.64	0.975
B7 ₉₅₀	24.16±0.43	9.13±0.54	82.0±0.4	8.944	33.29	0.937
B7 ₁₀₅₀	16.51±0.27	15.51±0.36	78.9±0.3	6.735	32.02	0.966
B8 _{ad}	45.30±0.46	8.00 ±0.47	126.7±0.5	2.564	53.31	0.556
B8 ₇₀₀	37.71±0.87	16.92 ±0.94	125.6±0.7	10.71	54.64	0.535
B8 ₈₀₀	39.87±0.80	16.34 ±0.85	124.2±0.6	9.672	56.21	0.511
B8 ₉₅₀	37.80±0.65	20.68±0.72	121.6±0.5	7.32	58.48	0.476
B8 ₁₀₅₀	20.92±0.53	34.61 ±0.63	119.7±0.4	6.388	55.53	0.521
B9 _{ad}	0±0.25	0±0.37	91.2±0.3	5.144	0	2
B9 ₇₀₀	0±0.28	0±0.41	87.5±0.3	5.49	0	2
B9 ₈₀₀	0±0.27	0±0.37	87.4±0.2	2.526	0	2
B9 ₉₅₀	0±0.26	0±0.37	87.0±0.2	4.786	0	2
B9 ₁₀₅₀	0±0.26	0±0.37	87.0±0.2	4.659	0	2
B9 ₁₁₅₀	0±0.23	0±0.33	87.0±0.2	4.295	0	2

Table 6.2: Summary of VASE measurement for experiment NC18. RTA temperature is displayed as subscript. The composition x is calculated using densities of Si and SiO₂ of 2.328 g/cm³ and 2.2 g/cm³ respectively.



(a) Evolution of ellipsometric angles of 120 nm SiO_x film on Si with rising annealing temperature. Black lines are fits of the raw data using model 2.



(b) Optical constants of 'excess-Si phase' of a $\text{SiO}_{0.54}$ film. Optical constants for bulk a-Si [155] and c-Si [164] are shown for comparison. The spectroscopic changes are attributed to an increasing fraction of crystalline Si NC for increasing annealing temperature.

Figure 6.11: Effect of annealing on averaged Si NC optical constants. Impact of a 30 s anneal in Ar/ N_2 at different temperatures on $\text{SiO}_{0.54}$ film, probed by ellipsometry. Fits were obtained using model 2.

Sample	A (eV)	E_n (eV)	C (eV)	E_g (eV)	d_{SiO_x} (nm)	d_{rough} (nm)	$f_{\text{cryst. Si in Si}}$ (vol %)	MSE
B8 _{ad}	204	3.81	3.34	1.52	122.8	2.6	0 (free)	0.8661
B8 ₇₀₀	267	3.64	2.87	1.80	121.3	2.4	0 (free)	1.335
B8 ₈₀₀	232	3.65	2.50	1.69	120.4	2.0	0 (free)	1.485
B8 ₉₅₀	186	3.69	2.13	1.52	120.1	0.8	0 (free)	1.412
B8 ₁₀₅₀	131	3.91	1.49	1.37	119.8	0.1	0 (fixed)	2.632
B8 ₁₀₅₀	132	3.89	1.59	1.36	119.9	0	10.8	2.344

Table 6.3: Fit parameters for the annealing dependent optical constants of a $\text{SiO}_{0.54}$ film (model 2).

those t_{Ox} values determined by XTEM for samples annealed at 1050 °C agree fairly well with the ellipsometry data (see Tab. 6.1, p. 66), slight deviations are within the typical variance of thickness across the wafer position. For a given sample the total Si excess volume fraction does hardly change between the anneals, which confirms the absence of oxidation effects. However the relative weight of a-Si and c-Si shifts between the anneals. For sample B8 having the highest Si excess (about 55%) for increasing annealing temperature there seems to be a systematic growth of the c-Si fraction on expense of the a-Si fraction. This effect is investigated in detail below.

Extraction of the optical constants of the excess Si phase in an $\text{SiO}_{0.5}$ film If the SiO_x thickness and composition are known spectroscopic ellipsometry can be used to obtain 'effective optical constants' for the excess Si phase. The latter can be assigned to the ensemble of Si NC, provided the phase separation of SiO_x into Si and SiO_2 is almost complete. For sample B8 investigated in the following, IR spectroscopy confirmed this to be the case for temperatures above 900 °C (Fig. 6.8, p. 78). Changes of these averaged Si NC optical constants with increasing annealing temperatures are expected. These changes account for the increasing mean size of Si NC and the transition from amorphous to crystalline state. Both effects modify the optical transitions of silicon in the energy range between 2 eV and 5 eV. For illustration, the spectra of optical constants of amorphous and crystalline Si are shown in Fig. 6.10. Many experimental reports agree in that the Si NC phase is amorphous for annealing temperatures below about 900 °C [70, 165, 86, 166]. The exact crystallization temperature of amorphous Si NC embedded in SiO_2 as function of size and strain is still an open question. The onset of crystallization probably occurs at even higher temperature for smaller Si NC (similar to the behavior of a-Si layers embedded in SiO_2 reported by Zacharias [167]). Due to the size distribution of Si NC a coexistence of amorphous and crystalline Si NC is likely, unless annealing temperatures near 1200 °C and long annealing times are used to force crystallization of all Si NC. For investigation of these annealing effects the model flexibility was increased as follows.

Model 2: The SiO_x was assumed to be a mixture of SiO_2 and an excess Si phase with unknown optical constants being a mixture of a-Si and c-Si. Instead of using tabulated values for a-Si the optical constants of the a-Si phase were parameterized using the Tauc-Lorentz (TL) formula, the best known parameterization for the dispersion of optical constants of amorphous semiconductors in the interband region [92, 93] (see

page 31). The model fits were further improved by addition of a surface roughness layer (Bruggemann effective medium of 50 % SiO_x and 50 % voids). The composition is fixed at the ERD result (54.3 vol% excess Si). Fit parameters are the SiO_x and the roughness layer thickness, the ratio of c-Si and a-Si and the four parameters of the TL formula. As initial values the XTEM-thickness and the TL-parameters describing bulk a-Si are used, while roughness and the c-Si/a-Si ratio were initialized with zero. The model procedure led to good fits, which are together with the raw data (ellipsometric angles Ψ and Δ) shown in Fig. 6.11a on p. 85. When parameter f_{c-Si} denoting the volume fraction of c-Si is let free, for all annealing temperatures except 1050 °C $f_{c-Si} = 0$ is obtained. In this case the TL parameters obtained by setting $f_{c-Si} = 0$ are shown for comparison. The fit parameters are summarized in Tab. 6.3, the average optical constants of the excess Si phase are shown in Fig. 6.11b. The effective optical constants of the excess Si phase are for low annealing temperatures close to the database values of evaporated amorphous Si. Since the deposition method influences structure and optical constants of a-Si, slight differences are normal. The fit parameter E_g , denoting the (indirect) energy band-gap, steadily decreases with increasing annealing temperature, which could be interpreted as consequence of Si NC growth resulting in weaker confinement. There is a significant difference between the optical constants obtained after the 950 °C and the 1050 °C anneal. The maxima in ϵ_1 and ϵ_2 shift towards higher energies, into the region of c-Si optical transitions. A plausible explanation would be that for higher annealing temperatures a higher percentage of the Si NC is crystalline and/or the mean size of crystalline Si NC is rising. In fact, for sample B8 crystalline NC with diameters up to 5 nm were observed by XTEM after the 30 s anneal at 1050 °C (p. 74, Fig. 6.5d). Since the TL-model is based on only a single inter-band transition it cannot reproduce the complex c-Si optical constants accurately. This shortcoming of the TL model is partly compensated by combination of the TL optical constants and c-Si optical constants, which apparently helps to improve the fit for 1050 °C. The expected trend of optical constants is shown correctly. The sensitivity of ellipsometric data to the Si NC optical constants decreases with the Si NC concentration, which limits the procedure to rather thick oxide films with a high Si excess.

T_{Anneal}	$f_{\text{Si}} = f_{\text{c-Si}} + f_{\text{a-Si}}$ (vol%)	$f_{\text{c-Si}}$ (vol%)	d_{SiO_x} (nm)	MSE
as dep.	57.97 ± 0.18	12.207 ± 1.03	442.6 ± 1.00	8.235
700 °C	56.278 ± 0.276	34.35 ± 1.89	448.3 ± 1.45	20.06
900 °C	59.461 ± 0.246	38.762 ± 1.68	440.85 ± 1.25	18.08
1000 °C	57.143 ± 0.201	71.041 ± 1.19	436.75 ± 1.01	14.64
1100 °C	57.66 ± 0.172	84.477 ± 0.719	430.94 ± 0.796	10.49
1200 °C	57.581 ± 0.217	88.932 ± 0.7	423.11 ± 1.01	13.27

Table 6.4: Sequential anneal of $\text{SiO}_{0.54}$ film at different temperature. From ellipsometry analysis using model 1 (BEMA of SiO_2 , a-Si and c-Si), the total Si excess and the sample thickness are determined. The model yields about the same Si excess after all anneals.

Confirmation with a thicker $\text{SiO}_{0.54}$ sample and higher annealing temperatures

To confirm the change of optical constants, a ~ 430 nm thick SiO_x film was deposited the same way as sample B8 and annealed for 2 min at temperatures of 700 °C, 900 °C, 1000 °C, 1100 °C and 1200 °C. After each anneal the samples were measured by spectroscopic ellipsometry between 1.2 eV and 4.9 eV at angles of 65°, 70° and 75°. The composition and thickness were determined again using model 1 described above and yielded results given in table 6.4. For anneals above 900° the relative weight of c-Si increases considerably. For parametrization of the optical constants of the excess Si phase, based on the composition and thickness derived with model 1, instead of model 2 the parametric semiconductor layer [168] available within the VASE software was employed. Because within the parametric semiconductor layer about 80 parameters can be varied, a detailed parameter listing is omitted. The evolution of averaged optical constants of the Si NC phase is shown in Fig. 6.12. Again for temperatures above 900 °C, the optical constants significantly differ from those of a-Si, indicating the onset of crystallization. For annealing temperatures of 1100 °C and 1200 °C the evolution of sharp structures near 3.2 eV is observed. From simulations of SiO_x annealing it is known that in films with a high Si excess from merging Si NC finally extended Si agglomerates are formed. The evolution of the characteristic double peak structure of ϵ_2 observed after the anneal at 1200 °C is attributed to the long range order in such extended crystalline agglomerates.

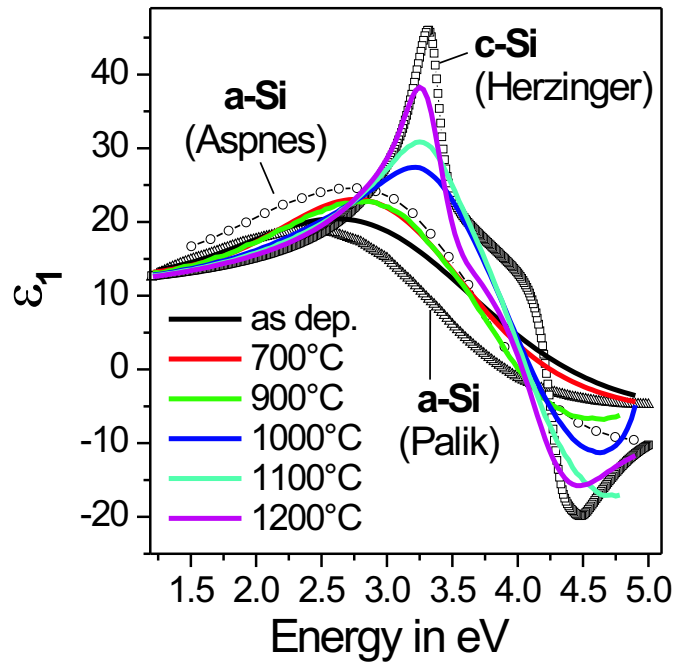
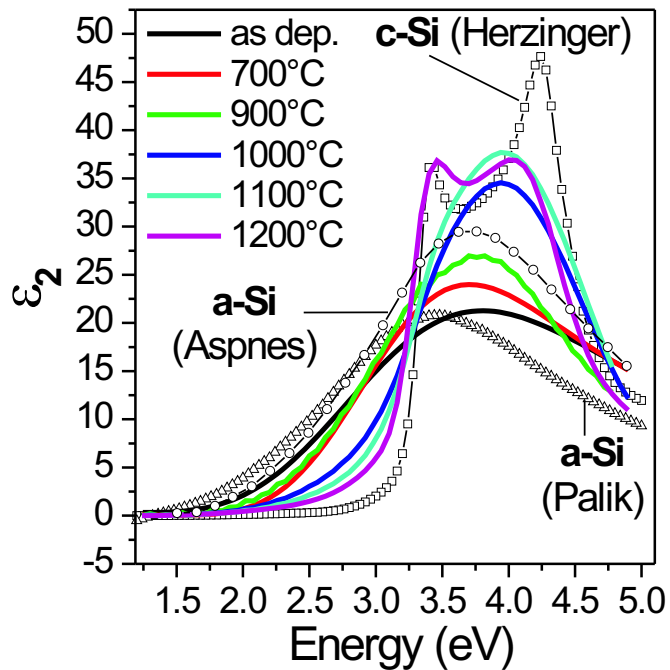
(a) Change of ϵ_1 with growth of Si NC(b) Change of ϵ_2 with growth of Si NC

Figure 6.12: Effective optical constants of excess Si phase in a 430 nm $\text{SiO}_{0.54}$ film after 2 min annealing in Ar/N_2 at the indicated temperatures. The optical constants were fitted using the parametric semiconductor model of the Woollam VASEtm software. Changes in optical constants reflect the growing Si NC size and ongoing crystallization.

7 Simulation of Si NC formation by annealing of SiO₂/SiO_x layer-stacks

Because of the experimental difficulties in tracking the evolution of a Si NC ensemble during ripening, simulations are very useful to develop an understanding of the experimental annealing results. I hereby acknowledge the beneficial collaboration with T. Müller, who in response to my request modified the K3DMC code developed by Dr. K.H. Heinig (both FZ Rossendorf) and triggered a simulation of the evolution of Si NC in selected SiO₂/SiO_x layer-stack designs that have been or could be prepared by sputtering. The resulting data complement my experimental findings and are therefore presented in this chapter.

7.1 The kinetic 3D lattice Monte-Carlo method

The precipitation in supersaturated solutions is a highly sophisticated problem. In many practical cases additional difficulties arise from a time- and space-dependent concentration of impurity atoms (IA), for example during ion-implantation or in presence of absorbing interfaces. Atomistic approaches such as the kinetic 3D lattice Monte-Carlo (K3DMC) method developed by Heinig et al. (see [50] and references therein) allow to study the evolution of a given distribution of impurity atoms in a neutral matrix also for a time dependent concentration of IA. A detailed description of this method was given by Strobel [42].

Also the evolution of excess Si IA in a SiO₂ matrix can be treated using the K3DLMC method: The Si IA are allowed to move on a 3D face centered cubic (fcc) lattice which, due to its symmetry, is well suited to represent the isotropic diffusion in the amorphous SiO₂ matrix. Each IA has a temperature and binding energy dependent probability to jump from its site to one of the $\xi = 12$ next neighbor lattice sites. The period of the fcc lattice ($a = 2.169 \text{ \AA}$) is chosen such that the mean atomic density of Si NC in the model corresponds to the real density of bulk silicon. The top interface of the oxide matrix is assumed to reflect excess Si atoms, whereas Si atoms reaching the bottom Si substrate stick to it or evaporate into the oxide matrix depending on the ratio of bond-strength between two Si next-neighbors J , and the thermal energy $k_B T$. This ratio also determines the balance between formation and dissolution of precipitates. *Because the experimental value of J is not precisely known, the ratio $J/k_B T$ is usually fixed at a plausible value. The unknown experimental parameter J does not allow to match the temperature parameter of the simulation to the one of the experiment. This is the main obstacle for attempts to correlate results of simulation and experiment.* Provided that the temperature in simulation and experiment are the same, the experimental anneal-

	S0	S1	S2	S3	S4
t _{COx} (nm)	20	20	20	6	6
t _{SiOx} (nm)	10	10	10	1.5	1.5
t _{TOx} (nm)	3	3	3	3	3
Repetitions of SiO _x /TOx	1	1	1	1	3
Si excess in SiO _x c _{Si} (at%)	5	12	20	25	25
J/k _B T	2	2	2	2	2

Table 7.1: Gate stack-configurations for which the evolution of Si NC was simulated. J is strength of a Si-Si bond, k_BT the thermal energy.

ing time corresponding to a single Monte Carlo step (MCS) is given by ([42] p. 41):

$$\tau = \frac{a^2/\xi}{D_{exp}} \quad (7.1)$$

Here D_{exp} is the temperature dependent experimental diffusion coefficient. For diffusion of Si in amorphous SiO₂ it has been estimated by Nesbit [169] according to $D_{exp} = D_0 \cdot \exp(-E_a/[k_B T])$ with $D_0 = 1.2 \cdot 10^{-9} \text{ cm}^2/\text{s}$ and $E_a = 1.9 \text{ eV}$. Since these values have not been independently confirmed yet, they should be considered with care. Müller [170] applied the K3DMC method to study the phase separation and formation of Si NC in low-energy Si ion-implanted SiO₂ films. In response to my request he additionally simulated the formation and evolution of Si NC in selected configurations of SiO₂/SiO_x stacks on top of a Si substrate.

7.2 Investigated configurations

The parameters of the simulated SiO₂/SiO_x stacks are summarized in Tab. 7.1. The configurations *S0*, *S1*, and *S2* correspond to the memory capacitors *C4*, *C5* and *C6* characterized experimentally (see Tab. 8.1, p. 104). In order to investigate the very interesting *limit of constrained growth of Si NC* (width of SiO_x layer \approx Si NC diameter), which could be realized in follow-up experiments, the arrangements S3 and S4 were included. In configuration S3, the initial width of the single SiO_x layer was chosen to be only 1.5 nm, whereas set of three 1.5 nm thin SiO_x layers is studied in configuration S4.

7.3 Results

7.3.1 Configurations S0, S1 and S2

The evolution of configurations S0, S1 and S2 is shown in columns a, b, and c of Fig. 7.1 respectively with the simulation time increasing from top to bottom. The excess Si atoms in the SiO_x-layer and the Si substrate atoms are shown as tiny spheres, whose color is determined by the number of Si next neighbors. For example red corresponds to

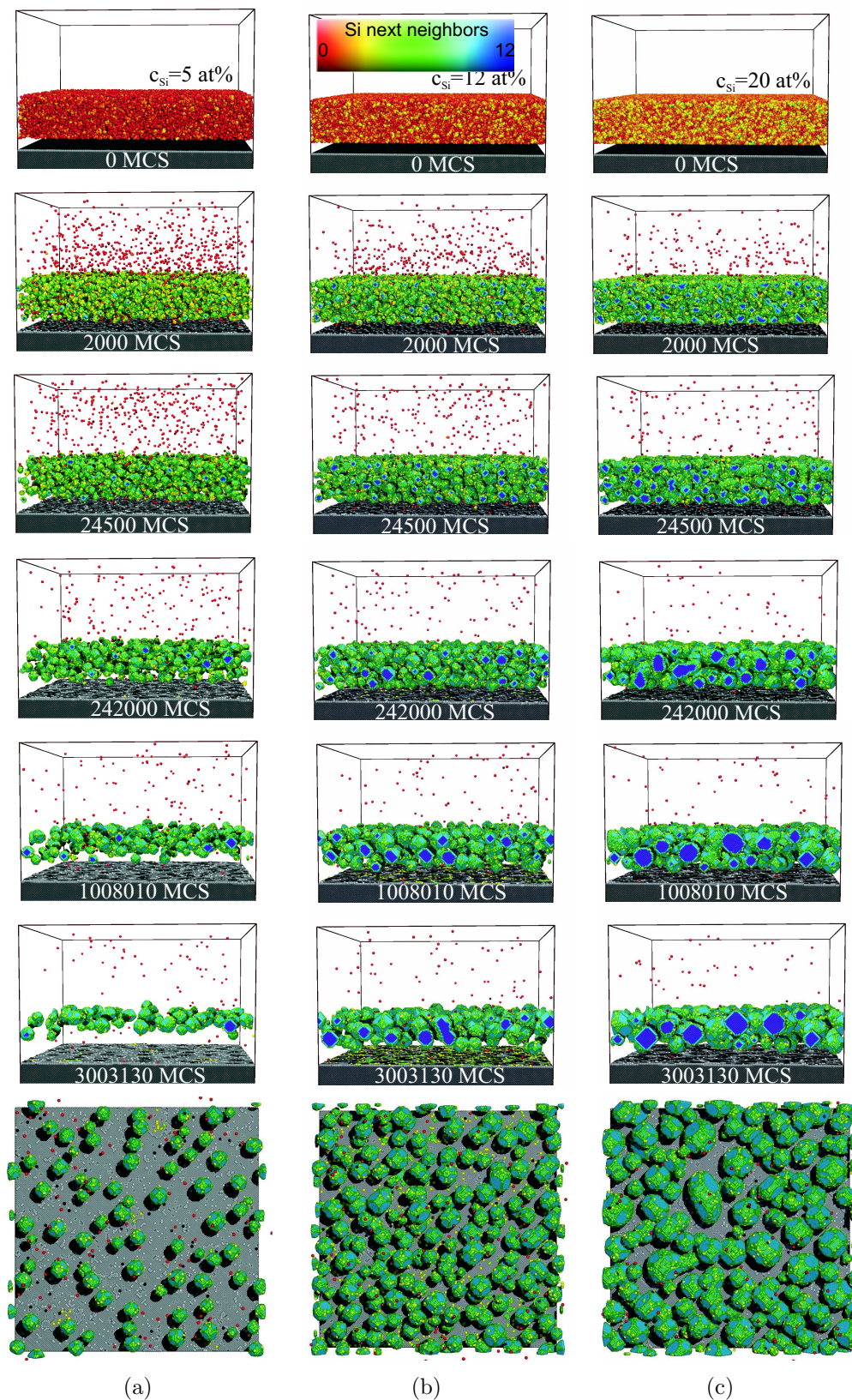


Figure 7.1: Evolution of a Si NC ensemble formed by annealing of a 3 nm SiO₂/ 10 nm SiO_x / 20 nm SiO₂ gate stack on Si with (a) 5 at%, (b) 12 at% or (c) 20 at% Si excess in the SiO_x layer. The number of Monte-Carlo steps (MCS) is proportional to the annealing time. Simulations by T. Müller, FZ-Rossendorf.

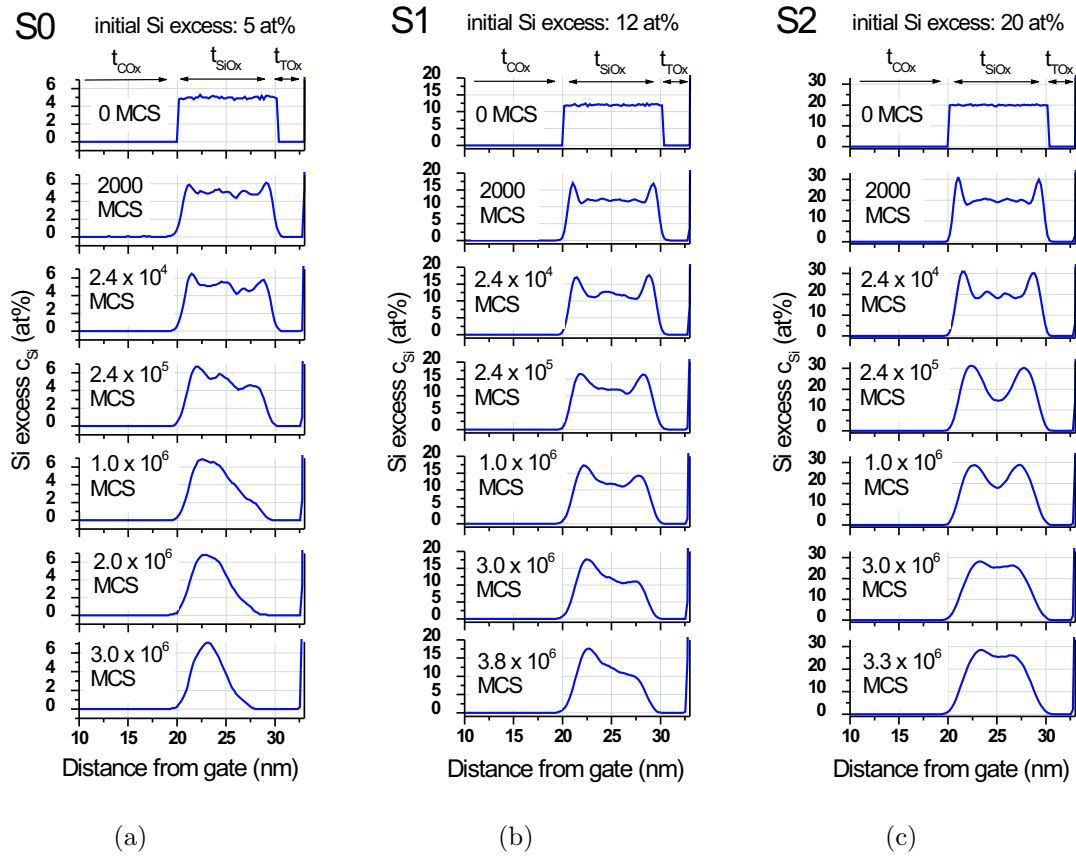


Figure 7.2: Evolution of the Si-excess concentration profile in 3 nm SiO_2 / 10 nm SiO_x / 20 nm SiO_2 stacks on Si with (a) 5 at%, (b) 12 at% or (c) 20 at% Si excess in the SiO_x layer during annealing. At a given annealing temperature the number of Monte-Carlo steps (MCS) is proportional to the annealing time.

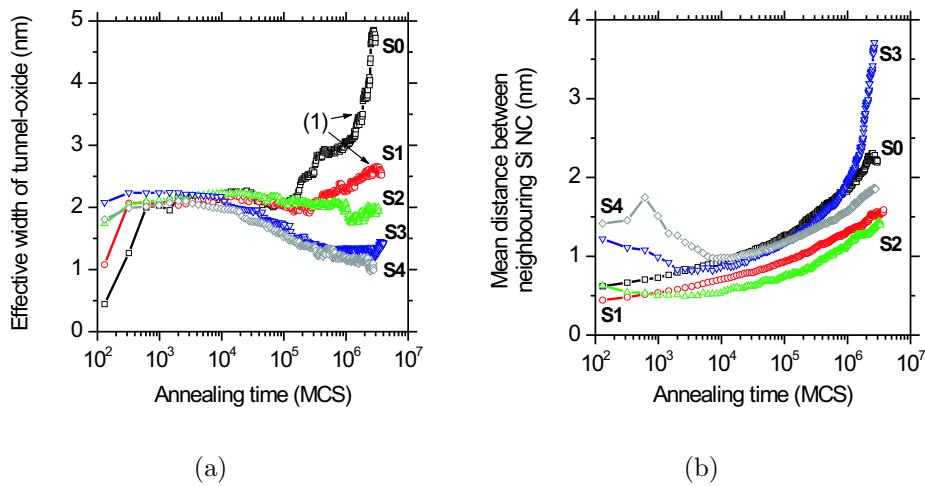


Figure 7.3: Evolution of (a) effective tunneloxide width and (b) mean distance between neighboring Si NC with annealing time for configurations S0 to S4.

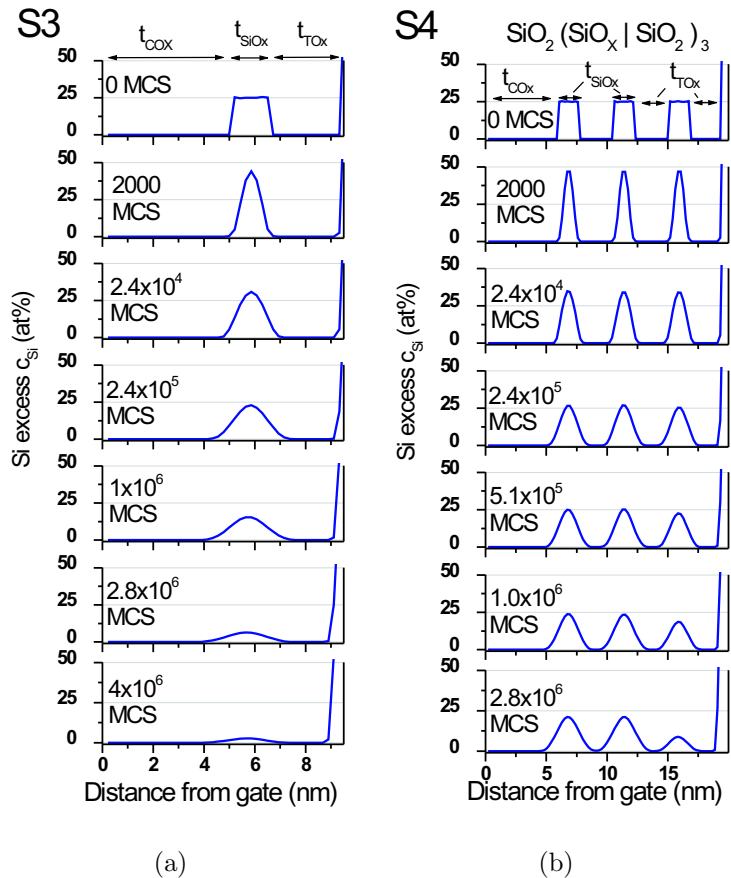


Figure 7.4: Evolution of the Si concentration profile of configurations S3 (a) and S4 (b) with 1.5 nm SiO_x layers during annealing. The excess Si atoms are confined by precipitates formed in the middle of the SiO_x layers, where temporarily the Si concentration even exceeds the initial one. Structures like S3 and S4 demonstrate how to prepare single layers of separated uniform Si NC in SiO_2 .

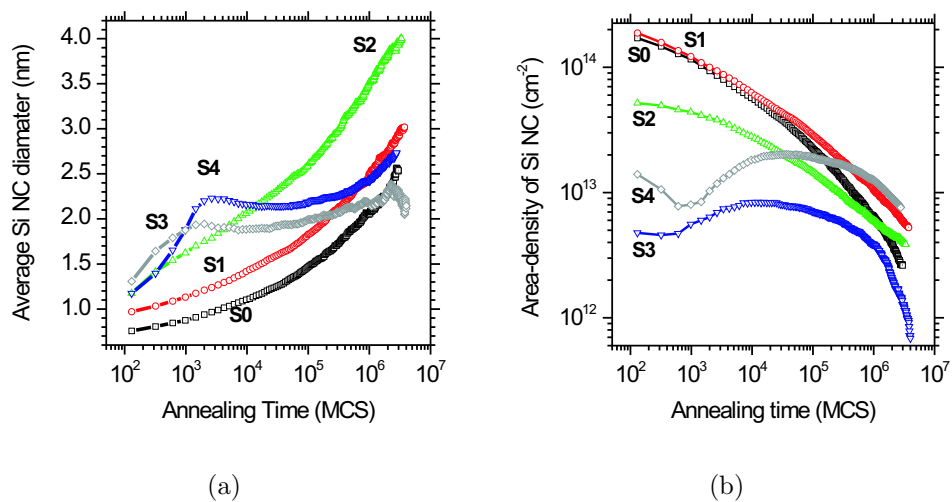


Figure 7.5: Evolution of (a) mean Si NC diameter and (b) area-density of Si NC with annealing time for configurations S0 to S4.

an uncoordinated Si IA whereas blue is the color of Si IA's for which all 12 next-neighbor positions on the fcc-lattice are occupied by other Si atoms. Si atoms initially belonging to the substrate are grey. In the initial state, the frequency of Si IA's coordinated with one, two or more other Si IA's increases with the total Si excess¹ as reflected by the color change from red for 5 at% Si excess to yellow-greenish for 20 at%².

After 2000 MCS the highest concentration of Si monomers in the initially stoichiometric top oxide is found for the configuration with the smallest average Si NC diameter d_{av} (i.e. S0). This is a consequence of the Gibbs-Thomson relation (Eqn. 2.6, p. 11).

For all three configurations the initial broadening of the box-type Si excess profile leads temporarily to a rapid decrease of tunnel-oxide thickness. Later on again a widening of the tunnel-oxide region by condensation of Si atoms onto the substrate is observed. Since smaller clusters dissolve faster the condensation effect is most pronounced for S0 (Fig.7.2), but later it also occurs in S1 (Fig. 7.3a). The large Si NC of configuration S2 are most stable, but in the limit of long annealing time all excess Si atoms will finally condense onto the substrate.

An instability in the concentration profile of Si atoms is observed to gradually grow from the edges to the center of the SiO_x layer³.

The plane-view image after 3·10⁶ MCS shows spherical Si NC for configuration S0, ellipsoidal ones are observed for S2. The ellipsoids correspond to merging Si NC, that have not yet minimized their surface energy.

The mean distance between neighbored Si NC is found to be smaller for higher Si excess (Fig. 7.3b).

Consequently for equal annealing conditions Si NC memory devices prepared from a low Si excess SiO_x layer are likely to show a rather localized charge storage at electrically isolated Si NC, while those prepared with high Si excess behave similar to continuous-floating-gate devices. For an Si excess above about 10-15 at% initially isolated Si NC merge in the process of annealing to form in the late ripening phase wire- or mesh-like agglomerates [170]. Since charges trapped in such floating gate structures are delocalized over the agglomerate this case must be avoided, when heading for devices based on localized charge storage.

With rising Si excess the mean diameter of Si precipitates increases (Fig. 7.5a). For rather short anneals the area-density of Si NC initially shows a maximum for a concentration between 5 at% and 20 at%. After excessive annealing the Si NC density will be largest for the highest initial Si concentration due to the condensation of Si atoms onto the Si substrate (Fig. 7.5b). *These effects show, that the spacial distribution of Si NC is practically hardly predictable when starting with SiO_x layers whose thickness exceed the screening length of diffusion* (Eqn. 2.7, p.13).

¹See random-bond model discussed on p. 21

²A corresponding experimental report: Hanaizumi [88] observed the red PL typical for Si NC even for un-annealed sputter-deposited SiO_x films. Very likely the high Si excess of 6-11 vol% excess-Si lowered the nucleation barrier and resulted in the formation of very small Si NC without any thermal annealing.

³See discussion of instabilities on p. 12.

7.3.2 Configurations S3 and S4

If instead of the broad initial concentration profile of configurations S0 to S2 spike like profiles as in S3 and S4 are used, the instabilities of the Si depth profile are effectively suppressed by the *confined growth of precipitates* (Fig. 7.4). Because the width of the SiO_x layer is on the order or below the diffusional screening length, only a single layer of Si NC results from each SiO_x layer. This is the key to the control over the Si NC location in vertical direction. Since essentially no excess Si atoms from above or below the SiO_x layer feed the precipitates, initially the ripening of Si NC is governed by the two-dimensional diffusion within the thin SiO_x -layer, whereas the interaction between multiple Si NC layers occurs on another timescale (Fig. 7.5a), which is determined by the thickness of the SiO_2 interlayers. This leads to a more homogeneous lateral and size distribution of Si NC (for an experimental proof see Zacharias [31]). Furthermore, in contrast to S0-S2 for S3 and S4 the mean Si NC diameter is insensitive with respect to the annealing time. In stack S4 the gradual dissolution of the near-interface Si NC layer efficiently stabilizes the upper Si NC layers, such that even the Si NC area density varies only by a factor of two throughout the simulation.

7.3.3 Conclusions

From the simulated configurations S0 to S1 one expects the following trends for the experimental MOS memory capacitors C4 to C6 (Tab. 8.1, p. 104) at a fixed anneal in the limit of short anneals (low Si condensation on the substrate):

- an increase of Si NC diameter with Si excess
- a decrease of Si spacing with growing Si excess
- a maximum of Si NC density for a Si excess between 5 at % and 20 at%
- localized charge trapping and best charge retention for 5 at% Si excess (widening of tunnel-oxide, highest mean Si NC separation)

When starting with SiO_x layers whose thickness exceeds the screening length of diffusion the spacial distribution of Si NC is hardly controllable, because the 3D diffusional ripening triggers instabilities in the Si concentration profile.

The opposite holds if the SiO_x layers embedded in SiO_2 are only 1-3 nm thick. A consequence of the slower quasi 2D diffusional ripening there is a lower sensitivity of the Si NC size and vertical Si excess profile to the experimental annealing parameters. The location, density and size of Si NC are closely coupled to the geometry and Si excess of the initial SiO_x layers. Deposited gate stacks incorporating $\text{SiO}_x/\text{SiO}_2$ superlattices with layers about 1-3 nm thick are therefore considered as the most promising approach towards optimized Si NC memory devices.

8 Si NC memory capacitors prepared by cosputtering

In the previous chapter a method to prepare SiO₂ with embedded Si NC by sputter deposition and annealing of oxygen deficient silicon oxide films has been established. Goal of this experiment is to apply this method for the formation of metal-oxide-silicon (MOS) capacitors with Si NC embedded in the gate oxide. The capacitors are formed by annealing a SiO₂/SiO_x stack deposited onto a thermally grown tunnel-oxide on silicon. The functionality of the resulting structure as a memory device is confirmed in various electrical tests.

8.1 Sample Preparation

The process flow is illustrated in Fig. 8.1. MOS capacitors (sample set C) were formed on n-type (100) float zone silicon (FZ Si) wafers¹. FZ Si was selected for two reasons: the breakdown strength of thermal oxides grown on Czochralski silicon (Cz Si) wafers is limited by void like surface defects², resulting from the accumulation of vacancies during crystal growth [171]. This problem is usually circumvented by deposition of an epitaxial silicon layer on top of the Cz Si wafer. Here the use of FZ Si eliminates these defects. In addition the oxygen-free FZ Si is favorable for the characterization of SiO_x annealing by IR spectroscopy (see p. 25). The near surface region (~50 nm) of backside surface of the substrate was implanted with phosphorus (50 keV, 5 · 10¹⁵ cm⁻²) through a 50 nm thermal oxide, and subsequently annealed (10 min at 900 °C in N₂) to generate a heavy n-doped region in the top 50 nm of substrate backside. This is necessary, since Al may diffuse into the n-type Si during the post-metallization anneal, where it forms a shallow electron acceptor level 0.067 eV above the Si valence band. In weakly n-doped Si a pn-junction between the Al-diffused p-type and bulk Si n-type substrate regions would result, which by heavy n-type doping is either suppressed or the width of its depletion layer is reduced such that electrons can easily traverse it by tunneling and virtually no potential drop occurs. After removal of the 50 nm oxide in hydrofluoric acid (HF), a tunnel-oxide (TOx) with a nominal thickness between 2 nm and 3 nm was grown by rapid thermal oxidation (RTO) using the process depicted in Fig. 8.2a. Rapid thermal oxidation allows the use of high temperatures favorable for oxide quality. While the main fraction of the oxide is grown at 800 °C, the short ramp up to 900 °C is introduced to reduce the width of the Si-SiO₂ transition layer [172, 38] and thus the density of interface states.

¹diameter: 3 inch, thickness: 0.99 mm, Phosphorus doped: $N_D = 1 \cdot 10^{15} \text{ cm}^{-3}$, resistivity: 5 Ω·cm

²crystal originated pits: COP

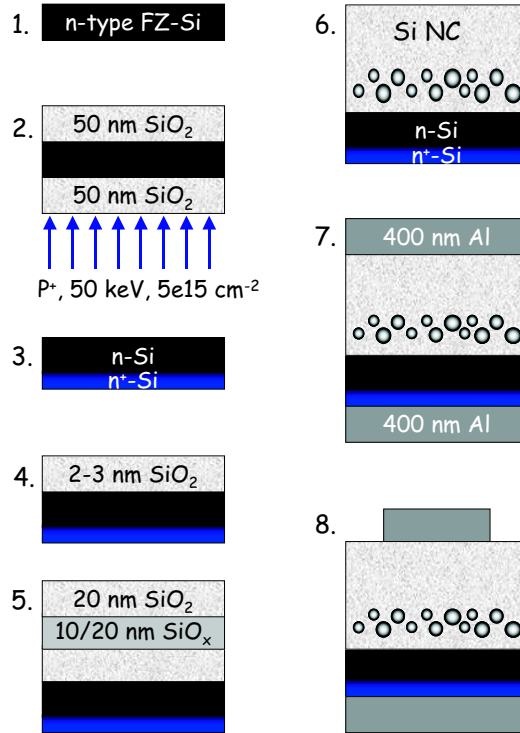
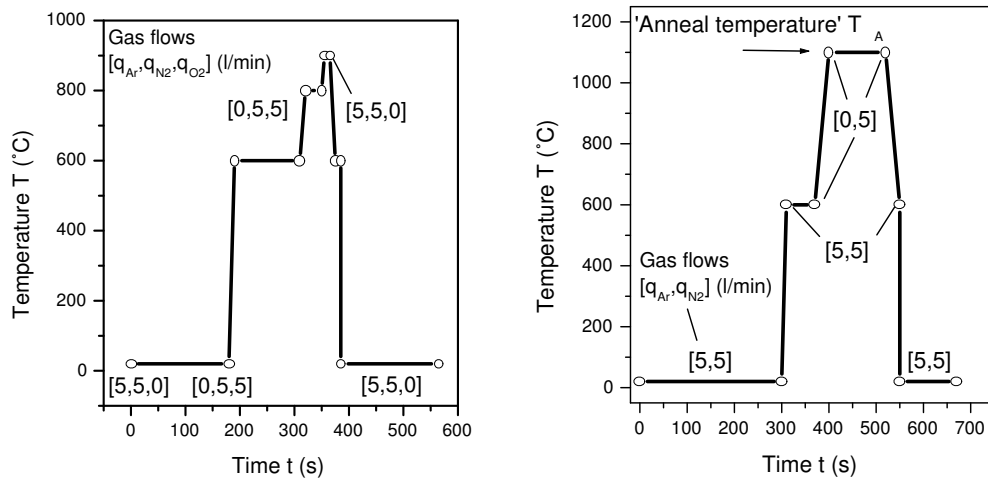


Figure 8.1: Sequence for preparation of Si NC MOS-memory capacitors: 1. cleaning, 2. growth of a sacrificial oxide layer, backside implant and activation anneal, 3. removal of sacrificial oxide by etching, 4. growth of tunnel-oxide, 5. deposition of SiO₂/SiO_x-stack, 6. rapid thermal post-deposition anneal (PDA) in Ar/N₂ for Si NC formation, 7. aluminum deposition and 8. post-metallization anneal (PMA) in forming gas (N₂ + 7% H₂) and contact pad formation



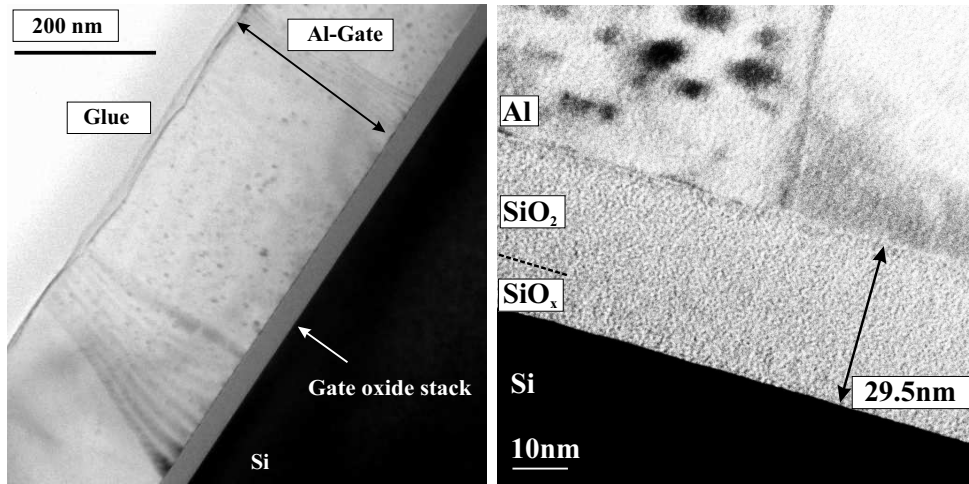
(a) Process for rapid thermal oxidation of a (b) Process for rapid thermal anneal of gate oxide stack.

Figure 8.2: Rapid thermal processes used in preparation of memory capacitors.

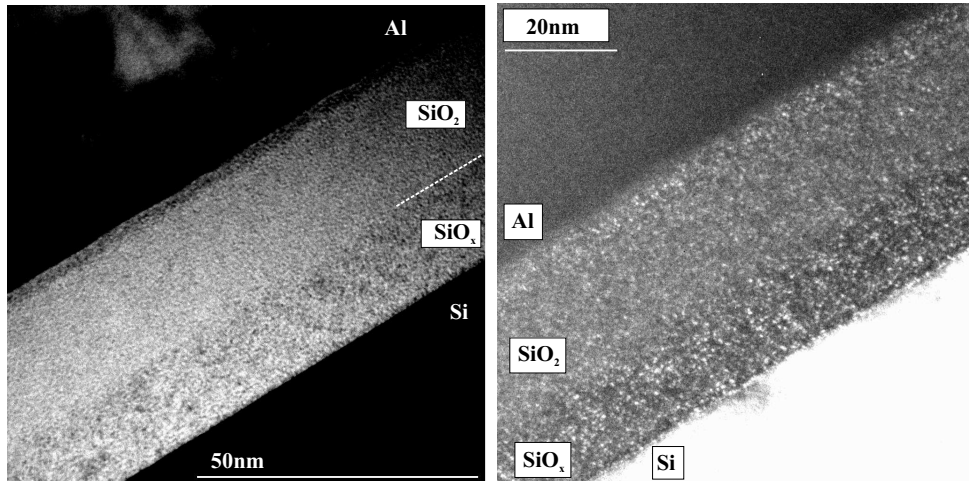
The thickness of the tunneloxide was measured by spectroscopic ellipsometry on a separately processed test wafer (sample E). On the other wafers, immediately after RTO, SiO_x films of about 10 nm or 20 nm thickness and a target O/Si ratio x of 1.3, 1.6 or 1.9 were sputter deposited using method 1 (defined on p. 65). Finally a 20 nm SiO_2 capping oxide (COx) film was deposited on set C using method 2 (p. 65). For comparison a homogeneous 50 nm SiO_2 reference sample was prepared the same way. The wafers were then cut to quarters and exposed to different isochronal (2 min) rapid thermal anneals (RTA) at 800 °C, 950 °C or 1100 °C in an $\text{Ar}/\text{N}_2 = 1/1$ mixture. The RTA process is shown in Fig. 8.2b. The samples were sputter-coated with aluminium on both sides and exposed to a 30 min anneal at 400 °C in forming gas ($\text{N}_2 + 7\% \text{H}_2$). Finally contact pads and windows for optical tests were defined by wet-chemical etching of the Al film. Simultaneously with set C a set of bare Si pieces (set D) was SiO_x coated, to enable a separate testing of the SiO_x film thickness and composition by ellipsometry.

8.2 Electron Microscopy

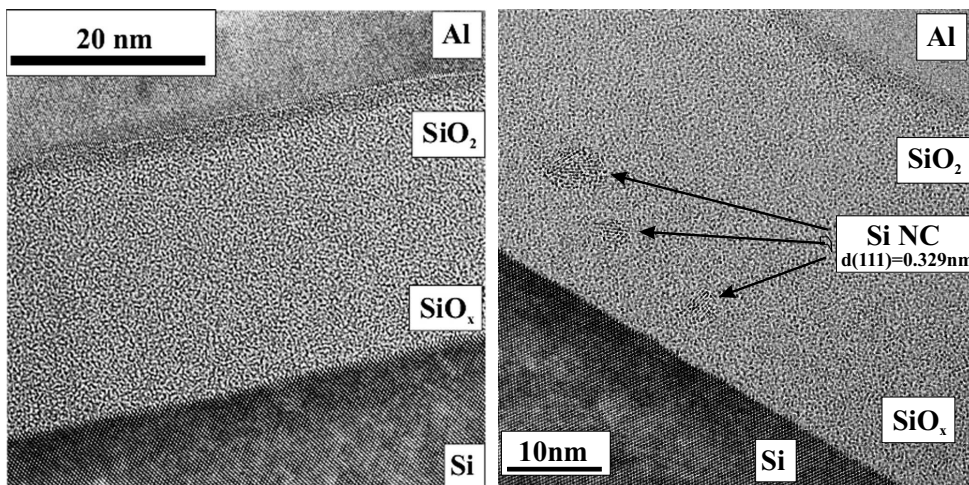
Those samples of set C, for which the oxide was annealed at 1100 °C were investigated by XTEM. The specimen were cut from the outer edge of the quarter-wafers, where the film thickness was slightly lower. Fig. 8.3a is a cross section through a MOS-capacitor of sample C5. The polycrystalline Al gate contact, the gate oxide stack and the Si substrate are distinguished. Bright field measurements at higher magnification allow to accurately determine the total thickness t_{Ox} of the gate stack. The inhomogeneous deposition rate will lead to slightly different values on other positions on the wafer. For all samples, except C3, the SiO_2 cap-oxide (Cox), the SiO_x layer and the tunnel oxide cannot be distinguished, because both materials scatter electrons with comparable efficiency (Fig. 8.3b). However, if, as for sample C3, the SiO_x region contains a sufficiently high concentration of crystalline Si NC, a higher fraction of electrons is scattered out of the primary beam and the SiO_x region appears darker than the SiO_2 layer (Fig. 8.3c). The corresponding dark field image (Fig. 8.3d) shows a higher contrast in those regions where nanocrystals either diffract electrons into or out of the (111) reflex used for imaging, compared to the more homogeneous scattering in the amorphous SiO_2 regions. In high resolution mode, (111) lattice planes of crystalline Si NC are only resolved for sample C3 (Fig. 8.3f). The absence of nanocrystals for sample C6 (Fig. 8.3e) which differs from sample C3 basically in the SiO_x thickness (C6: 10 nm, C3: 20 nm), might be an indication of a loss of excess Si either by evaporation of gaseous SiO or by oxidation during annealing caused by residual (O_2 or H_2O). Also the condensation of Si monomers onto the substrate might have a stronger impact on the thinner SiO_x film (C6). The spacing of (111) nanocrystal-lattice planes oriented perpendicular to the Si interface measured from a cluster oriented along the interface direction is with $3.2 \pm 0.01 \text{ \AA}$ slightly higher than the tabulated value of bulk-Si (3.1355 \AA).



(a) Bright field image showing the cross section through a MOS-capacitor of sample C5. (b) Bright field image of sample C6. No contrast is observed between SiO_2 and SiO_x layer.



(c) Bright field image of sample C3. Contrast between SiO_2 and SiO_x due to diffraction by crystalline Si NC. (d) Dark field image of sample C3 using (111) reflex. Nanocrystals cause the intensity fluctuations in SiO_x region.



(e) High resolution image of sample C6. No crystallites are observed. (f) High resolution image of sample C3. Individual (111) lattice planes of Si nanocrystals are clearly observed.

Figure 8.3: Results of XTEM investigation of sample set C (Measurement by M. Mücklich, FZ Rossendorf).

8.3 Ellipsometry

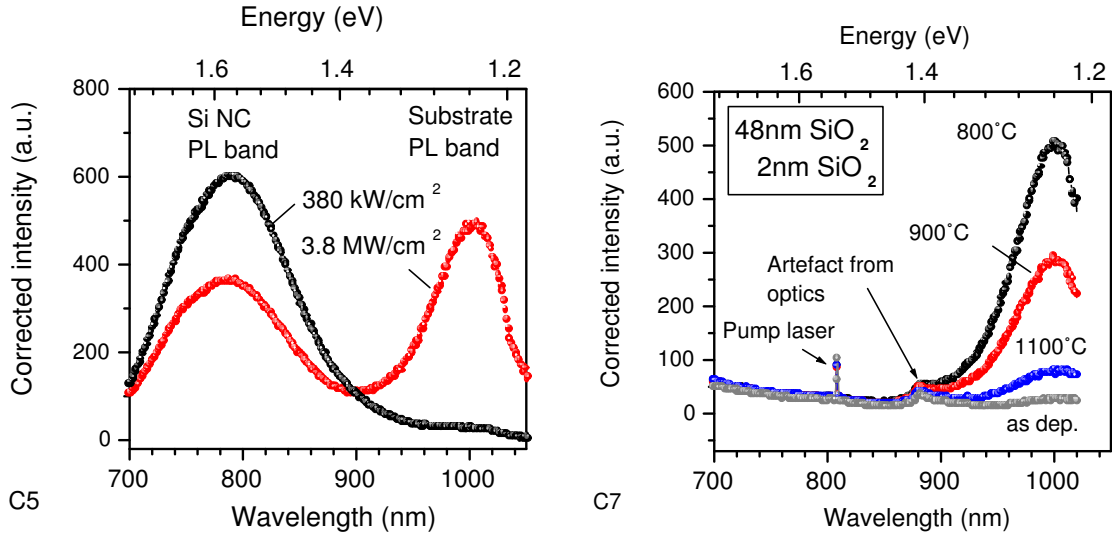
The XTEM measurements showed again that other techniques are needed for the metrology of SiO₂/SiO_x stacks. By ellipsometry of both, the reference wafers E/set D and the stacks of set C, the parameters of the single layers in the multi stack can be extracted.

Tunneloxide For the optical metrology of ultrathin (<5 nm) thermal oxides grown on silicon, it is necessary to take into account the existence of a silicon rich transition region between the Si substrate and the bulk of the thermal oxide [173, 174, 175, 176]. The transition region has a higher refractive index than bulk-SiO₂ and its width varies depending on processing between 0.3 nm and 2 nm, where higher values are found for lower oxide growth temperature. Derived thicknesses of ultrathin oxides therefore depend significantly on the chosen model. Wafer E was measured by spectroscopic ellipsometry in the range between 1.54 eV and 4.8 eV at angles of 60°, 65° and 70°. The simplest model, SiO₂ [164] on bulk Si [164], yielded $t_{Ox} = 2.167 \pm 0.082$ nm at MSE = 1.514, indicating a slight mismatch between fit and measurement. An analysis using the Sellmeier approach (eqn. 3.24) yields an improved fit: $A1 = 0.00247 \pm 0.00018$, $\lambda1 = 54.641 \pm 2.88$ and $t_{Ox} = 1.63 \pm 0.04$ nm, MSE = 0.98. When the oxide layer is assumed to have fix n and k values, a very good fit is obtained ($n = 1.5461 \pm 0.044$, $k = 0.1786 \pm 0.0264$, $t_{Ox} = 2.25 \pm 0.09$ nm, MSE = 0.5123). $t_{Ox} \approx 2$ nm is considered a good estimate.

SiO_x and cap-SiO₂ layers To confirm the desired film thicknesses and compositions, sample set D and C were investigated by spectroscopic ellipsometry in the range between 1.54 eV and 4.8 eV at an entrance angle of 65°. To measure the individual layers in the gate stack, samples C0 to C7 were represented by a SiO₂/SiO_x/SiO₂/Si model stack, set D was represented by a SiO_x/Si stack, where the SiO_x film was treated as Bruggemann effective medium (see p. 34) composed of a-Si, c-Si and SiO₂ as above (p. 83). To reduce the ambiguity, introduced by the interdependence of fitting parameters, the parameters of corresponding samples of set C and D were fitted simultaneously using the multi-sample analysis feature of the Woollam-VASE software. Since, owing to the simultaneous preparation, the thickness and composition of the SiO_x-layer was the same for the corresponding samples in both sets, this was added as additional constraint in the multi-sample analysis. Still, the variance in deposition rate across the wafer (≈ 5 -10 %) introduces a little error. The TOx thickness was fixed at the separately determined value of ~ 2 nm. Fit parameters were the COx thickness and the SiO_x composition and thickness. The reference sample C8 was represented by a simple SiO₂/Si stack using database optical constants. The fitted values are summarized in table 8.1, p. 104. These results independently confirm that the SiO_x composition changes as expected for the changed Si target power while the thickness of the SiO_x layer equals roughly the nominal values of 10 nm or 20 nm. The composition values x were calculated assuming using the densities of bulk Si and SiO₂ (2.328 gcm^{-3} and 2.2 gcm^{-3}) respectively.

	C0	C1	C2	C3	C4	C5	C6	C7
P_{Si} (W)	0	50	130	210	50	130	210	0
Gas	Ar	Ar	Ar	Ar	Ar	Ar	Ar	Ar/ O ₂
VASE f_{Si}	-	4.63	8.8	15.15	4.37	9.4	14.3	-
$x = O/Si$	2	1.80	1.64	1.42	1.81	1.62	1.37	2
t_{CO_x} (nm)	48.0	21.2	21.2	21.2	21.2	21.2	21.2	47.6
t_{SiO_x} (nm)	-	20.9	19.2	18.7	10.7	8.0	9.2	-
t_{TO_x} (nm)	2	2	2	2	2	2	2	2
t_{O_x} (nm)	50.0	44.1	42.4	41.9	33.9	31.2	32.4	49.6
HFCV $t_{O_x, 800^\circ C}$ (nm)	54- 61	39- 42	39- 40	38- 39	33- 34	32- 33	31- 32	48- 51
XTEM $t_{O_x, 1100}$ (nm)	-	37.5	38.2	39.3	30	30	29.5	-
Si NC	-	no	no	yes	no	no	no	-
PL $\lambda_{800^\circ C}$ (nm/eV)	-	-	-	750/ 1.653	-	-	-	-
$\lambda_{950^\circ C}$ (nm/eV)	-	-	-	790/ 1.569	-	-	780/ 1.589	-
$\lambda_{1100^\circ C}$ (nm/eV)	-	740/ 1.675	780/ 1.589	806/ 1.538	-	738/ 1.680	800/ 1.550	-
$I_{800^\circ C}$ (a.u.)	-	-	20	53	-	-	-	-
$I_{950^\circ C}$ (a.u.)	-	-	25	37	-	-	18	-
$I_{1100^\circ C}$ (a.u.)	-	55	240	70	-	17	57	-
$d_{800^\circ C}$ (nm)	-	-	-	2.0- 3.0	-	-	-	-
$d_{950^\circ C}$ (nm)	-	-	2.4- 3.3	2.5- 3.4	-	-	2.2- 3.2	-
$d_{1100^\circ C}$ (nm)	-	1.9- 2.8	2.3- 3.2	2.8- 3.7	-	1.9- 2.8	2.7- 3.5	-

Table 8.1: Characteristics of sample set C, derived by XTEM, VASE, HFCV and PL measurements. Si NC diameters d_{T_A} , estimated from the PL energy for anneals at different temperature T_A are also shown.



(a) Sample C5: Substrate and Si NC related photoluminescence for two different power densities. Excitation at 632.8 nm. (b) Sample C7: Dependence of substrate peak on annealing. Excitation at 532 nm. The 810 nm peak is a sideband of the exciting laser.

Figure 8.4: The PL from the Si substrate corrected for spectral response of CCD detector.

8.4 Photoluminescence Measurements

PL spectra were acquired from as-deposited gate oxides and from completely processed capacitors. Fig. 8.4 shows the PL spectrum of sample C5 ($T_A = 1100^\circ\text{C}$), measured between the gate contacts of neighbored capacitors. In contrast to the PL spectra of thick annealed SiO_x films, it shows two emission bands, the one between 700 nm and 950 nm is attributed to Si NC. The other one, at about 1000 nm, is observed for high excitation power densities obtained by focussing the laser beam with a microscope objective. It is attributed to inter-band transitions in the Si substrate. High power densities result in a high density of electron-hole pairs in the substrate, which at these non-equilibrium conditions have a higher probability to radiatively recombine than in thermal equilibrium [177]. This interpretation is supported by the fact that the intensity of the 1000 nm band decreases drastically when the power density is decreased by a factor of ten while the tenfold collection time is used. The 1000 nm band is also observed for deposited stoichiometric SiO_2 gate stacks (Fig. 8.4b). The effect of annealing on the intensity of the 1000 nm band is the same for all samples C0-C7: While the as deposited sample shows a low intensity, a high intensity is observed for samples annealed at 800°C , which decreases for annealing at higher temperatures. The low intensity for the as deposited oxides could be caused by surface recombination due to non-passivated interface defects (all high temperature annealed samples were exposed also to a low temperature anneal in Ar/H_2). The other three spectra are from completely processed capacitors, treated identically, except of the high temperature anneal. Considering a change of interfacial stress during the high temperature anneal as a likely explanation, after the 800°C anneal the stress would be smallest. This is plausible, because an increasing structural relaxation of the oxide for higher annealing

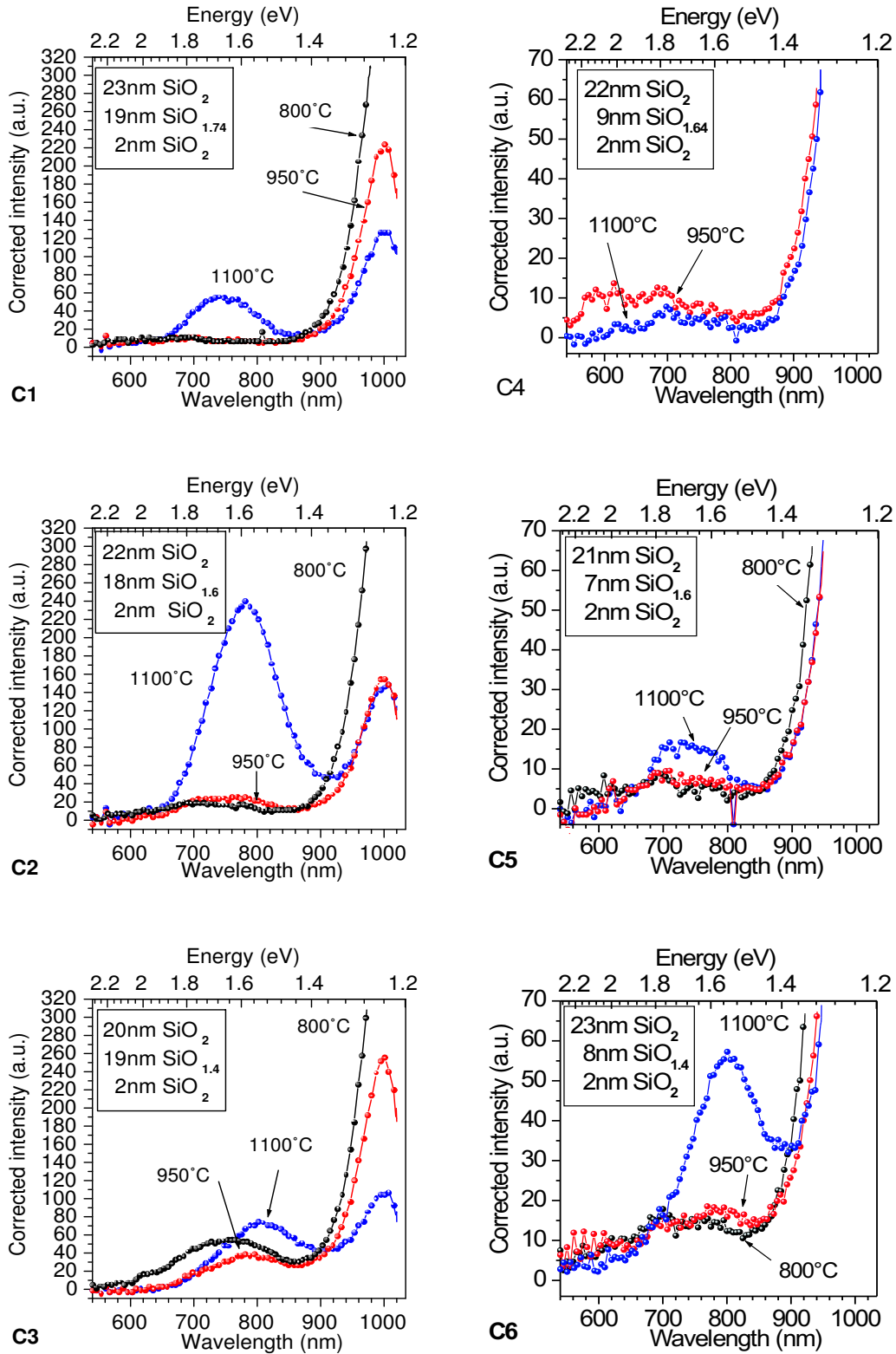


Figure 8.5: Survey of Si NC related photoluminescence under excitation at 532 nm, measured between the contacts of completely prepared MOS capacitors C1-C6 with 10 nm (left) or 20 nm (right) SiO_x film. The Si excess in the SiO_x layer increases from the top to the bottom. Shown are the difference spectra between the annealed and as-deposited samples, divided by the detector response. The annealing temperature T_A is indicated.

temperatures decreases the interfacial stress at the annealing temperature, but due to the different thermal expansion coefficients of the Si substrate and SiO₂³ also results in a higher stress at room temperature. A survey of PL spectra from all prepared gate stacks before and after the different anneals is shown in Fig. 8.5. For the higher annealing temperatures, the red PL band confirms the presence of Si NC and allows to estimate their size by comparison to experimental data, such as those summarized by Takeoka et al. [80], shown in Fig. 3.7 on p. 29. The Si NC diameters estimated from the PL peak wavelengths after are summarized in Tab. 8.1 on p. 104. They should be considered as upper limits, since a too high excitation power density may cause a broadening of the PL spectrum and an apparent red-shift of the peak energy [76]. According to the XTEM-results shown above, only in sample C3 crystalline Si NC are present, such that the observed Si NC PL is probably mainly due to amorphous Si NC. This is consistent with works of Nesbit [169], Rinnert et al. [86] and Kahlert [69], who assume that annealing a SiO_x phase with rather low Si excess initially results in amorphous Si NC that subsequently grow and eventually, but not necessarily crystallize. Crystallinity is not a requirement for an efficient PL from Si NC, instead, a theoretical work by Allan et al. [85], yielded that the radiative recombination rates of (not-hydrogenated) amorphous and crystalline Si NC are comparable for small clusters (1 nm), but for larger (2 nm) clusters, the rate is about 100 times higher for the amorphous phase due to disorder induced breaking of selection rules. According to this findings the crystallization of clusters would actually lower the PL intensity. When considering the sequence of samples C1, C2, C3, for which the initial Si excess increases, one observes a drastic increase in intensity between C1 and C2, but again a decrease for sample C3 containing the Si NC. While the first fact is in agreement with an increase in the density of amorphous Si NC, the second one has probably several origins: the density of Si NC decreases and additionally, both, the weaker confinement in larger Si NC and the partial crystallization of Si NC lower the probability of radiative recombinations. When comparing the corresponding MOS-capacitors with a ~ 20 nm/ ~ 9 nm SiO_x layer (C1/C4, C2/C5, C3/C6), one finds that the PL bands of the thinner films are systematically shifted to the blue, indicating on average smaller clusters. This suggests a relatively higher loss of Si in the thinner samples by either oxidation (residual humidity or oxygen in the RTA chamber), condensation of excess Si onto the SiO₂/substrate-interface, or by out-diffusion of gaseous SiO [178]. Consistent with this observation is that in contrast to the investigation of thick SiO_x samples (p. 80) with nominally the same composition (same deposition conditions), here the maximum PL-intensity is observed *always at the highest annealing temperature (1100 °C)* and attributed to an ongoing nucleation increasing the Si NC density. A common feature of both experiments is the red-shift of PL with increasing Si excess and increasing annealing temperature attributed to the increasing mean size of the Si NC (see p. 26). As shown below, for samples annealed at higher temperature, simultaneously the PL intensity and the density of trapping centers increases, which confirms that the Si NC act as trapping centers. But the electrical tests indicate the presence of amphoteric neutral traps of a large capture cross section even in those Si NC memory capacitors that do not show the characteristic Si-NC PL-emission (e.g. all samples annealed at 800 °C): a capacitive measurement of charge trapped in Si NC detects them more

³linear thermal expansion coefficient:

Si: $2.6 \cdot 10^{-6}$ /K, SiO₂: $0.5 \cdot 10^{-6}$ /K

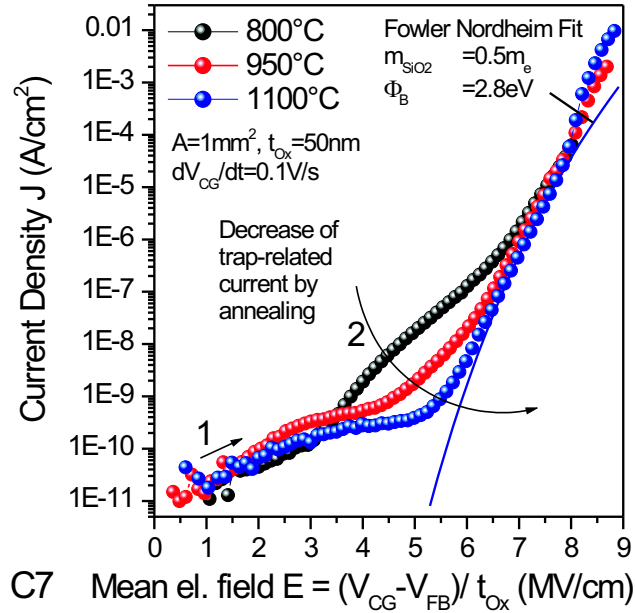


Figure 8.6: Current-voltage curves for the stoichiometric SiO₂ film (C7), annealed at 800 °C, 950 °C and 1100 °C. Arrow 1 indicates the sweep direction, arrow 2 shows the effect of increasing annealing temperature.

sensitively then a measurement of the Si NC PL intensity.

8.5 Current-Voltage (IV) Measurements

Reference oxide deposited in Ar/O₂ (C7) To characterize the current transport mechanisms, current-voltage (IV) measurements were performed using a Keithley 237 source measure unit. In addition the oxide thickness t_{Ox} was determined from the accumulation capacitance. Fig. 8.6 shows the effect of annealing temperature on the current-voltage characteristics of the reference oxide. In accumulation three regimes are found: a small leakage current at low field ($E_{Ox} \leq 3$ MV/cm), a region of higher leakage currents at medium-fields ($E_{Ox} \approx 3$ -5.5 MV/cm) decreasing strongly with rising annealing temperature, and a region of Fowler-Nordheim (FN) tunneling ($E_{Ox} \geq 5.5$ MV/cm). A FN-fit to the curve obtained for $T_A = 1100$ °C assuming a relative electron mass $m_{SiO_2}/m_e = 0.5$ results in a Si-SiO₂ barrier height $\Phi_B = 2.85$ eV. Most likely the leakage current in the mid-field region related to traps whose density can be more efficiently reduced by anneals at higher annealing temperature T_A . For the sample annealed at $T_A = 800$ °C, the currents in the mid-field region were measured for electron injection from the Al gate at temperatures T_M of 100 °C and 200 °C to stimulate the generation of minorities. If the measured current is displayed in a diagram of current density J [A/cm²] versus $1/E_{ox}$ [MV⁻¹cm] the data points are located on straight lines, which is consistent with a trap-assisted tunneling (TAT) mechanism described on p. 38. Assuming a single trap elastic TAT model as described by eqn. 3.43 [105], the trap energies Φ_T (with respect to the SiO₂ conduction band edge) for the two cases are found to be

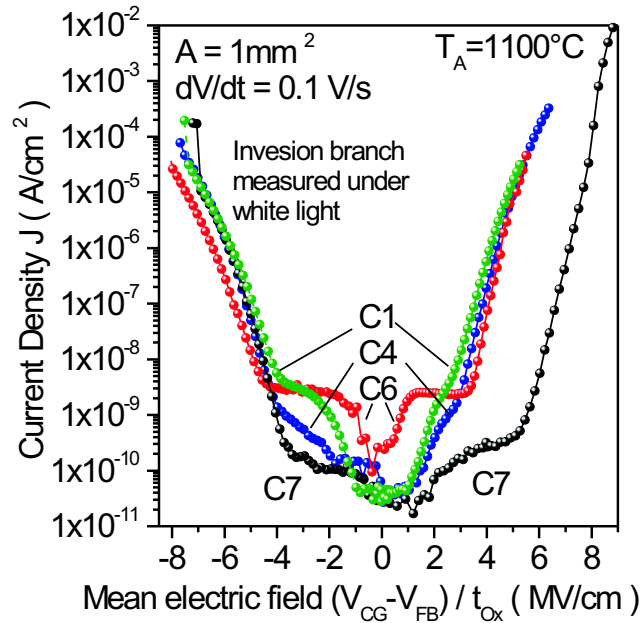
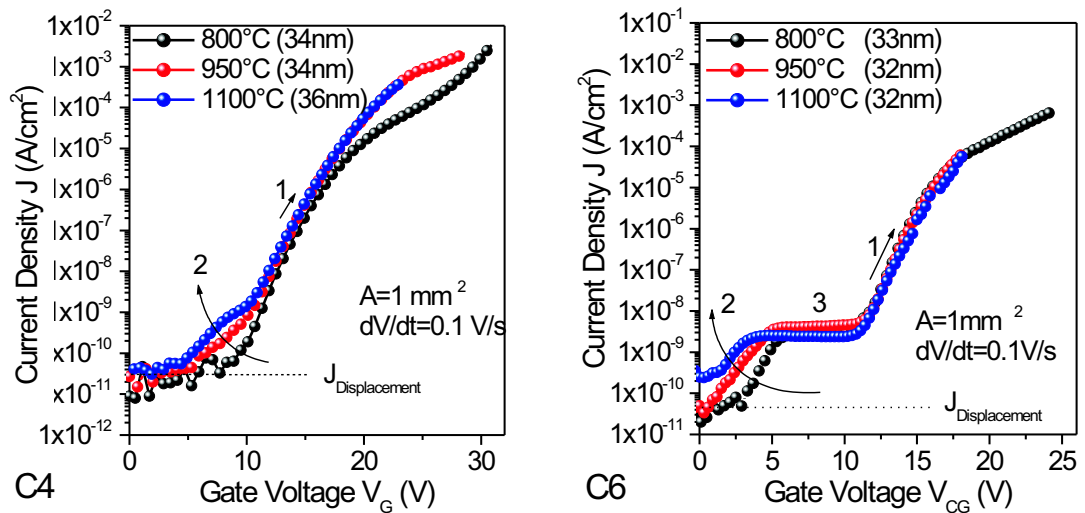


Figure 8.7: Current-voltage curves for reference sample C7 and the memory capacitors C1, C4, and C6



(a) Sample C4 (low Si NC density), annealed at 800 °C, 950 °C and 1100 °C. Arrow (1): Sweep direction. Arrow (2): Effect of decreasing Si NC spacing. The apparent capacitive oxide thickness is shown in brackets. (b) Sample C6 (high Si NC density), annealed at 800 °C, 950 °C and 1100 °C. Arrow (1): Sweep direction. Arrow (2): Effect of decreasing Si NC spacing. (3): Plateau region.

Figure 8.8: IV characteristics of memory capacitors vs. annealing regime.

1.65 eV and 1.5 eV. Because more complex TAT models (i.e. the inelastic TAT model proposed by Chang et al. [179]) might yield different trap energies, these values should be used with care.

Memory capacitors (C1-C6) For an annealing temperature of 1100°C the current-voltage behavior of selected samples (C1: 20 nm Si NC-film, Si excess 4.6 *vol%*, C4: 11 nm Si NC-film/Si excess 4.4 *vol%* and C6: 9 nm Si NC-film/Si excess 14 *vol%* and 48 nm SiO₂ reference sample C7) is shown in Fig. 8.7. The IV trace of the reference sample C7 is dominated by Fowler-Nordheim (FN) tunneling at high electric fields. The reference sample C7 and samples C1, C4 and C6 have only one common feature: the FN-injection of electrons from the gate electrode into the stoichiometric control-oxide layer at large negative field. For fields between -4 MV/cm and zero significant currents are observed for samples C1, C4 and C6. Because at low fields the control oxide blocks the currents to and from the gate electrode, the observed low field currents reflect an exchange of carriers between the substrate and traps in the former SiO_x film. This assumption is consistent with the fact that the current ceases if instead of a constant voltage ramp a single voltage stair is applied. In addition the injection of electrons at low positive field from the substrate into the former SiO_x film results in an increased local field across the control-oxide and shifts the onset of FN-tunneling towards lower fields. For the samples C4 and C6 the Figures 8.8a and b show the effect of Si excess and annealing temperature on the charging currents: The magnitude of charging current increases and its onset-field decreases with rising Si excess and higher annealing temperature, i.e. simultaneously with decreasing spacing between Si precipitates. Therefore the charging currents are considered in terms of multiple tunneling processes (MTP) between Si NC. For low Si excess and/or low annealing temperature the Si NC spacing is large such that MTP are highly unlikely. In this case only Si NC close to the Si/SiO₂ interface are charged at low fields. For higher Si excess and/or higher annealing temperature the Si NC spacing is smaller and charge is easily transferred from Si NC near the interface to those closer to the gate. A consequence of this is the plateau region(3) observed for sample C6 (Fig. 8.8b) and C5. The origin of this plateau region can be understood as follows: If the potential drop across the Si NC layer is small, the gate stack can be considered in terms of a two-capacitor model (Fig. 3.11, p. 3.11). The potential of the floating gate V_{FG} is then [180]:

$$V_{FG} = \frac{C_{COx}}{C_{TOx} + C_{COx}} \cdot V_{CG} + \frac{Q_{FG}}{C_{TOx} + C_{COx}} \quad (8.1)$$

In equilibrium the potential drop across the tunnel-oxide is zero, which implies $V_{FG} = 0$. Simple transformations yield an expression for the current into the floating gate I_{FG} :

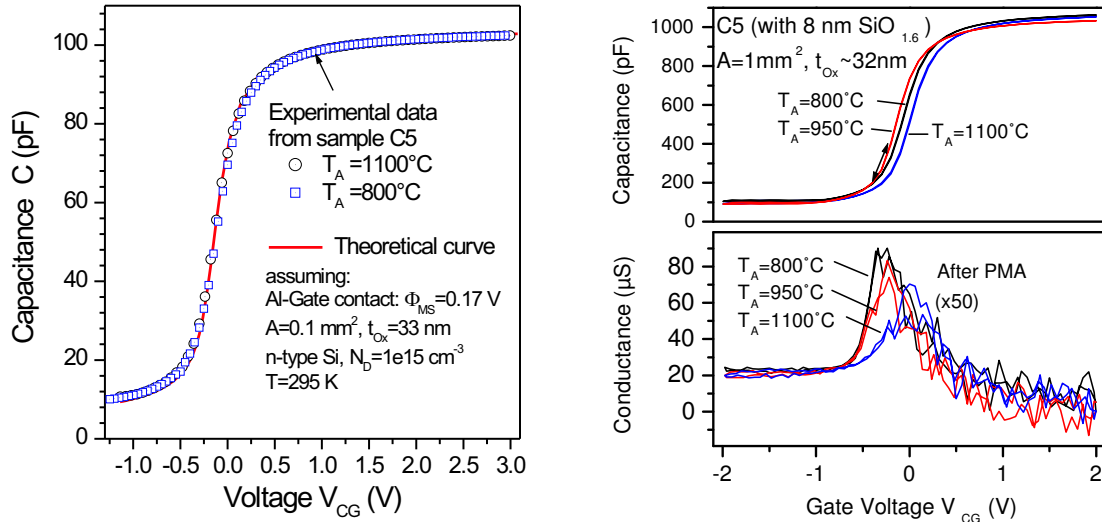
$$I_{FG} = \frac{dQ_{FG}}{dt} = -\frac{dV_{CG}}{dt} \cdot C_{COx} = -\frac{dV_{CG}}{dt} \cdot \frac{\epsilon_0 \epsilon_{Ox} \cdot A}{t_{COx}} \quad (8.2)$$

This means, if the injection is not limited by the time constants of tunneling through the tunnel oxide or the MTP in the Si NC layer, a constant voltage ramp applied to the gate results in a constant quasi-equilibrium charging current. The mean voltage ramp for the measurement of sample C6 was $dV/dt = 0.14$ V/s and the contact area $A = 0.01$ cm². With $\epsilon_0 = 8.85 \cdot 10^{-14}$ F/cm and $\epsilon_{Ox} \sim 3.9$ we find $I_{FG} = 2.4 \cdot 10^{-10}$ A translating

into a current density of $J_{FG} = 2.4 \cdot 10^{-8} \text{ A/cm}^2$. Experimentally a saturation current density of $J_{FG} = 2.5 \cdot 10^{-9} \text{ A/cm}^2$ is observed. The discrepancy is due to the fact that the Keithley 237 voltage source does not really use a constant voltage ramp. Instead the voltage is increased stepwise. Each increment is followed by a delay (200 ms), then four current values are acquired and averaged. Owing to this principle, the measured transient currents are smaller than those one would obtain for a constant voltage ramp.

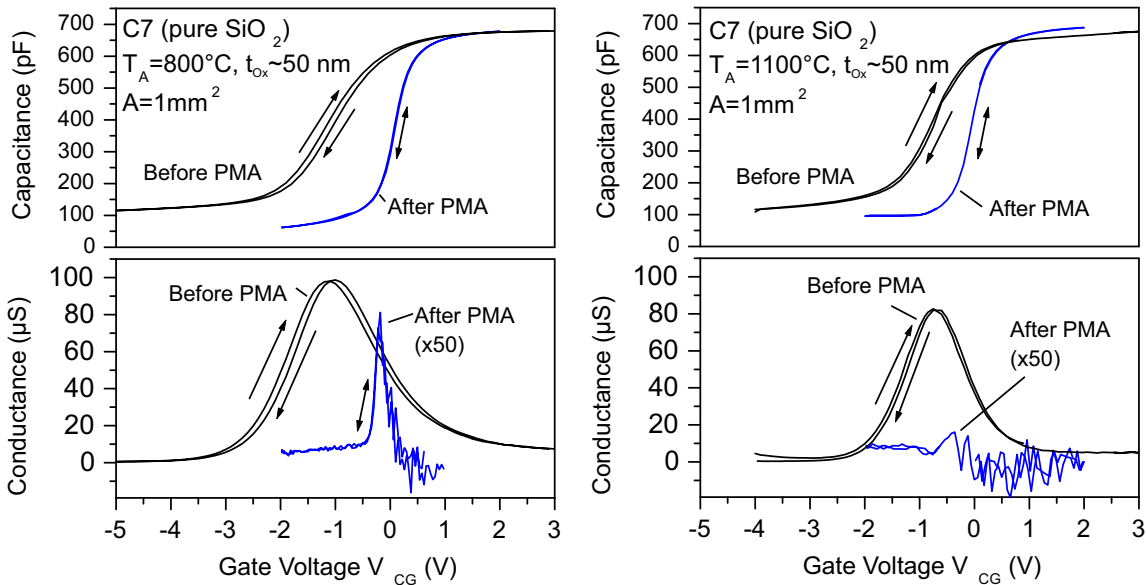
8.6 High-frequency capacitance-voltage (HFCV) measurements of uncharged capacitors

High frequency capacitance-voltage (HFCV) curves were acquired using a Keithley 590 CV-meter. Fig. 8.9a shows HFCV measurements of sample C5 after post-deposition anneals (PDA) at 800 °C and 1100 °C. The two curves match perfectly and coincide with a simulation whose parameters are given in the inset of Fig. 8.9a. For details on the calculations see [101]. The good fit confirms the high quality of the annealed oxide: both the density of interface states and the density of charges trapped in the bulk of the gate oxide are negligible. This also implies that in as prepared samples the Si NC are mainly uncharged. Fig. 8.9b shows the effect of PDA temperature T_A on the conductance measured for sample C5. The conductance peak systematically decreases with increasing T_A . Conductance peaks arise from Si/SiO₂ interface dipoles ([97] pp. 287), near interface traps (such as Si NC) responding to the 100 kHz modulation of the gate bias or from inhomogeneities of the surface potential. Recently Huang et al. [181] observed a conductance peak for MOS capacitors with Si NC embedded in the oxide in about 2 nm distance to the Si/SiO₂ interface. Since a corresponding peak was not observed for a reference sample without Si NC, the authors attributed it to a modulation of the Si NC charge state. To check whether this interpretation holds also for the samples prepared in this work the conductance peak was investigated as function of anneal and Si excess. Fig. 8.9c and Fig. 8.9d show the behavior of the SiO₂ reference sample C7 for $T_A = 800 \text{ °C}$ and $T_A = 1100 \text{ °C}$ respectively. Before the PMA in forming gas, both samples show a broad conductance peak and a stretched CV-curve indicating a high density of near-interface defects in the oxide, although the anneal at $T_A = 1100 \text{ °C}$ is slightly more efficient. This is because the formation of oxide defects is triggered by DUV-radiation occurring during sputter-deposition of the Al contacts. During the PMA most oxide defects react with the mobile hydrogen atoms formed at the Al gate and become electrically inactive. While a response from remaining interface defects is still observed for $T_A = 800 \text{ °C}$, no conductance peak is detected for $T_A = 1100 \text{ °C}$. Because both samples were exposed to the same PMA, the differences must be due to the different PDA temperatures, 800 °C and 1100 °C. A comparison of Fig. 8.9b and Fig. 8.9c shows that probably the low growth temperature of the tunnel-oxide gave rise to interfacial defects, that are annealed only at temperatures above the growth temperature of the oxide and are not efficiently saturated by protons. Hence below PDA temperatures of 1100 °C effects of Si NC and interface defects cannot be distinguished. However, sample C5 still shows a conductance peak after PDA at $T_A = 1100 \text{ °C}$ and PMA (Fig. 8.9b) whereas the stoichiometric reference sample C7 doesn't Fig. 8.9d. This is consistent with both of the following possibilities:



(a) Comparison of experimental and theoretical CV-curve for sample C5, $T_A = 1100\text{ }^\circ\text{C}$.

(b) Sample C5: after PMA, effect of T_A



(c) Effect of PMA on sample C7: $T_A = 800\text{ }^\circ\text{C}$

(d) Sample C7: $T_A = 1100\text{ }^\circ\text{C}$

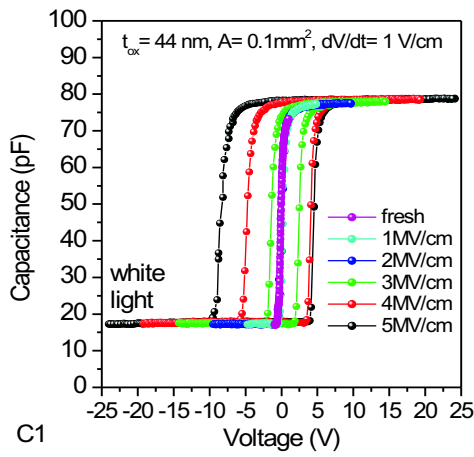
Figure 8.9: Reduction of interface state density of MOS (memory) capacitors by post-metallization anneal and comparison of theoretical and experimental HFCV curves.

- (a) The off-stoichiometric oxide layer getters hydrogen such that the passivation of near-interface oxide defects is less effective for C5 than for the reference sample C7.
 (b) As proposed by Huang the presence of the off-stoichiometric layer causes the formation of near-interface oxygen deficiency related defects (such as Si NC) that may exchange charge with the substrate at a time constant of 1/100 kHz.

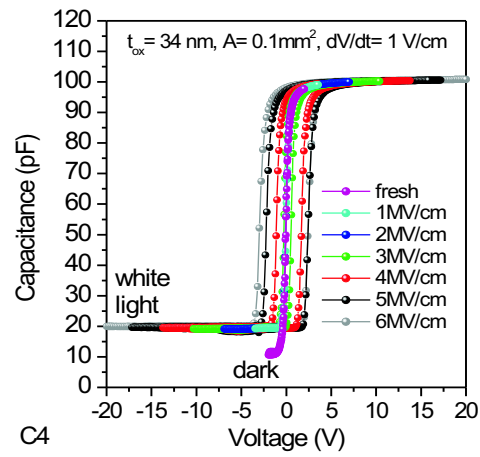
From the MOS capacitance in strong accumulation the effective oxide thickness (EOT) can be calculated according to $t_{Ox} = \epsilon_0 \epsilon_r / C_{Ox}$. Here ϵ_0 and $\epsilon_r \approx 3.9$ are the permittivity of vacuum and the relative permittivity of the oxide, C_{Ox} is the MOS capacitance per area in strong accumulation. The range of obtained thicknesses is listed in table 8.1 and consistent with ellipsometry results. The thickness variation of about 3 % across the roughly 4 cm x 4 cm sample area is caused by the inhomogeneous deposition rate.

8.7 Capacitance-voltage cycling test: The memory window of Si NC capacitors

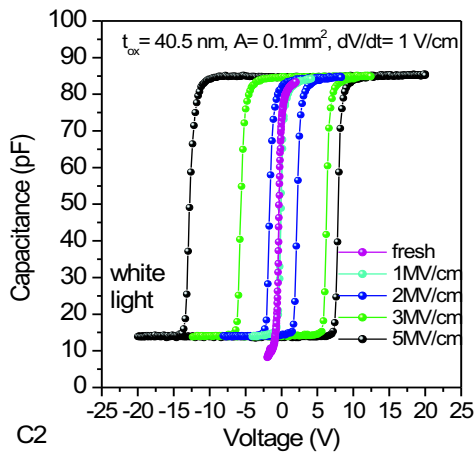
Slow capacitance-voltage cycling tests allow to estimate amount of trapped charge at a quasi-equilibrium condition from the shift of flat-band voltage. In order to check the effect of SiO_x composition and thickness on the obtainable memory window, for samples annealed at 1100 °C CV-measurements were performed repeatedly through widening voltage intervals (Fig. 8.10). Hereby white light illumination enabled the formation of minority carriers in the silicon substrate areas between the opaque Al contact pads. At inversion therefore generation-recombination currents result in an apparently increased capacitance. While no charging was observed for small sweep amplitudes, higher sweep amplitudes led to an increasing hysteresis in the CV-curves of samples C1-C6. Hereby the sign of flat band shift equaled the sign of gate voltage. Because the 20 nm thick top oxide layer blocks currents from and to the gate for fields below about 3 MV/cm, the hysteresis is due to charge exchange between the Si NC layer and the substrate or due to a shift of the charge centroid in the Si NC layer. For the corresponding samples C1/C4, C2/C5 and C3/C6 the total hysteresis increases with Si excess (higher density of Si NC) and the SiO_x layer thickness (Si NC throughout the SiO_x may be charged). The maximum positive flat-band voltage of the the high Si excess sample C6 is smaller than that of the moderate Si excess sample C5. The reason for this behavior will be discussed in the next paragraph. In Fig. 8.11 the flat-band voltages obtained for the different sweep amplitudes are summarized. The shifts of flat band voltage (up to 20 V) are very large compared with typical values for Si NC memories with a single layer of Si NC (<1 V). The reason lies in the high density of very small Si NC achieved by the used preparation method and the vertical stacking of Si NC. According to eqn. 3.35, a flat band shift of 1 V corresponds to a charge density in the Si NC layer of $5 \cdot 10^{11} \text{cm}^{-2}$ for samples C1 to C3 and $8 \cdot 10^{11} \text{cm}^{-2}$ for samples C4-C6. The sample C0, deposited like C1-C6 in Ar, but with zero power at the Si target, shows only a weak hysteresis. Moreover, the flat band shift and gate voltage have opposite sign. Evidently, in this case a different trapping mechanism (hole trapping) dominates. The reference sample C7 does not show significant charge trapping.



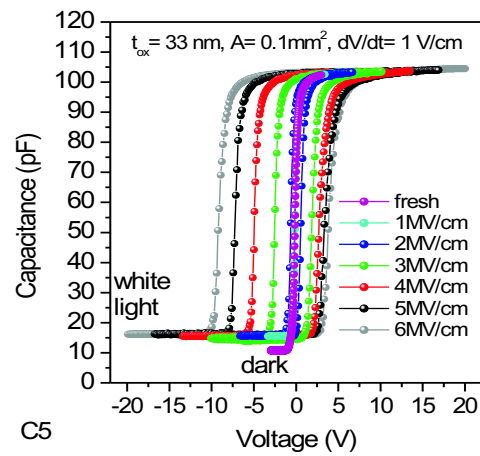
(a) Sample C1 (21 nm SiO_{1.8})



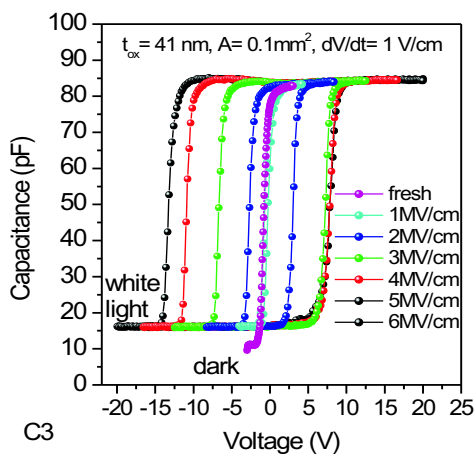
(b) Sample C4 (11 nm SiO_{1.8})



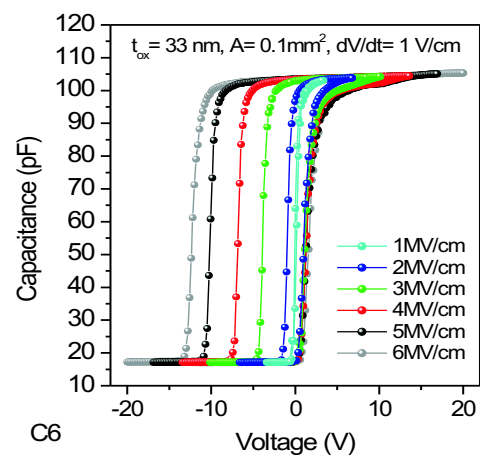
(c) Sample C2 (19 nm SiO_{1.6})



(d) Sample C5 (8 nm SiO_{1.6})

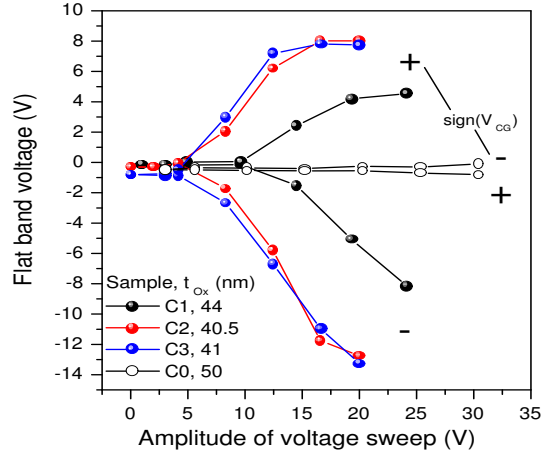


(e) Sample C3 (19 nm SiO_{1.4})

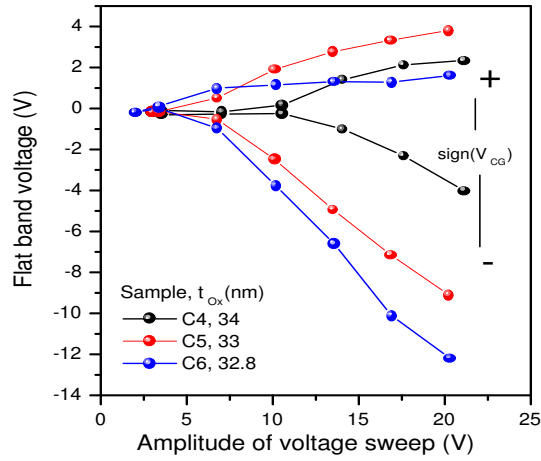


(f) Sample C6 (9 nm SiO_{1.4})

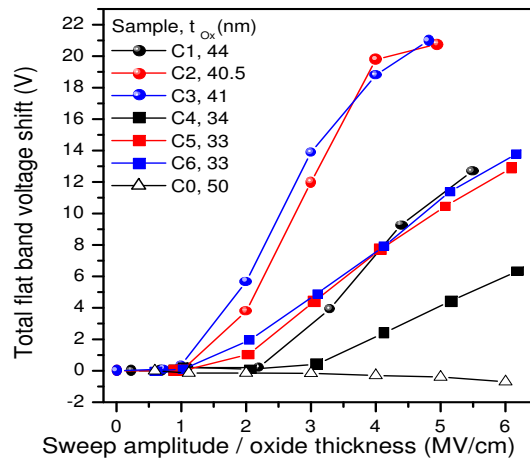
Figure 8.10: The Si NC memory capacitors C1-C6 annealed at 1100 °C: capacitance-voltage cycling tests.



(a) C1, C2 and C3 with thick (19 nm) SiO_x layer and reference C0.



(b) C4, C5 and C6 with thin (9 nm) SiO_x layer.



(c) Total flat band shift vs. average electric field for samples C0-C6.

Figure 8.11: The memory window of Si NC memory capacitors with 9 nm or 19 nm thick SiO_x film annealed at 1100 °C vs. amplitude of gate voltage sweep. + and - denote the sign of the applied gate voltage.

8.8 Current-voltage cycling test: Transient currents due to charging of Si NC

To investigate transient charging currents the HFCV cycling tests were complemented by current-voltage cycling tests. During slow sweeps of the gate voltage through an interval corresponding to a mean electric field of ± 4 MV/cm, current transients related to Si NC charging were measured. The area of the used capacitors was 1 mm^2 and the voltage ramp 0.1 V/s . During the measurements the sample was illuminated with white light. The Figs. 8.12 and 8.13 show measurements of samples C1-C3 and C4-C6 respectively for anneals at $800 \text{ }^\circ\text{C}$ and $1100 \text{ }^\circ\text{C}$. Capacitance-voltage traces measured on a neighbored dot using the same voltage ramp are plotted for reference. Starting the IV measurement with an uncharged sample, the voltage is swept towards positive values until a mean field of $+4 \text{ MV/cm}$ is reached. At this field according to the IV-measurements (Fig. 8.7) a Fowler-Nordheim current across the samples enables charging of the complete Si NC layer. Sweeps to -4 MV/cm and back to $+4 \text{ MV/cm}$ follow. Low currents on the initial branch confirm that displacement currents are negligible compared to the charging currents. In addition the onset of charging current shifts to lower voltages for higher Si excess in the SiO_x layer and higher annealing temperature.

Magnitude of charging current The area between the current-traces of forward and backward-scan is proportional to the injected charge. It is evident that the magnitude of charging currents increases with the Si excess. But, as clearly observed for the samples C1 and C4, it also increases with annealing temperature. The reason is that without annealing or after annealing at low temperatures the SiO_x film is dominated by oxygen deficiency related defects acting as rather shallow traps. In contrast, the formation of Si NC can be regarded as the formation of a deep trapping center, approximately homogeneously distributed throughout the SiO_x layer. These deep traps not only enable a more efficient trapping owing to their large capture cross section. By mechanisms like Poole conduction, Hopping-conduction or trap assisted tunneling (TAT) described on p. 39 they also cause a more efficient injection at low and moderate electric fields. In the limit of low Si NC density, before the onset of Fowler-Nordheim tunneling charge injection is restricted to near-interface Si NC. In contrast for a higher Si NC density multiple tunneling processes enable charging of precipitates within the complete Si NC layer. Since time constants of charge injection and vertical spreading depend in a complex manner on the depth distribution and spacing of Si NC the IV-traces have different shapes depending on Si excess and anneal.

Negative differential resistance region The HFCV-reference curves show that after trapping of carriers in the Si NC the accumulation/inversion transition of the n-type Si substrate coincides with a negative differential resistance (NDR) region in the IV-characteristics. NDR regions are a common feature of floating gate memory devices and were reported also for Si NC based memories [182, 183, 184]. For example consider Fig. 8.13b. Let the substrate be strongly inverted while holes are being stored in the Si NC. When the gate voltage rises, the sample equilibrates and holes gradually

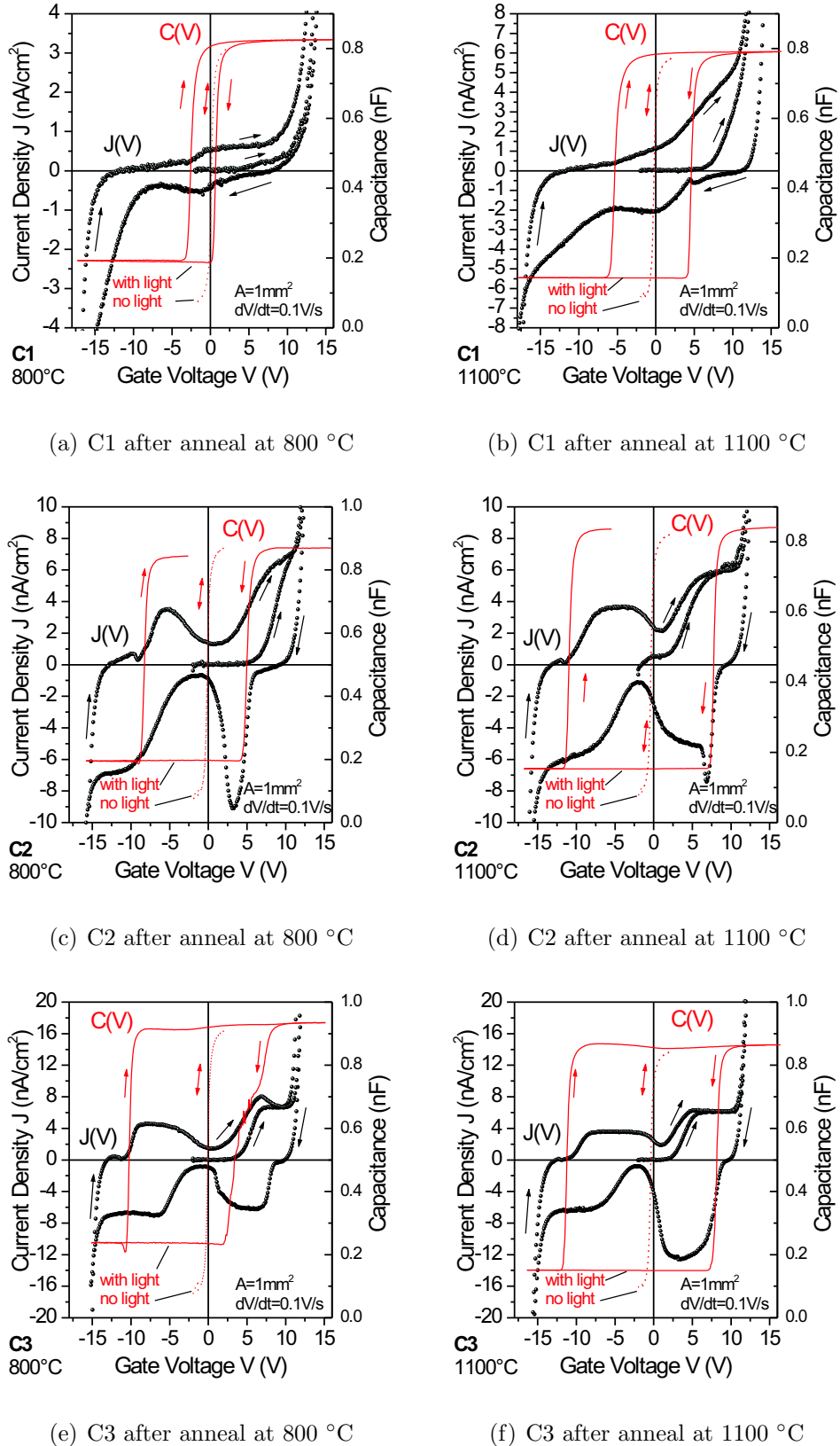


Figure 8.12: Current-voltage cycling tests using memory capacitors with 20 nm SiO_x layer. The gate voltage is swept through ± 13.5 V (± 4 MV/cm). Current transients indicate Si NC charging. Negative differential resistance regions occur at flat bands since for sweeps from negative to positive gate voltages at this point an electron current adds to the discharge currents of holes and enables a sudden partial recombination (vice versa for the other sweep direction).

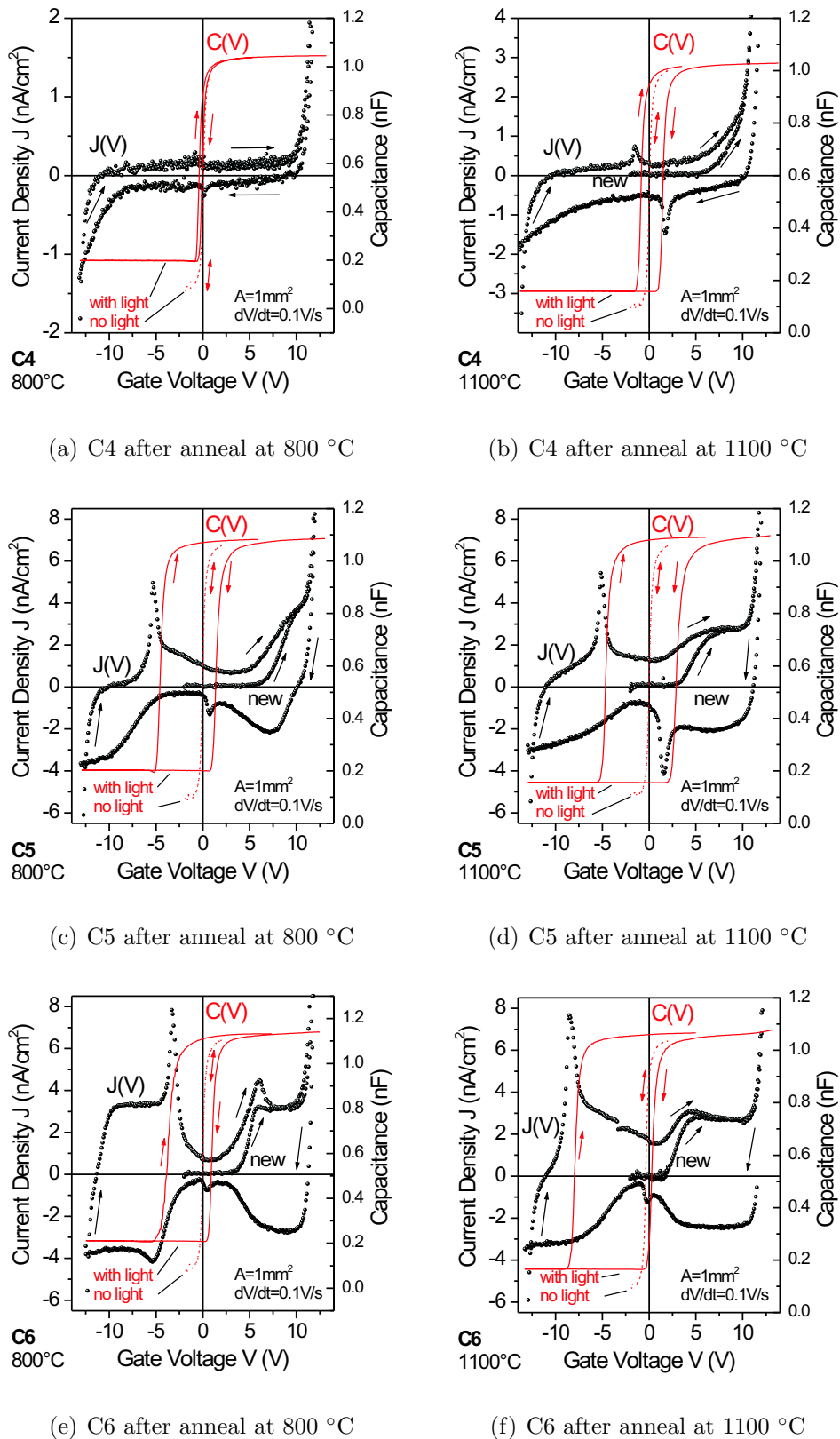


Figure 8.13: Current-voltage cycling tests using memory capacitors with 10 nm SiO_x layer. The gate voltage is swept through ± 13.5 V (± 4 MV/cm). Current transients indicate Si NC charging. Negative differential resistance regions occur at flat bands since for sweeps from negative to positive gate voltages at this point an electron current adds to the discharge currents of holes and enables a sudden partial recombination (vice versa for the other sweep direction).

tunnel back into the inversion layer. The equilibrium charge of Si NC depends on the concentration of holes in the inversion layer, which particularly at weak inversion changes in a strongly non-linear fashion with gate voltage. The sudden change of substrate charge density near flat bands enables a momentarily higher discharge current to flow and leads to the NDR region. With a similar argument also the NDR region in the backward scan is understood. In Fig. 8.13e and f two additional NDR regions are observed, apparently at the beginning of carrier injection from the substrate or the gate respectively. These peaks reflect the recombination of residual trapped charge with injected carriers of opposite sign. In the considered cases of Fig. 8.13e and 8.13f the high carrier mobility within the Si NC layer causes the recombination processes to occur instantaneously for the whole layer. In samples with lower Si NC density recombination occurs gradually, first for the Si NC closest to the injecting electrode and later for the more distant ones such that no NDR region occurs.

Effect of high Si excess: formation of agglomerates According to the HFCV cycling of sample C6 (Fig. 8.10) a sweep through large positive voltages leads to only a small positive shift of flat-band voltage. This would be consistent with an inefficient injection. But the large current transients observed in Fig. 8.13e and 8.13f confirm that electrons are efficiently injected. Although a high density of charge tunnels into the Si NC layer, most of it is lost again to the substrate before the steep region of the HFCV curve is reached, which indicates the transition from accumulation to depletion. Apparently the high Si excess resulted in a very small spacing of Si NC, such that the injected charge has a high mobility within the Si NC layer. Monte-Carlo-Simulations of Si NC ripening by Müller et al. [170] showed that the 'percolation limit' (i.e. the Si excess concentration above which instead of isolated Si NC, Si agglomerates or wires are formed) lies roughly between 10 vol% and 25 vol% depending on annealing time and temperature. With about 14 vol% the Si excess sample C6 is falls in that range, whereas with about 9 vol% sample C5 doesn't. Provided Si agglomerates were present in sample C6, carriers in the Si NC layer would have a much higher mobility, because the conduction along agglomerates is fast, whereas multiple tunnel from Si NC to Si NC is slow. The fact, that the electron mobility in silicon is much higher than the mobility of holes, could explain the asymmetry of the CV characteristics: Electrons rapidly move across the agglomerates towards the tunnel-oxide and tunnel back to the substrates, while holes move much slower.

8.9 Retention tests

8.9.1 Basics of charge retention test

Conventional non-volatile memories: Dominant loss by thermionic emission The retention measurement probes the loss of charge trapped in the memory node of the capacitor with time. If the depopulation of trapping centers involves only optically or thermally stimulated activation of carriers, it can be described using an extension of the Shockley-Read-Hall model as discussed by Barbottin [185]. This approximation is appropriate for conventional non-volatile memories with a floating gate layer surrounded by at least 7 nm pure SiO₂. When the gate voltage is zero, and the charge density on the floating gate is not too high, the tunneling currents from the floating gate to the gate electrode or substrate are negligible. Charge leakage is then governed by activation of trapped carriers into the conduction or valence band of the oxide, and their subsequent drift (in the field of the remaining charge) towards gate or substrate. If additional assumptions are made, the detrapping kinetics can be described in a particularly simple fashion. The assumptions are:

1. Only one type of carriers (in the following: electrons) is considered. The contribution of hole trapping and detrapping is negligible.
2. The only free electrons in the dielectric are those released optically or electrically by the traps (during the study of detrapping no injection from the electrodes takes place).
3. The traps can only exchange electrons with the conduction band, which has a sufficiently high number of empty states, such that the emission probability is not limited.
4. The density of free electrons in the oxide, n , is zero at the onset of depopulation.
5. Within the considered time interval the density of traps (N_T) and trapped charge (n_T) is large compared to the density of free carriers n : re-trapping is therefore unlikely and neglected. This leads to the following equation:

$$\frac{dn}{dt} = -\frac{dn_T}{dt} = (e_n^t + e_n^o)n_T \quad (8.3)$$

Here e_n^o and e_n^t [s⁻¹] are the emission coefficients due to optical and thermal stimulation respectively. The equation states that the loss rate is linear proportional to the number of trapped carriers. Hence, the density of trapped carriers n_T and the trapped oxide charge per area Q_{ot} decay exponentially according to:

$$n_T(t) = n_T(t=0) \cdot \exp(t/\tau_e) \quad Q_{ot}(t) = Q_{ot}(t=0) \cdot \exp(t/\tau_e) \quad (8.4)$$

$\tau_e = (e_n^t + e_n^o)^{-1}$ is called emission time constant. If initially all traps were filled with one charge then the magnitude of stored charge is related with the total density of traps $N_T(X)$ [cm⁻³] in the oxide at distance X from the top electrode according to:

$$Q_{ot}(t=0) = q \int_0^{t_{ox}} N_T(X) dX \quad (8.5)$$

Here t_{ox} is the oxide thickness. *The simple time dependence allows extrapolation of long time charge retention behavior from the measurement of charge loss in rather short time intervals.* If leakage is only due to thermionic emission, rapid retention measurements

are more accurately done at high temperatures, where it is possible to employ the exponential temperature dependence of the thermal emission coefficient, which is for an electron trap:

$$e_n^t = \sigma_n v_{th} N_C \exp\left(-\frac{E_n}{kT}\right) \quad (8.6)$$

Here σ_n is the capture cross section for electrons, v_{th} the thermal velocity of electrons, N_C the density of states in the conduction band, and E_n is the ionization energy of the electron trap (with respect to the bottom of the conduction band). *From retention measurements at different temperatures the trap ionization energy can be found. If the ionization energy is known, from an 'accelerated' retention measurement at high temperature one can calculate the retention behavior at typical operational conditions.*

Si NC memory: Dominant loss by direct tunneling The above model considered only thermal and optical detrapping of carriers into the SiO₂ conduction band. In general, both, thermionic and tunneling emission determine the retention behavior. In a Si NC memory the retention mechanism differs strongly from the one of conventional non-volatile memories with polycrystalline (poly) Si floating gate. The much thinner tunnel oxide between Si NC region and substrate ($\sim 1-4$ nm) renders direct tunneling to the substrate the dominant loss mechanism. Thermal detrapping is inefficient for charge storage in both poly Si and Si NC. According to DiMaria [12] the Si NC behave as deep traps with large activation energies of ≈ 3 eV (for activation from Si NC conduction band to SiO₂ conduction band) and ≈ 4 eV (for activation from Si NC valence band to SiO₂ conduction band). The higher activation energies also distinguish the Si NC memory from novel FLASHTM memories using floating gates based on silicon nitride with much smaller trap activation energies of 0.82 eV, 0.93 eV, 1.09 eV and 1.73 eV [14]. Tunneling between laterally or vertically neighbored Si NC has a strong effect on the retention behavior. Thus, the spacing of Si NC, which determines the tunneling distance and the tunneling resistance is an important parameter. According to Ohba et al. [186] multiple (vertically stacked) Si NC, as obtained from SiO_x layers thicker than ≈ 5 nm yield better charge retention, than a single Si NC layer.

The charge loss by direct tunneling also has consequences on the relation between stored charge and storage time. In the following it will be shown that *in contrast to depopulation by thermal or optical stimulation, the charge loss rate by the direct tunneling is not simply proportional to the total trapped charge. This implies that the dynamics of trap depopulation cannot be described by a simple exponential decay, which rules out a simple extrapolation from short-time to long time retention behavior*⁴:

The driving force for loss by direct tunneling is the electric field across the tunnel oxide, i.e. the potential difference between substrate and Si NC floating gate. When the Si NC are distributed homogeneously and the resistance between them is small compared to the resistance of the tunnel-oxide, the potential drop across the Si NC layer is small and can be neglected⁵. If the substrate is in accumulation (substrate surface potential is nil), the capacitor can be modelled according to Fig. 3.11, p. 36. The potential of

⁴For a detailed discussion on numerical modelling of Si NC memory devices see De Salvo[180]. For a quantum mechanical model of the erase time of a single Si NC memory see Hinds [30].

⁵Otherwise the potential drop across the depletion layer must be taken into consideration

the floating gate is then given by:

$$V_{FG} = \frac{C_{COx}}{C_{TOx} + C_{COx}} \cdot V_{CG} + \frac{Q_{FG}}{C_{TOx} + C_{COx}} \quad (8.7)$$

Here V_{FG} and V_{CG} are the voltages at Si NC floating gate and control gate with respect to the substrate, Q_{FG} is the charge per area in the Si NC layer and C_{TOx} and C_{COx} are the capacitances between Si NC layer and substrate or gate electrode respectively (Fig. 3.11). When $V_{CG} = 0$, $V_{FG} \propto Q_{FG}$: the potential of the Si NC floating gate is proportional to the stored charge. Assuming further that the cap-oxide is much thicker than the tunnel-oxide, at $V_{CG} = 0$ one can neglect tunneling currents between Si NC layer and gate electrode. The rate of the charge loss is therefore given by the electronic direct tunneling current from Si NC layer to the substrate (electron injection from substrate into Si NC is negligible):

$$\frac{dQ_{FG}}{dt} = J_{FG,sub} \quad (8.8)$$

Adapting the analysis by De Salvo et al. (see [180]) $J_{FG,sub}$ is given by:

$$J_{FG,sub} = \frac{4\pi q^3 m_{Si}(kT)^2}{h^3} \cdot \exp\left(\frac{E_{F,dot}(V_{FG})}{kT}\right) \cdot \Theta_{dot,sub}(kT, V_{FG}) \quad (8.9)$$

$\Theta_{dot,sub}$ is the transparency of the tunneling barrier, given in the Wentzel-Kramer-Brillouin (WKB) approximation by:

$$\Theta_{dot,sub}(kT, V_{FG}) = \quad (8.10)$$

$$\exp\left(\frac{4(2qm_{ox})^{1/2}}{3\hbar} \cdot \frac{t_{TOx}[(\Phi_B - kT)^{3/2} - H(\Phi_B - V_{FB} - kT) \cdot (\Phi_B - V_{FB} - kT)^{3/2}]}{V_{FG}}\right) \quad (8.11)$$

m_{Si} and m_{ox} are the effective electron masses in the Si NC and SiO₂, kT is the thermal energy, $E_{F,dot}$ the Fermi-level of the Si NC, Φ_B the height of the barrier between the Si and SiO₂ conduction bands, $\hbar = \frac{h}{2\pi}$ is Planck's constant and H is the Heavyside function. Together with eqn.8.7 this yields a transcendent differential equation of first order in V_{FG} which can be solved only numerically:

$$\frac{dV_{FG}(t)}{dt} = (C_{TOx} + C_{COx}) \cdot J_{FG,sub}(V_{FG}) \quad (8.12)$$

This analysis shows that an extrapolation of long-term retention behavior is not straightforward for the case of less than 4.5 nm wide tunnel-oxides.

8.9.2 Ways to test charge retention in MOS memory capacitors

For MOS-transistors, the retention behavior is usually studied by monitoring the source-drain current. The manufacturing of transistor structures was beyond the scope of this work, so the investigations are restricted to MOS capacitors. There are several ways to test charge retention of MOS-capacitors:

Repeated measurement of CV-curves Periodically a CV curve is measured from which the current flat-band voltage is determined. This method is problematic for Si NC memories with direct tunnel injection, since the CV-measurement itself may alter the charge state of the device if the measured voltage interval is too large.

Constant voltage mode (CVM) An improved approach is the continuous measurement of the capacitance at a fixed reference voltage and the subsequent interpolation of the flat-band shift under the assumption that charging of Si NC basically causes the CV-curve to shift along the voltage axis. This method requires the measurement of the CV-characteristics of an uncharged sample and can only be applied, if the flat band shift is small, since an accurate interpolation of $V_{CG}(C)$ is only possible for capacitance values on the steep section of the CV-curve. It is impossible, if at the reference potential the sample is in inversion or strong accumulation, where C is independent of V_{CG} .

Constant capacitance mode (CCM) From a CV-curve of an uncharged sample the substrate doping and the effective oxide thickness are determined. Using these values the flat band capacitance is calculated (eqn.3.33). Now the initial flat-band voltage is interpolated from the measured CV-curve. A write pulse is applied to the gate and shifts the CV-curve along the voltage axis (eqn. 3.35). Next, at the initial flat-band voltage, the capacitance is measured. From the difference between the measured capacitance and the flat-band capacitance the shift of the CV-curve ΔV_{FB} is interpolated. V_{CG} is increased by ΔV_{FB} , such that the next measured capacitance again roughly equals C_{FB} . This procedure is repeated by a feedback-loop (Fig. 8.14). Thus that at each time t from $\Delta V_{FB}(t) = V_{CG}(C_{FB},t) - V_{CG}(C_{FB},t = 0)$ the stored effective charge can be calculated using eqn. 3.35. This mode was reported by Shi et al. [187] and implemented in a home-made software. The retention time of a Si NC memory depends sensitively on the quiescent gate voltage V_{CG} . The longest retention times are obtained if the substrate is depleted or close to flat-bands [30, 184]. In CCM by variation of the gate voltage the feedback keeps the sample constantly at flat bands ($V_{FG} \sim 0$) and the electric field across the tunnel oxide close to zero, which leads to very small direct-tunneling leakage current. Therefore one may have concerns that a measurement in CCM corresponds to an unrealistic *best case* scenario. In a real memory transistor, after the write pulse the control gate voltage would be tied to ground via a high resistor, which, compared to the CCM, results in a higher electric field across the tunnel-oxide and higher tunneling leakage currents. A retention measurement, adapting these more realistic conditions has been implemented as described below.

Intermittent constant capacitance mode (ICCM) In this mode the feedback loop (Fig. 8.14) is enabled only intermittently (about 3 times per time decade) for roughly 5 s to determine V_{FB} . Between the measurements V_{CG} is set to zero. When the bias is switched on again, the first gate voltage used is the previous flat-band voltage. Therefore the range of applied bias voltages does never exceed the interval between the previous and the current V_{FB} value and the perturbation of the retention behavior by the measurement is negligible. *The ICCM developed in the course of this work is*

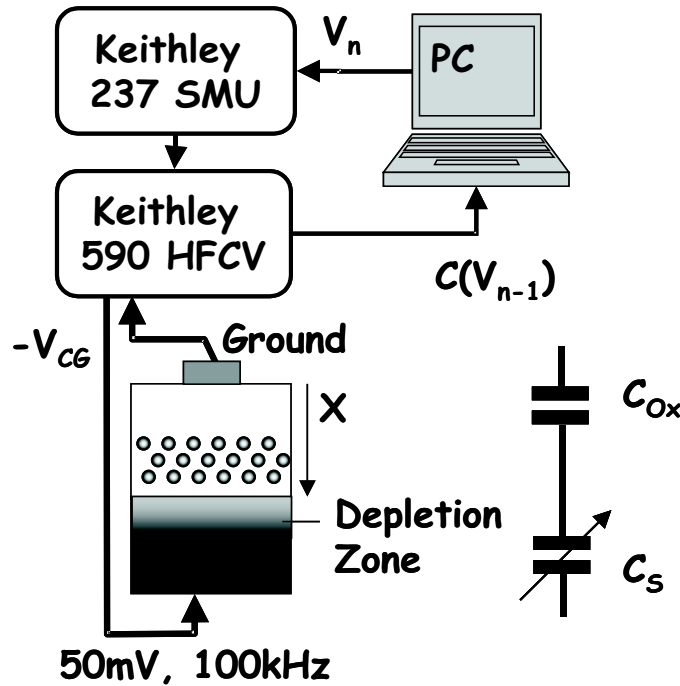


Figure 8.14: Sensing of the flat-band voltage shift (i.e. the stored charge) by the constant capacitance mode (CCM) or interrupted constant capacitance mode (ICCM). In both methods a feedback loop adjusts the control gate voltage such that the measured capacitance equals the flat-band capacitance. In CCM the feedback operates continuously and keeps the sample at the flat band condition. In ICCM the feedback loop is switched on intermittently, while $V_{CG} = 0$ for the remaining time.

therefore regarded as a simple and favorable way to determine the realistic retention behavior of MOS memory-capacitors or transistors ⁶.

8.9.3 Retention measurements

Short-term retention behavior ($t < 1000$ s) Figure 8.15 shows the short term retention behavior of sample C7 ⁷ and samples C4, C5 and C6 ⁸, after anneals at different temperatures. Initially, a positive voltage pulse (C4, C5, C6: +11.5 V, 10 s / C7: +25 V, 10 s) is applied at the gate contact and results in electron injection from the substrate. The trapped charge is sensed by a CCM-measurement. Despite higher write pulses, the pure oxide sample C7 shows only slight hole trapping attributed to oxygen-vacancy defects ($\Delta V_{FB} < 0$), whereas in samples containing Si NC, electron trapping dominates ($\Delta V_{FB} > 0$). The initial density of trapped charge increases with annealing temperature for the samples with low (C4) and intermediate Si excess (C5), whereas the samples with highest Si excess (C6) again shows a smaller positive flat band shift,

⁶I hereby acknowledge helpful discussions with V. Beyer (FZ-Rossendorf) during the development of the ICCM and the implementation into the home made Testpoint-based probing software.

⁷50 nm pure SiO_2

⁸total thickness: ~ 33 nm, ~ 9 nm Si NC layer with varied Si excess

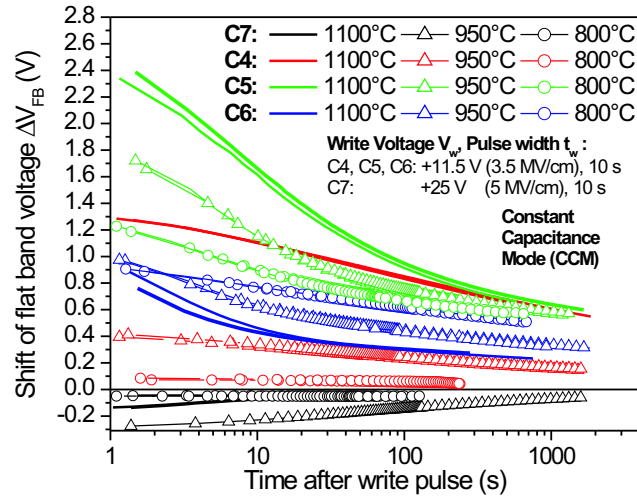


Figure 8.15: Test of charge retention at room temperature in constant-capacity mode for samples C4-C7 and the three annealing temperatures T_A .

as observed already in Fig. 8.11b. A possible explanation, corroborated by the results of PL measurements, is that the density of Si NC increases with annealing temperature for all samples C4, C5 and C6 since nucleation is the dominant process for all anneals. The decreasing spacing of Si NC enhances the tunneling processes between them. The vertical transport within the Si NC layer becomes more efficient. In addition, a higher mean diameter of Si NC also results in a lower Coulomb barrier, such that in the bigger Si NC a higher number of electrons are stored. The smaller initial ΔV_{FB} of sample C6 is in this context explained by the higher charge loss within the 2 seconds between charging and the establishment of the feedback loop.

Effect of measurement temperature on long-term retention behavior ($t > 10^4$ s)

As discussed above, a strong temperature dependence is not expected, since the charge loss by direct tunneling dominates over the thermionic emission. Hinds et al. [30] found for a memory operating with a single Si NC a $1/T^2$ temperature dependence of erase time, consistent with the temperature of the density of states in the channel to tunnel into ($T^{3/2}$) times the thermal velocity of the stored electron ($T^{1/2}$). In the present samples, most of the Si NC exchange charge with the substrate not by a single direct tunneling event, but instead by tunneling across multiple Si NC. Therefore contributions from thermally assisted tunneling processes cannot be excluded. Fig. 8.16a and b show the retention behavior of sample C5 for annealing temperatures T_A of 800 °C and 1100 °C. The measurements were done using ICCM and a variety of write conditions and measurement temperatures. Despite charge injection by direct tunneling, the samples show clearly a quasi-non-volatile behavior, i.e. a measured finite memory window after times of up to 10^{+5} s (about 1 day). This is comparable to what has been reported by Tiwari [100] for a Si NC memory with a tunnel oxide thickness of about 1.8 nm. However, in the present work, owing to the vertically stacked Si NC, the

memory window is much wider. At first glance there is no strong impact of measurement temperature for both samples. Instead, the writing conditions have the strongest impact on the initial charge loss rate. This is expected since the potential drop across the tunneling oxide, determined by the magnitude and depth distribution of stored charge, determines the leakage current. The measurements at room temperature are consistent with those of Fig. 8.15 done using CCM. So a moderate quiescent bias does not dominate the retention in the present case. All measurements of sample C5 show two stages: a rapid initial lowering of ΔV_{FB} and following slower process dominating the long time retention behavior. In sample C4, with a significantly lower density of Si NC, the turnover to the slow process is observed almost two time decades later, after several hours. Although the higher Si NC density of sample C5 leads to an initially higher absolute value of ΔV_{FB} , the charge is initially lost faster than for C4, such that after about 1h the remainder is of the same magnitude. Assuming that the charge is stored in centers of the same type, this indirectly rules out a dominant loss by of thermionic emission. Instead, it is an indication that the higher density of Si NC and the larger Si NC diameter in sample C5 lowers the average tunneling resistance between the Si NC. Then, the rapid initial lowering of ΔV_{FB} can be explained by several effects: (I) When the write voltage is switched off, an equilibrium distribution of charge establishes in the direction normal to the SiO_x layer. This might take less time for smaller Si NC spacing. Part of the change of ΔV_{FB} could be due to a shifting charge centroid. However, the initial decrease of ΔV_{FB} is too large for charge redistribution being the main factor. (II) Initially groups of Si NC, having access to a low resistance current path to the substrate (e.g. a line of closely neighbored Si NC) will leak the charge by multiple tunneling processes, delocalized charge on large Si agglomerates leaks by a single tunneling event. Si NC that are well isolated from those current paths will hold the charge considerably longer. (III) Large Si NC storing multiple charges lose them rapidly driven by electrostatic repulsion. The last charge in a single Si NC "feels" interacts only with charges in distant Si NC and is therefore on an energetically lower, more stable level.

The interpretation in terms of Si NC density is supported by the fact that samples with higher Si excess (C5) annealed at only 800 °C (Fig. 8.16c) behave similar to samples with low Si excess (C4) annealed at the higher temperature of 1100 °C.

8.10 Effect of height and duration of write/erase pulses

For gate voltages corresponding to an average electric field of 5 MV/cm the dependence of the flat-band voltage shift (memory-window) on the duration of the write pulse is shown in Fig. 8.17. The flat-band voltages were determined in the erased states (V_{FB-}) and in the written states (V_{FB+}). The memory window was then calculated as $\Delta V_{FB+} = V_{FB+} - V_{FB-}$. A strong dependence of ΔV_{FB+} on the write time is observed in the limit of a small Si excess (Fig. 8.17a and b). For the samples C1 and C4 with the lowest Si excess the anneal at 1100 °C yields a higher memory window than the anneal at 800 °C. For annealing at 800 °C also a higher Si excess leads to a higher memory window. This is consistent with the fact that the Si NC nucleation barrier decreases with Si excess. Consistently a wider Si NC layer in the gate oxide leads to a wider

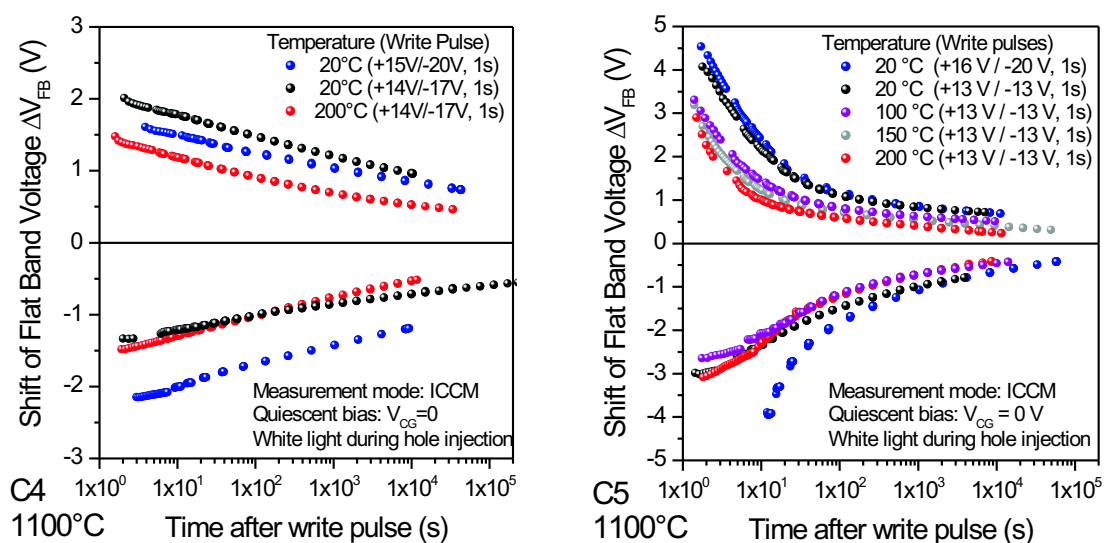
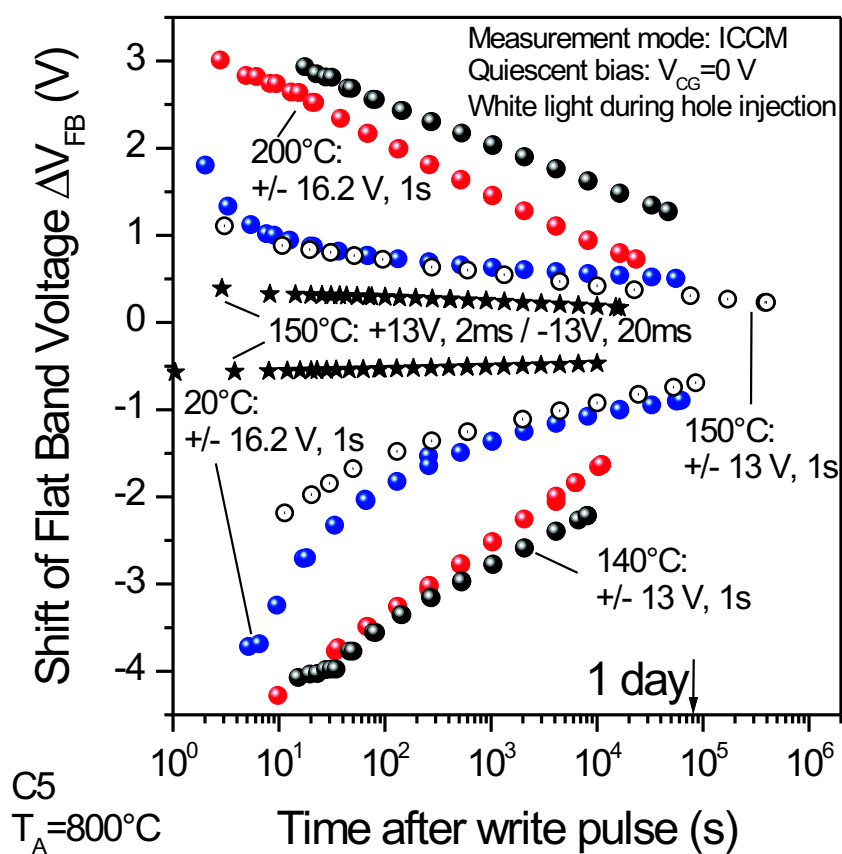
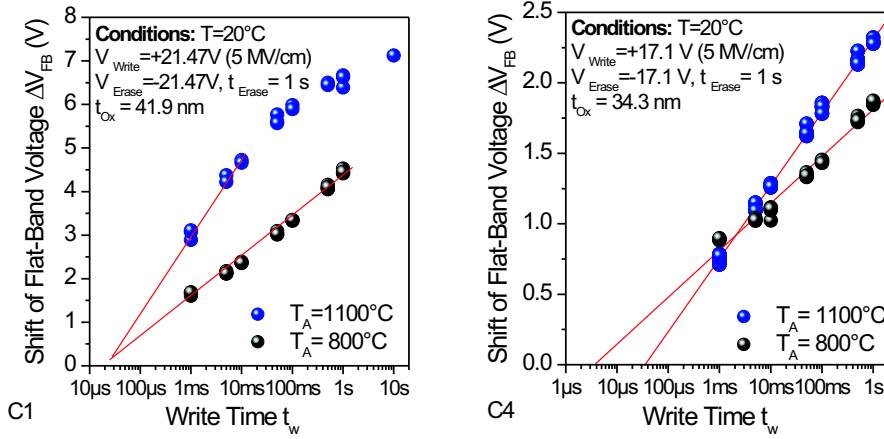
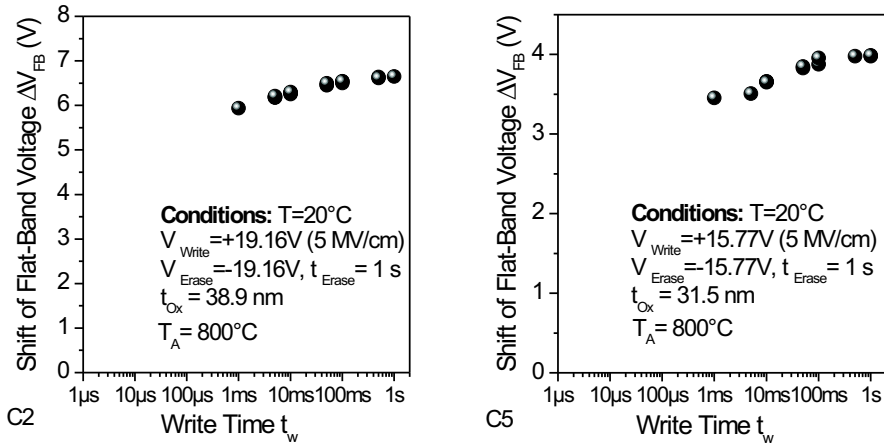
(a) C4 ($T_A = 1100^\circ\text{C}$)(b) C5 ($T_A = 1100^\circ\text{C}$)(c) C5 ($T_A = 800^\circ\text{C}$)

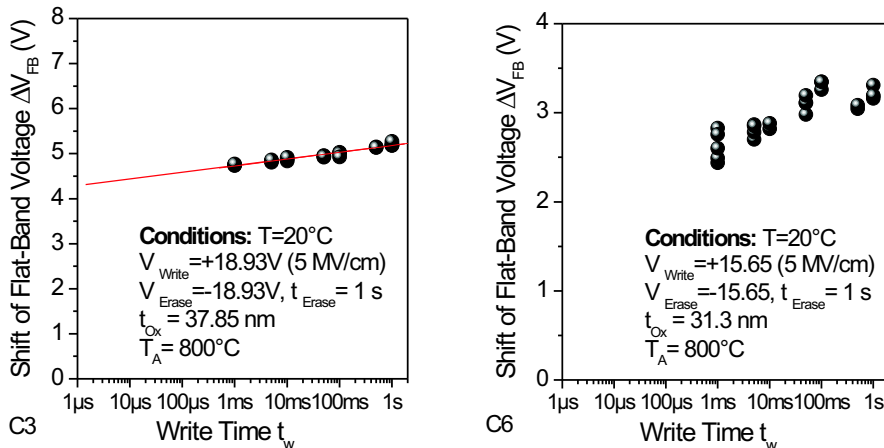
Figure 8.16: Retention tests in intermittent constant capacity mode (ICCM). The write conditions and measurement temperature are indicated in the graphs.



(a) Sample C1 annealed at 800 °C and (b) Sample C4 annealed at 800 °C and 1100 °C.



(c) Sample C2 annealed at 800 °C. (d) Sample C5 annealed at 800 °C.



(e) Sample C3 annealed at 800 °C. (f) Sample C6 annealed at 800 °C.

Figure 8.17: Effect of write pulse duration on flat-band voltage shift. A strong dependence is observed only for low Si NC densities (Samples C1 and C4). Large flat-band shifts even at pulse durations of only 1 ms are obtained for all samples.

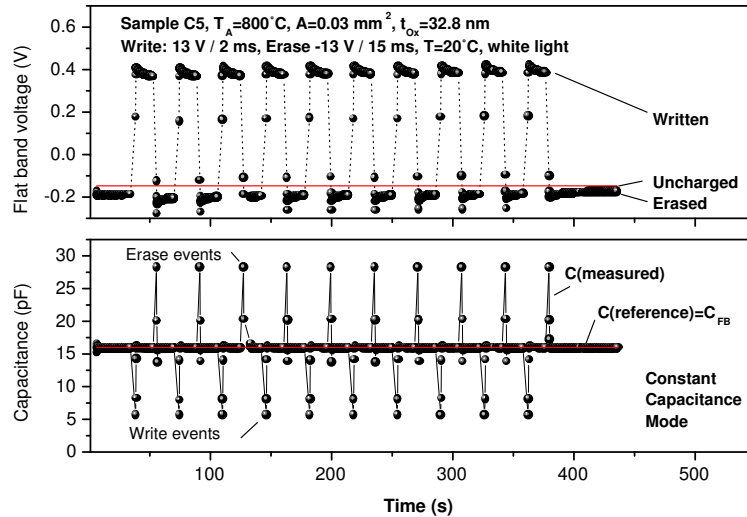
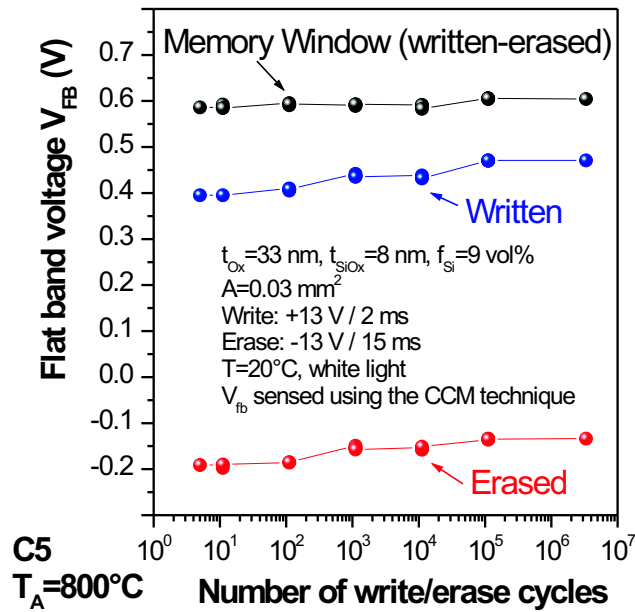


Figure 8.18: Principle of the implemented endurance test using MOS capacitors: After defined sequence of write/erase pulses the flat-band voltage $V_{FB} = V(C_{FB})$ is determined in the written and the erased states using the const. capacitance method.

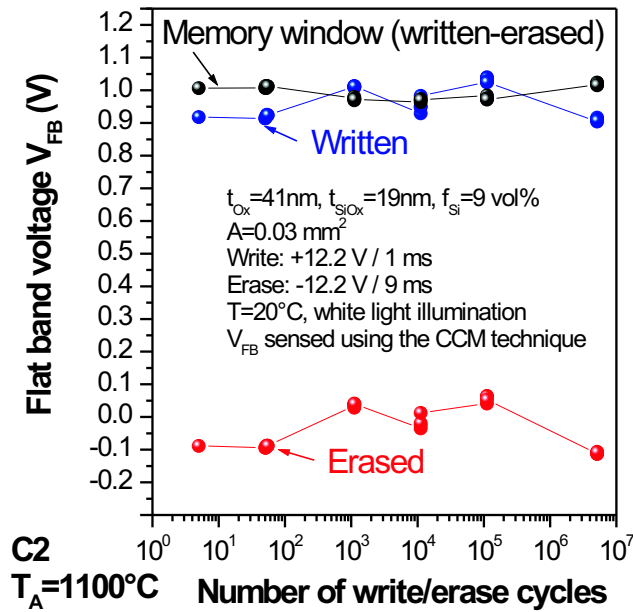
memory window. Finally the widest memory windows are found for the intermediate Si excess of about 9 vol% (oxide composition $\approx \text{SiO}_{1.6}$).

8.11 Endurance tests

The endurance denotes the number of write/erase cycles performed until the memory device fails due to dielectric breakdown. This figure depends considerably on the used write/erase voltage, since the energy of injected electrons determines the mechanisms of defect generation in the oxide. The physics of trap generation in oxides is not completely understood. It has been proposed that during high voltage stress, possibly catalyzed by the release of hydrogen by the anode, the electric field causes a displacement of the bridging oxygen atom in Si-O-Si structures, leading to the formation of oxygen vacancy defects or E' centers. These traps can be either positive, negative or neutral. The field, time and current dependencies of trap generation have been investigated by Qian et al. [188]. For a demonstration of the endurance behavior, the on-state of the memory was assigned to Si NC charged with electrons, the off state was selected to correspond to discharged neutral clusters. The CCM technique was used to sense the flat band potential after applying an increasing number of step-like write/erase pulses with a programmable function generator. Appropriate operating conditions for sample C5 ($T_A = 800^\circ\text{C}$) were found to be +13 V/2 ms for write and -13 V/15 ms for erase as demonstrated in Fig. 8.18. No degradation was observed up to device failure between $3 \cdot 10^6$ and $1 \cdot 10^7$ cycles (Fig. 8.19a). Useful operating conditions for sample C2 ($T_A = 1100^\circ\text{C}$) were found to be +12.2 V/1 ms for write and -12.2 V/9 ms for erase. The slight variation of the "written" and "erased" states



(a) Endurance test of sample C5 annealed at 800 °C. Failure after about $3 \cdot 10^6$ cycles.



(b) Endurance test of sample C2 annealed at 1100 °C. Failure after about $5.2 \cdot 10^6$ cycles.

Figure 8.19: Endurance measurements of selected random samples.

are artefacts introduced by the measurement. Failure occurred between $5.2 \cdot 10^6$ and $1 \cdot 10^7$ cycles (Fig. 8.19b). The device performance seems to be limited by the quality of the tunnel oxide, not by a decreasing memory window. It should be noted that the presented endurance tests are the only measured random samples. For statistically significant results automated parallel testing of large sample sets was required, but for such tests there were no technical capabilities.

9 Summary and outlook

9.1 Summary

Aim of this work was to investigate an alternative technology for a novel EEPROM-like memory device relying on charge trapping in silicon nanoclusters (Si NC) embedded in the gate oxide of a field-effect transistor, the "Silicon nanocrystal-memory". In the selected new approach one first prepares a dielectric gate stack by sputter-depositing SiO_x ($x < 2$) and SiO_2 layers onto a thermal tunnel-oxide on silicon. Thereafter a high temperature anneal transforms the homogeneous SiO_x layer into a layer of SiO_2 with embedded Si NC and completes the processing of the dielectric gate stack. The realization of this approach was split into the following steps:

Two sputtering techniques for SiO_x deposition were evaluated: reactive rf sputtering from a Si target and rf/dc co-sputtering from SiO_2 and Si targets respectively. The first technique allowed to control the SiO_x composition by adjusting the O_2 partial pressure during deposition using a feedback based on optical emission spectroscopy as described in [124]. However a co-sputtering technique for SiO_x was found to be more suitable with respect to a reliable composition control at low deposition rates and negligible particle generation. SiO_x films as thin as 10 nm with compositions x between 2 and 0.5 were prepared. SiO_2 films were rf sputtered from a SiO_2 target.

The composition of SiO_x thin films has been investigated by variable angle spectroscopic ellipsometry (VASE), elastic recoil detection (ERD), Rutherford backscattering (RBS), and Fourier-transform infrared (FTIR) spectroscopy. ERD and, in particular VASE turned out to be well suited to characterize the SiO_x thin films, while RBS results were less accurate due to the rather low mass of the measured elements silicon and oxygen. Because of a superposition of density- and composition-related effects, the energy of the IR-active Si-O stretch vibration was found to be only a qualitative measure of SiO_x composition.

To select suitable thermal anneals, the nucleation and growth of Si NC were probed by cross-section transmission electron microscopy (XTEM), photoluminescence (PL) spectroscopy, FTIR spectroscopy and VASE. While Si NC smaller than 2.5-3 nm showed too little contrast for imaging by XTEM, energy and intensity of the Si NC-related PL band at 1.2-1.75 eV and of the the IR-active Si-O stretch vibration at $900\text{-}1100\text{ cm}^{-1}$ were found to be good probes of the progress in SiO_x phase separation. The characteristic differences in the optical constants of amorphous and crystalline Si were used to investigate the transformation of small amorphous Si NC into larger crystalline Si NC in the course of multiple anneals at successively higher temperature by VASE.

Rapid thermal anneals at temperatures in the range of $800\text{-}1100^\circ\text{C}$ were found suitable

for the formation of a high density of isolated Si NC in SiO_x films. A systematic study of the red Si NC PL band showed that, to obtain Si NC of a given size, lower temperatures can be used for SiO_x films with higher Si excess. At fixed annealing temperature, a higher Si excess results in a lower critical size of stable precipitates, resulting in a higher density of precipitates and a more rapid condensation of excess Si atoms onto them. The effect of a more rapid phase separation for a higher Si excess but fixed temperature has been confirmed also by FTIR spectroscopy.

By means of a kinetic 3D Monte-Carlo code developed by Heinig et al. [50], the annealing process of differently designed $\text{SiO}_2/\text{SiO}_x$ gate stacks was simulated to complement corresponding experiments, but also to compare two limiting cases: The growth of 1-2 nm wide Si NC in comparably thick (10-20 nm) or thin (1.5 nm) SiO_x films embedded in SiO_2 . In the first case the mean Si NC parameters were strongly dependent on annealing time. The vertical Si NC distribution showed oscillations growing from the interfaces of the SiO_x film. Contrary, in the second case the Si NC size and vertical position were governed by thickness and position of the SiO_x film. Therefore a superlattice of ultrathin $\text{SiO}_2/\text{SiO}_x$ films is considered as an even more favorable gate stack design for a Si nanocrystal memory. It guarantees a high density of isolated Si NC with a narrow size distribution, is rather insensitive to the annealing regime and allows the highest degree of control over the resulting gate stack structure. In addition the vertical and in-plane separation of Si NC can be adjusted separately by adjusting the SiO_2 interlayer thickness and the SiO_x composition respectively.

Finally *MOS capacitors with Si NC embedded in the gate oxide* were prepared: Onto a 2 nm thermal tunnel oxide 10 nm or 20 nm SiO_x films ($x = 1.8, 1.6, 1.4, 2$) were deposited and covered with a 20 nm SiO_2 layer. Si NC were formed by a 2 min rapid thermal annealing (RTA) step in Ar/ N_2 at temperatures of 800 °C, 950 °C or 1100 °C. After annealing and formation of Al-electrodes the capacitors were electrically characterized by means of a developed Testpoint-based software. The charge trapping and retention behavior were evaluated using the constant-capacity method. In addition the samples were characterized by XTEM, VASE, and PL.

Reference capacitors *without SiO_x interlayer* showed small leakage currents, and breakdown fields as high as 8 MV/cm. For capacitors *with SiO_x interlayer* the effective sheet density of electron and hole-traps increased with annealing temperature. The growth of Si NC related PL intensity with annealing temperature indicated a correlation with an increasing density of Si precipitates. From the PL energy, the mean Si NC size was estimated to lie between 1.9 nm and 3.7 nm, depending on Si excess and anneal. Charging tests showed that a reasonable memory window (1 V) can be achieved using 2 ms write pulses of 12.5 V, while the charge retention time was measured to exceed 1 day. Since for the investigated samples the charge loss was governed by direct tunneling, a simple extrapolation of the long term retention was not possible. The stability of the tested capacitors was very good. Random-samples selected for endurance tests showed virtually no degradation after 10^7 write/erase cycles. Increasing Si excess or increased annealing temperatures resulted in higher charging currents, but also in a rapid loss of trapped charge: The growing density of Si NC caused a transition from local charge storage in isolated Si NC to a continuous-floating-gate-like behavior (The trapped charge is delocalized over groups of neighbored Si NC).

9.2 Outlook

According to the summarized results, the developed sputtering method is well suited for preparation of Si nanocrystal memories. All processing steps including the thermal anneal required for Si NC formation are fully compatible with the constraints of advanced CMOS technology. Follow-up experiments should take place in a production-environment and focus on the integration of the method in the technology of commercial memory devices.

In order to further improve the device properties, in particular the charge retention behavior, it is suggested to replace the homogeneous 10-20 nm SiO_x layer by a sequence of 3-4 $\text{SiO}_2/\text{SiO}_x$ (Si excess ≈ 25 at%) double-layers with SiO_x and SiO_2 layer thicknesses of 1-2 nm and 2-5 nm respectively. Thermal annealing will in this case lead to constrained growth of single layers of Si NC in the SiO_x regions, which enables a better control over location, diameter and lateral distribution of Si NC. Such superlattices could be applied not only in Si nanocrystal memories, but also in the field of Si-based light emitters and optical interconnects.

Bibliography

- [1] L. Pavesi, “A review of the various efforts to a silicon laser,” in *Optoelectronic Integration on Silicon. Proceedings of SPIE (Photonic West, San Diego 2003)*, D. J. Robbins and G. E. Jabbour, Eds.
- [2] L. T. Canham, “Silicon quantum wire array fabrication by electrochemical and chemical dissolution of wafers,” *Appl. Phys. Lett.*, vol. 57, pp. 1045–1047, 1990.
- [3] A. G. Cullis and L. T. Canham, “Visible light emission due to quantum size effects in highly porous crystalline silicon,” *Nature*, vol. 353, pp. 335–338, 1991.
- [4] L. Pavesi, L. DalNegro, C. Mazzoleni, G. Franzo, and F. Priolo, “Optical gain in silicon nanocrystals,” *Nature*, vol. 408, pp. 440–444, 2000.
- [5] M. E. Castagna, “Quantum dot materials and devices for light emission in silicon,” 32th European Solid-State Device Research Conference (ESSDERC), 24–26 September 2002, Firenze, Italy, Si Optoelectronics, Bio-and Nano-Systems Group, Corporate Technology Research and Development, STMicroelectronics, Catania,.
- [6] S. Tiwari, F. Rana, K. Chan, H. Hanafi, W. Chan, and D. Buchanan, “Volatile and nonvolatile memories in silicon with nano-crystal storage,” *IEDM Tech. Dig.*, pp. 521–524, 1995.
- [7] K. Yano, T. Ishii, T. Sano, T. Mine, F. Murai, T. Kure, and K. Seki, “Status of single-electron memories,” *IEDM Tech. Dig.*, p. 107, 1998.
- [8] B. Hradsky, R. Rao, R. F. Steimle, M. Sadd, S. Straub, R. Muralidhar, and B. White, “Local charge storage in silicon nanocrystal memories,” 19th IEEE Non-Volatile Semiconductor Memory Workshop, February 16 - 20, 2003, Monterey, CA, USA.
- [9] C. Gerardi, G. Ammendola, M. Melanotte, S. Lombardo, and I. Crupi, “Reliability and retention study reliability and retention study of nanocrystal cell of nanocrystal cell arrays,” 32th European Solid-State Device Research Conference (ESSDERC2002), September 24-26, 2002, Firenze, Italy.
- [10] D. Lammers, “Moto lab builds 4-Mbit ‘nanocrystal’ memory,” EETimes, (URL: <http://www.eetimes.com/story/OEG20030331S0023>), March 31, 2003.

- [11] B. Eitan, P. Pavan, I. Bloom, E. Aloni, A. Frommer, and D. Finzi, "NROM: A novel localized trapping, 2-bit nonvolatile memory cell," *IEEE Electron Device Lett.*, vol. 21, pp. 543–545, 2000.
- [12] D. J. DiMaria, D. W. Dong, C. Falcony, T. N. Theiss, J. R. Kirtley, J. C. Tsang, D. R. Young, F. L. Pesavento, and S. D. Brorson, "Charge transport and trapping phenomena in off-stoichiometric silicon dioxide films," *J. Appl. Phys.*, vol. 54, no. 10, pp. 5801–5827, 1983.
- [13] V. V. Afanasev and A. Stesmans, "Photoionization of silicon particles in SiO₂," *Phys. Rev. B*, vol. 59, no. 3, pp. 2025–2034, 1999.
- [14] M. Naich, G. Rosenman, and M. Molotskii, *Trap spectroscopy in Si₃N₄ ultrathin films using exoelectron emission method*, ser. Mat. Res. Soc. Proc., 2003, vol. 745, p. N.5.21.1.
- [15] S. H. Zhang, *Aerosol Sci. Technol.*, vol. 23, pp. 357–372, 1995.
- [16] I. G. Kim, S. Han, H. Kim, J. Lee, B. Choi, S. Hwang, D. Ahn, and H. Shin, "Room temperature single electron effects in Si quantum dot memory with oxide-nitride tunneling dielectric," *IEDM Tech. Dig.*, p. 111, 1998.
- [17] Y. C. King, T. J. King, and C. Hu, "A long refresh dynamic/quasi-nonvolatile memory device with 2-nm tunneling oxide," *IEEE Electron Device Lett.*, vol. 20, p. 409, 1999.
- [18] Y. Kim, K. H. Park, T. H. Chung, H. J. Bark, J.-Y. Yi, W. C. Choi, and E. K. Kim, "Ultralarge capacitance-voltage hysteresis and charge retention characteristics in metal oxide semiconductor structure containing nanocrystals deposited by ion-beam-assisted electron beam deposition," *Appl. Phys. Lett.*, vol. 78, no. 7, pp. 934–936, 2001.
- [19] T. Ohzone, T. Matsuda, and T. Hori, "Erase/write cycle tests of n-MOSFETs with Si-implanted gate-SiO₂," *IEEE Trans. Electron Devices*, vol. 43, pp. 1374–1381, 1996.
- [20] J. von Borany, T. Gebel, K.-H. Stegemann, H.-J. Thees, and M. Wittmaack, "Memory properties of Si⁺ implanted gate oxides: from MOS capacitors to nvS-RAM," *Solid-state electronics*, vol. 46, pp. 1729–1737, 2002.
- [21] H. I. Hanafi and S. Tiwari, "Fast and long retention-time nano-crystal memory," *IEEE Trans. Electron Devices*, vol. 43, no. 9, pp. 1553–1558, 1996.
- [22] R. Compano, Ed., *European Commission IST programme Future and Emerging Technologies : Technology Roadmap for Nanoelectronics*, 2nd ed., November 2000.
- [23] K. K. Likharev, "Layered tunnel barriers for nonvolatile memory devices," *Appl. Phys. Lett.*, vol. 73, no. 15, pp. 2137–2139, 1998.

-
- [24] A. Korotkov and K. Likharev, “Resonant Fowler-Nordheim tunneling through layered tunnel barriers and its possible applications,” *Techn. Dig. IEDM*, pp. 223–226, 1999.
- [25] J. D. Casperson, L. D. Bell, and H. A. Atwater, “Materials issues for layered tunnel barrier structures,” *J. Appl. Phys.*, vol. 92, no. 11, pp. 261–267, 2002.
- [26] L. Guo, E. Leobandung, and S. Y. Chou, “Si single-electron MOS memory with nanoscale floating-gate and narrow channel,” *IEDM Tech. Dig.*, pp. 955–956, 1996.
- [27] —, “A room temperature single electron MOS memory with nanoscale floating gate and ultranarrow channel,” *Appl. Phys. Lett.*, vol. 70, no. 7, pp. 850–852, 1997.
- [28] A. Nakajima, T. Futatsugi, K. Kosemura, T. Fukano, and N. Yokoyama, “Room-temperature operation of Si single-electron memory with self aligned floating dot gate,” *IEDM Tech. Dig.*, pp. 952–954., 1996.
- [29] J. J. Welser, S. Tiwari, S. Rishton, K. Y. Lee, and Y. Lee, “Room temperature operation of a quantum-dot flash memory,” *IEEE Electron Device Lett.*, vol. 18, p. 278, 1997.
- [30] B. J. Hinds, T. Yamanaka, and S. Oda, “Emission lifetime of polarizable charge stored in nano-crystalline si based single-electron memory,” *J. Appl. Phys.*, vol. 90, no. 12, pp. 6402–6408, 2001.
- [31] M. Zacharias, J. Heitmann, R. Scholz, U. Kahler, M. Schmidt, and J. Bläsing, “Size-controlled highly luminescent silicon nanocrystals: A SiO/SiO₂ superlattice approach,” *Appl. Phys. Lett.*, vol. 80, no. 4, pp. 661–663, 2002.
- [32] T. Baron, F. Martin, P. Mur, C. Wyon, M. Dupuy, C. Buseret, A. Souifi, and G. Guillot, “Low pressure chemical vapor deposition growth of silicon quantum dots on insulator for nanoelectronics devices,” *Appl. Surf. Sci.*, vol. 164, no. 1-4, pp. 29–34, 2000.
- [33] K. K. Likharev, “Single electron devices and their application,” *Proc. IEEE*, vol. 87, no. 4, pp. 606–632, 1999.
- [34] G. F. Grom, D. J. Lockwood, J. P. McCaffrey, H. J. Labbe, P. M. Fauchet, B. White, and J. Diener, “Ordering and self-organization in nanocrystalline silicon,” *Nature*, vol. 407, pp. 358–361, 2000.
- [35] H. B. Kim, L. Montes, R. Krishnan, P. M. Fauchet, and L. Tsybeskov, “Carrier transport and lateral conductivity in nanocrystalline silicon layers,” in *2000 Fall Meeting proceedings, MRS Proceedings Volume 638, Symposium F (Microcrystalline and Nanocrystalline Semiconductors)*, F5.12, 2000.
- [36] G. Eftekhari, “Electrical conduction in rapidly annealed sputter-deposited SiO₂ films (in O₂-Ar atmosphere) on Si,” *phys. stat. sol. (A)*, vol. 151, pp. 129–133, 1995.

- [37] K. Haberle and E. Fröschele, “MOS device fabrication using sputter deposited gate oxide and polycrystalline silicon layers,” *Solid State Electronics*, vol. 23, pp. 855–862, 1980.
- [38] E. V. Jelenkovic and K. Y. Tong, “Effect of annealing temperature on electrical stability of radio frequency magnetron sputtered silicon oxides,” *J. Vac. Sci. Technol. B*, vol. 15, no. 2, pp. 209–213, 1997.
- [39] —, “Effect of deposition conditions on stability of sputtered oxide in MOS structures,” *Microelectron. Reliab.*, vol. 37, no. 1, pp. 159–169, 1997.
- [40] V. V. Afanasev and A. Stesmans, “Leakage currents induced in ultrathin oxides on (100) Si by deep-UV photons,” *Mater. Sci. Eng. B*, vol. 71, pp. 56–61, 2000.
- [41] K. Binder, “Spinodal decomposition in confined geometry,” *J. Non-Equilib. Thermodyn.*, vol. 23, pp. 1–44, 1998.
- [42] M. Strobel, “Modeling and computer simulations of ion beam synthesis of nanostructures,” Ph.D. dissertation, University of Technology Dresden, Germany, 1999.
- [43] J. Schmelzer, G. Roepke, and R. Mahnke, *Aggregation phenomena in complex systems*. Weinheim: Wiley-VCH, 1999.
- [44] M. Volmer and A. Weber, “Keimbildung in übersättigten Gebilden,” *Z. Phys. Chem.*, vol. 119, p. 277, 1926.
- [45] R. Becker and W. Döring, “Kinetische Behandlung der Keimbildung in übersättigten Dämpfen,” *Ann. Phys.*, vol. 24, p. 719, 1935.
- [46] F. C. Goodrich and A. I. Rusanov, Eds., *The modern theory of capillarity*. Berlin: Akademie Verlag, 1981.
- [47] I. M. Lifshitz and V. V. Slyozov, “The kinetics of precipitation from supersaturated solid solutions,” *J. Phys. Chem. Solids*, vol. 19, p. 35, 1961.
- [48] C. Wagner, “Theorie zur Alterung von Niederschlägen durch Umlösen,” *Z. Electrochem.*, vol. 65, p. 581, 1961.
- [49] S. Reiss, R. Weber, K.-H. Heinig, and W. Skorupa, “Experimental study and modeling of structure formation in buried layers at ion beam synthesis,” *Nucl. Instr. Meth. B*, vol. 89, pp. 337–341, 1994.
- [50] M. Strobel, K.-H. Heinig, and W. Möller, “Three-dimensional domain growth on the size scale of the capillary length: Effective growth exponent and comparative atomistic and mean-field simulations,” *Phys. Rev. B*, vol. 64, pp. 245 422 1–14, 2001.
- [51] A. D. Brailsford, “Diffusion to a random array of identical spherical sinks,” *J. Nucl. Mat.*, vol. 60, p. 257, 1976.
- [52] B. Fultz and J. M. Howe, *Transmission Electron Microscopy and Diffractometry of Materials*. Berlin Heidelberg New York: Springer-Verlag, 2001.

- [53] H. E. M. Worch and, W. Blum, and E. Zschech, "Cross-sectional thin film characterization of Si compounds in semiconductor device structures using both elemental and ELNES mapping by EFTEM," *Thin Solid Films*, vol. 405, pp. 198–204, 2002.
- [54] J. R. Tesmer and M. A. Nastasi, Eds., *Handbook of Modern Ion Beam Materials Analysis*. Pittsburgh, PA: Materials Research Society, 1995.
- [55] D. Harding, "Using ion-beam techniques to determine the elemental composition of ICF targets," *LLE Review*, vol. 75, pp. 171–181, 1998.
- [56] C. R. Gruhn, M. Binimi, R. Legrain, R. Loveman, W. Pang, M. Roach, D. K. Scott, A. Shotter, T. J. Symons, J. Wouters, M. Zisman, R. Devries, Y. C. Peng, and W. Sondheim, "Bragg curve spectroscopy," *Nucl. Instr. Meth.*, vol. 196, pp. 33–40, 1982.
- [57] B. Schrader, Ed., *Infrared and Raman Spectroscopy: Methods and Applications*. Weinheim: VCH, 1995.
- [58] C. T. Kirk, "Quantitative analysis of the effect of disorder-induced mode coupling on infrared absorption in silica," *Phys. Rev. B*, vol. 38, no. 2, pp. 1255–1273, 1988.
- [59] K. Huebner, *phys. stat. sol. (A)*, vol. 40, p. 487, 1977.
- [60] R. A. B. Devine, "Structural modifications in a-SiO₂," *J. Non-Cryst. Solids*, vol. 152, pp. 50–58, 1993.
- [61] A. Lehmann, L. Schuhmann, and K. Huebner, "Optical phonons in amorphous silicon oxides 1. calculation of the density of states and interpretation of LO-TO splittings of amorphous SiO₂," *phys. stat. sol. (B)*, vol. 117, pp. 689–698, 1983.
- [62] —, "Optical phonons in amorphous silicon oxides 2. calculation of phonon spectra and interpretation of IR transmission of SiO_x," *phys. stat. sol. (B)*, vol. 121, pp. 505–511, 1984.
- [63] I. P. Lisovskii, V. G. Litovchenko, V. B. Lozinskii, S. I. Frolov, H. Flietner, W. Fussel, and E. G. Schmidt, "IR study of short-range and local order in SiO₂ and SiO_x films," *J. Non-Cryst. Solids*, vol. 187, pp. 91–95, 1995.
- [64] I. P. Lisovskii, V. G. Litvichenko, V. G. Lozinskii, and G. I. Steblovskii, "IR spectroscopic investigation of SiO₂ film structure," *Thin Solid Films*, vol. 213, pp. 164–169, 1992.
- [65] W. A. Pliskin and H. S. Lehmann, "Structural evaluation of silicon oxide films," *J. Electrochem. Soc.*, vol. 112, pp. 1013–1019, 1965.
- [66] D. Berreman, "Infrared absorption at longitudinal optic frequency in cubic crystal films," *Phys. Rev.*, vol. 130, p. 2193, 1963.
- [67] H. R. Philipp, "Optical properties of non-crystalline Si, SiO, SiO_x and SiO₂," *J. Phys. Chem. Solids*, vol. 32, pp. 1935–1945, 1971.

- [68] —, “Optical and bonding model for non-crystalline SiO_X and SiO_XN_Y materials,” *J. Non-Cryst. Solids*, vol. 8-10, pp. 627–632, 1972.
- [69] U. Kahlert, “Preparation, characterization and surface-modification of silicon nano-particles in SiO_2 ,” Ph.D. dissertation, Martin-Luther University Halle-Wittenberg, 2001.
- [70] B. J. Hinds, F. Wang, D. M. Wolfe, C. L. Hinkle, and G. Lucovsky, “Investigation of postoxidation thermal treatments of Si/ SiO_2 interface in relationship to the kinetics of amorphous Si suboxide decomposition,” *J. Vac. Sci. Technol. B*, vol. 16, no. 4, pp. 2171–2176, 1998.
- [71] Y. Nishi and R. D. (edts.), *Handbook of semiconductor manufacturing technology*, 1st ed. New York: Marcel Dekker, Inc., 2000, ch. Silicon materials, pp. 35–87.
- [72] Y. Tarui, Ed., *VLSI technology, fundamentals and applications.*, 1st ed., ser. Springer series in electrophysics 12. Berlin and Heidelberg: Springer, 1986.
- [73] L. I. Murin, T. Hallberg, V. P. Markevich, and J. L. Lindström, “Experimental evidence of the oxygen dimer in silicon,” *Phys. Rev. Lett.*, vol. 80, pp. 93–97, 1998.
- [74] F. A. Johnson, “Lattice absorption bands in silicon,” *Proc. Phys. Soc., (London)*, vol. 73, pp. 265–272, 1959.
- [75] V. Lehmann and U. Goesele, *Appl. Phys. Lett.*, vol. 58, p. 856, 1991.
- [76] D. Kovalev, H. Heckler, G. Polisski, and F. Koch, “Optical properties of Si nanocrystals,” *phys. stat. sol. (B)*, vol. 215, pp. 871–932, 1999.
- [77] G. C. John and V. A. Singh, “Theory of photoluminescence spectra of porous silicon,” *Phys. Rev. B*, vol. 50, no. 8, pp. 5329–5334, 1994.
- [78] Y. Kanemitsu, T. Ogawa, K. Shiraishi, and K. Takeda, “Visible photoluminescence from oxidized Si nanometer-sized spheres: Exciton confinement on a spherical shell,” *Phys. Rev. B*, vol. 48, no. 7, pp. 4883–4886, 1993.
- [79] J. Valenta, R. Juhasz, and J. Linnros, “Photoluminescence spectroscopy of single silicon quantum dots,” *Appl. Phys. Lett.*, vol. 80, no. 6, pp. 1070–1072, 2002.
- [80] S. Takeoka, M. Fujii, and S. Hayashi, “Size-dependent photoluminescence from surface-oxidized Si nanocrystals in a weak confinement regime,” *Phys. Rev. B*, vol. 62, no. 24, pp. 16 820–16 825, 2000.
- [81] B. Garrido-Fernandez, M. Lopez, C. Garcia, A. Perez-Rodriguez, J. R. Morante, C. Bonafos, M. Carrada, and A. Claverie, “Influence of average size and interface passivation on the spectral emission of Si nanocrystals embedded in SiO_2 ,” *J. Appl. Phys.*, vol. 91, no. 2, pp. 798–807, 2002.
- [82] A. Puzder, A. J. Williamson, J. C. Grossman, and G. Galli, “Surface chemistry of silicon nanoclusters,” *Phys. Rev. Lett.*, vol. 88, no. 9, p. 97401(4), 2002.

-
- [83] I. Vasiliev, J. R. Chelikowsky, and R. M. Martin, “Surface oxidation effects on the optical properties of silicon nanocrystals,” *Phys. Rev. B*, vol. 65, p. 121302(R), 2002.
- [84] M. V. Wolkin, J. Jorne, and P. M. Fauchet, “Electronic states and luminescence in porous silicon quantum dots: The role of oxygen,” *Phys. Rev. Lett.*, vol. 82, no. 1, pp. 197–200, 1999.
- [85] G. Allan, C. Delerue, and M. Lanoo, “Electronic structure of amorphous silicon nanoclusters,” *Phys. Rev. B*, vol. 78, no. 16, pp. 3161–3164, 1997.
- [86] H. Rinnert, M. Vergnat, and A. Burneau, “Evidence of light-emitting amorphous silicon clusters confined in a silicon oxide matrix,” *J. Appl. Phys.*, vol. 89, no. 11, pp. 237–243, 2001.
- [87] F. Bassani, S. Menard, I. Berbezier, F. A. d’Avitaya, and I. Mihalescu, “Improvement in the luminescence properties of Si/CaF₂ nanostructures,” *Mater. Sci. Eng. B*, vol. 69-70, pp. 340–344, 2000.
- [88] O. Hanaizumi, K. Ono, and Y. Ogawa, “Blue-light emission from sputtered Si:SiO₂ films without annealing,” *Appl. Phys. Lett.*, vol. 82, no. 4, pp. 538–540, 2003.
- [89] N.-M. Park, T.-S. Kim, and S.-J. Park, “Band gap engineering of amorphous silicon quantum dots for light-emitting diodes,” *Appl. Phys. Lett.*, vol. 78, no. 17, pp. 2575–1577, 2001.
- [90] N.-M. Park, C.-J. Choi, T.-Y. Seong, and S.-J. Park, “Quantum confinement in amorphous silicon quantum dots embedded in silicon nitride,” *Phys. Rev. Lett.*, vol. 86, no. 7, pp. 1355–1357, 2001.
- [91] A. R. Forouhi, “Optical dispersion relations for amorphous semiconductors and amorphous dielectrics,” *Phys. Rev. B*, vol. 34, no. 10, pp. 7018–7026, 1986.
- [92] J. G. E. Jellison and F. A. Modine, “Parameterization of the optical functions of amorphous materials in the interband region,” *Appl. Phys. Lett.*, vol. 69, no. 3, pp. 371–373, 1996.
- [93] ———, “Erratum: Parameterization of the optical functions of amorphous materials in the interband region [Appl. Phys. Lett. 69, 371 (1996)],” *Appl. Phys. Lett.*, vol. 69, no. 14, p. 2137, 1996.
- [94] J. C. M. Garnett, *Philos. Trans. R. Soc. London, Ser. A*, vol. 203, p. 385, 1904.
- [95] D. A. G. Bruggemann, “Berechnung verschiedener physikalischer Konstanten von heterogenen Substanzen. 1. Dielektrizitätskonstanten und Leitfähigkeiten der Mischkörper aus isotropen Substanzen.” *Annalen der Physik (1900)*, vol. 22, pp. 636–679, 1935.
- [96] H. Fujiwara, J. Koh, P. I. Rovira, and R. W. Collins, “Assessment of effective-medium theories in the analysis of nucleation and microscopic surface roughness evolution for semiconductor thin films,” *Phys. Rev. B*, vol. 61, no. 16, pp. 10 832–10 844, 2000.

- [97] E. H. Nicollian and J. R. Brews, *MOS (metal oxide semiconductor) physics and technology*. New York, USA: John Wiley & sons, 1982.
- [98] D. K. Schröder, *Semiconductor Material and Device Characterization*, 2nd ed. New York, USA: John Wiley & sons, 1998.
- [99] S. M. Sze, *Physics of semiconductor devices*, 2nd ed. New York, USA: John Wiley & sons, 1981.
- [100] S. Tiwari, F. Rana, H. Hanafi, A. Hartstein, E. F. Crabbé, and K. Chan, “A silicon nanocrystals based memory,” *Appl. Phys. Lett.*, vol. 68, no. 10, pp. 1311–1435, 1996.
- [101] G. Barbottin and A. Vapaille, *Instabilities in silicon devices - silicon passivation and related instabilities*, G. Barbottin and A. Vapaille, Eds. Amsterdam: Elsevier Science Publishers B.V., 1986, vol. 1.
- [102] K. F. Schuegraf and C. Hu, “Reliability of thin SiO₂,” *Semicond. Sci. Technol.*, vol. 9, pp. 989–1004, 1994.
- [103] R. H. Fowler and L. W. Nordheim, “Electron emission in intense electric fields,” *Proc. R. Soc. A*, vol. 119, pp. 173–181, 1928.
- [104] M. Lenzlinger and E. H. Snow, “Fowler-Nordheim tunneling into thermally grown SiO₂,” *J. Appl. Phys.*, vol. 40, no. 1, pp. 278–283, 1969.
- [105] M. P. Houng, Y. H. Wang, and W. J. Chang, “Current transport mechanism in trapped oxides: A generalized trap-assisted tunneling model,” *J. Appl. Phys.*, vol. 86, no. 3, pp. 1488–1491, 1999.
- [106] B. D. Salvo, G. Ghibaudo, G. Pananakakis, B. Guillaumot, and G. Reimbold, “A general bulk-limited transport analysis of a 10 nm-thick oxide stress-induced leakage current,” *Solid State Electronics*, vol. 44, pp. 895–903, 2000.
- [107] J. S. Chapin, “Sputtering process and apparatus,” U.S. Patent 4,166,018 (filed Jan. 1974), August 1979.
- [108] H. Conrads and M. Schmidt, “Plasma generation and plasma sources,” *Plasma Sources Sci. Technol.*, vol. 9, pp. 441–454., 2000.
- [109] S. M. Rossnagel, J. J. Cuomo, and W. D. W. W. D, Eds., *Handbook of Plasma Processing Technology*. Park Ridge: Noyes, 1990.
- [110] J. M. Schneider, S. Rohde, W. D. Sproul, and A. Matthews, “Recent developments in plasma assisted physical vapour deposition,” *J. Phys. D: Appl. Phys.*, vol. 33, pp. R173–R186., 2000.
- [111] J. A. Thornton, “Influence of substrate temperature and deposition rate on structure of thick sputtered Cu coatings,” *J. Vac. Sci. Technol. A*, vol. 12, no. 4, p. 830, 1975.

-
- [112] L. Maissel, *Application of sputtering to the deposition of films*, ser. Handbook of Thin Film technology, eds L. I. Maissel and R. Glang. New-York: McGraw-Hill, 1970, ch. Chapter 4.
- [113] W. A. Pliskin and R. A. Gdula, *Passivation and insulation*, ser. Handbook on Semiconductors (ed. by T. S. Moss, vol. 3 ed. by S. P. Keller). IBM East Fishkill Facility, Hopewell Junction, NY 12533, USA: North-Holland, 1980, vol. 3, ch. 11, pp. 641–687.
- [114] J. Struempfel, G. Beister, D. Schulze, M. Kammer, and S. Rehn, “Reactive dual magnetron sputtering of oxides for large area production of optical multilayers,” Presentation on the 40th Annual Technical Conference of the Society of Vacuum Coaters, New Orleans, USA, April 12 - 17 1997.
- [115] N. Kaiser and H. K. Pulker, Eds., *Optical interference coatings*, 1st ed., ser. Springer Series in Optical Sciences. Berlin, Heidelberg, New-York: Springer, 2003.
- [116] T. Serikawa and F. Omata, “High mobility poly-Si thin film transistors fabricated on stainless steel-foils by low temperature processing using sputter depositions,” *Jpn. J. Appl. Phys. Part 2*, vol. 39, no. 5A, pp. L393–395, 2000.
- [117] T. Serikawa and S. Shirai, “Ultra-thin silicon-oxide films by sputter-deposition and their application to high quality TFTs,” *Vacuum*, vol. 51, no. 4, pp. 781–783, 1998.
- [118] S. Berg, H. O. Blom, T. Larsson, and C. Nender, “Modeling of reactive sputtering of compound materials,” *J. Vac. Sci. Technol. A*, vol. 5, no. 2, pp. 202–207, 1987.
- [119] S. Berg, H. O. Blom, M. Moradi, and C. Nender, “Process modeling of reactive sputtering,” *J. Vac. Sci. Technol. A*, vol. 7, no. 3, pp. 1225–1229, 1989.
- [120] S. Berg, T. Larsson, C. Nender, and H. O. Blom, “Predicting thin-film stoichiometry in reactive sputtering,” *J. Appl. Phys.*, vol. 63, no. 3, pp. 887–891, 1988.
- [121] S. Berg, T. Nyberg, H. O. Blom, and C. Nender, “Computer modeling as a tool to predict deposition rate and film composition in the reactive sputtering process,” *J. Vac. Sci. Technol. A*, vol. 16, no. 3, pp. 1277–1285, 1998.
- [122] T. Larsson, H. O. Blom, C. Nender, and S. Berg, “A physical model for process instabilities in sputtering,” *J. Vac. Sci. Technol. A*, vol. 6, no. 3, pp. 1832–1836, 1988.
- [123] A. Ershov and L. Pekker, “Model of d.c. magnetron reactive sputtering in Ar-O₂ gas mixtures,” *Thin Solid Films*, vol. 289, pp. 140–146, 1996.
- [124] H. Seifarth, J. U. Schmidt, R. Groetzschel, and M. Klimenkov, “Phenomenological model of reactive r.f.-magnetron sputtering of Si in Ar/O₂ atmosphere for the prediction of SiO_x thin film stoichiometry from process parameters,” *Thin Solid Films*, vol. 389, no. 1-2, pp. 108–115, 2001.

- [125] H. Seifarth, R. Groetzschel, A. Markwitz, W. Matz, P. Nitzsche, and L. Rebohle, "Preparation of SiO₂ films with embedded Si nanocrystals by reactive r.f. magnetron sputtering," *Thin Solid Films*, vol. 330, pp. 202–205, 1998.
- [126] G. Este and W. D. Westwood, "Reactive deposition of low loss Al₂O₃ optical waveguides by modified dc planar magnetron sputtering," *J. Vac. Sci. Technol. A*, vol. 2, no. 3, pp. 1238–1247, 1984.
- [127] P. D. Davidse and L. I. Maissel, "Dielectric thin films through rf sputtering," *J. Appl. Phys.*, vol. 37, no. 2, pp. 574–579, 1966.
- [128] C. V. Macchioni, "Mechanical properties of high deposition rate SiO₂ films," *J. Vac. Sci. Technol. A*, vol. 8, no. 3, pp. 1340–1343, 1990.
- [129] ———, "The effect of substrate temperature and bias on stress, chemical etch rate, and microstructure of high deposition rate sputtered SiO₂ films," *J. Vac. Sci. Techn. A*, vol. 9, no. 4, pp. 2302–2308, 1991.
- [130] L. I. Maissel, R. E. Jones, and C. L. Standley, "Re-emission of sputtered SiO₂ during growth and its relation to film quality," *IBM J. Res. Develop.*, pp. 176–181, 1970.
- [131] S. Suyama, A. Okamoto, and T. Serikawa, "The effect of oxygen-argon mixing on properties of sputtered silicon dioxide films," *J. Electrochem. Soc.*, vol. 134, no. 9, pp. 2260–2264, 1987.
- [132] T. W. Hickmott, "Defect centers in oxygen-deficient rf-sputtered SiO₂ films. 1. electron spin resonance," *J. Appl. Phys.*, vol. 45, no. 3, pp. 1050–1058, 1974.
- [133] T. Serikawa and T. Yachi, "Magnetron-sputtered SiO₂ films in hydrogen-argon mixtures," *J. Electrochem. Soc.*, vol. 131, no. 9, pp. 2105–2109, 1984.
- [134] T. Serikawa and S. Shirai, "Deposition characteristics and properties of SiO₂ films prepared by reactive sputtering in hydrogen-, oxygen- and nitrogen-argon mixtures," *Jpn. J. Appl. Phys. Part 1*, vol. 33, no. 7B, pp. 4465–4468, 1994.
- [135] F. Gourbilleau, X. Portier, C. Ternon, P. Voivenel, R. Madelon, and R. Rizk, "Si-rich/SiO₂ nanostructured multilayers by reactive magnetron sputtering," *Appl. Phys. Lett.*, vol. 78, no. 20, pp. 3058–3060, 2001.
- [136] G. Eftekhari, "Stability of rapidly annealed reactive sputter deposited nitrided silicon dioxide," *J. Vac. Sci. Technol. A*, vol. 15, no. 2, pp. 433–435, 1997.
- [137] S. Suyama, A. Okamoto, and T. Serikawa, "Electrical characteristics of MOS-FET's utilizing oxygen-argon sputter-deposited gate oxide films," *IEEE Trans. Electr. Dev.*, vol. ED-34, no. 10, pp. 2124–2128, 1987.
- [138] W. D. Westwood, *Reactive sputtering*, ser. Physics of thin films: Advances in research and development - Contemporary preparative techniques. London: Academic press, 1989, vol. 14, ch. 1, pp. 1–73.

-
- [139] E. V. Jelenkovic and K. Y. Tong, "Stability of nitrided silicon oxide deposited by reactive sputtering," *Appl. Phys. Lett.*, vol. 67, no. 18, pp. 2693–2695, 1995.
- [140] J. S. Logan, F. S. Maddocks, and P. D. Davidse, "Metal edge coverage and control of charge accumulation in rf sputtered insulators," *IBM J. Res. Develop.*, vol. 14, pp. 182–191, 1970.
- [141] S. Petersson, G. Linker, and O. Meyer, "Impurity incorporation during rf sputtering of silicon oxide layers," *phys. stat. sol. (A)*, vol. 14, pp. 605–611, 1972.
- [142] T. N. Kennedy, "Sputtered insulator film contouring over substrate topography," *J. Vac. Sci. Technol.*, vol. 13, no. 6, pp. 1135–1137, 1976.
- [143] H.-U. Schreiber and E. Fröschle, "High quality rf-sputtered silicon dioxide layers," *J. Electrochem. Soc.*, vol. 123, no. 1, pp. 30–33, 1976.
- [144] S. Suyama, A. Okamoto, T. Serikawa, and H. Tanigawa, "Electrical conduction and dielectric breakdown in sputter-deposited silicon dioxide films on silicon," *J. Appl. Phys.*, vol. 62, pp. 2360–2363, 1987.
- [145] S. Suyama, A. Okamoto, and T. Serikawa, "Electrical conduction mechanism and breakdown property in sputter-deposited silicon dioxide films on polycrystalline silicon," *J. Appl. Phys.*, vol. 65, no. 1, pp. 210–214, 1989.
- [146] S. Suyama, A. Okamoto, S. Shirai, T. Serikawa, S. Takaoka, and K. Murase, "Electrical characteristics at 4.2 K and high magnetic fields in metal-oxide-semiconductor field-effect transistors utilizing sputter-deposited gate-oxide films," *J. Appl. Phys.*, vol. 71, no. 1, pp. 494–497, 1992.
- [147] E. V. Jelenkovic and K. Y. Tong, "Effect of deposition conditions on stability of sputtered oxide in MOS structures," in *Proc. 20th international conference on microelectronics (MIEL '95)*, Vol. 1, Nis, Serbia, September 1995.
- [148] M. F. Lambrinos, R. Valizadeh, and J. S. Colligon, "Electrical properties of ion beam sputtered and ion assisted SiO_2 SiO_xN_y and SiN_x films on silicon," *J. Vac. Sci. Technol. B*, vol. 16, no. 2, pp. 589–597, 1998.
- [149] E. V. Jelenkovic and K. Y. Tong, "Charge relaxation in nitrided and non-nitrided sputtered oxide," *J. Non-Cryst. Solids*, vol. 254, pp. 99–105, 1999.
- [150] J. U. Schmidt and B. Schmidt, "Investigation of Si nanocluster formation in sputter deposited silicon sub-oxides for nanocluster memory structures," *Mat. Sci. Engin. B*, vol. 101, pp. 28–33, 2003.
- [151] "MV-112 piezoelectric gas valve by MAXTEK, Inc., <http://www.maxtekinc.com/products/valve/>."
- [152] "REACTAFLO - a reactive sputtering controller based on optical emission spectroscopy," <http://www.genco.com/acc/reactaflo.html>.
- [153] "Micropole mass analyzer," <http://www.ferran.com/>.

- [154] PCV 25 piezoelectric gas valve by Ardenne Anlagentechnik, <http://www.ardenne-at.de/dehome/pdf/docupem.pdf>.
- [155] E. D. Palik, Ed., *Handbook of optical constants of solids*, 1st ed. 24-28 Oval road, London, NW1 7DX: Academic Press, 1985, vol. 1.
- [156] T. Karabacak, Y.-P. Zhao, G.-C. Wang, and T.-M. Lu, "Growth-front roughening in amorphous silicon films by sputtering," *Phys. Rev. B*, vol. 64, p. 085323, 2001.
- [157] W. G. Perkins and D. R. Beagal, "Diffusion and permeation of He, Ne, Ar, Kr, and D₂ through silicon oxide thin films," *J. Chem Phys.*, vol. 54, no. 4, pp. 1683–1694, 1971.
- [158] F. J. Norton, *Nature*, vol. 91, p. 701, 1961.
- [159] C. Bonafos, B. Colombeau, A. Altibelli, M. Carrada, G. B. Assayag, B. Garrido, M. López, A. Pérez-Rodríguez, J. R. Morante, and A. Claverie, "Kinetic study of group IV nanoparticles ion beam synthesized in SiO₂," *Nucl. Instr. Meth. B*, vol. 178, pp. 17–24, 2001.
- [160] B. Garrido, J. Samitier, S. Bota, and J. A. Moreno, "Reconstruction of the SiO₂ structure damaged by low-energy Ar-implanted ions," *J. Appl. Phys.*, vol. 81, no. 1, pp. 126–134, 1997.
- [161] G. Lucovsky, M. J. Manitini, J. K. Srivastava, and E. A. Irene, "Low temperature growth of silicon dioxide films: A study of chemical bonding by ellipsometry and infrared spectroscopy," *J. Vac. Sci. Technol. B*, vol. 5, no. 2, pp. 530–537, 1987.
- [162] S. Schuppler, S. L. Friedman, M. A. Marcus, D. L. Adler, Y. H. Xie, F. M. Ross, Y. J. Chabal, T. D. Harris, L. E. Brus, W. L. Brown, E. E. Chaban, P. F. Szaajowski, S. B. Christman, and P. H. Citrin, "Size, shape, and composition of luminescent species in oxidized Si nanocrystals and H-passivated porous Si," *Phys. Rev. B*, vol. 52, no. 7, pp. 4910–4925, 1995.
- [163] S. Adachi, H. Mori, and S. Ozaki, "Model dielectric function for amorphous semiconductors," *Phys. Rev. B*, vol. 66, p. 153201, 2002.
- [164] C. M. Herzinger, B. Johs, W. A. McGahan, J. A. Woollam, and W. Paulson, "Ellipsometric determination of optical constants for silicon and thermally grown silicon dioxide via a multi-sample, multi-wavelength, multi-angle investigation," *J. Appl. Phys.*, vol. 83, no. 6, pp. 3323–3336, 1998.
- [165] T. Inokuma, Y. Wakayama, T. Muramoto, R. Aoki, Y. Kurata, and S. Hasegawa, "Optical properties of Si clusters and Si nanocrystallites," *J. Appl. Phys.*, vol. 83, no. 4, pp. 2228–2234, 1998.
- [166] L. X. Yi, J. Heitman, R. Scholz, and M. Zacharias, "Si rings, Si clusters, and Si nanocrystals - different states of ultrathin SiO_x layers," *Appl. Phys. Lett.*, vol. 81, no. 22, pp. 4248–4250, 2002.

-
- [167] M. Zacharias, J. Blaesing, P. Veit, L. Tsybeskov, K. Hirschman, and P. M. Fauchet, "Thermal crystallization of amorphous Si/SiO₂ superlattices," *Appl. Phys. Lett.*, vol. 74, no. 18, pp. 2614–2616, 1999.
- [168] C. M. Herzinger and B. D. Johs, "Dielectric function parametric model, and method of use," US patent 5,796,983, 1998.
- [169] L. A. Nesbit, "Annealing characteristics of Si-rich SiO₂ films," *Appl. Phys. Lett.*, vol. 46, no. 1, pp. 38–40, 1985.
- [170] T. Müller, K.-H. Heinig, and W. Möller, "Size and location control of Si nanocrystals at ion beam synthesis in thin SiO₂ films," *Appl. Phys. Lett.*, vol. 81, no. 16, pp. 3050–3051, 2002.
- [171] M. Itsumi, H. Akiya, and T. Ueki, "The composition of octahedron structures that act as an origin of defects in thermal SiO₂ on Czochralski silicon," *J. Appl. Phys.*, vol. 78, no. 10, pp. 5984–5988, 1995.
- [172] G. Lucovsky, A. Banjeree, B. Hinds, B. Claffin, K. Koh, and H. Yang, "Minimization of suboxide transition regions at Si-SiO₂ interfaces by 900 °c rapid thermal annealing," *J. Vac. Sci. Technol. B*, vol. 15, no. 4, pp. 1074–1079, 1997.
- [173] F. J. Grunthaner and P. J. Grunthaner, "Chemical and electronic structure of the Si/SiO₂ interface," *Mater. Sci. Rep.*, vol. 1, pp. 65–160, 1986.
- [174] D. A. Muller, T. Sorsch, S. Moccio, F. H. Baumann, K. Evans-Lutterodt, and G. Timp, "The electronic structure at the atomic scale of ultrathin gate oxides," *Nature*, vol. 399, pp. 758–761, 1999.
- [175] H. Yang, H. Niimi, Y. Wu, G. Lucovsky, J. W. Keister, and J. E. Rowe, "Effect of interfacial suboxide transition regions on direct tunneling in oxide and stacked oxide-nitride gate dielectrics," *Microel. Eng.*, vol. 48, pp. 307–310, 1999.
- [176] G. Lucovsky, "Atomic structure and thermal stability of silicon suboxides in bulk thin films and in transition regions at Si-SiO₂ interfaces," *J. Non-Cryst. Solids*, vol. 227-230, pp. 1–14, 1998.
- [177] P. Yu and M. Cardona, *Fundamentals of Semiconductors-Physics and Materials Properties*. Berlin: Springer, 2001.
- [178] H. Kageshima, K. Shiraishi, and M. Uematsu, "Universal theory of Si oxidation rate and importance of interfacial Si emission," *Jpn. J. Appl. Phys. Part 2*, vol. 38, no. 9A/B, pp. L971–974, 1999.
- [179] W. J. Chang, M. P. Houng, and Y. H. Wang, "Simulation of stress-induced leakage current in silicon dioxides: A modified trap-assisted tunneling model considering gaussian-distributed traps and electron energy loss," *J. Appl. Phys.*, vol. 89, no. 11, pp. 6285–6293, 2001.
- [180] B. D. Salvo, G. Ghibaudo, G. Pananakakis, P. Masson, T. Baron, N. Buffet, A. Fernandes, and B. Guillaumot, "Experimental and theoretical investigation of nano-crystal and nitride-trap memory devices," *IEEE Trans. Electron Devices*, vol. 48, no. 8, pp. 1789–1799, 2001.

- [181] S. Huang, S. Banerjee, R. T. Tung, and S. Oda, "Electron trapping, storing, and emission in nanocrystalline Si dots by capacitance-voltage and conductance-voltage measurements," *J. Appl. Phys.*, vol. 93, no. 1, pp. 576–581, 2003.
- [182] S. J. Baik, J. H. Choi, J. Y. Lee, and K. S. Lim, "Metal-oxide-semiconductor field effect transistor using 'oxidized μ c-si/ultrathin oxide' gate structure," *Superlattices and Microstructures*, vol. 28, no. 5-6, pp. 477–483, 2000.
- [183] A. Kohno, H. Murakami, M. Ikeda, H. Nishiyama, S. Miyazaki, and M. Hirose, "Single electron charging to a Si quantum dot floating gate in MOS structures," *Extended abstracts of the 1998 Conference on Solid State Devices and Materials, Hiroshima*, pp. 174–175, 1998.
- [184] R. Ohba, N. Sugiyama, J. Koga, K. Uchida, and A. Toriumi, "Influence of channel depletion on the carrier charging characteristics in Si nanocrystal floating gate memory," *Jpn. J. Appl. Phys. Part 1*, vol. 39, no. 3a, pp. 989–993, 2000.
- [185] G. Barbottin and A. Vapaille, *Instabilities in silicon devices - silicon passivation and related instabilities*. Amsterdam: Elsevier Science Publishers B.V., 1986, vol. 2, ch. 10.
- [186] R. Ohba, N. Sugiyama, K. Uchida, J. Koga, and A. Toriumi, "Non volatile Si quantum dot memories with self aligned doubly-stacked dots," *IEEE Trans. Electron Devices*, vol. 49, no. 8, pp. 1392–1398, 2002.
- [187] Y. Shi, K. Saito, H. Ishikuro, and T. Hiramoto, "Effects of interface traps on charge retention characteristics in silicon-quantum-dot-based metal-oxide-semiconductor diodes," *Jpn. J. Appl. Phys. Part 1*, vol. 38, no. 1B, pp. 425–428, 1999.
- [188] D. Qian and D. J. Dumin, "The field, time and fluence dependencies of trap generation in silicon oxides between 5 and 13.5 nm thick," *Semicond. Sci. Technol.*, vol. 15, pp. 854–861, 2000.

Danksagung

An dieser Stelle möchte ich diejenigen würdigen, die mir diese interessante Forschungsarbeit ermöglicht bzw. zu ihrem Erfolg beigetragen haben. Mein besonderer Dank gilt PROF. DR. WOLFHARD MÖLLER, der trotz der zeitaufwendigen Leitung des Instituts immer ein offenes Ohr für die Belange der Doktoranden hatte, ebenso wie PROF. DR. MANFRED HELM, der darüberhinaus die Betreuung der Dissertation übernahm und wertvolle kritische Hinweise beim Korrekturlesen des Manuskripts gab. FRAU PD. DR. MARGIT ZACHARIAS und PROF. DR. JÖRG WEBER danke ich insbesondere für ihre freundliche Bereitschaft, als Gutachter aufzutreten.

Es war DR. HERMANN SEIFARTH, der das Projekt anregte und mir in den letzten drei Monaten seiner Tätigkeit in Rossendorf half, mit der Plasmatechnik vertraut zu werden. HERRN DR. BERND SCHMIDT, der als Abteilungsleiter die Projektverantwortung trug, möchte ich für das in mich gesetzte Vertrauen, das gute persönliche Verhältnis, kompetente Hinweise zu Fragen der Halbleitertechnologie und nicht zuletzt für die durch ihn geförderte gute Atmosphäre unter der Reinraum-Crew danken. Sein guter Draht zur Theoriegruppe um DR. KARL-HEINZ HEINIG, aber auch dessen angenehme Angewohnheit, mit einem Stück Kreide in der Hand an der Wandtafel Probleme zu wälzen, bewirkten stets ein fruchtbares Miteinander von Theorie und Experiment und förderten die Kommunikation zwischen Doktoranden und Mitarbeitern. An der lithographischen und nasschemischen Prozessierung meiner Proben im Reinraum hatten DIPL.-ING. INGRID BEATUS, HEIKE FELSMAN, GUDRUN SCHNABEL und CLAUDIA NEISSER Anteil. BERND SCHEUMANN möchte ich insbesondere für seine Unterstützung bei der aufwendigen Reparatur der Sputteranlage und DIPL.-ING. KLAUS-DIETER BUTTER für Unterstützung in Fragen der elektrischen Messtechnik danken. Zur Analyse der Proben trugen eine Reihe von Mitarbeitern bei. Dazu gehören vor allem DR. ARNDT MÜCKLICH (TEM), DR. RAINER GRÖTZSCHEL und LARS ROENTZSCH (RBS), DR. ULLRICH KREISIG (ERD), desweiteren DR. FRIEDRICH PROKERT (XRD), DR. DIETER GRAMBOLE (NRA) und FRAU CHRISTALLE (SEM). DR. THOMAS DEKORSY danke ich für die Einweisung am PL/Raman-Spektrometer, DR. RAUL GAGO für die AFM-Messungen an a-Si. DR. J. S. LIEBIG vom Fraunhofer Institut für Elektronenstrahl- und Plasmatechnologie danke ich für die kostenlose Kohlenstoffbeschichtung von Si Wafern. Eine sehr gute und von gegenseitiger Hilfsbereitschaft geprägte Atmosphäre herrschte auch unter den Rossendorfer Doktoranden und Postdocs. TORSTEN MÜLLER ermöglichte mir durch Anpassung der von ihm weiterentwickelten Monte-Carlo Software Einblick in zu erwartende Phänomene bei der Nanoclusterbildung in gesputterten Stapelschichten, wogegen ich meinem Zimmernachbarn VOLKHARD BEYER besonders für seine Anregungen zur MOS Messtechnik danke. DR. MYKOLA VINNICHENKO war mir stets ein angenehmer und insbesondere auf dem Gebiet der Ellipsometrie sehr kompeten-

ter Gesprächspartner. An DR. THIERRY CHEVOLLEAU schätzte ich nicht nur, dass er ganz selbstverständlich seine Kenntnisse zur Infrarotspektroskopie an mich und andere Doktoranden weitergab, sondern auch, dass er durch seine offene integrierende und freundliche Art viel zum menschlichen und wissenschaftlichen Austausch unter den Doktoranden beigetragen hat.

Anteil am Gelingen dieser Arbeit haben auch meine Eltern, die mir eine optimale Ausbildung ermöglichten, sowie meine Freundin Kristine.

Lebenslauf

Jan Uwe Schmidt

Geboren	08.12.1971 in Leipzig
Anschrift	Hohnsteiner Str. 5, 01099 Dresden
Ausbildung/ Werdegang	
09/78-07/86	Polytechnische Oberschule in Dresden
09/86-07/90	Spezialschule math.-techn. Richtung "Martin-Andersen-Nexö" in Dresden
08/90-07/91	Wehrersatzdienst am Universitätsklinikum in Dresden
09/91-11/97	Physik-Studium an der Technischen Universität Dresden
12/96-12/97:	Diplomarbeit am Institut für Angewandte Photophysik (Eigenbau und Erprobung eines Raster-Nahfeldmikroskops)
01/98-12/99	Stipendiat am Graduiertenkolleg "Sensorik" der TU Dresden
01/00-05/03	Wissenschaftlicher Mitarbeiter am Forschungszentrum Rossendorf
seit 06/03	Wissenschaftlicher Mitarbeiter am Fraunhofer Institut für Photonische Mikrosysteme (IPMS) in Dresden
Abschlüsse	
1997	Diplom-Physiker (TU-Dresden): "sehr gut"
1990	Abitur (Spezialschule Dresden): "sehr gut"
Auslands- aufenthalte	
09/93-07/94	Auslandsstudium am Department of Physics der Heriot-Watt University Edinburgh, UK
01/98-03/98	Forschungsaufenthalt am Department of Physics University of North Carolina at Charlotte, USA
Publikationen	8 Publikationen als Autor und Co-Autor (Stand: November 2003)

Wissenschaftliche Publikationen

Artikel in Zeitschriften

1. *Investigation of Si nanocluster formation in sputter deposited silicon sub-oxides for nanocluster-memory structures*
J. U. Schmidt, and B. Schmidt, *Mat. Sci. Engin. B* **101**, 28-33 (2003).
2. *Silicon Nanocrystal Memory Devices prepared by Magnetron Sputtering*
J. U. Schmidt, and B. Schmidt,
Jahresbericht des Instituts für Ionenstrahlphysik und Materialforschung am Forschungszentrum Rossendorf (2002).
3. *Phenomenological model of reactive r.f.-magnetron sputtering of Si in Ar/O₂ atmosphere for the prediction of SiO_x thin film stoichiometry from process parameters*
H. Seifarth, J. U. Schmidt, R. Grötzschel, and M. Klimenkov, *Thin Solid Films* **389**, 108-115 (2001).
4. *Surface enhanced Raman scattering spectroscopy of carbon domains on individual Ag nanoparticles on a 25 millisecond time scale*
P. J. Moyer, J. U. Schmidt, L. M. Eng, A. J. Meixner, G. W. Sandmann, H. Dietz, and W. Plieth, *J. Am. Chem. Soc.* **122** 5409-5410 (2000).
5. *Dependence of radiative lifetimes of porous silicon on excitation wavelength and intensity*
P. J. Moyer, A. Pridmore, T. Martin, J. U. Schmidt, T. Hasche, L. M. Eng, and J. L. Gole, *Appl. Phys. Lett.* **76** (19), 2683-2685 (2000).
6. *Shear force interaction in the viscous damping regime studied at 100 pN force resolution*
J. U. Schmidt, H. Bergander, and L. M. Eng, *J. Appl. Phys.* **87**, 3108-3112 (2000).
7. *Experimental and theoretical analysis of shear-force interaction in the non-contact regime with 100 pN force resolution*
J. U. Schmidt, H. Bergander, and L. M. Eng, *Appl. Surf. Sci.* **157** (4), 295-301 (2000).
8. *Nanocrystalline structures of metal deposits studied by locally resolved Raman spectroscopy*

W. Plieth, H. Dietz, G. Sandmann, A. J. Meixner, D. Weber, P. Moyer, and J. U. Schmidt, *Electrochim. Acta* **44** (4), 2025-2036 (1999).

9. *Non-Contact Shear Force Microscopy with 100 pN Force Resolution*
J. U. Schmidt, H. Bergander, and L. M. Eng
in: G. Gerlach (ed.): *Dresdner Beiträge zur Sensorik*, Volume 3, 29-40 (1999).
Dresden University Press (1999).

Vorträge auf Konferenzen und Workshops

1. *Plasma-PVD für "Nano-Flash"-Speicher auf der Basis von Silizium-Nanokristallen*
J. U. Schmidt,
Frühjahrssitzung 2003 des Arbeitskreises Plasmaphysik, 19.-20.03.2003, Leipzig
2. *Si-nanocluster based memory structures - preparation by thermal annealing of sputtered silicon suboxides, optical and electrical characterization*
J. U. Schmidt,
Woollam Workshop "Spectroscopic Ellipsometry", 15.-16.10.2002, Darmstadt
3. *Si nanocluster layers embedded in SiO₂ prepared by sputtering and annealing of SiO₂/SiO_x stacks - electrical and optical characterization*
J. U. Schmidt,
International Workshop on "Nanostructures for Electronics and Optics (NEOP)",
06.-09.10.2002, Dresden
4. *Investigation of Si nanocluster formation in sputter deposited silicon suboxides and application to nanocluster memory structures*
J. U. Schmidt, B. Schmidt,
EMRS 2002 Spring Conference, 18.-21.07.2002, Strassburg, France
5. *Si-nanoclusters for memory applications - preparation by magnetron sputtering, electrical and optical characterization*
J. U. Schmidt,
Institutsseminar am Institut für Tieftemperaturphysik der TU Dresden, 23.05.2002
6. *Investigation of silicon-nanocrystal memory structures obtained by r.f. sputtering*
J. U. Schmidt,
Frühjahrstagung der DPG, 26.-30.03.2001, Hamburg
7. *Spectral investigations of intermittent surface-enhanced Raman scattering (SERS) from individual silver nanoclusters on a 25 millisecond time scale*
J. U. Schmidt, P. J. Moyer, W. Plieth und A. J. Meixner,
Frühjahrstagung der DPG, 22.03.-26.03.1999, Münster
8. *Non-contact shear force feedback for near-field scanning optical microscopy*
J. U. Schmidt, H. Bergander, and L. M. Eng
2nd Int. Workshop on non-contact Atomic Force Microscopy (nc-AFM '99),
01.-04.09 1999, Pontresina, Schweiz

9. *Optical phenomena of single silver and gold nuclei*
W. Plieth, H. Dietz, G. Sandmann, A. J. Meixner, D. Weber, and J. U. Schmidt
1999 Joint International Meeting:
196th Meeting of The Electrochemical Society and
1999 Fall Meeting of The Electrochemical Society of Japan with technical cosponsorship of The Japan Society of Applied Physics,
17.10-22.10.1999, Honolulu, Hawaii

Poster auf Konferenzen

1. *Si-nanocrystal memory devices prepared by r.f. magnetron sputtering*
J. U. Schmidt, and B. Schmidt,
MRS 2002 Fall Meeting,
24-29.11.2002, Boston, USA
2. *Investigation of MOS structures with embedded Si-nanocrystals obtained by r.f.-sputtering*
J. U. Schmidt, and B. Schmidt,
12th International School on Vacuum, Electron and Ion Technologies (VEIT '01),
17-21.09.2001, Varna, Bulgarien
3. *Shear force interaction in the viscous damping regime studied at 100 pN force resolution*
L. M. Eng, J. U. Schmidt, and H. Bergander
6th International Conference on Near Field Optics and Related Techniques (NFO '6),
27-31.08.2000, University of Twente, Niederlande

Erklärung

Hiermit versichere ich, dass ich die vorliegende Arbeit ohne unzulässige Hilfe Dritter und ohne Benutzung anderer als der angegebenen Hilfsmittel angefertigt habe; die aus fremden Quellen direkt oder indirekt übernommenen Gedanken sind als solche kenntlich gemacht. Die Arbeit wurde bisher weder im Inland noch im Ausland in gleicher oder ähnlicher Form einer anderen Prüfungsbehörde vorgelegt.

Diese Dissertation wurde am Institut für Ionenstrahlphysik und Materialforschung des Forschungszentrums Rossendorf e.V. unter Betreuung durch DR. BERND SCHMIDT angefertigt. Es haben keine früheren erfolglosen Promotionsverfahren stattgefunden. Die Promotionsordnung der Technischen Universität Dresden vom 20. März 2000 wird anerkannt.

Dresden, am 01. Februar 2004

Major statements (Thesen)

- Aim of this work was to investigate an alternative technology for a novel EEPROM-like memory device whose operation principle is based on charge trapping in silicon nanoclusters (Si NC) embedded in the gate oxide of a field-effect transistor ("Silicon nanocrystal-memory"). In the proposed new two-step approach first a dielectric gate stack is prepared by sputter-depositing SiO_x ($x < 2$) and SiO_2 layers onto a thermal tunnel-oxide on silicon. Later a high temperature anneal transforms the homogeneous SiO_x layer into a layer of SiO_2 with embedded Si NC and completes the processing of the dielectric gate stack.
- Different sputtering techniques for SiO_x deposition were evaluated: reactive rf sputtering from a Si target and rf/dc co-sputtering from SiO_2 and Si targets respectively. The co-sputtering technique for SiO_x was found to be most suitable with respect to a good composition control at low deposition rates and negligible particle generation. SiO_2 films were rf sputtered from a SiO_2 target.
- SiO_x thin films were investigated with respect to composition by variable angle spectroscopic ellipsometry (VASE), and ion beam techniques like elastic recoil detection (ERD), and Rutherford back-scattering (RBS). Structure and the effect of film composition on the nucleation of Si NC were probed using cross-section electron microscopy (XTEM), and optical methods, such as photoluminescence (PL), Fourier transform infrared spectroscopy (FTIR) and VASE.
- Annealing conditions enabling the formation of a high density of small isolated Si NC were derived. XTEM and PL were used to estimate the mean size of Si NC. It was found that for decreased annealing times or lowered annealing temperatures an unchanged mean Si NC size can be obtained if the Si excess is increased. The growth and crystallization of Si NC was confirmed by an investigation of the mean optical constants of Si NC after different anneals using VASE.
- Using the Kinetic 3D Monte-Carlo method developed by Heinig et al. [50], the annealing process of differently designed $\text{SiO}_2/\text{SiO}_x$ gate stacks was simulated to complement corresponding experiments, but also to compare two limiting cases: The growth of 1-2 nm wide Si NC in comparably thick (10-20 nm) or thin (1.5 nm) SiO_x films embedded in SiO_2 . In the first case the mean Si NC parameters were strongly dependent on annealing time. The vertical Si NC distribution showed oscillations growing from the interfaces of the SiO_x film. In contrast in the second case the Si NC size and vertical position were governed by thickness and position of the SiO_x film instead of the annealing regime. Consequently a superlattice of ultrathin $\text{SiO}_2/\text{SiO}_x$ films is considered as an even more favorable gate stack

design for a Si nanocrystal memory. It guarantees a high density of isolated Si NC with a narrow size distribution, is rather insensitive to the annealing regime and allows the highest degree of control over the resulting gate stack structure. In addition the vertical and in-plane separation of Si NC can be adjusted separately by adjusting the SiO₂ interlayer thickness and the SiO_x composition respectively.

- Finally *MOS capacitors with Si NC embedded in the gate oxide* were prepared: Onto a 2 nm thermal tunnel oxide 10 nm or 20 nm SiO_x films ($x = 1.8, 1.6, 1.4, 2$) were deposited and covered with a 20 nm SiO₂ layer. Si NC were formed by a 2 min rapid thermal annealing (RTA) step in Ar/N₂ at temperatures of 800 °C, 950 °C or 1100 °C. The samples were investigated using XTEM, VASE, PL and various electrical tests implemented in an accordingly developed TEST-POINT application. In particular the charge trapping and retention behavior were evaluated using the constant-capacity method. The main experimental results are summarized below.
- MOS reference capacitors *without SiO_x interlayer* showed small leakage currents, and breakdown fields as high as 8 MV/cm. For MOS capacitors *with SiO_x interlayer* the effective sheet density of both electron and hole-traps increased with annealing temperature. The growth of Si NC related PL intensity with annealing temperature indicates that this effect corresponds to an increasing density of Si precipitates. From the PL energy, the mean Si NC size was estimated to range between 1.9 nm and 3.7 nm, depending on Si excess and anneal. Charging tests showed that a reasonable memory window (1 V) can be achieved using 2 ms write pulses of 12.5 V, while the charge retention time was measured to exceed 1 day. Since for the investigated samples the charge loss was governed by direct tunneling, the field of the stored charge acted as driving force of the current, which rendered a simple extrapolation of the long term retention behavior (as common practice for memories with tunnel-oxides above 5 nm) impossible. The stability of the tested capacitors was very good. Random-samples selected for endurance tests showed virtually no degradation after 10⁷ write/erase cycles. At high Si excess, increased annealing temperatures resulted in higher transient charging currents, but a faster de-trapping of charge carriers. The increasing density of Si NC causes a transition from localized charge storage in isolated Si NC to a continuous-floating-gate-like behavior (electrons delocalized over sets of Si NC).
- In summary, the developed sputtering method was shown to be well suited for preparation of Si nanocrystal memories. All processing steps, including the thermal anneals for Si NC formation, are fully compatible with the constraints of advanced CMOS technology.
- Outlook: In order to further improve the device properties, in particular the charge retention behavior, it is suggested to replace the homogeneous SiO_x layer by a sequence of 3-4 SiO₂/SiO_x layers with a SiO_x layer thickness of 1-2 nm and a Si excess of 25 at%. Rapid thermal annealing will in this case lead to constrained growth of single layers of Si NC in the SiO_x regions, which enables a better control over location, diameter and lateral distribution of Si NC. Such superlattices could be applied not only in Si nanocrystal memories, but also in the field of Si based light emitters and optical interconnects.